A NON-LINEAR FORCE-FREE FIELD MODEL FOR THE SOLAR MAGNETIC CARPET

Karen Alison Meyer

A Thesis Submitted for the Degree of PhD
at the
University of St Andrews

2012

A Non-Linear Force-Free Field Model for the Solar Magnetic Carpet

K. A. Meyer

Thesis submitted for the degree of Doctor of Philosophy

of the University of St Andrews

13th March 2012

Abstract

The magnetic carpet is defined to be the small-scale photospheric magnetic field of the quiet Sun. Observations of the magnetic carpet show it to be highly dynamic, where the time taken for all flux within the magnetic carpet to be replaced is on the order of just a few hours. The magnetic carpet is continually evolving due to the Sun's underlying convection and the interaction of small-scale magnetic features with one another. Due to this, the small-scale coronal field of the magnetic carpet is also expected to be highly dynamic and complex. Previous modelling has shown that much of the flux from the magnetic carpet is stored along low-lying closed connections between magnetic features. This indicates that significant coronal heating could occur low down in the small-scale corona.

In this thesis, a new two-component magnetic field model is developed for the evolution of the magnetic carpet. A 2D model is constructed to realistically simulate the evolution of the photospheric field of the magnetic carpet, where many of the parameters for the model are taken from observational studies. The photospheric model contains a granular and supergranular flow profile to describe the motion of the small-scale magnetic features, and includes the processes of flux emergence, cancellation, coalescence and fragmentation. This 2D model then couples to a 3D model as the lower boundary condition, which drives the evolution of the coronal field through a series of non-linear force-free states, via a magnetofrictional relaxation technique.

We first apply the magnetofrictional technique to consider the coronal evolution of three basic small-scale photospheric processes: emergence, cancellation and flyby. We consider the interaction of the magnetic features with an overlying coronal magnetic field, and quantify magnetic energy build-up, storage and dissipation. The magnetofrictional technique is then applied to synthetic magnetograms produced from the 2D model, to simulate the evolution of the coronal field in a situation involving many hundreds of magnetic features. We conduct a preliminary analysis of the resultant 3D simulations, considering the magnetic energy stored and dissipated, as well as regions of enhanced velocity and electric current density within the coronal volume. The simulations show that the so-called 'quiet Sun' is not quiet and a significant amount of complex interactions take place.

Declaration

I, Karen Meyer, hereby certify that this thesis, which is approximately 52,000 words in length, has been written by me, that it is the record of work carried out by me and that it has not been submitted in any previous application for a higher degree.

I was admitted as a research student in September 2008 and as a candidate for the degree of Doctor of Philosophy in September 2009; the higher study for which this is a record was carried out in the University of St Andrews between 2008 and 2012.

Date: _____ Signature of Candidate: _____.

I hereby certify that the candidate has fulfilled the conditions of the Resolution and Regulations appropriate for the degree of Doctor of Philosophy in the University of St Andrews and that the candidate is qualified to submit this thesis in application for that degree.

Date: _____ Signature of Supervisor: _____.

In submitting this thesis to the University of St Andrews we understand that we are giving permission for it to be made available for use in accordance with the regulations of the University Library for the time being in force, subject to any copyright vested in the work not being affected thereby. We also understand that the title and the abstract will be published, and that a copy of the work may be made and supplied to any bona fide library or research worker, that my thesis will be electronically accessible for personal or research use unless exempt by award of an embargo as requested below, and that the library has the right to migrate my thesis into new electronic forms as required to ensure continued access to the thesis. We have obtained any third-party copyright permissions that may be required in order to allow such access and migration, or have requested the appropriate embargo below.

The following is an agreed request by candidate and supervisor regarding the electronic publication of this thesis:

Access to printed copy but embargo of electronic publication of thesis for a period of 2 years on the following ground(s): publication would preclude future publication.

Date: _____ Signature of Candidate: _____.

Date: _____ Signature of Supervisor: _____.

Acknowledgements

First I would like to thank my supervisor, Duncan Mackay, for his guidance, patience and encouragement over the last three and a half years. The fact that this PhD has gone so smoothly is largely down to him, and this work would not have been possible without him. I am also grateful to the rest of the staff in the solar group for always being willing to give help and advice over the years, and to the UK Science and Technology Facilities Council (STFC) for financial support.

I would like to thank Aad van Ballegooijen for hosting me at the CfA for two summers, and for many useful discussions and helpful input into my projects during my stay. Also thanks to the rest of the CfA for their warm hospitality, and to all the wonderful people I met through the REU programme - I miss you all!

Thanks to all my friends in the solar group in St Andrews for making my time here such an enjoyable one - for the fantastic company and for making me laugh til it hurts. With all the coffee, cake and procrastinatory web pages it's a wonder we get anything done at all! I would also like to thank Greg Kiddie for his support and for keeping me fuelled with tea and chilli con carne.

Last, but not least, I would like to thank my family for always supporting and encouraging me in everything I do.

Publications

The following published papers include material from this thesis:

1. Meyer, K.A., Mackay, D.H., van Ballegooijen, A.A., & Parnell, C.E.: 2011, 'Solar Magnetic Carpet I: Simulation of Synthetic Magnetograms', *Sol. Phys.* **272**, 29.

2. Meyer, K.A., Mackay, D.H., & van Ballegooijen, A.A.: 2012, 'Solar Magnetic Carpet II: Coronal Interactions of Small-Scale Magnetic Fields', *Sol. Phys.* **278**, 149.

3. Meyer, K.A., Mackay, D.H., & van Ballegooijen, A.A.: 2012, 'Solar Magnetic Carpet III: Coronal Modelling of Synthetic Magnetograms', *Sol. Phys. in preparation.*

A quote is mandatory.

– D. H. Mackay

Contents

Chapter 1

Introduction

1.1 Structure of the Sun

The Sun is an average, middle-aged, main sequence star of spectral type G2. It is roughly 4.5 billion years old, of mass $M_\odot = 1.99 \times 10^{30}$ kg and radius $R_\odot = 696,000$ km. Situated at the centre of the solar system, it is 149 million km from the Earth, and contains over 99% of the solar system's mass. The Sun is of great importance to our planet, providing us with heat, light and energy. Without it, life would not exist on the Earth. It is also our closest star; the next nearest is Proxima Centauri at $270,000$ times the distance of the Sun. This makes the Sun the only star that can be studied in any detail. Understanding the Sun can give us an understanding of stars in general.

The Sun is structured into many distinct layers, as illustrated in Figure 1.1(a). One area of Solar research, *helioseismology*, the study of wave oscillations in the Sun, has allowed us to learn a great deal about the interior of our star such as its temperature, composition and flows. The structure of the Sun is described below.

The core of the Sun spans from its centre to roughly $0.25R_\odot$, and has a temperature of 1.5×10^7 K (Noyes, 1982). This extremely high temperature, in addition to the high pressure within the core, allows the process of nuclear fusion to occur. This involves the fusing together of hydrogen atoms into helium, which releases a significant amount of energy in the form of photons and neutrinos. Every second, over 6×10^{11} kg of hydrogen is converted into helium within the Sun's core (Phillips, 1992).

The next layer of the Sun is the radiative zone, spanning from approximately $0.25R_\odot - 0.7R_\odot$. The temperature in this region is still high, at around 8×10^6 K. It is so hot that any electrons orbiting atomic nuclei are quickly stripped away, creating many free particles. Within the

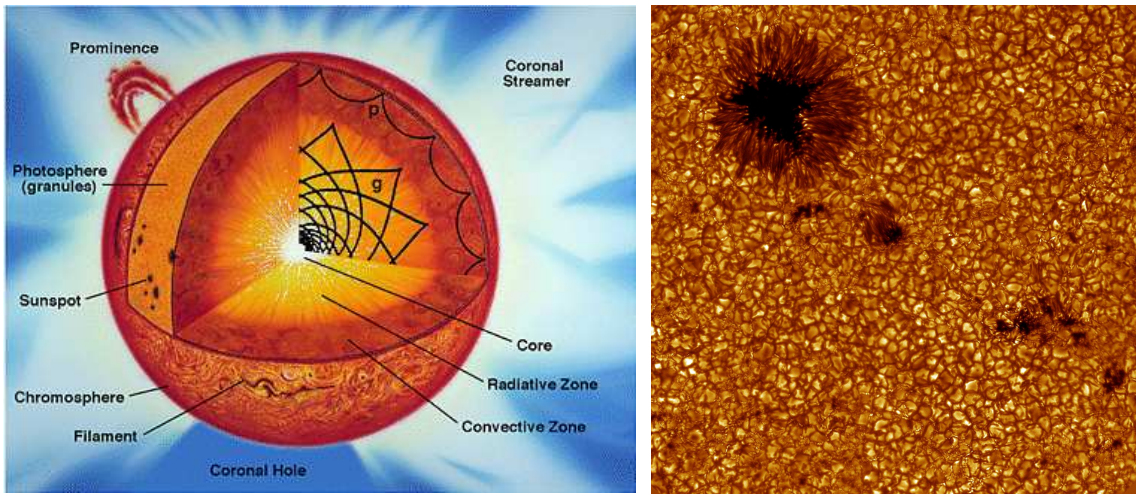

(a) **(b)**

Figure 1.1: (a) Cartoon illustrating the layers of the Sun and solar atmosphere. (Image credit: http://sohowww.nascom.nasa.gov/) (b) A continuum image (at 436.4 nm) of a sunspot and granulation observed by the Swedish Solar Telescope (Image credit: O. Engvold, J. E. Wiik, L. Rouppe van der Voort, Oslo, 2003).

radiative zone, energy diffuses outward from the core as photons, which are continually scattered due to encounters with particles such as electrons and protons. The result is a random walk, causing the photons to take an estimated 1.7×10^5 years to reach the surface of the Sun from its core (Mitalas and Sills, 1992).

Moving further away from the core, the temperature decreases to a point where elements larger than hydrogen may be only partially ionised, i.e. some atomic nuclei may have some orbiting electrons ($\sim 1 - 2 \times 10^6$ K). This allows electromagnetic radiation to be more easily absorbed by the atoms, and the plasma becomes more opaque. Since the outflow of energy via radiation is reduced, temperature gradients in the plasma result in it becoming convectively unstable, forming convective currents. The region where this occurs is called the convection zone, and spans from $0.7R_\odot$ to the solar surface. Hot material rises to the surface, cools and falls, forming large convective cells (Priest, 1982). On the solar surface these convective cells are known as granules when on the scale of $0.5 - 2$ Mm or supergranules when on the scale of 30 Mm (Rieutord and Rincon, 2010) and give the appearance of a bubbling, boiling viscous fluid, such as jam (see Figure 1.1(b)).

The visible surface of the Sun is known as the photosphere. At this level, the temperature has dropped to around $6,000$ K. The photosphere is only a few hundred km in depth, and is constantly in motion due to the convection occurring beneath. Many interesting features and phenomena may be observed on the solar surface, some of which will be discussed in the following sections.

As we move away from the photosphere into the first layer of the solar atmosphere, the chro-

mosphere, the temperature briefly continues to drop, reaching $4,300$ K at its coolest (500 km above the photosphere). Then something surprising happens. As we ascend through the chromosphere into a narrow layer known as the transition region, the temperature suddenly increases to several million degrees within the Sun's outer atmosphere, the solar corona (see Figure 1.2). The question of why the corona is so hot is a long-standing mystery in the field of solar physics. Because the surface of the Sun is so much cooler, the corona cannot be heated by thermal energy transport. Many theories exist that try to explain coronal heating, but we have yet to fully comprehend the heating mechanism. Theories include heating by electro-magnetic waves (e.g. Kuperus et al. (1981); Heyvaerts and Priest (1983); Roberts (2000)), and magnetic reconnection (e.g. Heyvaerts and Priest (1984); Longcope (2004); Hood et al. (2009); Wilmot-Smith et al. (2011)). Magnetic reconnection causes restructuring of the magnetic field within the coronal volume in response to footpoint motions on the photosphere (Galsgaard and Nordlund, 1996; Priest et al., 2002; Mellor et al., 2005; De Moortel and Galsgaard, 2006). No matter the exact mechanism employed, coronal heating appears to be intimately linked with the Sun's magnetic field (Erdélyi, 2004).

Within the quiet Sun corona, energy may be released in a variety of ways, such as described below. Withbroe and Noyes (1977) determined that the amount of heating required to maintain the quiet Sun corona is 3×10^5 ergs cm^{-2} s^{-1}. There are a number of small-scale, transient phenomena associated with sporadic energy release, such as X-ray bright points (XBP) or nanoflares. XBPs are localised brightenings within the quiet Sun corona, observed as point-like features or small loops (Golub et al., 1974). They are typically associated with opposite polarity magnetic features on the photosphere, and in most cases with cancellation events (Webb et al., 1993). While XBP are not believed to be the primary source of quiet Sun heating, as they radiate only around 5×10^4 ergs cm^{-2} s^{-1} (Habbal and Grace, 1991), they do provide a contribution (Longcope and Kankelborg, 1999). Many authors have considered the interaction between pairs of small-scale magnetic elements in association with XBP (e.g. Priest et al. (1994), Longcope (1998), Longcope and Kankelborg (1999), von Rekowski et al. (2006)). Nanoflares are localised, impulsive bursts of energy, releasing energy on the order of 10^{24} ergs (Parker, 1988; Golub and Pasachoff, 1997). It is believed that nanoflares provide a contribution to coronal heating by dissipating energy through magnetic reconnection. Several authors have considered nanoflares in this context, including Cargill (1993), Browning et al. (2004), Browning et al. (2008) and Sakamoto et al. (2009).

1.2 The Sun's Magnetic Field

In addition to having a global dipolar magnetic field which varies in strength throughout the solar cycle, complex distributions of magnetic fields exist within the Sun on all spatial and time-scales. One of the most important discoveries in solar physics was made by Hale (1908). He found that

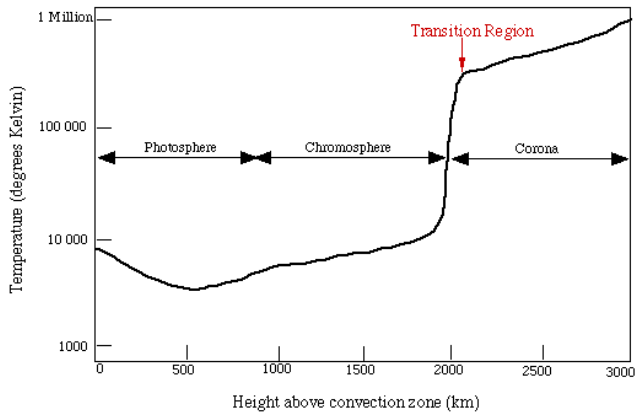

Figure 1.2: Graph showing how the temperature of the solar atmosphere varies as a function of height above the photosphere. A dramatic increase in temperature occurs in the transition region between the chromosphere and the corona. (Image credit: http://solar.physics.montana.edu/)

sunspots are in fact locations of extremely strong magnetic fields on the solar surface. An example of a sunspot can be seen in the top left corner of Figure 1.1(b). They appear dark because they are cooler than the surrounding photosphere, at around $4,500$ K (Leblanc, 2010). The reason for this lower temperature is that convection is suppressed by the intense magnetic field ($\sim 2,000$ G, Priest (1982)), which reduces the amount of hot plasma that is brought to the surface.

Figure 1.3(a) is a *magnetogram* taken by the Helioseismic and Magnetic Imager (HMI) on board the spacecraft Solar Dynamics Observatory (SDO). Photospheric magnetograms show the line-of-sight component of magnetic fields on the surface of the Sun. White and black regions correspond to positive and negative magnetic field, respectively. Magnetograms are produced by taking advantage of the Zeeman effect, which is the splitting of spectral lines under the presence of a magnetic field. The strength of the magnetic field is proportional to the distance of the split between the lines. Using the four Zeeman-split stokes parameters, I, Q, U and V, vector magnetograms may also be constructed, which give the full 3D magnetic field (Skumanich and Lites, 1987). An excellent overview of observational and theoretical methods for the investigation of solar magnetic fields can be found in Solanki (1993).

In the magnetogram, sunspots appear in large bipolar regions. Figure 1.3(b) is an image taken at the same time as the magnetogram by SDO's Atmospheric Imaging Assembly (AIA) in 171 Å. This corresponds to a coronal temperature of roughly $630,000$ K. One can clearly see that the bright, hot regions in the AIA image lie exactly above the strong magnetic fields observed at the photosphere, indicating that the magnetic field plays an important role in the heating and structuring of the solar corona. The amount of magnetic flux on the Sun varies significantly, as the Sun undergoes an 11-year cycle of activity. At *solar maximum*, many sunspots are observed and in turn, the solar corona is very bright and dynamic. At *solar minimum*, few or no sunspots

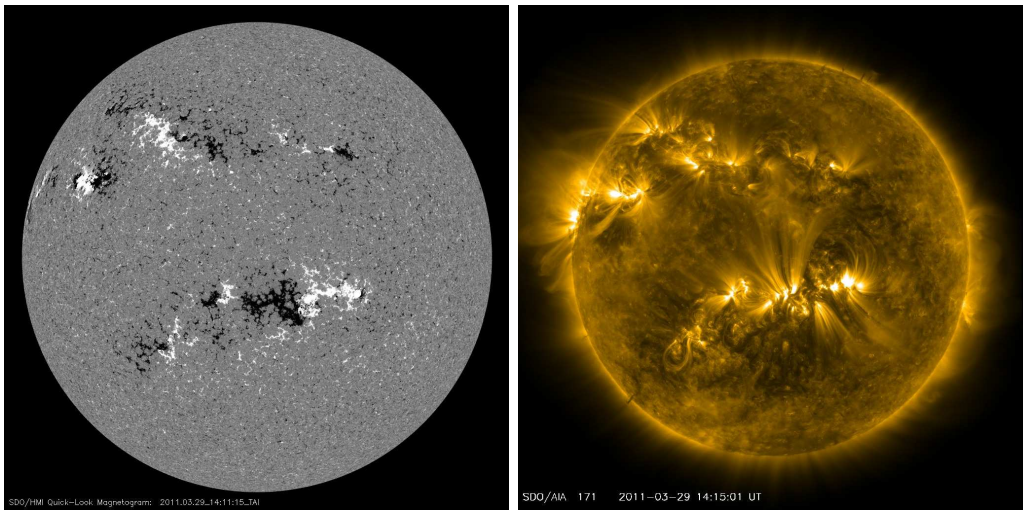

(a) **(b)**

Figure 1.3: (a) A full-disc magnetogram taken by SDO/HMI on the 29th of March, 2011. (b) An SDO/AIA 171 Å image taken on the same day. (Image credit: http://sdo.gsfc.nasa.gov/)

are observed, and the corona is quiet. Solar magnetic fields are observed on a wide variety of scales, however, within this thesis we are interested in small-scale magnetic fields observed in quiet regions of the Sun.

1.2.1 The Solar Magnetic Carpet

The *magnetic carpet* is the term given to the small-scale photospheric magnetic field of the quiet Sun. It is composed of a mixture of randomly oriented positive and negative magnetic flux features that are continually evolving. An example of the solar magnetic carpet can be seen in Figure 1.4(a), which shows a magnetogram taken by SDO/HMI. The magnetogram is 70×70 Mm^2, so its width is around twenty times smaller than the diameter of the Sun ($1,392$ Mm).

Photospheric motions on the scale of the magnetic carpet are dominated by the flow pattern of convective cells known as supergranules. These cells range in diameter from roughly $10,000$ km to $50,000$ km, with an average diameter of $14,000$ km (Hagenaar et al., 1997). Their flow pattern takes the form of an upflow at the cell centre, followed by a horizontal flow that moves radially out from the cell centre at roughly 0.5 km s^{-1} and downflow at the cell boundaries (Simon and Leighton, 1964; Paniveni et al., 2004; Rieutord and Rincon, 2010). Wang and Zirin (1989) found the magnitude of a supergranule's vertical velocity, both upflow and downflow, to have an upper limit of 0.1 km s^{-1}. The strongest downflows occur at locations where two or more cells meet and as a result, magnetic flux tends to build up along the boundaries of supergranular cells after being swept from the centre by the radial outflow. This is illustrated by the SOHO/MDI magnetogram

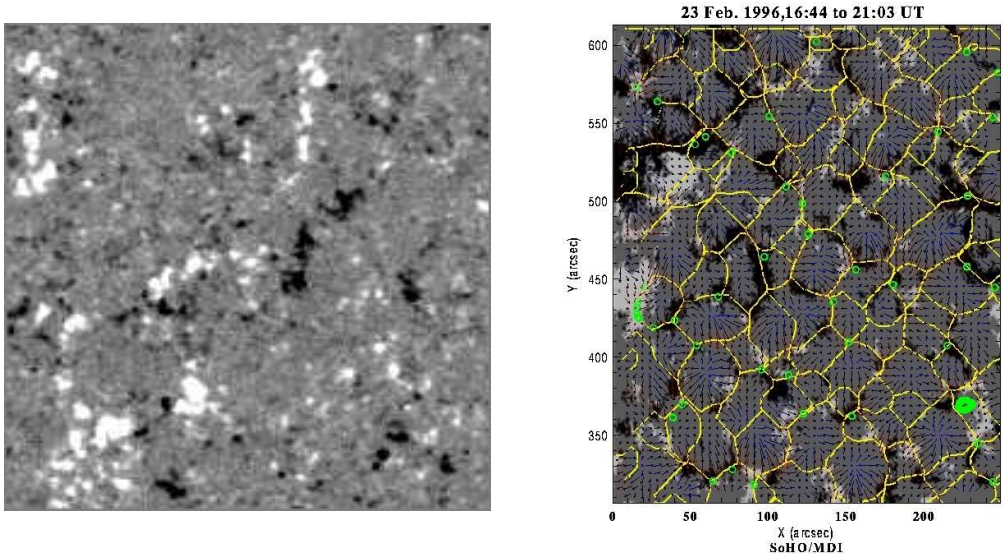

(a) **(b)**

Figure 1.4: (a) An SDO/HMI magnetogram of area 70×70 Mm^2, saturated at ± 30 G. (b) A SOHO/MDI magnetogram. The boundaries of supergranule cells are marked in yellow, and arrows indicate the supergranular flow pattern. (Image credit: http://sohowww.nascom.nasa.gov/)

shown in Figure 1.4(b). The supergranule cell boundaries are marked in yellow, and it can be seen that the majority of the magnetic flux features are located along these lines, and in particular at the intersection of multiple cells.

Over the last two decades, our understanding of the magnetic carpet has greatly increased due to missions such as SOHO/MDI (launched December 2, 1995) and Hinode/SOT (launched September 23, 2006). Through these missions, many observational studies of the properties of the magnetic carpet have been carried out (Schrijver et al., 1997; Hagenaar, 2001; Parnell, 2002; Hagenaar et al., 2003; DeForest et al., 2007; McIntosh et al., 2007; de Wijn et al., 2008; Hagenaar et al., 2008; Lamb et al., 2008; Lites, 2009; Parnell et al., 2009; Lamb et al., 2010; Thornton and Parnell, 2011). Small-scale quiet Sun flux is generally categorised into three main classifications: ephemeral regions, network features and internetwork fields.

Ephemeral regions are newly emerging bipolar pairs, that appear within supergranular cells. They have an average lifespan of 4.4 hr (hours) and typical diameters of $3,000-5,000$ km (Harvey and Martin, 1973). Wang (1988) found that ephemeral regions have a slight tendency to emerge near the boundaries of supergranules, rather than at the cell centre. For the first 30 min (minutes) after appearing, the two opposite polarities are found to separate from one another at a velocity of $4.5 - 5$ km s^{-1} (Harvey, 1993; Title, 2000). Later, they slow to a velocity that is on the order of the underlying supergranular flow, ~ 0.5 km s^{-1} (Hagenaar et al., 2003). Schrijver et al. (1997) gave the average absolute flux of an ephemeral region to be 1.3×10^{19} Mx, whereas Chae et al.

(2001) found a slightly higher value of 2.8×10^{19} Mx.

Network features are larger features, with diameters in the range $1,000 - 10,000$ km and fluxes of $10^{18} - 10^{19}$ Mx, that are typically found at sites of strong downflow, *i.e.* the edges of the supergranular cells (Martin, 1988). They are slow moving, with an average velocity of just 0.06 km s^{-1} (Zirin, 1985). They do not emerge as network features; rather they are produced from the residuals of other flux features. Around 90% of their flux originates from ephemeral regions, with the remaining 10% arising from *internetwork features* (Martin, 1990).

Internetwork features are the smallest of the three types of small-scale magnetic flux features. They also emerge within supergranule cells as bipolar pairs, and are swept towards the boundaries by radial flows in a similar manner to ephemeral regions, where they interact with the magnetic network (Martin, 1988). Their mean diameter is $2,000$ km, and their fluxes extend down to the detection limit of present instruments (on the order of 10^{15} Mx for the IMaX instrument on board the Sunrise mission (Barthol et al., 2011)). Wang et al. (1995) found their flux to be in the range $10^{16} - 2 \times 10^{18}$ Mx, with a peak in the distribution at 6×10^{16} Mx. De Wijn et al. (2008) found a rms velocity of 1.57 ± 0.08 km s^{-1}, and an average lifetime of just 10 min for internetwork features. More recently, Zhou et al. (2010) deduced an even smaller average lifespan of just 2.9 ± 2.0 min.

In addition to supergranular flows, there are four main processes by which the magnetic flux within the magnetic carpet may evolve. Flux *emergence* is the appearance of pairs or clusters of new magnetic flux, with equal amounts of flux emerging in both the positive and negative polarities. *Cancellation* occurs when features of opposite polarity come into contact and mutually lose flux (Livi et al., 1985; Martin et al., 1985). If two or more features of the same polarity merge together, this is known as *coalescence*. Finally, *fragmentation* is the splitting of a large feature into several smaller features. Parnell (2001) suggested granulation as a possible cause of fragmentation. Granulation occurs on the scale of roughly $1,000$ km (Spruit et al., 1990). Since granules are much smaller than supergranules, granulation has little effect on the overall photospheric motion of magnetic features. However, as larger network features may be spread over several tens of granules, their continual evolution and flow could be a factor in breaking apart large features into smaller ones.

Due to these motions and flux evolution processes, the quiet Sun photosphere is highly dynamic. Using a series of full-disc 96 min MDI magnetograms, Hagenaar (2001) found that the time taken for all flux within the quiet Sun photosphere to be replaced, 'the flux replacement timescale', was around 14 hr. However, later studies determined this value to be an order of magnitude smaller, at just $1 - 2$ hr (Hagenaar et al. (2008)). The difference in results is due to the fact that the later study used a magnetogram series of cadence $\Delta t = 5$ min, whereas in the study of Hagenaar (2001), the data had a cadence of $\Delta t = 96$ min. It will be interesting to see if this value lowers even further with the study of new higher cadence, higher resolution data from Hinode and

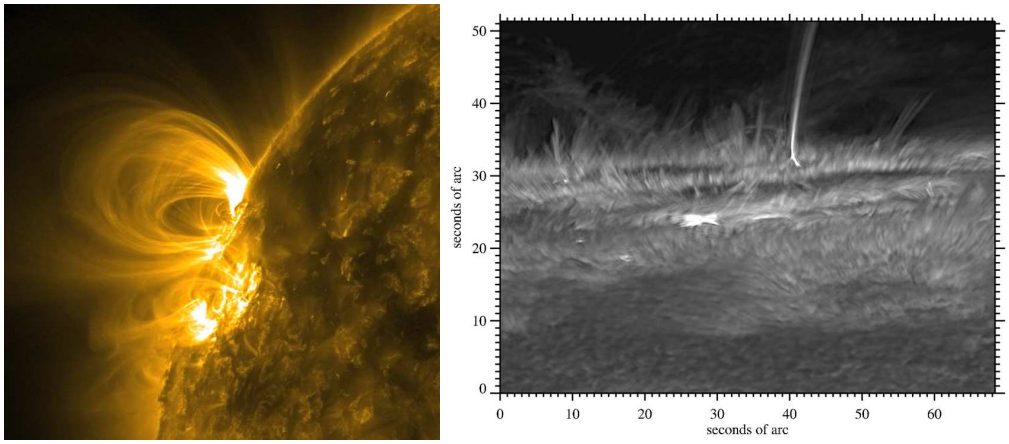

(a) **(b)**

Figure 1.5: (a) Coronal loops observed in 171 Å by SDO/AIA. (Image credit: http://sdo.gsfc.nasa.gov/) (b) Spicules and a surge observed in Ca II H by the Dutch Open Telescope. (http://dot.astro.uu.nl/)

SDO. Since magnetic fields from the magnetic carpet extend up into the solar chromosphere and lower corona, it is expected that the quiet Sun corona is also highly dynamic.

1.2.2 The Solar Corona

It is currently very difficult to measure the coronal magnetic field, particularly on the solar disc. This is because the coronal magnetic field is much weaker than that of the photosphere, so the Zeeman splitting effect is too small to be measured accurately, except above active regions with strong magnetic field (Raouafi et al., 2009). In addition, as the coronal plasma is optically thin, it means that any measurements are integrated along the line-of-sight.

Although we cannot directly observe the coronal magnetic field, we can see some of the effects that it has on the surrounding plasma. Figure 1.5 shows two examples of how the magnetic field can structure the coronal plasma. Figure 1.5(a) is an SDO/AIA image of coronal loops at the solar limb, observed in 171 Å. These loop structures are created by hot plasma constrained by magnetic fields. The loops in the image are several hundred Mm in length, but such structures may occur on all scales, wherever the magnetic field threads the surface of the Sun and extends into the corona. Figure 1.5(b) is a chromospheric image in Ca II H taken by the Dutch Open Telescope on La Palma in 2003. The large, bright spike at the centre of the image is a surge that occurred just before a large solar flare. The surrounding strands originating in the photosphere/chromosphere are known as *spicules*. These small-scale features are also the result of plasma structured by magnetic fields. A typical spicule may be between a few thousand to $10,000$ km in length and live for $3-15$ min (de Pontieu, 2007). The dark patches towards the photospheric limb in the image

are sunspots.

In recent years some progress has been made in determining the coronal magnetic field on the limb of the Sun. Raouafi et al. (2009) studied the diagnostic properties of the H I Lyα and Lyβ lines in determining the off-limb coronal magnetic field, via the Hanle effect (Hanle, 1924). The Hanle effect has different symmetry properties and sensitivity to magnetic fields than the Zeeman effect (Stenflo, 2004). It may therefore provide information on the magnetic field where the Zeeman effect is insensitive or 'blind' (Stenflo, 2008). Raouafi et al. (2009) extrapolated a full Sun potential field from SOHO/MDI synoptic magnetograms in order to test the technique. Although they concluded that their model for computing the polarisation of hydrogen lines was simple and required improvement, they were optimistic that this method could prove useful in measuring the coronal magnetic field in the future. Kramar et al. (2006) and Kramar and Inhester (2007) attempted to obtain the 3D structure of the off-limb coronal magnetic field via the Zeeman and Hanle effects, again, using a large-scale extrapolated potential field to test the method. Their conclusion was that neither effect on its own was sufficient for reconstructing the coronal magnetic field, however better results were found when the Zeeman and Hanle effect data were combined. Presently, the only location where magnetic fields may be measured with any certainty within the corona is in solar prominences, where the coronal density is sufficiently high (e.g. Leroy et al., 1983).

The methods discussed above are only effective for large-scale observations off the limb of the Sun. At present, no measurements can be made of the structure of small-scale coronal magnetic fields arising from the Sun's magnetic carpet. This is one motivation driving the theoretical modelling of the small-scale coronal magnetic field, which is carried out in this thesis.

1.3 Modelling the Solar Magnetic Field

The interaction between a plasma and a magnetic field may be described by the equations of *magnetohydrodynamics* (MHD, see e.g. Priest (1982)). They are derived by coupling Maxwell's Equations for electromagnetism to the equations of fluid dynamics using Ohm's Law. Figure 1.6 is a photograph of Maxwell's Equations as they are inscribed at the base of his statue in Edinburgh. As written, $\mathbf{D}$ represents the electric displacement and $\mathbf{H}$ represents the magnetic field. However, in MHD these vectors are expressed as scalar multiples of the electric field, $\mathbf{E}$, and magnetic flux density, $\mathbf{B}$, respectively[1]. We write $\mathbf{D} = \epsilon_0 \mathbf{E}$ and $\mathbf{H} = \mathbf{B}/\mu_0$, where ϵ_0 and μ_0 are the permittivity of free space and the permeability of free space. For the purpose of this thesis, we will refer to $\mathbf{B}$ as the magnetic field since it is proportional to $\mathbf{H}$.

[1]Note that from now on we use $\mathbf{B}$ to represent the magnetic field.

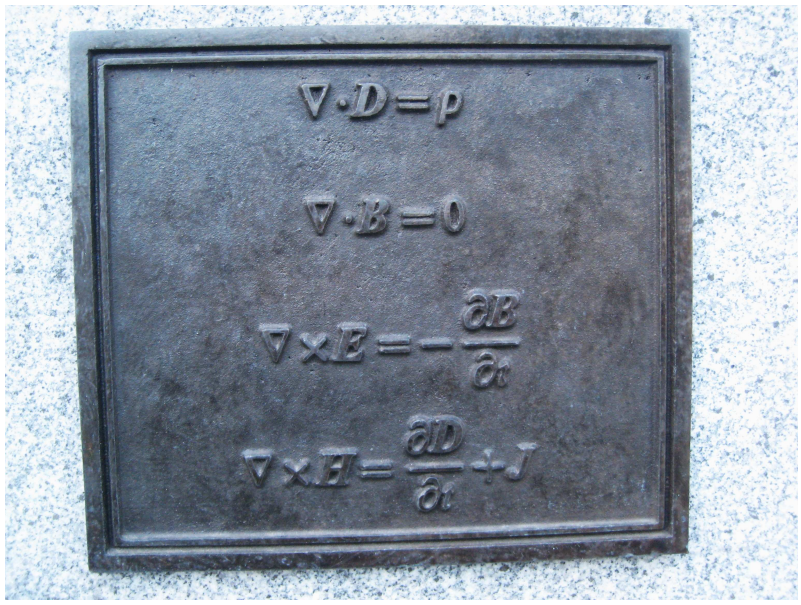

Figure 1.6: Maxwell's Equations inscribed at the base of James Clerk Maxwell's statue, George Street, Edinburgh. In order: Gauss' Law for Electric Fields, Gauss' Law for Magnetic Fields (Solenoidal Constraint), Faraday's Law and Ampère's Law.

1.3.1 Equations of MHD

In the MHD approximation, the plasma is treated as a single fluid that is composed of both electrons and ions. The plasma has velocity $\mathbf{v}$, pressure p, density ρ, and interacts with magnetic field $\mathbf{B}$.

The MHD equations include three of Maxwell's Equations: the Solenoidal Constraint, Faraday's Law and Ampère's Law. The Solenoidal constraint forbids the existence of magnetic monopoles, and is given by

$$\nabla \cdot \mathbf{B} = 0. \tag{1.1}$$

Faraday's Law,

$$\frac{\partial \mathbf{B}}{\partial t} = -\nabla \times \mathbf{E}, \tag{1.2}$$

states that a spatially varying electric field $\mathbf{E}$ can induce a magnetic field. A key assumption within the MHD approximation is that plasma motions are much less than the speed of light. Therefore, the displacement current term in Ampère's Law, $\frac{1}{c^2}\frac{\partial \mathbf{E}}{\partial t}$, may be neglected. Ampère's Law is then written as

$$\nabla \times \mathbf{B} = \mu_0 \mathbf{j}, \tag{1.3}$$

where $\mathbf{j}$ is the electric current density.

The above electromagnetic equations couple to the plasma fluid equations via Ohm's Law,

which is chosen to be of the form

$$\frac{1}{\sigma}\mathbf{j} = \mathbf{E} + \mathbf{v} \times \mathbf{B}, \tag{1.4}$$

where σ is electrical conductivity. Using Equations 1.1, 1.2, 1.3 and 1.4 we may eliminate the electric field $\mathbf{E}$ and derive the *magnetic induction equation*.

$$\frac{\partial \mathbf{B}}{\partial t} = \nabla \times (\mathbf{v} \times \mathbf{B}) + \eta \nabla^2 \mathbf{B} \tag{1.5}$$

The first term in Equation (1.5) is an advective term that describes how the magnetic field changes in response to plasma flows. The second term describes the diffusion of the magnetic field, where $\eta = \frac{1}{\mu_0 \sigma}$ is the magnetic diffusivity, which is taken to be constant.

The MHD Equations also include four fluid equations. The Equation of Motion for the plasma is given by

$$\rho \frac{D\mathbf{v}}{Dt} = \mathbf{j} \times \mathbf{B} - \nabla p + \rho \mathbf{g} + \mathbf{F}_e, \tag{1.6}$$

where $\mathbf{g}$ is gravity and $\mathbf{F}_e$ is any other external force.

$$\frac{D}{Dt} = \frac{\partial}{\partial t} + \mathbf{v} \cdot \nabla$$

is the convective time derivative. The Equation of Mass Continuity, which states that mass is neither created nor destroyed, is

$$\frac{\partial \rho}{\partial t} + \nabla \cdot (\rho \mathbf{v}) = 0. \tag{1.7}$$

The Energy Equation may take several forms, but can be expressed as

$$\frac{\rho^\gamma}{\gamma - 1} \frac{D}{Dt} \left(\frac{p}{\rho^\gamma} \right) = -\mathcal{L}, \tag{1.8}$$

where $\mathcal{L}$ is the energy loss and gain function, and γ is the ratio of specific heats, normally taken to be $\gamma = 5/3$. The final MHD equation is the Ideal Gas Law,

$$p = \frac{\rho R T}{\tilde{\mu}}, \tag{1.9}$$

where T is the plasma temperature, $R = 8.3 \times 10^3$ J K^{-1} kg^{-1} is the gas constant and $\tilde{\mu}$ is the mean atomic weight. In the solar corona, $\tilde{\mu} = 0.6$.

1.3.2 The Lorentz Force

The term $\mathbf{j} \times \mathbf{B}$ that appears within Equation (1.6) is known as the *Lorentz force*, and is the force that the magnetic field exerts on the plasma. Together with Ohm's Law, it creates a link between

the plasma and the magnetic field. From Ampère's Law, the Lorentz force may be expressed as

$$\mathbf{j} \times \mathbf{B} = \frac{1}{\mu_0}(\mathbf{B} \cdot \nabla)\mathbf{B} - \nabla\left(\frac{B^2}{2\mu_0}\right). \tag{1.10}$$

The first term represents a *magnetic tension force*, a restoring force that arises due to the curvature of magnetic field lines. The second term represents a *magnetic pressure force*, which acts from regions of high magnetic pressure (strong magnetic field) to low magnetic pressure (weak magnetic field).

1.3.3 Non-Linear Force-Free Fields

Within this thesis, we use a reduced form of the MHD equations to model the solar corona. We do so by considering series of force-free equilibria, rather than solving the full time-dependent MHD equations. This allows us to make several approximations that greatly simplify the equation of motion (1.6) within the corona. Since we are considering static equilibria, we may neglect any explicit time dependence. Assuming $\mathbf{F}_e = 0$, this leaves a balance of the remaining three forces:

$$0 = \mathbf{j} \times \mathbf{B} - \nabla p + \rho \mathbf{g}.$$

We neglect gravity because the length scales (l) that we are considering are much less than the coronal pressure scale height (Λ). In addition, we may neglect the pressure term as the ratio of plasma to magnetic pressure is much less than 1 within the corona ($\beta = \frac{2\mu_0 p_0}{B_0^2} \ll 1$). This leaves us with the *force-free* condition that the magnetic field must satisfy, namely that the Lorentz force vanishes everywhere:

$$\mathbf{j} \times \mathbf{B} = 0. \tag{1.11}$$

This implies that $\mathbf{j}$ is parallel to $\mathbf{B}$, thus $\mathbf{j}$ may be expressed as a scalar multiple of $\mathbf{B}$. By Ampère's Law,

$$\nabla \times \mathbf{B} = \mu_0 \mathbf{j} = \alpha \mathbf{B}, \tag{1.12}$$

where $\alpha = \alpha(\mathbf{r})$ is a scalar function of position. It can be shown that α must be constant along magnetic lines.

If $\alpha = 0$, then $\nabla \times \mathbf{B} = 0$ and hence $\mathbf{B} = \nabla\psi$ for some scalar magnetic potential ψ. By the solenoidal constraint,

$$\nabla \cdot \mathbf{B} = \nabla \cdot (\nabla\psi) = 0,$$

hence

$$\nabla^2 \psi = 0. \tag{1.13}$$

This is known as the *potential field* approximation. A unique solution to Equation (1.13) may be found analytically once boundary conditions have been specified, making this approximation attractive. However, a potential field contains no electric currents and is the lowest energy solution for the coronal magnetic field. Thus while it is a useful approximation, it is limited and cannot describe eruptive phenomena on the Sun.

If $\alpha \neq 0$, it describes the *twist* or *non-potentiality* of the magnetic field. The simplest non-potential field arises when α is constant. Equation (1.12) together with (1.1) describes a *linear force-free field*.

$$\nabla^2 \mathbf{B} = -\alpha^2 \mathbf{B} \tag{1.14}$$

Equation (1.14) may also be solved analytically. A linear force-free field is in a higher energy state than the corresponding potential field, but yields the minimum energy state for a given helicity (Berger, 1985). This means that we cannot get energy out of the system without changing the magnetic helicity, however helicity is known to be conserved on the Sun over long timescales.

Finally, if α is allowed to vary from field line to field line, then the governing equations for the force-free field are

$$\nabla \times \mathbf{B} = \alpha(\mathbf{r})\mathbf{B} \quad \text{and} \quad \mathbf{B} \cdot \nabla \alpha = 0. \tag{1.15}$$

This describes a *non-linear force-free field*. A non-linear force-free field may contain electric currents and free magnetic energy. Another important property is that it allows for both regions of high and low twist (high/low α), and may therefore model a wide variety of coronal structures. In addition, a non-linear force-free field is much less computationally intensive to compute than solving the full set of MHD equations, allowing us to model complex simulations relatively fast.

1.4 Thesis Outline

In this thesis, a non-linear force-free field model for the solar magnetic carpet is constructed. The model consists of two components. The first is a realistic 2D model for the photospheric evolution of the magnetic carpet. This model describes the time and spatial evolution of the normal magnetic field component B_z. This is then coupled to the 3D coronal evolution model as a prescribed, time dependent photospheric boundary condition. The 3D model produces a continuous evolution of the small-scale coronal magnetic field through a series of non-linear force-free equilibria, in response to photospheric motions.

Chapter 2 provides a literature review of previous models for the solar magnetic carpet. Chapter 3 describes our 2D model for the photospheric evolution of the magnetic carpet, and the results of varying the range of fluxes that a newly emerging bipole may take. The technique used to model the 3D coronal field is introduced in Chapter 4, in which we test the method on three small-

scale basic interactions occurring between two magnetic elements – emergence, cancellation and flyby. The coronal modelling technique is then applied to the full 2D magnetic carpet model in Chapter 5, where the synthetic magnetograms produced in Chapter 3 are used as the evolving photospheric boundary condition. In particular, we are interested in the amount of energy built up, stored and dissipated within the simulations, and the locations of energy storage and dissipation in the coronal volume. Conclusions and avenues for further work are given in Chapter 6.

Chapter 2

Previous Models

The following text is a review of models for the magnetic carpet that exist at present. These fall roughly into two categories, although there is a natural overlap between them. The first set are models of the magnetic carpet photospheric field that aim to reproduce the time and space evolution as seen in observations. These are discussed in Section 2.1. In Section 2.2 we discuss the second type, which are those that simulate the small-scale coronal magnetic field, usually from static photospheric boundary conditions. In Section 2.3 we summarise the main conclusions of these models. We then extend the concept of these models in future chapters.

2.1 Models for Photospheric Evolution

Schrijver et al. (1997) investigated how the quiet Sun photospheric network is sustained. They constructed a statistical model that included flux emergence, cancellation, coalescence and fragmentation. Their study only considered fluxes exceeding $\approx 2 \times 10^{18}$ Mx, so it did not incorporate contributions from internetwork elements. Their aims were to (i) reproduce the observed flux distribution function; (ii) determine the collision frequency and fragmentation rates of magnetic features; and (iii) provide an estimate of the timescales for various photospheric network processes.

They began by studying a 10 hr sequence of high-resolution MDI magnetograms from February 1996. From this data, the number density of magnetic features[1] as a function of their flux content was determined, and local correlation tracking was used to determine the supergranular flow pattern. It should be noted that their number density function was for all magnetic features,

[1]Note that within observational studies, magnetic flux concentrations are referred to as 'magnetic features'. In contrast, we will later define a 'magnetic element' within our models. A magnetic feature as seen in observations may be composed of several of our magnetic elements.

not just those emerging, as will be discussed in later chapters (e.g. Thornton and Parnell (2011)). They determined that most of the magnetic features were indeed confined to the boundaries between supergranule cells. They used this information, together with some estimates of magnetic feature velocities and supergranular cell diameters, to obtain an expression for the frequency of collisions between magnetic features.

In their model, they constructed a time dependent equation for the evolution of the number density $N_{\pm}(\phi)d\phi$ of magnetic features of a given polarity, with absolute flux in the range $[\phi, \phi + d\phi]$. The evolution of the number density was prescribed by several terms that represented either loss or gain of magnetic features of flux ϕ through fragmentation, cancellation or coalescence, in addition to a source term representing emergence. In their model, they also allowed for the re-emergence elsewhere of flux that had previously cancelled. Such bipoles re-emerged with the same flux as they had contained when they cancelled. The authors explored several analytical solutions to the model, and other solutions beyond this via Monte Carlo simulations. In particular they studied the effects of different source functions on the number density.

They concluded that their model successfully reproduced the observed distribution of magnetic features ($\phi \geq 2 \times 10^{18}$ Mx), by modelling random collisions with the effect of an underlying supergranular flow. They obtained an average fragmentation timescale of between $35\frac{10^{19}}{\phi}$ hr and $70\frac{10^{19}}{\phi}$ hr for a magnetic feature of absolute flux ϕ. This implied that fragmentation was largely flux dependent, where larger magnetic features fragmented faster. They determined that almost all network flux must be generated locally, and only a small quantity arises as the result of decaying large active regions. In addition, they established that the emergence of ephemeral regions cannot simply be the reappearance of previously cancelled magnetic flux, and suggested that they originate from a dynamo action within the solar convection zone.

In van Ballegooijen et al. (1998), the authors studied the interaction of magnetic fields and convection, to investigate their contribution to coronal heating. They began by studying observational data from the Swedish Vacuum Solar Telescope (SVST), in order to obtain a time-dependent granulation flow-field, which they used to drive the horizontal motions of photospheric magnetic features. Since it is believed that bright points correspond to regions of strong magnetic field, they tracked the motions of bright points in SVST G-band images.

G-band bright points were tracked by inserting ‘corks’ into the observational data. The corks were defined to move towards the brightest regions in the image. The cork clusters were able to take on the shapes of the actual G-band bright points, and fragmented and merged as the real G-band bright points did. Figure 2.1 shows two images taken from van Ballegooijen et al. (1998). Figure 2.1(a) is the 40th frame taken from a time series of 180 difference images. The difference images were obtained by subtracting 4686 Å continuum images from the corresponding G-band images, taken from the SVST. Many bright points can be seen in the lanes between granules. In

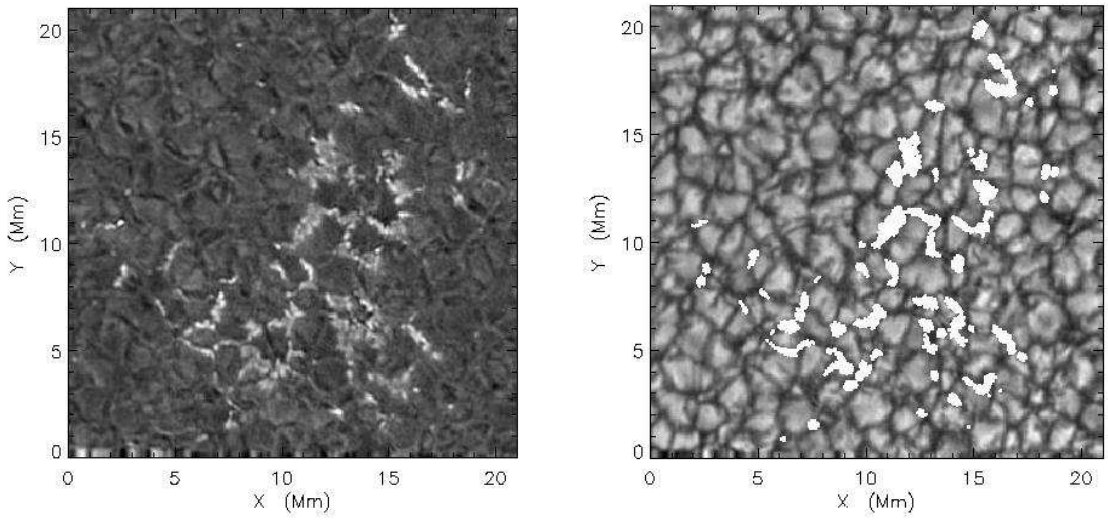

(a) (b)

Figure 2.1: (a) Figure 1a from van Ballegooijen et al. (1998): Difference image obtained by subtracting G-band and continuum images obtained at the Swedish Solar Observatory on La Palma, October 5th 1990, frame 40. (b) Figure 2a from van Ballegooijen et al. (1998): Frame 40 - tracking bright points with finite-size corks. The image shows the corrected granulation intensity.

Figure 2.1(b), they have corrected the granulation intensity by removing the bright points from the continuum images; this allows us to see the granulation pattern much more clearly. Also plotted on the image are the bright point tracking corks. Visually, the cork clusters match the real bright points in Figure 2.1(a) to a high degree of accuracy.

The authors constructed a 2D model for the granulation flow from the granulation intensity image. From the observational data, the authors found no evidence of deep-seated flows. For this reason, they assumed that magnetic flux tubes within their model could be passively advected by the granulation flow. Corks were once again inserted, this time to represent rigid flux tubes, and were advected by the 2D granulation flow model. Figure 2.2(a) shows the positions of the corks in frame 40 of the simulation, for comparison with Figures 2.1(a) and (b). The authors pointed out that although the corks did not reproduce the bright point locations exactly, the agreement between the observed pattern and the one produced by the model was good. This indicates that flow processes are the key element in determining the location and size of the G-band bright points.

Finally, the authors extrapolated a potential field from their model of surface magnetic flux features, where each cork represented a point source, $\mathbf{B}_k(\mathbf{r}, t)$. They investigated velocities within the solar chromosphere, which were determined as follows. The authors assumed that the magnetic field was 'frozen-in' to the plasma, implying that $\mathbf{E} + \mathbf{v} \times \mathbf{B} = 0$, where $\mathbf{v}(\mathbf{r}, t)$ is the field

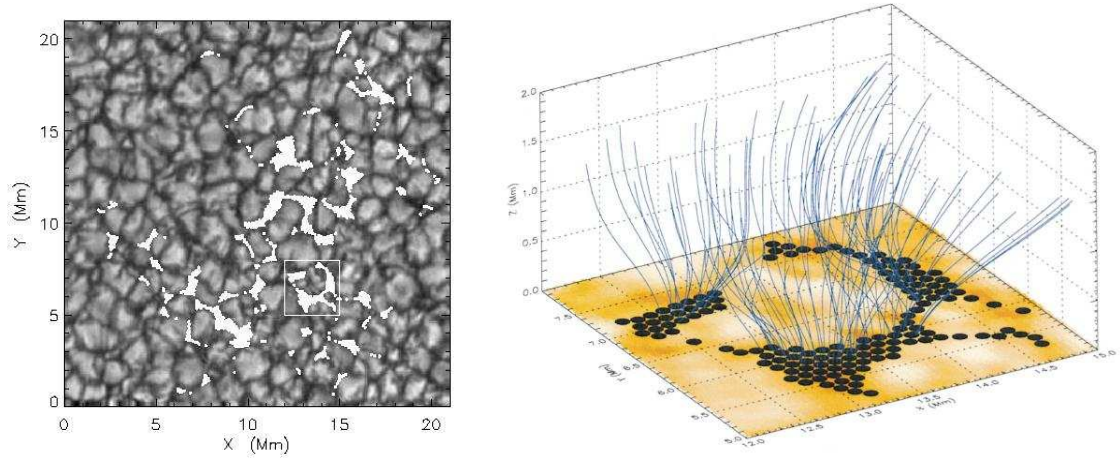

(a) (b)

Figure 2.2: (a) Figure 6a from van Ballegooijen et al. (1998): positions of corks in frame 40. The corks represent rigid flux tubes that are advected by granular flows. (b) Figure 9 from van Ballegooijen et al. (1998): 'flux tubes in the solar atmosphere'. This is produced by tracing field lines downward from a height of 1.5 Mm in a potential field extrapolation of frame 40. The region shown here is the small region indicated by the box in (a).

line velocity and $\mathbf{E}(\mathbf{r}, t)$ the electric field. By Faraday's Law:

$$\nabla \times \mathbf{E} = -\frac{\partial \mathbf{B}}{\partial t} = -\sum_k \frac{\partial \mathbf{B}_k}{\partial t} = \sum_k \nabla \times \mathbf{E}_k,$$

where $\mathbf{E}_k(\mathbf{r}, t) = -\mathbf{v}_k(t) \times \mathbf{B}_k(\mathbf{r}, t)$. This implies that the electric field may be written in the form:

$$\mathbf{E}(\mathbf{r}, t) = \sum_k \mathbf{E}_k(\mathbf{r}, t) - \nabla\phi,$$

for a scalar function $\phi(\mathbf{r}, t)$. The frozen-in condition implies $\mathbf{E} \cdot \mathbf{B} = 0$, therefore

$$\mathbf{B} \cdot \nabla\phi = \sum_k \mathbf{B} \cdot \mathbf{E}_k. \tag{2.1}$$

The right-hand side of Equation 2.1 may be computed from the known positions and velocities of the magnetic sources. The boundary condition $\phi(x,\, y,\, 0,\, t) = 0$ was taken and Equation 2.1 was integrated along a field line to obtain ϕ at a point $\mathbf{r}$. From this, $\mathbf{E}$ was be calculated. The field line velocity was then

$$\mathbf{v} = \frac{\mathbf{E} \times \mathbf{B}}{|\mathbf{B}|^2},$$

which is perpendicular to the magnetic field by definition.

The authors traced field lines downward from a height of 1.5 Mm and ignored closed field

lines that connected between the sources. They found that dramatic increases in velocity were produced as flux tubes passed one another at *separatrix surfaces*. These are defined as surfaces that separate two regions which are topologically distinct (see e.g. Priest et al. (2005)). The chromospheric velocities they obtained from their model were several km s^{-1}, which was significantly larger than the velocities determined for the magnetic features at the photosphere. The authors concluded that this velocity enhancement could significantly increase the coronal heating rate, and affect the way that currents build up near separatrix surfaces in various models for coronal heating. The authors noted that in some regions the predicted chromospheric velocities became so large that plasma inertia could not be neglected, so a potential field model was no longer applicable. They suggested that, for example, an MHD model could produce a more realistic description of flows in a model of interacting flux tubes.

Simon et al. (2001) investigated how the Sun's magnetic network is sustained, via a theoretical model that they constructed for the magnetic carpet. Their model also represented magnetic features by corks that were passively advected by photospheric flows. Supergranular flows were represented by a horizontal velocity flow, $v(r)$, given by:

$$v(r) = 2.332V[(r/Re^{-(r/R)^2})], \tag{2.2}$$

where V is the peak velocity, R is the radius of the supergranule, and r is the distance from the cell centre. The authors chose values for these parameters that agreed with observations: $V = 0.5$ km s^{-1} and $R = 20'' \simeq 14.5$ Mm, and they assumed a mean lifetime for a supergranule of 30 hr.

Newly emerging bipoles within the model were composed of clusters of 20 negative and 20 positive corks, and emerged within 3.6 Mm of the centre of a randomly chosen supergranule. Each bipole had a fixed absolute flux of 3×10^{18} Mx. Once the two clumps of opposite polarity had emerged and had a minimum separation distance, the corks were free to be advected by supergranular flows. They were swept towards the cell boundaries, where they formed a network. Oppositely signed corks that came into contact cancelled with each other and were removed. Since the magnetic features were composed of many individual corks, fragmentation and coalescence were also able to occur. The authors introduced granulation, which 'jiggled' the corks and caused broadening in the network, and they investigated the effect of varying the model parameters. It was determined that the model was robust, as it was not very sensitive to variations of the main parameters.

The authors determined that the network would decay within a few days if it was not continually replenished. Therefore the only way of sustaining it was to continually introduce newly emerged magnetic flux. They found that the average lifetime of magnetic flux within the network was around 2 days for an emergence rate of 3×10^{21} Mx hr^{-1} and only 17 hr for an emergence rate of 2×10^{22} Mx hr^{-1}. In addition, they determined that an emergence rate of 7×10^{22} Mx

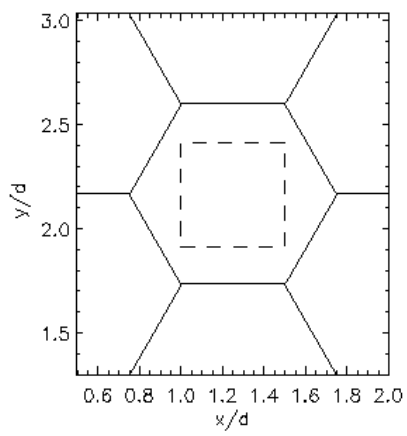

Figure 2.3: Figure 3 from Parnell (2001). The dashed box indicates the region within the hexagonal supergranule in which ephemeral regions may emerge. The axes have been non-dimensionalised with respect to the width, d, of a supergranule.

day^{-1} would maintain a total unsigned flux of $2-3\times10^{23}$ Mx over the whole solar surface. They concluded that a steady emergence of ephemeral regions of flux around $10^{18}-10^{19}$ Mx could maintain the Sun's observed magnetic network, and the observed width of the magnetic network could be reproduced by introducing jiggling from granulation into their model. The authors suggested that while the passive advection of the corks was consistent with the motion of small-scale magnetic flux features, a 3D model that took into account the dynamics below the photosphere via helioseismology would give rise to a fuller understanding of the solar surface.

Another theoretical model for the evolution of the magnetic carpet was developed by Parnell (2001). In the model, three parameters were imposed. These were the flux emergence rate, the distribution of newly emerging flux, and the rate of fragmentation. Cancellation and coalescence arose as a natural consequence within the model. The author's aim was to investigate how varying the three imposed parameters affected the distribution of flux, the average flux density, and the rate of cancellation.

Supergranules within the model were represented by a series of hexagonal cells of diameter 14 Mm. New bipoles emerged in a randomly chosen supergranule, somewhere within a square centred in the cell (see Figure 2.3). Each bipole emerged with a random orientation, and the two polarities within the bipole initially moved apart along their axis in opposite directions. The absolute flux of the bipole was also chosen randomly, but under the constraint that the distribution of emerging flux values had a mean of 1.3×10^{19} Mx, as determined by Schrijver et al. (1997). Parnell (2001) investigated four different flux distributions for the newly emerging bipoles; two exponential and two skewed-normal. Another constraint was that all flux features must have absolute flux equal to an integer multiple of 10^{16} Mx. This prevented infinitesimally small features from arising due to cancellation or fragmentation, and was equivalent to an individual flux feature

being composed of an integer number of small flux tubes. The rate at which emergence occurred was also varied. The speed of each magnetic feature was proportional to its absolute flux; smaller features moved more quickly. The final parameter that was varied was the rate of fragmentation of magnetic features. Any feature was allowed to fragment except those of minimum flux (10^{16} Mx), where a feature of larger flux had a greater probability of fragmenting.

The author found that the absolute flux density within the system relaxed towards a state where it oscillated around an average value. They were confident that the model had reached a steady state as the rates of emergence and cancellation became roughly equal. Through investigating the effect of varying the three model parameters, it was found that the average absolute flux density increased with increasing emergence rate and with decreasing rate of fragmentation. The choice of flux distribution, however, had almost no effect on the absolute flux density. The author suggested the most likely combination from their parameter range in order to reproduce the observed distribution of magnetic features was: an emergence rate of $6 \times 10^{-6} - 1 \times 10^{-5}$ Mx cm^{-2} s^{-1} and a fragmentation rate of more than 12×10^{-5} s^{-1}. As stated before, the model reached a stage where the rate of cancellation was approximately equal to the rate of emergence, however, the frequency of cancellation was found to be much greater than the frequency of emergence. This suggested that cancellations tended to occur between many small features arising due to fragmentation, whereas emergence involved relatively large features. The author proposed that the energy release from many small cancellation events could supply a significant amount of the energy required to heat the solar corona. This energy could also be built up and released by small-scale flyby and flux braiding events due to the large number of features arising from fragmentation.

Cranmer and van Ballegooijen (2010) modelled the evolution of small-scale photospheric magnetic fields, and constructed a potential coronal field to investigate the structure of the magnetic field in the corona. Their aim was to determine whether it was likely that the solar wind could be driven by reconnection occurring within the solar magnetic carpet. They ran Monte Carlo simulations of the magnetic carpet evolution. Their flux emergence rate was taken from the study of Hagenaar et al. (2008), in which the photospheric recycle time was determined to be on the order of $1 - 2$ hr. Cranmer and van Ballegooijen (2010) modelled both a flux balanced region to represent the quiet Sun, as well as an imbalanced region to represent coronal holes. Both region types are locations at which the slow and fast solar wind originate respectively. Due to the high emergence rate, they required a relatively high velocity for their photospheric features (around 6 km s^{-1}), and large ranges over which magnetic features could interact (between 1 Mm and 10 Mm) in order to reproduce a realistic photospheric evolution. They found that their model agreed with observed values of surface flux densities and magnetic feature number distributions, even though they applied a random walk to describe the motion of magnetic features rather than granular or supergranular flows.

In order to investigate whether the solar wind could be accelerated from such regions, they

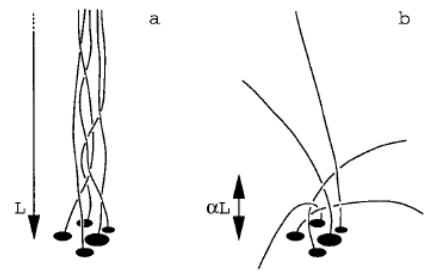

Figure 2.4: Figure 11 from Schrijver and Title (2002), cartoons illustrating the braiding of magnetic field lines. In (a), the field lines are almost parallel, so braiding may propagate along their entire length, L. In (b), the field lines connect to many distant sources, and the braiding may only propagate up to the point at which the field lines significantly diverge, αL.

extrapolated a potential field from their 2D photospheric model, and calculated recycle times for open flux. This is the rate at which closed field lines become open. From this they estimated the energy flux produced by the opening of these field lines. They concluded that for quiet regions, the energy fluxes calculated were too low to be able to accelerate the solar wind. For flux imbalanced regions representing coronal holes they obtained higher energy fluxes, but found that the flux recycle times involved were too long for the solar wind to be accelerated at this location. They therefore concluded that it was unlikely that the solar wind could be accelerated by reconnection within the solar magnetic carpet. However, it should be noted that this was carried out under a potential field approximation. A non-potential simulation may give different results.

2.2 Coronal Field Models

Rather than trying to reproduce the dynamics of the magnetic carpet photospheric motions, Schrijver and Title (2002) studied the topology of the quiet Sun corona. The authors represented photospheric magnetic features by a series of randomly positioned magnetic point sources. This random positioning avoided any special symmetries from arising. Each source was assigned a random sign, with flux in the range $0.5 \times 10^{18} - 5 \times 10^{18}$ Mx from an exponential distribution, as in Schrijver et al. (1997). The authors then extrapolated a potential coronal field and investigated its topology.

After their analysis of the potential field, the authors compared their simulations to actual observational data. They studied 171 Å and 195 Å TRACE images, and superimposed contours of magnetic field from SOHO/MDI magnetograms of the same region on top of these images. They found that, in general, bright points existed either between two features of opposite polarity, or above larger features of a single polarity.

Within their simulations, they found that there were roughly the same number of null points

as there were sources. Of these, around 91% were photospheric nulls. They found no evidence for a comparative number of coronal brightenings within the TRACE data that would correspond to the expected number density of null points. They concluded from this that any coronal heating that arose due to null points or separators is negligible compared to the total heating, otherwise they would have observed many bright patches far from the photospheric flux features.

The authors found that each source connected to many other sources: between 1 and 30. From this they concluded that any braiding-induced coronal heating from the magnetic carpet could only be important low down, close to the photosphere. This was similar to the findings of Priest et al. (2002), who proposed that a significant amount of heating arises low down in the corona. This was due to the fact that around 95% of connections between small-scale magnetic features closed low down in the magnetic carpet model of Priest et al. (2002). Schrijver and Title (2002) explained that since each source connected to so many others, any braiding could only propagate along such field lines to the point at which those field lines significantly diverged. This is illustrated by a cartoon, shown in Figure 2.4. They proposed that as a result of this, the heating scale height from braiding is probably similar to the typical source separation of around 10 Mm.

Close et al. (2003) and Close et al. (2004) investigated the properties of a coronal field constructed through a potential field extrapolation of magnetogram data. In Close et al. (2003), they performed a similar study to Schrijver and Title (2002) of coronal field connectivity. They also studied flux tube lengths, heights and foot-point separations, and the effect of a flux imbalance within the region. For a set of high resolution SOHO/MDI magnetograms of the quiet Sun, they replaced each pixel by a point source. Through this they constructed a potential field for two 264×264 Mm^2 regions of a magnetogram, and studied only the inner 88×88 Mm^2 in order to avoid boundary effects. Both large regions were roughly flux balanced, but the inner regions were centred on (i) a flux balanced area, and (ii) an area with a strong imbalance.

They investigated the statistical properties of the resulting flux tubes. Magnetic flux features were found to connect preferentially to their nearest neighbour of opposite polarity. Around $60 - 70\%$ of flux closed within 9 Mm of the feature from which it originated, although some connections reached as far as several supergranule diameters. They found that even for this quiet Sun region, some flux tubes were as long as 100 Mm, and that around 10% of flux originating from the photosphere was contained within such tubes. However, most of the flux was contained within low-lying flux tubes, where 50% of connections closed below 2.5 Mm and only $5 - 10\%$ reached a height above 25 Mm (Figure 2.5(a)). For this reason, they proposed that the magnetic field strength of the corona falls off much faster than $1/R^3$. Whilst larger flux features tended to have higher reaching connections, they found that even the smallest of features could contribute to fields above 50 Mm. They also found that around $60 - 70\%$ of flux from a single magnetic feature connected to just one other feature of opposite polarity. Of the remaining flux, $25 - 30\%$ connected to one or two further opposite polarity features, but the remainder could connect to up

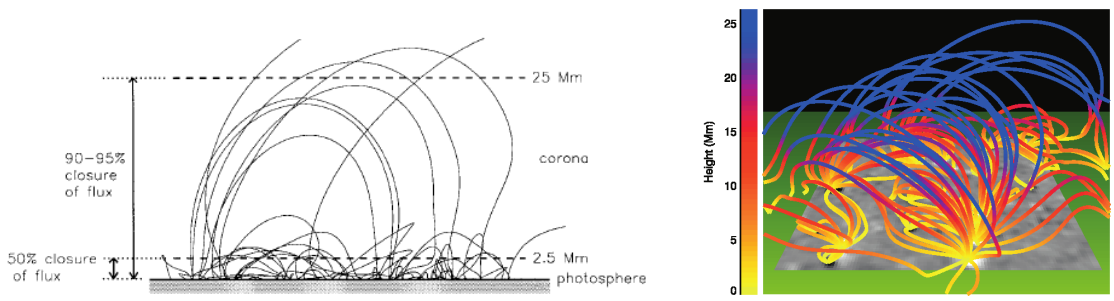

(a) (b)

Figure 2.5: (a) Figure 19 from Close et al. (2003). A view of a potential field from the side. 50% of flux closes below 2.5 Mm and around $5-10\%$ extends above 25 Mm. (b) Figure 2 from Close et al. (2004). A potential field extrapolation of an MDI magnetogram. 1/200th of the field lines computed are plotted in the image. The varying colour scheme refers to different heights of the field lines within the corona.

to 50 additional magnetic features.

Close et al. (2004) again studied a potential field representation (Figure 2.5(b)) of MDI high resolution magnetograms, this time with the aim of establishing a time-scale for the recycling of the solar coronal magnetic field. The coronal field recycle time is the time taken for all coronal connections between existing features to break and be replaced by new ones. They used a 12.5 hr sequence of 240×240 Mm^2 magnetograms with a time cadence of $\Delta t = 15$ min. In contrast to their previous study, they represented each magnetic feature by just one point source, rather than a collection of sources, and tracked the motions of individual elements. By considering the effects of emergence, cancellation and reconnection within the coronal field, they obtained a coronal recycling time of 1.4 hr. They found that emergence and cancellation drove a significant amount of reconnection within the coronal field. The authors concluded that the quiet Sun coronal field is indeed highly dynamic. They suggested that a future study could also incorporate contributions from internetwork features, which were not present in their investigation. Schrijver and Title (2003) found that as much as 50% of the quiet Sun coronal magnetic field may originate from internetwork features rather than network flux. Since these features evolve more rapidly than the larger network features, this would likely further reduce the coronal recycling time.

A more recent study of a potential field extrapolation from magnetogram data was carried out by Régnier et al. (2008). They used data from Hinode/SOT, which is of resolution 3.8 times higher than SOHO/MDI high-resolution magnetograms. Rather than representing the photospheric magnetic field by isolated point sources as Close et al. (2003) did, they considered a continuous magnetic field throughout the base. Their aims were to investigate the complexity of the coronal field, with a view to understanding the occurrence of reconnection and heating of the corona.

By defining the photosphere as being the region from $0-1$ Mm above the base, the chromo-

sphere between 1 Mm and 3.5 Mm, and the corona above; they found that 54% of nulls occurred in the photosphere, 44% in the chromosphere, and just 2% within the corona. In contrast to the study of Schrijver and Title (2002) who found approximately the same number of nulls as photospheric flux features, they found that the ratio of the number of null points to magnetic flux features was only $3-8\%$. However, 91% of the null points found by Schrijver and Title (2002) were photospheric. Régnier et al. (2008) did not find any nulls at the base since their photospheric magnetic field description was continuous. They concluded that the number density of null points is not a good quantity to be used as an indicator of the complexity of the coronal field, since it relies on both the model used, and the way in which magnetic flux features are defined. They also concluded that due to the low spatial density of nulls in the coronal field, coronal heating at null points is unimportant. However, magnetic features may still have a key role in heating the corona as reconnection does not have to occur at null points; it may also occur in their absence at locations such as separators or quasi-separatrix layers (QSLs, e.g. Restante, 2011).

2.3 Summary and Conclusions

This chapter has provided a literature review of models that have been produced for both the photospheric evolution and the small-scale coronal field of the solar magnetic carpet. Below we summarise the main features and results of these models, and also highlight improvements that could be made.

In a realistic model for the photospheric evolution of the magnetic carpet, the main effects that should be included are the four flux evolution processes of emergence, cancellation, coalescence and fragmentation, as well as some description of the motion of magnetic features.

2.3.1 Photospheric Flows

All of the models in Section 2.1 apart from that of Cranmer and van Ballegooijen (2010) included a granular or supergranular flow profile that advects the magnetic features. These flow profiles may be taken from observations (van Ballegooijen et al., 1998) or specified through a mathematical description (Schrijver et al., 1997; Simon et al., 2001; Parnell, 2001). The flow profile may also be time evolving (van Ballegooijen et al., 1998; Simon et al., 2001) or steady (Parnell, 2001). Cranmer and van Ballegooijen (2010) did not include a supergranular flow, but chose instead to advect magnetic features in random directions. They found that they still obtained a realistic model that reproduced observed flux and number density distributions. From this we conclude that:

- A description of the velocities of magnetic features is required, however an evolving flow pattern is not necessary for the photospheric evolution model to reproduce observed results.
- No deep-seated flows appear to affect magnetic features on the scale of the magnetic carpet (van Ballegooijen et al., 1998), therefore a 2D flow description is sufficient.
- Granulation represented by random 'jiggling' of magnetic features can reproduce network broadening (Simon et al., 2001), and will also prevent features from becoming stationary in the network.

As a result, we choose to use a steady supergranular flow profile that we specify analytically, and also include the effect of granulation as random motions in our model in Chapter 3.

2.3.2 Photospheric Flux Evolution Processes

Most of the photospheric models discussed above included the processes of emergence, cancellation, coalescence and fragmentation. In many cases, the rate of emergence was a parameter that was taken from observational studies. Schrijver et al. (1997) deduced an emergence rate for their model from a study of MDI magnetogram data that they conducted; Parnell (2001) used various emergence distributions that took the mean value for newly emerging flux from the study of Schrijver et al. (1997); Cranmer and van Ballegooijen (2010) used the emergence rate determined by Hagenaar et al. (2008).

The subsequent evolution of magnetic features depended upon the authors' description of a 'feature'. The studies of van Ballegooijen et al. (1998) and Simon et al. (2001) had magnetic features composed of clusters of corks representing intense flux tubes. Fragmentation and coalescence then arose naturally within their models due to the underlying flow pattern. Parnell (2001) and Cranmer and van Ballegooijen (2010) treated magnetic features of varying flux as single elements. In this way it is easy to keep track of each process that a magnetic feature undergoes, however, it also means that the fragmentation process must be artificially built into the model. Schrijver et al. (1997), Parnell (2001) and Cranmer and van Ballegooijen (2010) all built a flux dependent fragmentation process into their models; the higher the flux of a magnetic feature, the more likely it is to fragment. For the flux evolution processes within our magnetic carpet model:

- We choose to describe magnetic concentrations by a distribution of small-scale magnetic elements, rather than have them composed of individual flux tubes represented by corks. We also take each element to have flux that is an integer multiple of some ϕ_{min}, as in Parnell (2001). These small-scale magnetic elements may overlap to form a larger magnetic feature in the photospheric distribution.

- We use a probability distribution for newly emerging bipoles that is taken from observations (Thornton and Parnell, 2011).
- Cancellation and coalescence within our model occurs when features are defined to be within interaction range, as with Parnell (2001); Cranmer and van Ballegooijen (2010).
- Fragmentation is artificially built into our model using the method of Parnell (2001).

All of these processes are described in detail in Chapter 3.

2.3.3 Coronal Evolution

Some interesting effects that previous authors have considered in their small-scale coronal field simulations are enhanced velocities at separatrices (van Ballegooijen et al., 1998); topology and connectivity of the field (Schrijver and Title, 2002; Close et al., 2003); null locations (Schrijver and Title, 2002; Régnier et al., 2008); and coronal recycle times (Close et al., 2004; Cranmer and van Ballegooijen, 2010).

Schrijver and Title (2002) and Régnier et al. (2008) proposed that heating at null points within the corona is unimportant. Schrijver and Title (2002) reached this conclusion because they did not find a comparative number density of coronal bright points in TRACE data to the coronal null density within their potential field extrapolation of MDI magnetograms; Régnier et al. (2008) because only 2% of the nulls they computed lay within the region they defined to be the corona (> 3.5 Mm). However, Régnier et al. (2008) found that 44% of nulls lay within the chromosphere of their model ($1-3.5$ Mm). Priest et al. (2002) suggested that heating may be more important low down in the solar atmosphere, as a result of many complex, low-lying connections close to the photosphere. Close et al. (2003) found that around 50% of connections within their magnetic carpet model closed below 2.5 Mm, and that each magnetic feature could connect to a large number of other magnetic features. Twisting and braiding of these low-lying connections could provide an important contribution towards coronal heating from the Sun's magnetic carpet (Parnell, 2001; Schrijver and Title, 2002; Priest et al., 2002). Within our model, we will look for evidence of such low-lying complexity.

All of the coronal models discussed in this chapter used potential field extrapolations, the simplest of force-free approximations. As van Ballegooijen et al. (1998) suggested, a more complex model could produce a more realistic description of the small-scale coronal magnetic field. In addition to being potential, the coronal field in each of these models was produced by an independent extrapolation at each frame. This means that each extrapolated field was unrelated to the previous coronal field. In contrast, the model that we will consider in the following chapters produces a continuous evolution of a non-linear force-free field. A non-linear force-free field is

a step up in complexity from a potential field. It allows for electric currents and free magnetic energy to build up, as well as twisting of the magnetic field. The fact that a continuous evolution is produced also means that magnetic connectivity is maintained within the corona from one step to the next. This will affect null locations, topology and the recycling of the field. The inclusion of internetwork features will also likely affect coronal recycle times within our model, as they evolve much more rapidly than larger flux features (Close et al., 2004). In addition, we will include an overlying field within our coronal evolution. This represents the influence of the Sun's large-scale magnetic field on small-scale magnetic features on the solar photosphere.

In Chapter 3 we introduce our model for the 2D evolution of the magnetic carpet photospheric field. From this model, we produce series of synthetic magnetograms. Our model for the coronal field evolution will be described fully in Chapter 4, in which it is applied to three common small-scale magnetic interactions: an emergence, cancellation and magnetic flyby. In Chapter 5, the coronal evolution is driven by the synthetic magnetograms produced by the model described in Chapter 3.

Chapter 3

Simulation of Synthetic Magnetograms

The model presented in this chapter has be published in Meyer et al. (2011).

This chapter describes a new 2D model for the photospheric evolution of the solar magnetic carpet. The model aims to reproduce the main observational properties of the Sun's small-scale photospheric magnetic field. Many of the parameters built into the model are taken from studies of observational data (such as *Hinode*/SOT or SOHO/MDI magnetograms). As described in the discussion in Chapter 2, we include a supergranular flow pattern; random small-scale motions representing granulation; and the four flux evolution processes that govern the magnetic carpet, namely emergence, fragmentation, cancellation and coalescence.

The model reproduces observed quantities, such as the power law flux distribution obtained by Parnell et al. (2009). Other objectives include reproducing the rapid photospheric recycle time on the order of $1 - 2$ hr deduced by Hagenaar et al. (2008); equality of the rates of emergence and cancellation of flux; and visually, the appearance of a magnetic network along the boundaries of supergranule cells. The output from this model is a series of synthetic magnetograms. These will be used as the lower boundary condition in the 3D model discussed in Chapter 5, which will simulate the evolution of a non-linear force-free coronal field, corresponding to the small-scale magnetic carpet.

The chapter is outlined as follows: Section 3.1 describes the technical aspects of the construction of the 2D magnetic carpet model and how each of the four flux evolution processes are specified. The results of the simulations are presented in Section 3.2 where we show that the model reproduces many observational parameters. Section 3.3 gives the discussion, conclusions and an outline of further work. A number of movies accompany this chapter and are held on the CD. A list of movies is given in Appendix C.1.

3.1 Model

The construction of the magnetic carpet model is now described. Whilst observational studies use the term 'feature' to describe small-scale magnetic flux concentrations, we will refer instead to magnetic 'elements'. This is to distinguish a 'magnetic element' in the model, which we choose to have a specific mathematical form. In contrast, an observational 'magnetic feature' as would appear in a magnetogram may be composed of several of our magnetic elements. Each magnetic element within the model is treated individually as a unique object. The sum of all elements then produces a synthetic magnetogram. This approach differs from other methods in several ways. In cork models (van Ballegooijen et al., 1998; Simon et al., 2001), each cork represents a single intense flux tube. In contrast, in our model we represent our magnetic elements with Gaussian peaks, allowing features to form which are made up of multiple elements and composed of many peaks and troughs in magnetic field strength. To avoid undesirable numerical effects such as numerical diffusion and pile-up at cancellation points, we move the centres of magnetic elements, keeping their profiles fixed, rather than advecting their Gaussian profiles through a velocity field and the induction equation. Such a treatment also allows us to easily keep track of the number of elements and exactly which elements are involved in each of the four processes of emergence, cancellation, coalescence and fragmentation at any time. We first describe the mathematical form of the magnetic elements which produce the synthetic magnetograms. Following this, examples of the magnetograms produced over a 250 hour period are shown. Finally, we discuss the rules that govern how the magnetic elements evolve.

3.1.1 Synthetic Magnetograms

For each discrete magnetic element we assume that the $z-$component of the element's magnetic field has a Gaussian profile,

$$B_z = B_0 e^{-r^2/r_0^2}, \tag{3.1}$$

where B_0 is the peak magnetic field strength, r_0 is the Gaussian half-width and r is the distance from the centre of the Gaussian. The total flux, Φ, of each element is:

$$\Phi = \int_A B_0 e^{-r^2/r_0^2} r dr d\theta = B_0 \pi r_0^2. \tag{3.2}$$

We specify the Gaussian half-width of each magnetic element to be $r_0 = d(\phi)/4$, where $d(\phi)$ is the diameter of the magnetic element and ϕ is its absolute flux, $\phi = |\Phi|$. The diameter is given by

$$d(\phi) = m_\phi \log_{10}(\phi) + c_\phi, \tag{3.3}$$

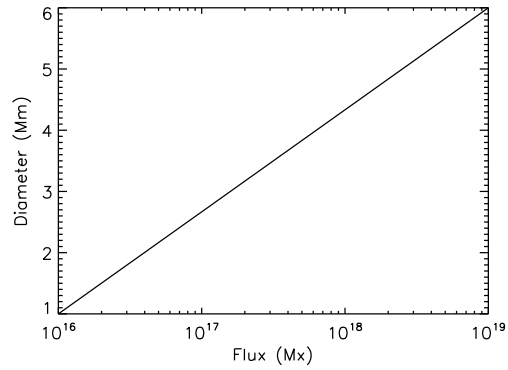

Figure 3.1: Diameter of a magnetic element (Mm) versus absolute flux (Mx).

where the parameters m_ϕ and c_ϕ are given by

$$m_\phi = \frac{d_{\text{max}} - d_{\text{min}}}{\log_{10}(\phi_{\text{large}}) - \log_{10}(\phi_{\text{small}})}, \quad \text{and} \quad c_\phi = d_{\text{min}} - m_\phi \log_{10}(\phi_{\text{small}}).$$

We let $d_{\text{min}} = 1$ Mm, $d_{\text{max}} = 6$ Mm, $\phi_{\text{small}} = 10^{16}$ Mx and $\phi_{\text{large}} = 10^{19}$ Mx so that the majority of magnetic elements within the simulation are confined to the range $d \in [1, 6]$ Mm. These values agree with observed diameters and fluxes for magnetic carpet features such as small network features and internetwork features (Harvey and Martin, 1973; Martin, 1988; Wang et al., 1995; Zhou et al., 2010). A plot of diameter versus flux is shown in Figure 3.1.

Equation (3.2) may be rearranged to give an expression for the peak magnetic field strength of a single magnetic element,

$$B_0 = \frac{16\Phi}{\pi d(\phi)^2}. \tag{3.4}$$

The contribution of the jth magnetic element to the normal component of the magnetic field is then:

$$B_{z,j} = B_{0,j} \exp\left\{\frac{-16r^2}{d(\phi_j)^2}\right\}, \tag{3.5}$$

$$r^2 = (x - x_j)^2 + (y - y_j)^2,$$

where (x, y) is an arbitrary position, and (x_j, y_j) is the position of the centre of the magnetic flux element. We sum up the contribution from every magnetic element to give B_z,

$$B_z = \sum_{j=1}^{N} B_{z,j}, \tag{3.6}$$

where N is the number of elements.

Figure 3.2(a) shows a contour plot of B_z for a simulation in which newly emerging bipoles

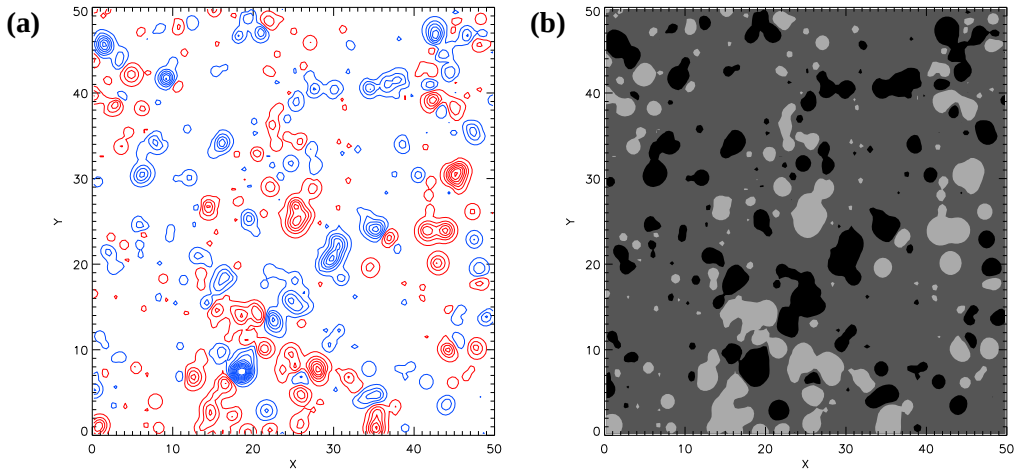

Figure 3.2: Synthetic magnetograms for a simulation with a flux emergence range of 8×10^{16} - 1×10^{19} Mx. Both are taken at $t = 20$ hr. (a) Red contours represent positive magnetic field, blue represents negative magnetic field, where ten contour levels are shown for each polarity with absolute values spaced evenly between 3.5 G and 66.5 G. (b) The same as image (a), with contours filled in to simulate a magnetogram image where the saturation level is ± 70 G.

have a total flux in the range 8×10^{16} - 1×10^{19} Mx. In total, 607 magnetic elements were summed over to produce this synthetic magnetogram. This simulation is described in more detail in Section 3.2. A black and white image of the same region is shown in Figure 3.2(b) to simulate a magnetogram. From this it can be seen that by summing up a number of discrete elements, a visually realistic distribution of flux can be found compared to that of the observed magnetic carpet.

In the following sections, full details of how Figure 3.2 is produced are given. Throughout the simulation, the motion of the magnetic elements is determined by an underlying supergranular flow, which is described next. In addition, details of the flux emergence and interaction processes are given in Sections 3.1.3, 3.1.4 and 3.1.5.

3.1.2 Steady Flow Profile

A supergranular velocity profile that is similar to that of Simon et al. (2001) is chosen for the model, except that the diameter of each cell varies from supergranule to supergranule. For simplicity our flow profile is currently steady throughout the simulation, although in reality, supergranules evolve in time. Various authors have estimated lifetimes of supergranules to be anywhere from 10 hr to 2 days, depending on the technique used (Rieutord and Rincon, 2010). However, we will show that our steady profile does not lead to an unphysical buildup of magnetic flux at the

Cell	Cell centre (x,y)	A_0	R_0	(x,y) Mm	R_{sg} (Mm)
0	$(0.12, 0.26)$	1.0	0.173	$(6.0, 13.0)$	17.3
1	$(0.75, 0.25)$	1.0	0.173	$(37.5, 12.5)$	17.3
2	$(0.7, 0.62)$	1.0	0.173	$(35.0, 31.0)$	17.3
3	$(0.29, 0.8)$	1.0	0.173	$(14.5, 40.0)$	17.3
4	$(0.43, 0.42)$	0.75	0.173	$(21.5, 21.0)$	12.98
5	$(0.95, 0.85)$	0.6	0.173	$(47.5, 42.5)$	10.38
6	$(0.42, 0.09)$	0.6	0.173	$(21.0, 4.5)$	10.38

Table 3.1: Columns $1-4$: Normalised coordinates of cell centres and values of A_0 and R_0 for the supergranule flow profile shown in Figure 3.3(b). Columns 5 and 6: The values of (x,y) and $R_{\text{sg}} = 2A_0R_0(x_{\text{max}} - x_{\text{min}})$ are also given in Mm, assuming a 50 Mm x 50 Mm region.

cell boundaries. The flow profile of a single supergranule is given by

$$v_R = A_0 R \exp\left\{\frac{-R^2}{R_0^2}\right\}, \tag{3.7}$$

where v_R is the velocity from cell centre in the $x-y$ plane. R is the distance from cell centre, and A_0 and R_0 are normalised values that determine the flow strength and radius of the supergranule, $R_{\text{sg}} = 2A_0R_0(x_{\text{max}} - x_{\text{min}})$. We set $R_0 = 0.173$ units for all supergranules, which corresponds to a half-width of 8.7 Mm in our simulations. A_0 is a number between 0 and 1 that determines the strength of each cell. We choose the positions $(x_{\text{c}}, y_{\text{c}})$ of the centres of n supergranules in the simulation. To introduce the influence of cells outside the computed domain, we translate the positions of these n cells eight times to surround the original pattern, as illustrated by Figure 3.3(a). The original domain is shown in black, and spans the range $[x_{\text{min}}, x_{\text{max}}] \times [y_{\text{min}}, y_{\text{max}}]$, where we choose $x_{\text{min}} = y_{\text{min}} = 0$ Mm and $x_{\text{max}} = y_{\text{max}} = 50$ Mm. Translation of the cells means that the supergranular flow matches through the side boundaries, which are periodic.

To produce the steady flow pattern, the velocity at any point is found by summing over the contributions of $9n$ supergranular cells. This includes the n original supergranules which describe the central region of Figure 3.3(a), outlined in black, and the eight sets of translations. Once the contribution of all cells has been calculated, the resulting velocity profile is scaled so that the maximum value of v_R is 0.5 km s^{-1} (Simon and Leighton, 1964; Paniveni et al., 2004; Rieutord and Rincon, 2010).

The flow profile used for the simulation illustrated in Figure 3.2 is shown in Figure 3.3(b). This flow profile is used for all of the simulations described in this chapter. The positions of the cell centres were selected to produce an irregular pattern, as would be seen in real observations of the solar surface. As a result of the translation previously described, one can also see flows contributing from the supergranules through the boundaries. The parameters defining each of the cells is given in Table 3.1.

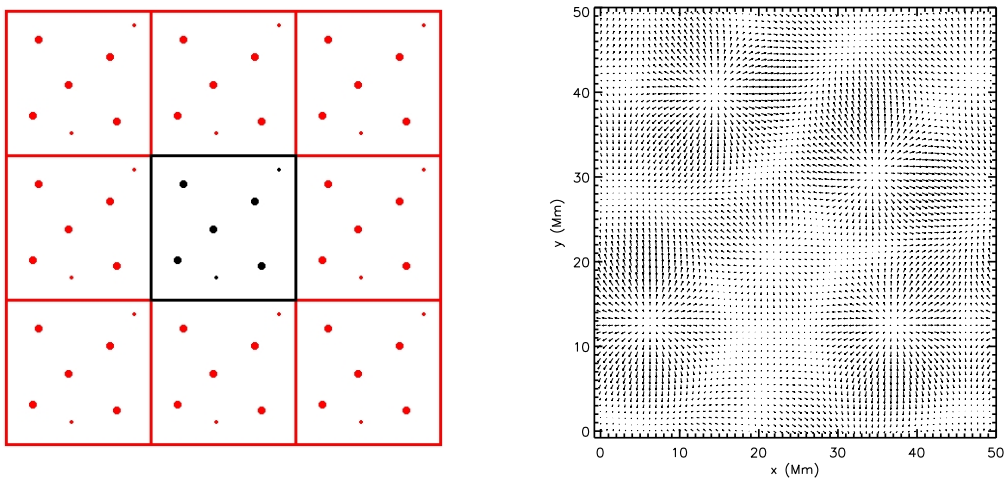

(a) **(b)**

Figure 3.3: (a) The positions of the supergranule cell centres are translated eight times to surround the originals. This simulates the influence of outside flows on the central domain. (b) A simulated supergranular flow profile in which seven cells have been specified in the computational region. The arrows denote the magnitude of the horizontal velocity, where the maximum flow speed is 0.5 km s^{-1}.

Contributions from granular motions are also added to each magnetic element's velocity at each time step. The granular velocity contribution is randomly chosen to be between 0 and 0.1 km s^{-1} if an element is within $0.75R_{\rm sg}$ of the centre of the supergranular cell, and between 0 and 0.2 km s^{-1} if it is further out than this, where $R_{\rm sg}$ is the radius of the supergranule. The direction of this velocity is also chosen as random. A slightly higher value for the granular velocity contribution is chosen if the magnetic element is near the boundary of the supergranule, since the contribution from the supergranular flow profile is small at these locations. This prevents elements from becoming stationary once they reach the network between supergranules. The movie sgflow.mpg, held on the accompanying CD, shows the steady supergranular flow profile of Figure 3.3(b) with random granular contributions added on. It can be seen that the resultant flow profile is non-steady.

One time step within the model is equal to 1 min. This is an arbitrary choice within the model and may be chosen to be higher or lower. We have chosen 1 min as the current cadence of magnetogram data from instruments such as SOHO/MDI and SDO/HMI are of a similar size. Full disc MDI magnetograms are typically of cadence 1 min at best (Scherrer et al., 1995), while HMI line-of-sight magnetograms are of cadence 45 seconds (Scherrer et al., 2012). Many authors studying the observational properties of the solar magnetic carpet have used magnetogram data sets of cadence roughly 1 min, occasionally averaged over a longer time period to reduce noise, for example see Hagenaar (2001), Parnell (2002), Zhou et al. (2010) and Thornton and Parnell (2011). As higher cadences become available for observational data, we may choose a smaller

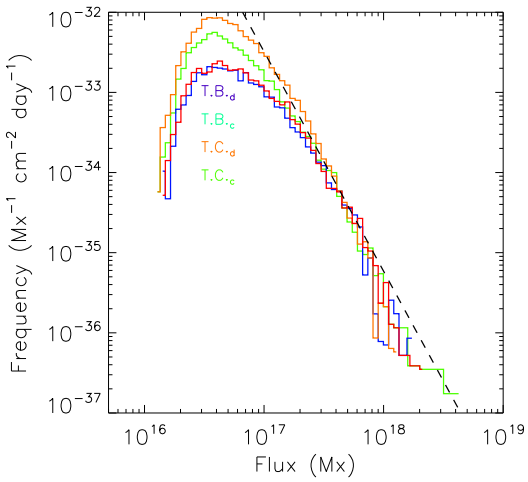

Figure 3.4: Log-log plot of the frequency of emergence against flux emerged in a 5 hour long set of *Hinode*/SOT magnetograms. Results were obtained using a tracked bipolar (TB) and tracked cluster (TC) method applied to clumping (subscript 'c') and downhill (subscript 'd') data. See Thornton and Parnell (2010) for definitions of tracking methods used. The dashed line is a power-law fit as described by Equation (3.8), with $n_0 = 1.77 \times 10^{-14}$ cm^{-2} day^{-1} and $\alpha = 2.74$.

time step in our model. The simulations in Section 3.2 are each run for 250 hr, which corresponds to $15,000$ time steps.

In the next three sections, we discuss the methods used to implement the processes of emergence, fragmentation, cancellation and coalescence.

3.1.3 Emergence

Each emerging bipole is made up of two individual magnetic elements that are of equal flux and opposite polarity. We use the term 'bipole' only when referring to a newly emerging pair of magnetic elements, at all other times we consider single magnetic elements. To simplify computations and prevent infinitesimally small flux elements from arising, we set the minimum unit of flux that a single polarity may have to be equal to $\phi_0 = 10^{16}$ Mx, and define all magnetic elements to have flux that is an integer multiple of ϕ_0 (Parnell, 2001). A bipole of absolute flux ϕ_{bp} consists of two magnetic elements of equal absolute flux, $\phi = \phi_{\text{bp}}/2$, but opposite polarity. The total signed flux of the bipole is therefore zero.

Parameters for Newly Emerging Bipoles

Flux emergence within the simulation is specified by the probability distribution for emerging bipoles from Thornton and Parnell (2011). This is determined from *Hinode*/SOT high resolution magnetograms and is in the form of a power law:

$$N(\phi_{\text{bp}}) = \frac{n_0}{\psi_0}\left(\frac{\phi_{\text{bp}}}{\psi_0}\right)^{-\alpha}, \tag{3.8}$$

where $n_0 = 1.77 \times 10^{-14}$ cm^{-2} day^{-1}, $\psi_0 = 10^{16}$ Mx and $\alpha = 2.74$. The values for n_0 and α come from a feature tracking study of *Hinode*/SOT data that is described by Thornton and Parnell (2011). Figure 3.4 shows a log-log plot of their results for the frequency of emergence versus flux emerged. The acronyms TB and TC indicated emergence detected by a *tracked bipolar* and a *tracked cluster* method respectively. A full description of these methods can be found in the original paper. The subscripts 'd' and 'c' stand for the *downhill* and *clumping* methods of magnetic feature identification, as are described by DeForest et al. (2007).

The quantity $N(\phi_{\text{bp}})d\phi_{\text{bp}}$ is the total number of bipoles that emerge with total absolute flux in the range $[\phi_{\text{bp}}, \phi_{\text{bp}} + d\phi_{\text{bp}}]$, where $d\phi_{\text{bp}}$ is very small. The flux emergence rate for bipoles with flux in the range $[\phi_a, \phi_b]$ in Mx cm^{-2} day^{-1} may be computed as:

$$F_{\text{emer}}(\phi_a, \phi_b) = \int_{\phi_a}^{\phi_b} N(\phi_{\text{bp}})\phi_{\text{bp}} d\phi_{\text{bp}} = \frac{n_0\psi_0}{2-\alpha}\left[\left(\frac{\phi_{\text{bp}}}{\psi_0}\right)^{2-\alpha}\right]_{\phi_a}^{\phi_b}. \tag{3.9}$$

Correspondingly, the number of bipoles emerging in the range $[\phi_a, \phi_b]$ in units of cm^{-2} day^{-1} is then

$$\int_{\phi_a}^{\phi_b} N(\phi_{\text{bp}})d\phi_{\text{bp}} = \int_{\phi_a}^{\phi_b} \frac{n_0}{\psi_0}\left(\frac{\phi_{\text{bp}}}{\psi_0}\right)^{-\alpha} d\phi_{\text{bp}} = \frac{n_0}{1-\alpha}\left[\left(\frac{\phi_{\text{bp}}}{\psi_0}\right)^{1-\alpha}\right]_{\phi_a}^{\phi_b}. \tag{3.10}$$

Let ϕ_{min} and ϕ_{max} be the minimum and maximum flux allowed for emerging bipoles in our simulation. They must both be integer multiples of $2\phi_0$, as each individual polarity will then have an absolute flux that is an integer multiple of $\phi_0 = 10^{16}$ Mx. In addition to this, we must have $\phi_{\text{min}} \geq 2\phi_0$. For our simulations, we choose to emerge only discrete values of flux from ϕ_{min} to ϕ_{max} in steps of size $d\phi = 2\phi_0$. If $m = (\phi_{\text{max}} - \phi_{\text{min}})/2\phi_0$, then the set of emerging flux values of bipoles is

$$\{\phi_k = \phi_{\text{min}} + 2k\phi_0, k = 0, 1, ..., m\},$$

where ϕ_k is the total absolute flux of a newly emerging bipole. For each discrete value ϕ_k, we integrate over the range $[\phi_k - \phi_0, \phi_k + \phi_0]$ to approximate the number of bipoles with absolute

flux ϕ_k that will emerge during the simulation:

$$N'_k = \int_{\phi_k-\psi_0}^{\phi_k+\psi_0} \frac{n_0}{\psi_0}\left(\frac{\phi_{\text{bp}}}{\psi_0}\right)^{-\alpha} d\phi_{\text{bp}} \times A \times D, \tag{3.11}$$

where A is the area of the domain in cm^2 and D is the number of days of the simulation. We cannot allow a non-integer number of bipoles to emerge, so N'_k must be converted to an integer, N_k, by rounding up or down randomly. The $N = \sum_{k=0}^{m} N_k$ bipoles are then randomly assigned a value from 0 to $t_{\text{max}} = 15,000$ (250 hr) using a uniform distribution, which will be the time step in which they emerge. This means that a random number of bipoles emerge each time step, and also a random total quantity of flux.

In addition to flux, diameter and sign, several other parameters must be chosen for each newly emerging bipole. For each bipole, a random uniform integer between 0 and $n-1$ is chosen. This is the index of the supergranule cell within which it will emerge. Its location within the cell is then randomly chosen. Since ephemeral regions have been observed to emerge with a preference towards the edge of a supergranule (Wang, 1988), we also build this into our model. We allow emergence to occur in the range $[0.5R_{\text{sg}}, 0.75R_{\text{sg}}]$, where R_{sg} is the radius of the supergranule. The final parameter that must be chosen for an emerging bipole is its tilt angle, θ. This is the angle of the axis along which the two polarities of the bipole will separate from one another and it is simply a random uniform number between 0 and 2π radians. The main arrays that contain the parameters for magnetic elements throughout the simulation are described in Appendix A.2. The separation velocities of newly emerging magnetic elements are discussed next.

Appearance of Newly Emerging Bipoles

At each time step, newly emerging bipoles are added into the simulation. Each magnetic element undergoes the specified emergence process outlined below until it has travelled $e_{\text{rad}} \times d(\phi) = 1.5d(\phi)$ from its initial position. $e_{\text{rad}} = 1.5$ is a constant that defines the separation that a magnetic element must reach from its emergence point before supergranular flows or other processes may take over its evolution. The element's velocity v_{sep} depends upon how long it has been emerging for and its direction is given by its tilt angle θ. Observational studies show that the two polarities of a newly emerging bipole initially separate at several km s^{-1}, later slowing to velocities that are of a similar order to those of the underlying supergranular flows (Harvey, 1993; Title, 2000; Hagenaar et al., 2003). Within our simulations, two elements will initially separate with a velocity of 3 km s^{-1}, slowing to $1.0 - 1.3$ km s^{-1} after 30 min (30 time steps) and later to 0.5 km s^{-1} which is on the order of the underlying supergranular flow. Initially, the positive and negative magnetic elements within the bipole move in opposite directions along the axis of their tilt angle. The computation of the velocities of newly emerging magnetic elements is described in more

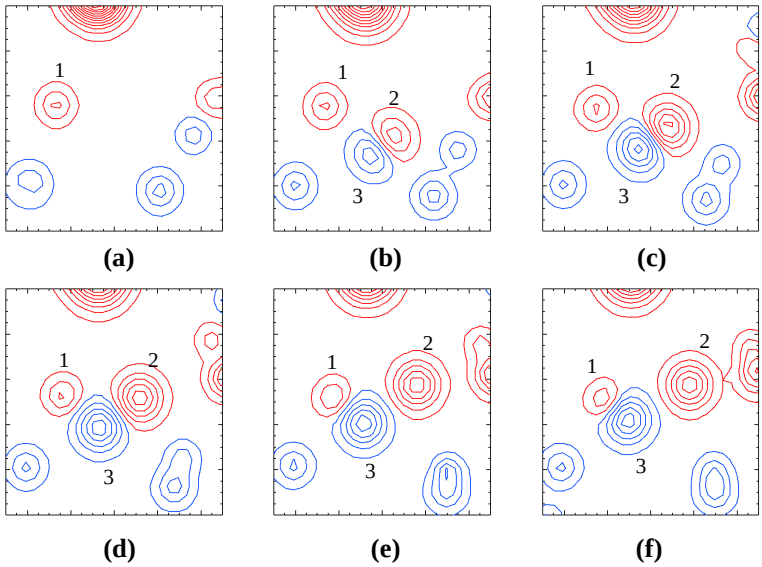

Figure 3.5: A sequence of still images (left to right) showing a newly emerging bipole (elements 2 and 3). Red contours represent positive magnetic field, blue contours represent negative magnetic field. In total, twenty contour levels are shown for each polarity, with absolute values spaced evenly from $1.8 - 68.3$ G. The region is 10 Mm $\times$ 10 Mm in area. The images are taken 4 min apart, and elements of interest have been numbered from 1 to 3, where elements 2 and 3 illustrate emergence. This event may be seen in the accompanying movie, mag2_em.mpg, held on the CD.

detail in Appendix A.3.

Figure 3.5, and the accompanying movie, mag2_em.mpg, show a sequence of images taken from a small region of the synthetic magnetograms produced by one of the simulations. The region is 10×10 Mm^2 in area, and the images are taken 4 min apart. One can see that between images (a) and (b), a new bipole begins to emerge in the centre of the box, the positive and negative polarities are marked ‘2’ and ‘3’ respectively. The two polarities grow in flux as they move apart. Towards the end of the sequence, magnetic element 3 begins to interact with a pre-existing magnetic element, indicated by ‘1’. Notice also that in addition to the two polarities moving in opposite directions to one another, there is a slight drift of the bipole towards the upper left due to the underlying supergranular flow, which also influences the motion. This can be seen more clearly in the movie.

3.1.4 Fragmentation

Fragmentation within our model is based upon the process described by Parnell (2001), where the process of fragmentation depends upon both the flux of the magnetic element and time. Every element is checked for fragmentation at each time step. The fragmentation rate R_{f} is an input parameter for the simulation. We assume that every element of sufficient flux will fragment within

$T_\mathrm{f} = 1/R_\mathrm{f}$ s (seconds). Parnell (2001) suggests that a fragmentation rate of $R_\mathrm{f} > 1.2 \times 10^{-4}$ s^{-1} is required to reproduce the correct absolute flux density and flux distribution, so we take $R_\mathrm{f} = 1.5 \times 10^{-4}$ s^{-1}. This means that a magnetic element of sufficiently large flux will fragment roughly once every $1/R_\mathrm{f} = 6667$ s ≈ 1 hr 50 min. For an element j to have *sufficient flux* to fragment, it must satisfy the inequality

$$\phi_j > \psi\Big(1 - \frac{k_\mathrm{f}}{q}\Big), \tag{3.12}$$

where q is a random number such that $k_\mathrm{f} < q < 1$, and $0 < k_\mathrm{f} \leq 1$. The parameter k_f is fixed at the start of the simulation, but a random q is chosen for every magnetic element every time we check whether it will fragment. Parnell (2001) take a value of ψ that is at the large end of their range of expected flux values, $\psi = 8 \times 10^{18}$ Mx, and $k_\mathrm{f} = 0.75$. Without observational evidence to suggest differently, we take the same values for our simulations. With these parameters, the largest value that the right hand side of Equation (3.12) can take is

$$\psi\left(1 - \frac{k_\mathrm{f}}{\max(q)}\right) = 8 \times 10^{18}\left(1 - \frac{0.75}{1.0}\right) = 2 \times 10^{18} \text{ Mx}.$$

Similarly, the minimum value that the right hand side of Equation (3.12) can take is zero. However, elements are not allowed to fragment if they are of unit flux, ϕ_0. This means that all magnetic elements of absolute flux $\geq 2\phi_0$ may fragment, but elements of greater flux have a higher probability of fragmentation.

Time dependence is built into the fragmentation process as follows. If ϕ_j satisfies Equation (3.12), we then choose a random number s such that $0 < s < 1$. Element j will only fragment during the current time step if

$$s < \frac{T_j}{T_\mathrm{f}},$$

where T_j is the 'age' of magnetic element j in seconds. An element's age is reset to zero every time it fragments, coalesces or cancels with another element. Clearly once $T_j > T_\mathrm{f}$ the right hand side will be greater than 1, meaning the inequality will be satisfied and the element must fragment. Therefore, all magnetic elements of flux greater than 2×10^{18} Mx are guaranteed to fragment within $T = T_\mathrm{f}/60$ time steps (1 hr 50 min), unless some other process takes over their evolution before then.

New Elements Arising From Fragmentation

Within our simulations, elements are allowed to split into just two new elements at a time. In reality, most fragmenting magnetic features only split into two (Thornton, 2011). Once it has

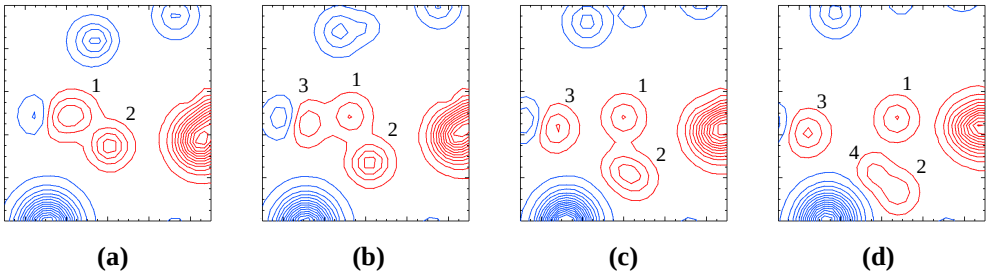

Figure 3.6: A sequence of still images (left to right) showing fragmentation of magnetic elements. Red contours represent positive magnetic field, blue contours represent negative magnetic field. In total, fifteen contour levels are shown for each polarity, with absolute values spaced evenly from $2.3 - 67.7$ G. The region is 10 Mm $\times$ 10 Mm in area. The images are taken 2 min apart, and elements of interest have been numbered from 1 to 4. These interactions may be seen in the accompanying movie, mag3_frag.mpg, held on the CD.

been determined that element j will fragment, a new element k is introduced to represent the element resulting from the fragmentation. The method for adding a new element to the simulation is described in Appendix A.4. The flux and diameter of j and k must now be recomputed. As in Parnell (2001), the original flux ϕ_j is split into two new fluxes, ϕ_1 and ϕ_2. If p is a random number between 0.55 and 0.95, then

$$\phi_1 = p\phi_j.$$

Since all fluxes within the simulation must be integer multiples of ϕ_0, we round ϕ_1/ϕ_0 to the nearest integer. We then take

$$\phi_2 = \phi_j - \phi_1.$$

Elements of flux ϕ_0 are not allowed to fragment. If $\phi_j = 2\phi_0$, then $\phi_1 = \phi_2 = \phi_0$, and if $\phi_j = 3\phi_0$, then $\phi_1 = 2\phi_0$ and $\phi_2 = \phi_0$. We may now set $\phi_j = \phi_1$ and $\phi_k = \phi_2$, then compute their new diameters $d(\phi_j)$ and $d(\phi_k)$.

Motion of Fragmenting Elements

An element's behaviour after it has fragmented depends upon the process that the original element was undergoing before the fragmentation occurred. If it was undergoing emergence, fragmenting from yet another element, or simply being advected by supergranular flows, then its velocity v_R returns to being determined by this process[1]. In the case of emergence, the two new elements produced by fragmentation are also treated as emerging. Their velocities therefore still decrease with time, though the directions of motion of the two new elements j and k are different. If θ is

[1]If the underlying supergranular velocity is very small (< 0.1 km s^{-1}), the new elements may be given a 'push' of $0.1 - 0.2$ km s^{-1} to help them separate.

the direction of motion of the original element, then

$$\theta_1 = \theta + 0.3\pi p \quad \text{and} \quad \theta_2 = \theta - 0.3\pi p,$$

where $0 < p \leq 1$ is randomly chosen for each individual fragmentation (Parnell, 2001). Therefore the two magnetic elements move in the same direction with slightly offset motions.

If the element determined to fragment was undergoing cancellation or coalescence with another element l before it fragmented, the treatment is slightly different. The fluxes and diameters of the two new elements j and k are computed. The new element j then continues to cancel or coalesce with l, while k moves off in a different direction at the velocity of the underlying supergranular flow[2]. The new direction of motion for k is given by

$$\theta_2 = \theta \pm 0.6\pi p,$$

with $0 < p \leq 1$ random.

The parameter f_{rad} defines the separation that a magnetic element will reach from its point of fragmenting, before the underlying supergranular flow takes over. An element j will continue to move away from its fragmentation site until it has reached a distance of $f_{\text{rad}} d(\phi_j) = 1.5 d(\phi_j)$.

Figure 3.6 (and the accompanying movie, mag3_frag.mpg) shows examples of fragmentation occurring within one of the simulations. Element 1 fragments to form a new element, 3; element 2 then begins to fragment to form element 4. Fragmentation may also be seen in the sequence in Figure 3.8 of the following section, where element 2 fragments into a large and a small element.

3.1.5 Coalescence and Cancellation

Every time step, each element that is not currently undergoing the emergence process is checked to see if it will cancel or coalesce with another element. In the current model, an element j may only cancel or coalesce with one single element at any given time. First we determine how many magnetic elements are within interaction range of j (including those through the periodic boundaries). An element k is defined to be within interaction range if d_{sep}, the separation distance, satisfies

$$d_{\text{sep}}(j,k) \leq c_{\text{rad}}(d(\phi_j) + d(\phi_k)),$$

where

$$d_{\text{sep}}(j,k) = |(x_j, y_j) - (x_k, y_k)| \quad \text{and} \quad c_{\text{rad}} = 0.5.$$

[2]Again, the element may be given a ‘push’ if the underlying supergranular velocity is very small.

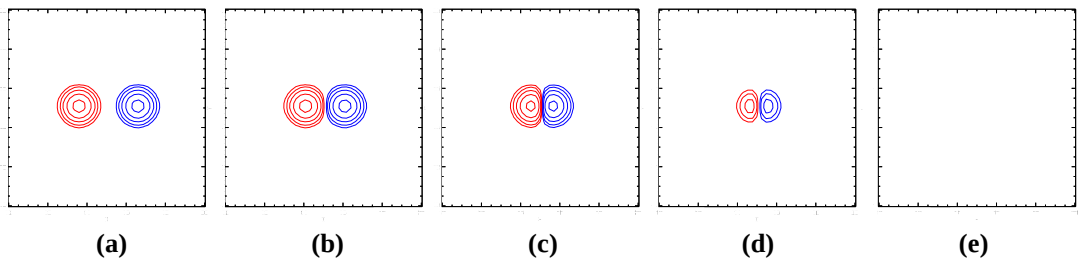

Figure 3.7: A cancellation between two magnetic elements of equal flux and opposite polarity. The bipole shrinks as the elements move together and their Gaussian profiles overlap. By the last frame the magnetic elements overlap completely and no contours of flux remain. This denotes complete cancellation.

The constant c_{rad} defines the interaction range between two magnetic elements. It is important that $c_{\text{rad}} < 0.75$ to prevent elements that have just separated from one another due to emergence from immediately cancelling with one another again. There are also several other conditions for the cancelling or coalescing of j with some element k:

- k must not currently be undergoing emergence,
- k must not currently be cancelling or coalescing with another element,
- If j and k are in the process of fragmenting from one another, then they are not allowed to immediately coalesce. If they are still within range after the fragmentation process has ended, they may then coalesce together (see Section 3.1.4).

If these conditions are all satisfied by more than one element within range of j, then j will cancel or coalesce with the closest element.

Once it has been determined that two elements will cancel or coalesce, they move together at a constant velocity of $v_{\text{C}} = 1.0$ km s^{-1} until their centres meet. Their direction of motion is along the axis defined by their centres.

Since each magnetic element is given a Gaussian profile, their profiles overlap as they move towards one another. In the case of cancellation, this results in both magnetic elements shrinking as they move towards one another. If they are of equal flux and opposite polarity, they will completely cancel one another. This is illustrated in Figure 3.7. Within the magnetic carpet model, both magnetic elements are removed at this stage. In the case of partial cancellation or coalescence, one of the elements is removed when the centres of the elements meet. The method for removing elements from the simulation is given in Appendix A.5. The remaining element's flux is then updated to be the difference between the two original flux values. This new element's motion is now determined by supergranular flows until another process takes over.

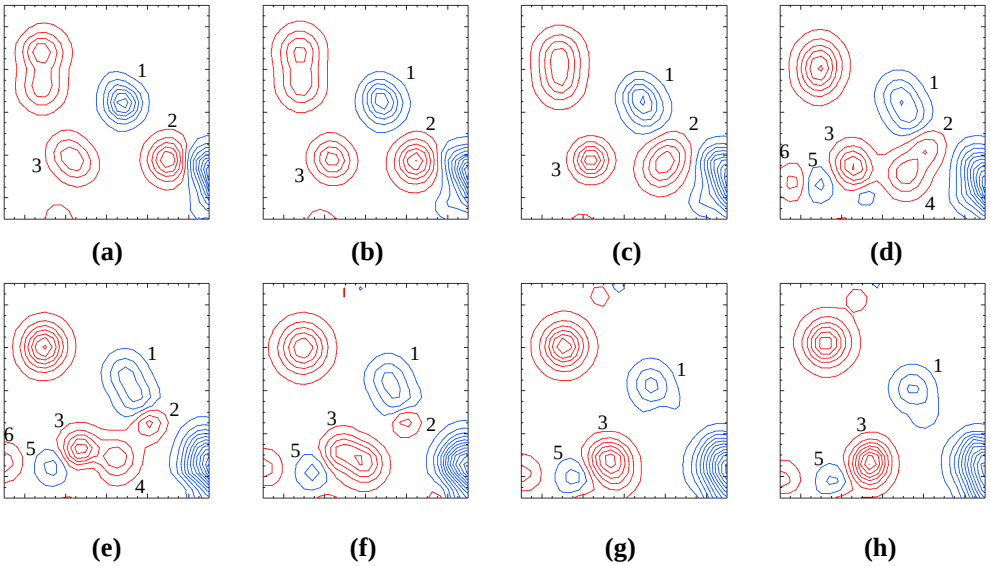

Figure 3.8: A sequence of still images (left to right) showing magnetic elements coalescing and cancelling. Red contours represent positive magnetic field, blue contours represent negative magnetic field. In total, fifteen contour levels are shown for each polarity, spaced evenly from $2.3 - 67.7$ G. The region is 10 Mm $\times$ 10 Mm in area. The images are taken 4 min apart, and elements of interest have been numbered from 1 to 6. These interactions may be seen in the accompanying movie, mag1_canc.mpg, held on the CD.

The processes of cancellation and coalescence occur frequently within the model, and can easily be detected by eye in the synthetic magnetograms. Figure 3.8 (and the accompanying movie, mag1_canc.mpg) shows a sequence of eight images taken from one of the simulations, in which examples of both cancellation and coalescence of magnetic elements can be seen. We follow the evolution of a negative polarity element 1, and two positive elements, 2 and 3. In frame (d) an emergence occurs in the bottom left (5 and 6) and element 2 begins to fragment, creating a new element, 4. As the sequence progresses, a cancellation occurs between 1 and 2, and elements 3 and 4 coalesce. By the end of the sequence, 2 and 4 have disappeared, and 3 has begun cancelling with 5.

3.1.6 Summary of Photospheric Evolution

After the parameters for newly emerging bipoles have been determined, we compute the magnetic field on the photosphere for each time step. At each time step, we first loop over all magnetic elements and determine their current velocities. In addition to the four flux evolution processes described in Sections 3.1.3, 3.1.4 and 3.1.5, we add a contribution from the underlying supergranular flow to each element's velocity. This prevents the motion of elements from being too linear, particularly when undergoing emergence. It seems likely that supergranular flows would continually have an effect on magnetic elements on the real solar surface. We also add a random motion

to every magnetic element that represents the effect of granulation. The main purpose of this is to prevent elements from becoming stationary once they reach the network between supergranules, as our supergranular flow profile does not currently evolve in time. The maximum velocity that an element can take is $3.6 - 3.7$ km s^{-1}. For this to occur, the element would have to be newly emerging ($v_{\text{sep}} = 3.0$ km s^{-1} for the first 15 min) and the contribution from supergranulation and granulation would have to be their maximum values of 0.5 km s^{-1} and 0.2 km s^{-1} respectively, in the same direction as the element's emergence velocity.

We now update the central positions of every element according to its velocity:

$$\mathbf{x} = \mathbf{x} + \mathbf{v_x} dt,$$

$$\mathbf{y} = \mathbf{y} + \mathbf{v_y} dt.$$

The next stage is to check which elements have just started or finished emerging, cancelling, coalescing or fragmenting. Elements are added and removed from the simulation as necessary, and parameters updated. We also check that no elements have moved out of the computational domain. If they have, their coordinates are translated so that they reappear at the opposite side of the box due to the periodic boundaries.

To construct synthetic magnetograms for the line-of-sight component of the magnetic field, we recompute B_z analytically at each time step from the information stored for each magnetic element. This simulated magnetogram is output to a file every time step. The method is as described in Section 3.1.1.

3.2 Results

Using the techniques described above, nine simulations are run keeping all interaction and evolution parameters fixed at values determined to produce the most realistic evolution. The only parameter that is varied is the lowest flux value taken by emerging bipoles. For the model, we consider a quiet region of the solar surface which has no contribution from active regions. Therefore there is no net transfer of flux through the domain. The parameters common to each model are given in Table 3.2. These parameters are described in more detail in Appendix A.1. The locations of supergranular cells and the parameters A_0 and R_0 that specify their strengths are also kept fixed, as described in Section 3.1.2. In the nine simulations, the varying values taken for the minimum absolute flux of our distribution of emerging bipoles are:

$$\phi_{\text{min}} = 10^{16} \times [4,\ 8,\ 10,\ 20,\ 30,\ 40,\ 60,\ 80,\ 100] \text{ Mx}.$$

Parameter	Value	Description
x_{min}, x_{max}	$0, 50$ Mm	$x-$range for computational box.
y_{min}, y_{max}	$0, 50$ Mm	$y-$range for computational box.
t_{max}	$15,000$	Length of simulation.
step_length	1 min	Number of min 1 time step represents.
ϕ_{max}	10^{19} Mx	Maximum absolute flux for newly emerging bipoles.
ϕ_0	10^{16} Mx	Minimum unit of flux.
e_{rad}	1.5	Scales distance a magnetic element will travel from its initial location under emergence.
c_{rad}	0.5	Scales interaction distance for cancellation and coalescence.
f_{rad}	1.5	Scales distance a magnetic element will travel from its initial location under fragmentation.
v_{sg}	0.5 km s^{-1}	Peak value for supergranular flow profile.
R_{f}	1.5×10^{-4} s^{-1}	Fragmentation rate.
ψ	8×10^{18} Mx	Fragmentation parameter.

Table 3.2: Key parameters within the magnetic carpet model, along with their specified. values

The results of the magnetic carpet simulations and the effect of varying ϕ_{min} are considered in the following five sections. Varying ϕ_{min} from high to low values may be regarded as what may be seen as observational instruments improve, and the flux detection limit for magnetograms becomes lower. Four movies showing the full field of view of the synthetic magnetograms accompany this chapter. The movies show the simulations with $\phi_{\text{min}} = 8 \times 10^{16}$ Mx (mag4_start.mpg and mag4_mid.mpg) and $\phi_{\text{min}} = 10^{17}$ Mx (mag1_start.mpg and mag1_mid.mpg). The two movies with the suffix '_start' show the simulations at the start, from $t = 0 - 20$ hr. The computational domain is initially empty of flux. New magnetic elements then emerge within the supergranules and are swept towards the boundaries where they interact with one another. Within both movies, a magnetic network begins to form after just a few hours, and the general shape of the underlying supergranular flow pattern can be seen. The two movies with the suffix '_mid' show the two simulations between the 50th and 60th hour. By this time, both simulations have reached an equilibrium state in which the rate of emergence roughly equals the rate of cancellation of magnetic flux. From these movies it can be seen that the magnetic carpet model is dynamic, with magnetic elements continually evolving and interacting with each other. Where several magnetic elements lie close to one another in the magnetic network, their Gaussian profiles overlap to form large, irregularly shaped magnetic features as would be seen in real magnetograms. Within all of the movies, tiny features can be seen to rapidly appear or disappear. This is due to small magnetic elements whose Gaussian profiles are lower than the contour levels we have chosen to show. Occasionally such elements overlap to produce a larger profile in B_z, and briefly appear in the synthetic magnetogram time series. This is reminiscent of 'noise' within our synthetic magnetograms, as occurs in real magnetograms. Although they are not all shown within the movies, we keep track of

all magnetic elements within each simulation at all times. Section 3.2.1 shows some still images from the simulation with $\phi_{\text{min}} = 8 \times 10^{16}$ Mx.

3.2.1 Example Synthetic Magnetograms

Figure 3.9 shows contour plots of B_z for a simulation in which newly emerging bipoles have a total flux in the range $8 \times 10^{16} - 1 \times 10^{19}$ Mx. The images are taken at $t = 0.1$, $t = 10$, $t = 20$, $t = 225$, $t = 230$ and $t = 249$ hr. These images may be compared with the flow profile in Figure 3.3(b) to compare the location of the magnetic elements with respect to the underlying supergranular flow pattern.

At $t = 0$ hr the box is empty of magnetic flux. As the simulation progresses, bipoles are allowed to emerge following a supergranular cell pattern. After 6 min (image (a)) small magnetic elements have begun to appear within the supergranular cells. At (b) $t = 10$ hr, many of the elements have begun to encounter one another and interact at the cell edges, and by (c) $t = 20$ hr a magnetic network of larger elements has formed along the supergranule boundaries. By this stage, the model has reached a steady state in which there is a balance between the rates of emerging and cancelling flux. As a result, a similar network of magnetic flux exists in each of the later images, (d), (e) and (f). Since the supergranular flow profile is steady throughout the simulation, the spatial location of the magnetic network does not vary greatly, however the exact distribution of magnetic flux elements significantly changes. From this it can be seen that the steady flow profile does not lead to the formation of unphysically large magnetic elements. However, it would not lead to the random walk of magnetic elements across the solar surface as proposed by Leighton (1964). Since we are presently only considering a small, localised area, such a random walk is not important. Comparing images (d) and (e) at $t = 225$ and $t = 230$ hr, it can be seen that the distribution of magnetic elements varies significantly between the two images, even though they are only spaced 5 hr apart. This implies that the photospheric recycle time of the simulated magnetograms is short, as desired. A plot of total absolute flux versus time is given in Figure 3.10(b) and discussed in Section 3.2.2.

3.2.2 Flux and Mean Magnetic Field

For all simulations, the computational box is initially empty of magnetic flux. As the simulation progresses, new magnetic bipoles emerge within the supergranular cells and magnetic elements interact with one another. It is important to verify that the model reaches a steady state in which the absolute flux density oscillates about an average value. Plots of the total absolute flux within the box as a function of time are shown in Figure 3.10 for $\phi_{\text{min}} = 4,\ 8,\ 10,\ 20,\ 30$ and 100×10^{16} Mx. Clearly, the lower the value of ϕ_{min}, the larger the range of flux values for emerging bipoles,

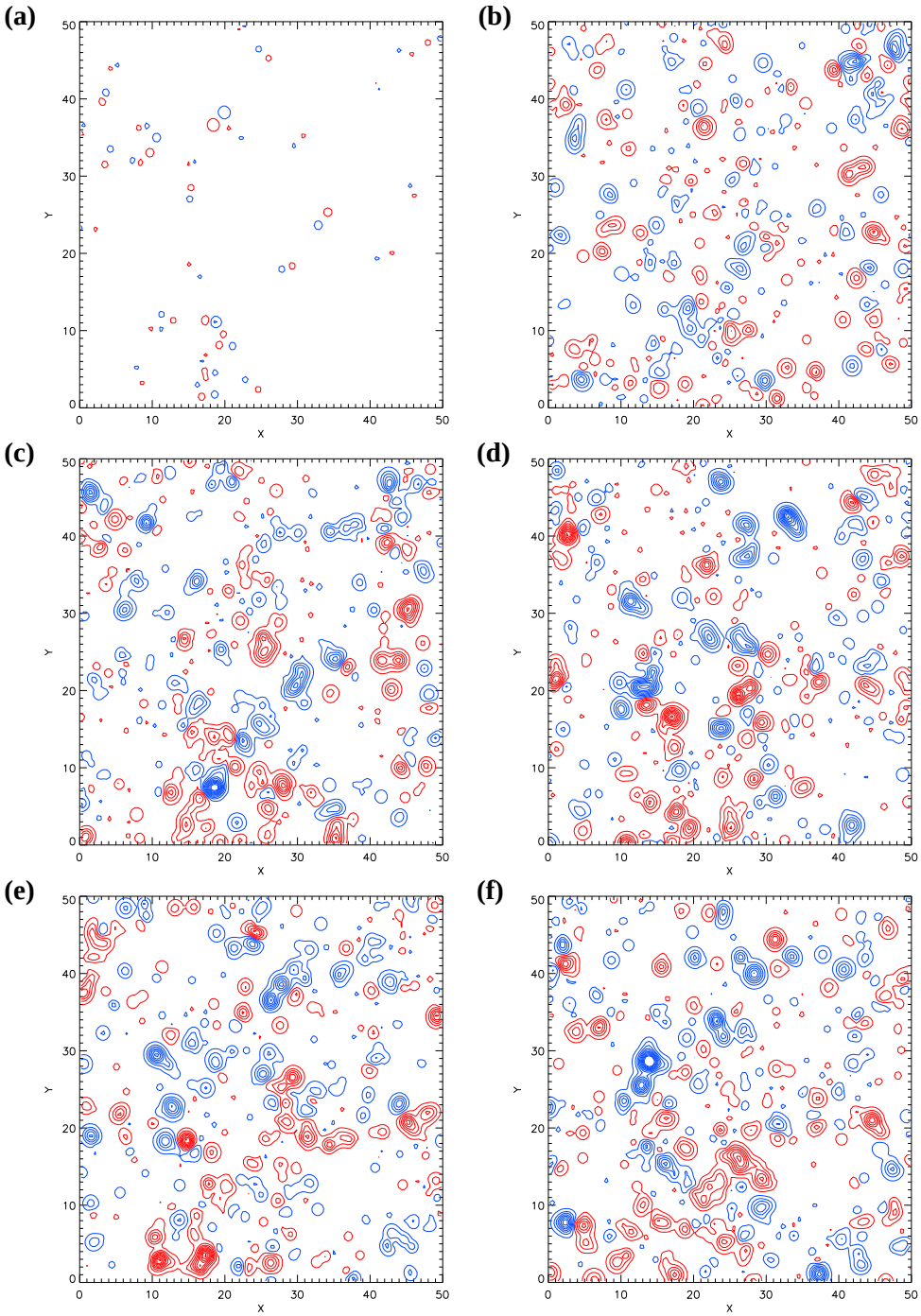

Figure 3.9: Synthetic magnetograms for a simulation with a flux emergence range of 8×10^{16} - 1×10^{19} Mx. Red contours represent positive magnetic field, blue contours represent negative, where ten contour levels are shown for each polarity with absolute values spaced evenly between 3.5 G and 66.5 G. The time in hours at which each image is taken and number of individual elements (ns) composing the magnetogram are as follows: (a) $t = 0.1$, ns=102, (b) $t = 10$, ns=550, (c) $t = 20$, ns=607, (d) $t = 225$, ns=595, (e) $t = 230$, ns=565 and (f) $t = 249$, ns=603. Two movies of this time series of synthetic magnetograms are given on the CD: mag4_start.mpg shows simulation from $t = 0 - 20$ hr; mag4_mid.mpg shows the simulation from $t = 50 - 60$ hr.

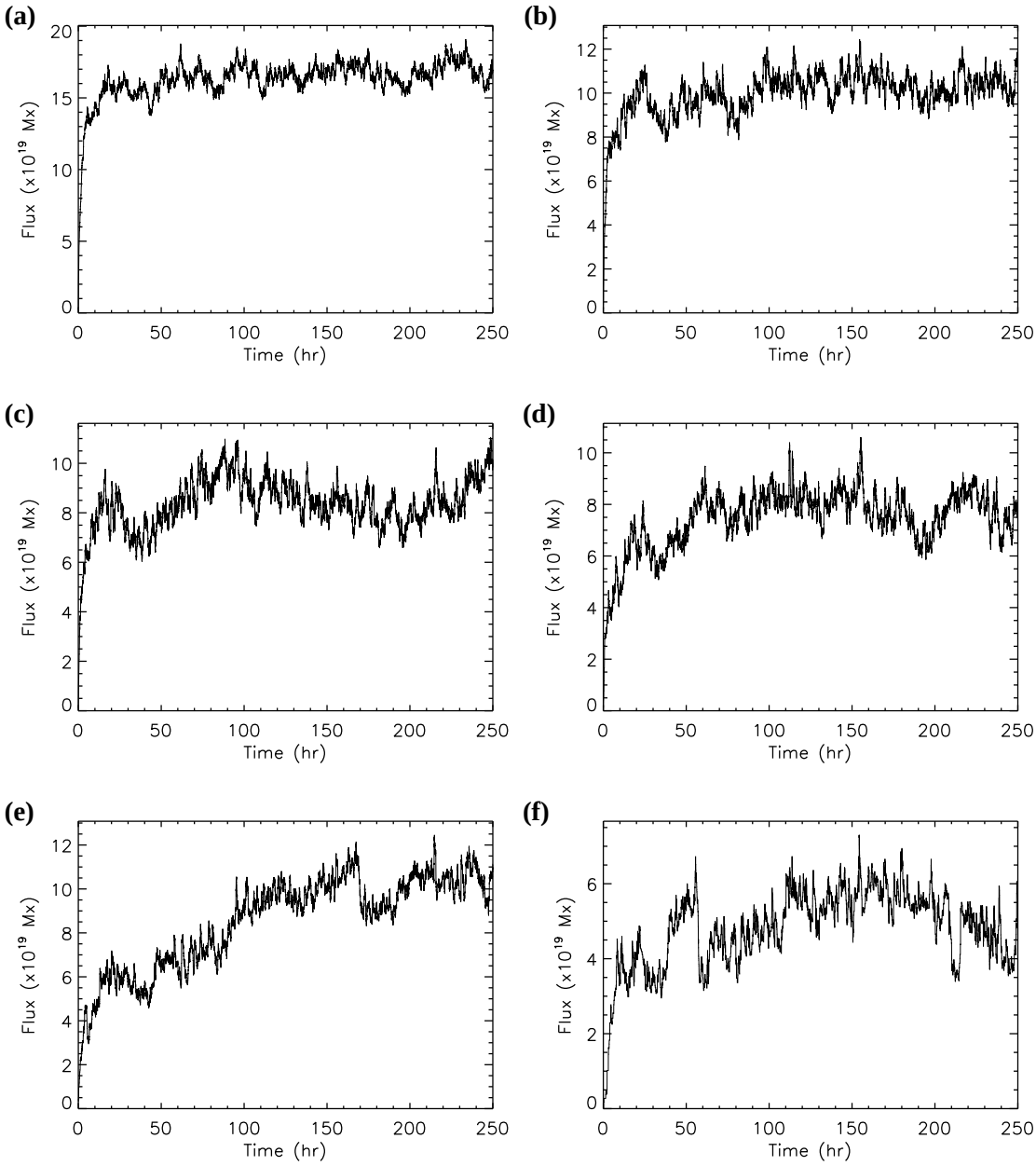

Figure 3.10: Total absolute flux within the computational box as a function of time for $\phi_{\rm min}$ of (a) 4×10^{16} Mx, (b) 8×10^{16} Mx, (c) 1×10^{17} Mx (d) 2×10^{17} Mx, (e) 3×10^{17} Mx and (f) 10^{18} Mx.

and thus the greater the rate of flux emergence. This in turn leads to the total absolute flux for the simulation levelling off at a higher value.

It can be seen from Equation (3.8) that $N(\phi_{\text{bp}})$ will be greater for smaller values of ϕ_{bp}. Therefore a lower value of ϕ_{min} results in a large number of small bipoles emerging. For the case where $\phi_{\text{min}} = 4 \times 10^{16}$ Mx (Figure 3.10(a)), the absolute flux levels off after approximately 24 hr. After this time it oscillates between 1.58×10^{20} Mx and 1.74×10^{20} Mx. This variation is around 5% from the mean value of 1.66×10^{20} Mx. When $\phi_{\text{min}} = 8 \times 10^{16}$ Mx, the absolute flux oscillates slightly more than this, but the total flux still becomes roughly steady after 24 hr. For even higher ϕ_{min}, and hence a smaller flux emergence range, the variation of the absolute flux is much more erratic. For these cases, small numbers of large elements emerge, which have a significant effect on the value of the overall absolute flux within the box at any one instant in time. When $\phi_{\text{min}} = 2 \times 10^{17}$ Mx or 10^{18} Mx (Figure 3.10(d) and (f)) there are several points where the total flux value spikes due to a large bipole emerging, or drops due to the lack of emergence of new bipoles, or the disappearance of two or more large flux elements through cancellation. However, it is clear from Figure 3.10 that if ϕ_{min} is chosen low enough, a steady state is soon found.

In several of the simulations with ϕ_{min} larger than 2×10^{17} Mx, the total absolute flux within the box steadily increases throughout the 250 hour period, and hence a steady state is not reached (e.g. when $\phi_{\text{min}} = 3 \times 10^{17}$ Mx, Figure 3.10(e)). The absolute flux for these simulations may level off if the simulations were run for longer, but there would still be a large variation about this value. In Figure 3.10(e) ($\phi_{\text{min}} = 3 \times 10^{17}$ Mx), the maximum value of flux that is attained is higher than in the $\phi_{\text{min}} = 1 \times 10^{17}$ Mx and $\phi_{\text{min}} = 2 \times 10^{17}$ Mx cases (Figures 3.10(c) and (d)). The flux eventually appears to level off around 10^{20} Mx, but the $\phi_{\text{min}} = 3 \times 10^{17}$ Mx simulation is something of an outlier compared with the other eight simulations. The mean values for the total absolute flux averaged over each simulation, and their percentage variation are shown in Table 3.3. The means are computed for values taken after 30 hr of the simulation have elapsed, so that the model has had a chance to reach a steady state. The highest flux values and lowest variation are found for the lowest value of ϕ_{min}.

Graphs of the mean magnetic field strength (red line) as a function of time are shown in Figure 3.11 for two of the simulations: (a) $\phi_{\text{min}} = 4 \times 10^{16}$ Mx and (b) $\phi_{\text{min}} = 3 \times 10^{17}$ Mx. Note that in each graph a different scale is used for the vertical axis. Over-plotted on each graph is the number of magnetic elements as a function of time (black line), divided by 100 so that the curve is in the same range as the mean field. As one would expect, the mean magnetic field strength is higher in simulations where emergence occurs over a larger range. The time averaged values for the mean magnetic field in each simulation are given in Table 3.3 along with the mean number of magnetic elements. The mean values for the simulations with a $\phi_{\text{min}} < 3 \times 10^{17}$ are within the observed range of $3 - 10$ G (Cranmer and van Ballegooijen, 2010). The mean flux densities calculated for $\phi_{\text{min}} \geq 4 \times 10^{17}$ Mx are slightly lower than observed values, but this is

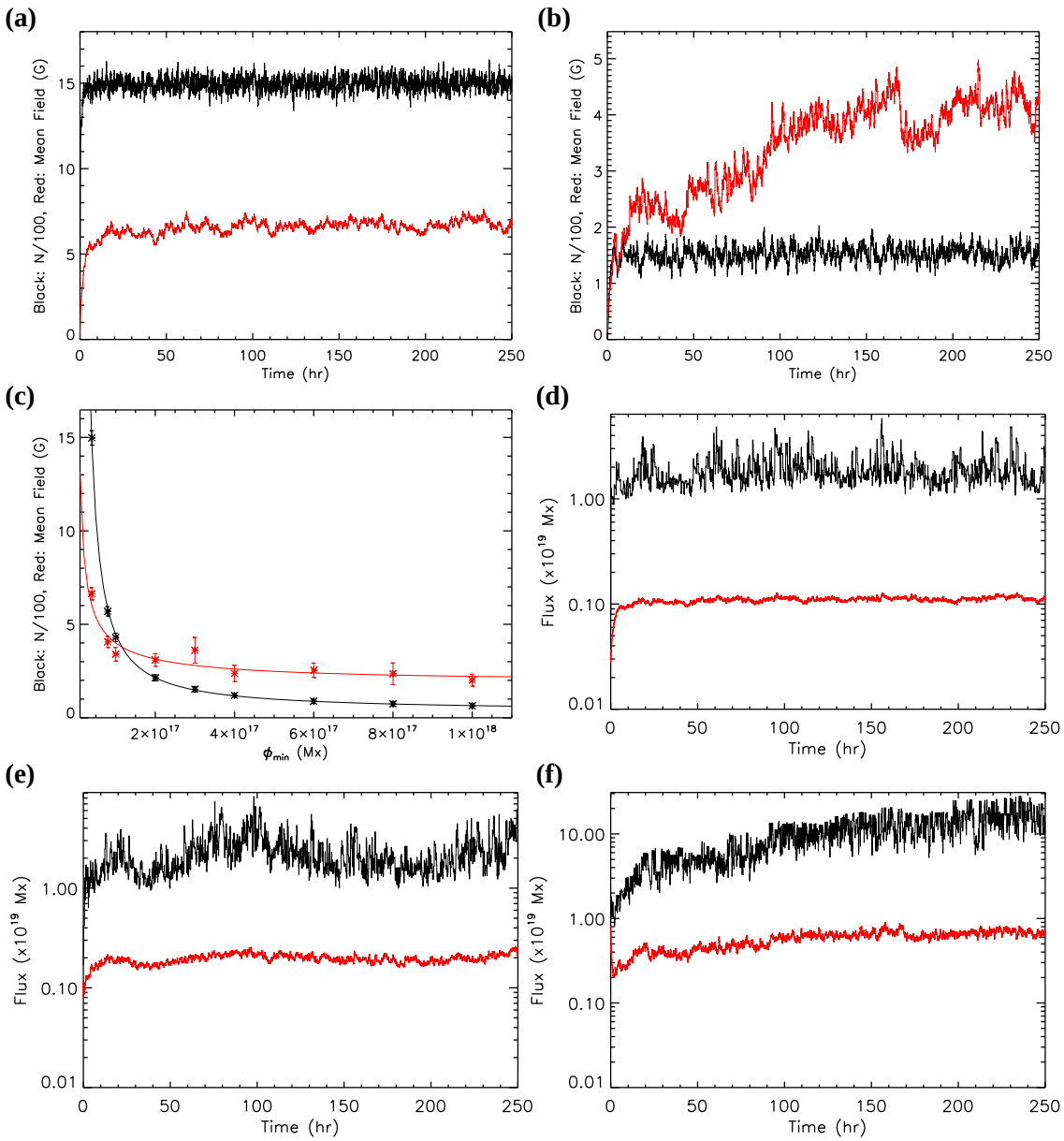

Figure 3.11: (a) and (b) Red line: mean magnetic field (G) and black line: total number of magnetic elements ($N/100$) as a function of time for ϕ_{min} of (a) 4×10^{16} Mx and (b) 3×10^{17} Mx. (c) Red fitted line: time averaged mean magnetic field (G) and black fitted line: average number of magnetic elements per frame ($N/100$), for each simulation. (d)-(f) Maximum flux (black line) and mean flux (red line) of a magnetic element as a function of time for ϕ_{min} of (d) 4×10^{16} Mx, (e) 1×10^{17} Mx and (f) 3×10^{17} Mx.

ϕ_{min} ($\times 10^{16}$ Mx)	Mean Total Absolute Flux ($\times 10^{19}$ Mx)	Percentage Variation of Total Absolute Flux	Mean Absolute Flux Density (G)	Mean Number of Elements per Frame
4	16.58	4.9	6.6	1497
8	10.14	7.4	4.1	570
10	8.50	10.7	3.4	430
20	7.72	10.8	3.1	213
30	9.02	19.1	3.6	153
40	5.92	18.4	2.4	120
60	6.35	15.2	2.5	88
80	5.88	24.7	2.4	74
100	5.03	15.8	2.0	63

Table 3.3: Mean values for each simulation for the total absolute flux, absolute flux density and number of magnetic elements within the box.

to be expected since realistically, small-scale flux emergence on the Sun is not restricted to such a limited range.

The number of magnetic elements that exist within the box as a function of time reaches a steady state very rapidly in all nine simulations, levelling off after just a few hours. This occurs shortly after the first magnetic elements within the simulation reach the network between supergranules and begin to coalesce and cancel. The average supergranular crossing time in the model, the time taken for a magnetic element to reach the edge of the supergranule once it has emerged, is around $3-4$ hr. A typical distance that a bipole might emerge from the edge of a supergranule is 7 Mm, if we assume an average velocity of 0.5 km s^{-1} then each polarity would reach the boundary after 3.9 hr. The levelling off of the total absolute flux and number of magnetic elements is therefore determined by the time scale of the flow profile. It can be seen for the $\phi_{\text{min}} = 3 \times 10^{17}$ Mx (Figure 3.11(b)) simulation, that the number of elements levels off rapidly and oscillates around a steady state, even though the mean field (and absolute flux) are increasing throughout the simulation. This indicates that roughly the same number of elements exist, but larger elements are forming as they meet and coalesce at the boundaries of the supergranules. Figure 3.11(c) shows the mean field and number of elements (/100) averaged over the simulation versus ϕ_{min}. Initially, both the mean field and number of elements drop very rapidly with increasing ϕ_{min}, then level off above $\phi_{\text{min}} = 2 \times 10^{17}$ Mx.

Figures 3.11(d)$-$(f) show plots of the maximum flux of a magnetic element (black line) and the mean flux of a magnetic element (red line) as a function of time for three of the simulations: (d) $\phi_{\text{min}} = 4 \times 10^{16}$ Mx, (e) $\phi_{\text{min}} = 1 \times 10^{17}$ Mx and (f) $\phi_{\text{min}} = 3 \times 10^{17}$ Mx. For $\phi_{\text{min}} = 4 \times 10^{16}$ Mx, the maximum flux that a magnetic element takes during the simulation oscillates around 2×10^{18} Mx, while the mean flux of a magnetic element is about 10^{17} Mx. When $\phi_{\text{min}} = 1 \times 10^{17}$ Mx, the maximum flux of a magnetic element during the simulation oscillates more and

is higher, between $\sim 2 \times 10^{18} - 5 \times 10^{18}$ Mx. Therefore a higher ϕ_{min} results in fewer magnetic elements within the simulation, but on average higher flux per magnetic element. Finally, in the $\phi_{\text{min}} = 3 \times 10^{17}$ Mx simulation, the maximum and mean flux of a magnetic element increase throughout the simulation, particularly the maximum flux of a magnetic element. This is further evidence that larger magnetic features are forming at the boundaries of supergranules within this simulation.

3.2.3 Rates and Frequencies

Within this thesis, the *rates* of magnetic flux emergence and cancellation are defined in terms of Mx cm^{-2} day^{-1}. The *frequency* of magnetic flux emergence and cancellation is defined to be the number of occurrences in cm^{-2} day^{-1}.

Figures 3.12(a) and (b) show plots of the variation of the rates of magnetic flux emergence (solid line) and magnetic flux cancellation (dashed line) during the (a) $\phi_{\text{min}} = 8 \times 10^{16}$ Mx and (b) $\phi_{\text{min}} = 3 \times 10^{17}$ Mx simulations, in Mx cm^{-2} day^{-1}. In all cases we find that the emergence and cancellation rates quickly become approximately equal, confirming that the model has reached a steady state. When $\phi_{\text{min}} = 8 \times 10^{16}$ Mx or less, the plots are steady, as a large number of small magnetic elements emerge and subsequently cancel, helping to keep the emergence and cancellation rates steady. As ϕ_{min} increases these curves become less steady (e. g.. Figure 3.12(b)), but the time averaged emergence and cancellation rates for each simulation are all of similar values.

In simulations with higher ϕ_{min} one would expect the average emergence rate to be slightly higher than the average cancellation rate, since the total absolute flux in several of these cases increases slightly throughout the simulation. This can be seen in Table 3.4, in which the average emergence and cancellation rates for each simulation are listed. In particular, for the $\phi_{\text{min}} = 3 \times 10^{17}$ Mx simulation the emergence rate is greater than the cancellation rate by roughly 0.2 Mx cm^{-2} day^{-1}. In all of the other simulations, the emergence rate is only around 0.1 Mx cm^{-2} day^{-1} higher than the cancellation rate, indicating again that the $\phi_{\text{min}} = 3 \times 10^{17}$ Mx is an outlier. Figure 3.12(c) shows a plot of the average emergence and cancellation rates for each simulation. The analytical solution for the emergence rate calculated from Equation (3.9) is over-plotted in blue.

Figures 3.12(d) and (e) show plots of the variation of the emergence and cancellation frequencies throughout the simulation for (d) $\phi_{\text{min}} = 8 \times 10^{16}$ Mx and (e) $\phi_{\text{min}} = 3 \times 10^{17}$ Mx. The solid line represents emergence, the dashed line represents cancellation. It can be seen that cancellation events occur more often than emergence events even though the two processes have similar rates. This is because large flux elements may fragment, which leads to more elements that may cancel. As with emergence and cancellation rates, the curves are steadier when ϕ_{min}

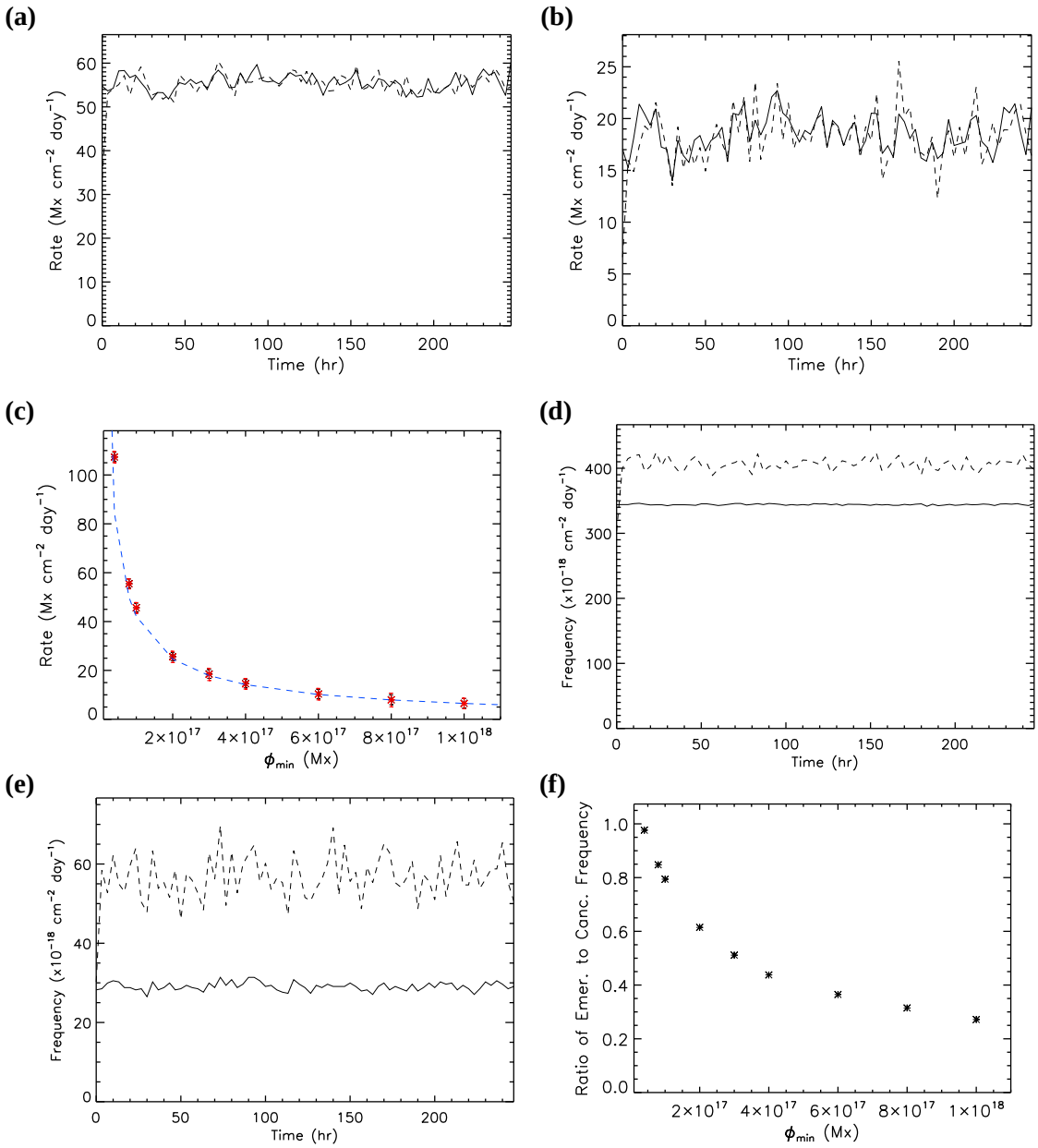

Figure 3.12: (a) and (b) emergence (solid line) and cancellation (dashed line) rates for the simulations with (a) $\phi_{\text{min}} = 8 \times 10^{16}$ Mx and (b) $\phi_{\text{min}} = 3 \times 10^{17}$ Mx. (c) Averaged emergence (black) and cancellation (red) rates for all nine simulations. The blue dashed line represents the emergence rates as calculated by Equation (3.9). (d) and (e) emergence (solid line) and cancellation (dashed line) frequencies for the simulations with $\phi_{\text{min}} = 8 \times 10^{16}$ Mx and $\phi_{\text{min}} = 3 \times 10^{17}$ Mx. (f) Ratio of average emergence to average cancellation frequencies for each simulation.

ϕ_{min} ($\times 10^{16}$ Mx)	Flux Emergence Rate (Mx cm^{-2} day^{-1})	Flux Cancellation Rate (Mx cm^{-2} day^{-1})	Emergence Frequency ($\times 10^{-18}$ cm^{-2} day^{-1})	Cancellation Frequency ($\times 10^{-18}$ cm^{-2} day^{-1})
4	107.37	107.30	1503.9	1540.6
8	55.52	55.41	344.2	406.0
10	45.69	45.59	222.1	279.7
20	25.66	25.52	60.4	98.3
30	18.56	18.32	29.1	56.9
40	14.61	14.50	17.4	39.6
60	10.34	10.27	8.5	23.2
80	8.00	7.89	5.1	16.2
100	6.53	6.45	3.4	12.5

Table 3.4: Time averaged emergence and cancellation rates and frequencies for each simulation.

is lower. The average emergence and cancellation frequencies for each simulation are given in Table 3.4. In agreement with Parnell (2001), the cancellation frequency is always greater than the emergence frequency.

The difference between the frequencies of emergence and cancellation increases with increasing ϕ_{min}. This is particularly apparent for larger values of ϕ_{min}, where emergence only produces a relatively small number of large elements (e.g. Figure 3.12(e)). These elements may then break apart multiple times to produce large numbers of small continually cancelling and coalescing elements, resulting in a significantly higher frequency of cancellation than emergence. This occurs because emergence within each simulation is restricted to a narrow range of flux values, whereas cancellation may occur on any scale. Figure 3.12(f) shows the ratio of emergence to cancellation frequencies. Note that even though the cancellation frequency (in cm^{-2} day^{-1}) may be much greater than the emergence frequency, the rates of emergence and cancellation (in Mx cm^{-2} day^{-1}) are still roughly equal. The same quantity of flux emerges and disappears throughout the simulation, only the size of the magnetic elements involved in these processes changes.

3.2.4 Distribution of Flux

Figures 3.13(a) and (b) show number density plots for the number of magnetic elements as a function of their flux for the simulations with $\phi_{\text{min}} = 4 \times 10^{16}$ Mx and $\phi_{\text{min}} = 8 \times 10^{16}$ Mx. In each case the black line represents the number density of magnetic elements versus their absolute flux value. This curve is produced by analysing the distribution every 600 time steps, which is equivalent to every 10 hr, and summing up all the flux distributions taken for a particular simulation. The length of time between samples was chosen so that the flux within the model will have recycled from one sample to the next. This prevents elements from being counted more than

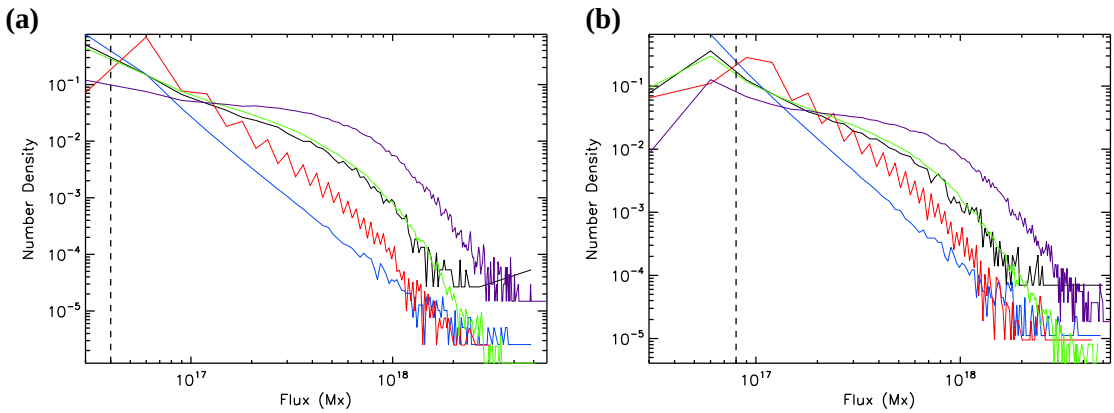

Figure 3.13: Number densities for (a) $\phi_{\text{min}} = 4 \times 10^{16}$ Mx and (b) $\phi_{\text{min}} = 8 \times 10^{16}$ Mx simulations: the black line represents the number density of flux elements versus absolute flux content. The blue line illustrates number of emergence events versus absolute flux emerging in an event. The red line illustrates number of cancellation events versus absolute flux lost in a cancellation event. The green line illustrates number of coalescence events versus absolute flux in a coalescence. The purple line illustrates number of fragmentation events versus absolute flux of the original element that fragmented. The black dashed line indicates the value of ϕ_{min}.

once.

The other four lines on each plot represent the occurrence of each of the four flux evolution processes described in Section 3.1. In the simulations it is possible to keep track of every event that occurs, so the sample size is much larger than the flux distribution sample size, as any one element may undergo a number of processes. The blue line corresponds to the number density of emergences versus the total absolute flux of the emerging bipole, while the red line represents the number density of cancellations versus flux removed during the cancellation event. It can be seen that the number density of cancellation events is greater than the number density of emergence events until $\phi > 10^{18}$ Mx. This fits with previous results that show many more cancellation events occur than emergence events, where the events tend to occur between smaller magnetic elements. Above a flux of 10^{18} Mx, fragmentation (purple) is so strong that it affects the elements before they can cancel (red). Since the rates of emergence and cancellation are roughly equal in each simulation, more large elements must emerge than cancel.

The green line represents the number density of coalescence events versus the absolute flux of the two coalescing elements. In all nine simulations (only two are illustrated here) this curve appears to follow the flux distribution curve (black) very closely, although the fit is not so good at higher ϕ (larger elements do not exist for very long within the simulation, so many are missed when sampling the flux distribution only once every 600 time steps). This supports the suggestion of Thornton and Parnell (2011), that coalescence is the dominant process for small-scale elements. They come to this conclusion because this is one of the reasons why fewer small-scale elements are observed on the solar photosphere than are found to emerge. It can be seen from the plots in

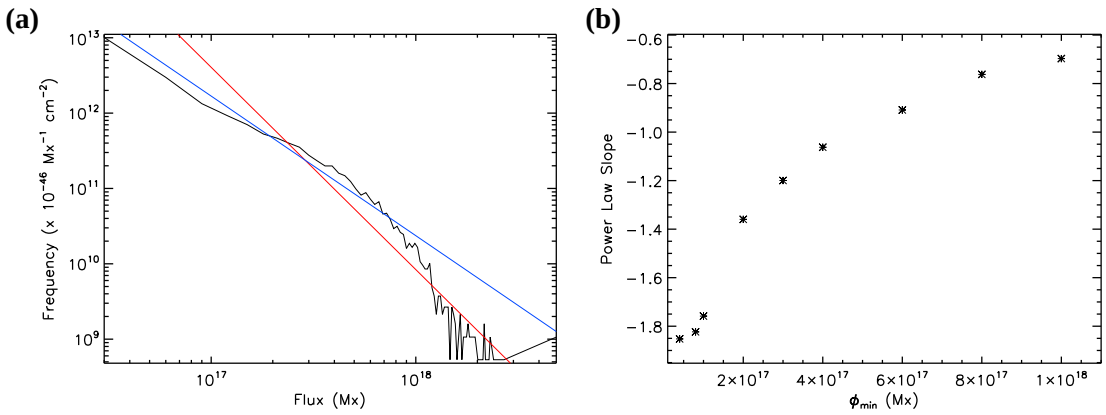

Figure 3.14: (a) For the simulation with ϕ_{min} of 4×10^{16} Mx. The black line represents flux density: log plot of frequency of occurrence versus absolute flux of magnetic element. The red line represents the fitted line for the full range of flux values, slope=-2.68. The blue line represents the fitted line for the range $\phi = [10^{16}, 10^{18}]$ Mx, slope=-1.85. (b) Slopes for flux distribution in the range $\phi = [10^{16}, 10^{18}]$ Mx for each simulation.

Figures 3.13(a) and (b) that for small values of ϕ, the number density of emerging events (blue) is greater than the flux distribution (black). This supports the fact that coalescence is dominant for small-scale fields. In order for our model to be more conclusive on this matter however, it is necessary to allow the existence and emergence of even smaller flux elements than $\phi_0 = 10^{16}$ Mx. Since the green (coalescence) line follows the flux distribution (black) so closely, this implies that any and all magnetic elements may undergo coalescence, it is not flux dependent.

Fragmentation is defined in our simulations to be strongly flux dependent. The purple line represents the number density of fragmentation events versus the flux of the original magnetic element. For small ϕ, the curve for fragmentation is lower than those of all of the other processes. However, it can be seen that as an element's absolute flux increases the fragmentation process becomes dominant.

Figure 3.14(a) is a plot of the frequency of occurrence of flux elements versus their flux content, for the simulation with $\phi_{\text{min}} = 4 \times 10^{16}$ (black line). Units of $\times 10^{-46}$ Mx^{-1} cm^{-2} have been chosen for the $y-$axis in order to compare the plot with Figure 5 of Parnell et al. (2009). Two straight lines have been fitted to the data. We note that our data does not span 3 orders of magnitude, as is technically required to compute a power law relation. However, power laws have been used for observational data so we have fitted one for comparison, taking into account this limitation. The red line is fitted using all of the data, and has a slope of -2.68. The blue line is fitted for elements in the range $10^{16} - 10^{18}$ Mx, therefore missing the low rate of emergence upper flux range, as the sample size for our model is much better for smaller elements. Note that as we are considering an isolated region of the solar surface, the upper bound is solely dependent on emergence and coalescence. No elements may enter the domain due to the dispersal of magnetic

flux from active regions. As a result, we find that our distribution of elements falls off faster than is observed at higher values of flux. Hence we restrict the power law index to those flux elements that we adequately model. The fit of the blue line is good in this range. It has a slope of -1.85, which is in agreement with the findings of Parnell et al. (2009). They fit a line with a slope of -1.85 to data for flux elements observed by SOHO/MDI and *Hinode*/SOT that spans the range $10^{16} - 10^{23}$ Mx. Therefore our model, which only models the lower range of this, fits this well. The method that they use to detect magnetic flux features also differs from the way that we define them. They use a 'clumping' method, whereas our definition of a magnetic element is more suited to the 'downhill' method of feature tracking (DeForest et al., 2007; Lamb et al., 2008, 2010). The downhill method is good at picking out individual peaks in magnetic flux. Particularly for larger magnetic regions, several peaks may be detected by downhill and counted as separate magnetic features. However, the same region may be counted as a single feature by the clumping method (see Figures 1 and 7 of DeForest et al. (2007)). A flux distribution detected using downhill would result in a lower 'tail' towards higher fluxes, as is seen in our Figure 3.14(a). A feature tracking study of our synthetic magnetograms would be of interest, using a clumping method such as is described by Thornton and Parnell (2011), to determine what effect it has on the tail.

The equation of Parnell et al. (2009) describing the frequency of occurrence of elements with an absolute flux of ϕ has the form

$$N(\phi) = \frac{N_{\mathrm{f}}}{\psi_0}\left(\frac{\phi}{\psi_0}\right)^{-1.85} \mathrm{Mx}^{-1}\ \mathrm{cm}^{-2}, \tag{3.13}$$

where $\psi_0 = 10^{16}$ Mx and $N_{\mathrm{f}} = 3.6 \times 10^{-17}$ is the value obtained using a clumping method of feature tracking[3]. In our simulations, we obtain $N_{\mathrm{f}} = 1.2 \times 10^{-16}$, which is 3.3 times larger. A possible reason for this is the difference between our definition of a flux element, and the way that features are defined by Parnell et al. (2009). As can be seen in their Figure 4(a), the clumping method they use produces relatively large, irregularly shaped 'flux massifs'. Since we define magnetic elements to be compact and circular, such a feature in our model would be composed of many elements. For this reason we require many more small magnetic elements to describe the flux distribution of the quiet Sun, hence the larger value of N_{f} in the number density equation. It should be noted that while our definition of a magnetic element is different from that of Parnell et al. (2009) after it has emerged, this does not affect the emergence power law Thornton and Parnell (2011), as during the process of emergence our definitions of magnetic elements agree.

Our reasoning for the difference in values of N_{f} is supported by some simple calculations. If $\alpha = 1.85$, then the average flux density (B_{avg}) and average flux of a magnetic element (ϕ_{avg}) are

[3] C. E. Parnell (private communication).

given by

$$B_{\text{avg}} = \int_{\phi_{\text{min}}}^{\phi_{\text{max}}} N(\phi)\phi d\phi = \frac{N_{\text{f}}\psi_0}{2-\alpha}\left[\left(\frac{\phi}{\psi_0}\right)^{2-\alpha}\right]_{\phi_{\text{min}}}^{\phi_{\text{max}}} \quad \text{Mx cm}^{-2} \tag{3.14}$$

and

$$\phi_{\text{avg}} = \frac{B_{\text{avg}}}{N_{\text{tot}}} \quad \text{Mx}, \tag{3.15}$$

where

$$N_{\text{tot}} = \int_{\phi_{\text{min}}}^{\phi_{\text{max}}} N(\phi)d\phi = \frac{N_{\text{f}}}{1-\alpha}\left[\left(\frac{\phi}{\psi_0}\right)^{1-\alpha}\right]_{\phi_{\text{min}}}^{\phi_{\text{max}}} \quad \text{cm}^{-2}.$$

Taking our values of $N_{\text{f}} = 1.2 \times 10^{-16}$ cm^{-2}, $\phi_{\text{min}} = 4 \times 10^{16}$ Mx and $\phi_{\text{max}} = 10^{18}$ Mx we find $\phi_{\text{avg}} = 1.5 \times 10^{17}$ Mx and $B_{\text{avg}} = 6.11$ Mx cm^{-2}($= 6.11$ G). Our B_{avg} is consistent with the values given in Table 3.3, and is realistic for the quiet Sun. If we now consider the $N_{\text{f}} = 3.6 \times 10^{-17}$ cm^{-2} of Parnell et al. (2009), but limit the range of flux values considered to be consistent with the quiet Sun ($4 \times 10^{16} - 10^{20}$ Mx), we get $\phi_{\text{avg}} = 5.0 \times 10^{17}$ Mx and $B_{\text{avg}} = 6.6$ Mx cm^{-2}. Our absolute flux density is very similar to theirs, but our average flux element is much smaller. We also find that we have around 3 times more magnetic elements per unit area than Parnell et al. (2009) ($N_{\text{tot}} = 4.06 \times 10^{-17}$ cm^{-2} compared with $N_{\text{tot}} = 1.30 \times 10^{-17}$ cm^{-2}). Therefore the difference in the parameters of the power law is due to our varying definition of 'magnetic elements' to 'magnetic features'.

The slope of the fitted line in the range $10^{16} - 10^{18}$ Mx for each simulation is plotted versus ϕ_{min} in Figure 3.14(b). One can see that as ϕ_{min} increases the slope becomes less steep. This is because as only larger elements emerge, these large elements have more of an impact on the number density. Such a limited range for emerging bipoles is less realistic, so we would expect this to be less of a match with the results obtained through observations. When the lower bound of emerging flux is less than 10^{17} Mx, the power law index converges around -1.85.

3.2.5 Lifetime of Magnetic Elements

The plots in Figure 3.15 relate to the *lifespan* of magnetic elements within each simulation. Within our model, an element is defined to 'die' when its flux changes, either by fragmenting into two new elements or cancelling or coalescing with another element. An element begins its life when it newly emerges; has just split from another as a result of fragmentation; or is produced by two separate elements cancelling or coalescing together.

Our definition of an element's lifespan likely differs somewhat from that of an observer studying magnetogram data, as does our counting of magnetic elements. It is easy to count and keep track of the processes that magnetic elements undergo within our model because they are treated as individual discrete sources. However, when the synthetic magnetogram is created using the

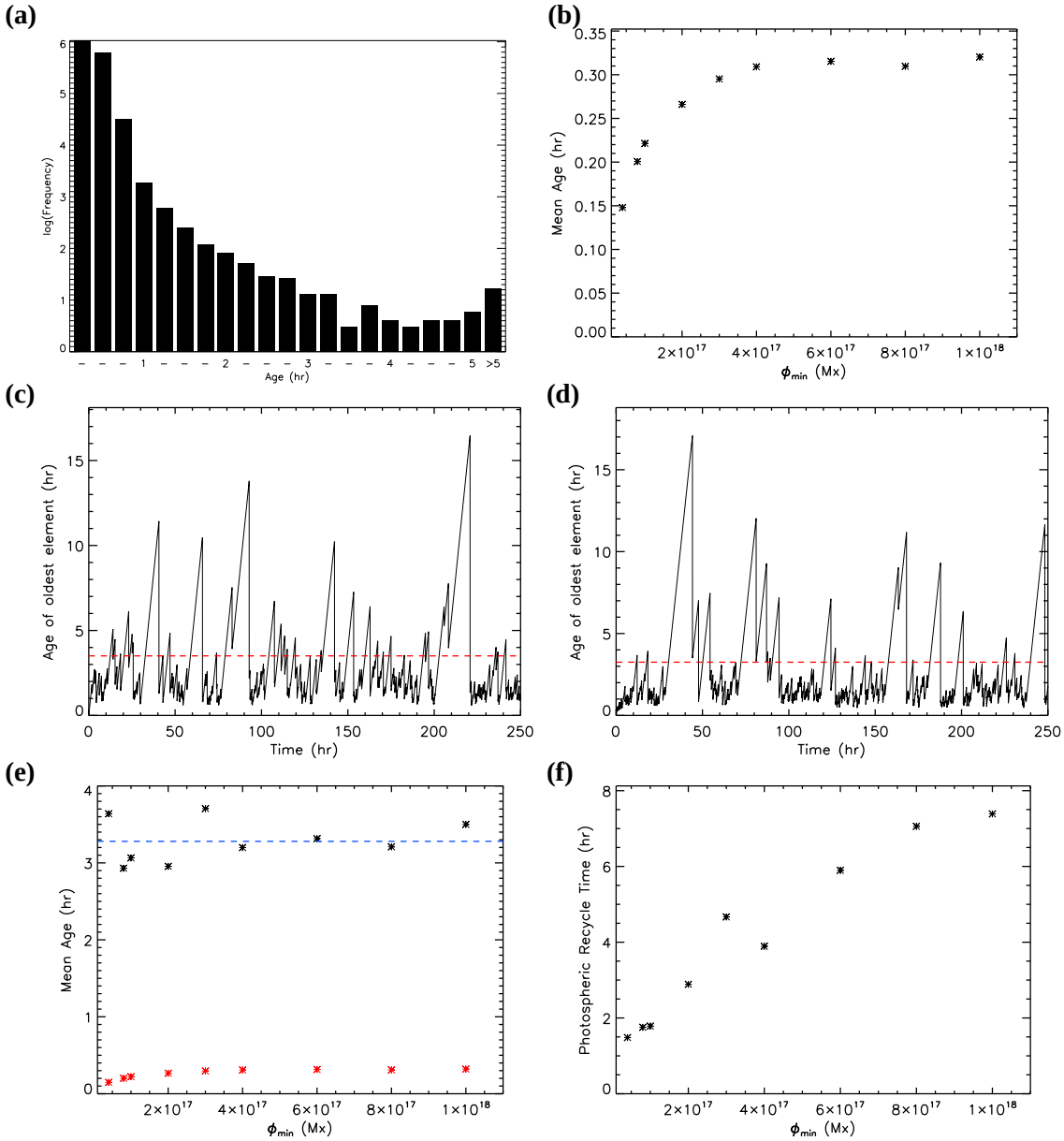

Figure 3.15: (a) Frequency of occurrence of magnetic elements with a lifespan of t hr, within the $\phi_{\text{min}} = 4 \times 10^{16}$ Mx simulation. (b) Mean lifespan of a magnetic element in hours for each of the simulations. (c) and (d) age of the oldest existing magnetic element throughout the simulation, for (c) $\phi_{\text{min}} = 4 \times 10^{16}$ Mx and (d) $\phi_{\text{min}} = 10^{18}$ Mx. The red dashed line represents the mean age of the oldest element averaged over the simulation. (e) Black stars: mean maximum age of an element averaged over each simulation. Blue line: mean maximum age of an element averaged over all simulations. Red stars: mean lifespan of a magnetic element within each simulation. (f) Photospheric recycle time in hours, for each simulation.

ϕ_{min} ($\times 10^{16}$ Mx)	Mean Lifespan (min)	Mean Maximum Age (hr)	Photospheric Recycle Time (hr)
4	8.88	3.64	1.48
8	12.04	2.93	1.75
10	13.28	3.06	1.78
20	15.96	2.95	2.89
30	17.71	3.71	4.67
40	18.54	3.20	3.89
60	18.92	3.31	5.90
80	18.58	3.21	7.06
100	19.22	3.50	7.39

Table 3.5: Mean lifespan of a magnetic element (min), mean maximum lifespan of a magnetic element (hr) and photospheric recycle time (hr) for each simulation.

method described in Section 3.1.1, many of these elements overlap to produce fewer, larger magnetic elements. In addition, the resolution and cadence of real data is not always high enough to be able to detect the smallest and fastest evolving elements. This is another reason that further study of the photospheric model using the synthetic magnetogram series as input into the variety of feature tracking techniques that have been produced would be of interest.

Figure 3.15(a) shows the log frequency of occurrence of magnetic elements with a lifespan of t hr, for the simulation in which $\phi_{\text{min}} = 4 \times 10^{16}$ Mx. The mean lifespan of all elements is plotted for each simulation in Figure 3.15(b). It can be seen that most elements do not even 'live' for one hour before fragmenting, cancelling or coalescing with another. The mean lifespan of an element is only around $9 - 20$ min, values are given in Table 3.5 for each of the simulations. Observationally, it makes more sense that larger, more isolated magnetic elements would be long-lived. However, since fragmentation is so frequent within our model, this is not the case for our simulations. The longest lived elements most likely occur at the beginning of the simulation before the number of magnetic elements increases to the point where they interact frequently; or are isolated small elements that do not fragment because their flux is so low. Within the synthetic magnetograms, large, irregularly shaped magnetic features form where several individual magnetic elements lie close together but have not yet coalesced. These elements tend to appear in the network between supergranules. Examples of these can be seen in the six images shown in Figure 3.9.

Figures 3.15(c) and (d) show plots of the age of the oldest magnetic element existing within the model versus time, within the (c) $\phi_{\text{min}} = 4 \times 10^{16}$ Mx and (d) $\phi_{\text{min}} = 1 \times 10^{18}$ Mx simulation. These simulations contain the largest and smallest range of emerging flux values respectively. The dashed red line represents the mean maximum age averaged over the simulation. The large spikes represent occasional long-lived magnetic elements, but in general the maximum age of an element throughout the simulation remains at roughly $3 - 4$ hr. In every case the mean maximum age

computed for the whole simulation is around this value, as can be seen in Figure 3.15(e) and Table 3.5. This is similar to the lifetime of ephemeral regions, determined by Harvey and Martin (1973) to be around 4.4 hr. Zhou et al. (2010) find the lifespan of internetwork features to be between 1 and 20 min, with a mean of 2.9 ± 2.0 min. The mean lifespan for magnetic elements within our model is $9 - 20$ min.

The *photospheric recycle time* or *flux replacement timescale* for the quiet Sun is defined to be the time taken for all flux within the quiet Sun photosphere to be replaced (Hagenaar, 2001). It is calculated by dividing the mean field by the emergence rate. For our two most realistic simulations, $\phi_{\text{min}} = 4 \times 10^{16}$ Mx and $\phi_{\text{min}} = 8 \times 10^{16}$ Mx, we find the recycle time to be 1.48 hr and 1.75 hr respectively. This is in excellent agreement with Hagenaar et al. (2008)'s recycle time of $1 - 2$ hr. The photospheric recycle times calculated for each simulation are given in Table 3.5 and shown in the plot in Figure 3.15(f). Once again, the $\phi_{\text{min}} = 3 \times 10^{17}$ Mx simulation is seen to be an outlier.

The next section considers one of many possibilities for future studies using this theoretical model for the magnetic carpet, in this example, emergence is switched off midway through the simulation.

3.2.6 Switching Off Emergence

Clearly, many other studies may be undertaken using our theoretical model simply by varying different input parameters to determine their effect upon photospheric evolution. One interesting test is to 'switch off' emergence at some stage in the simulation to observe how rapidly flux disappears. An example of such a simulation was run with identical parameters to those described in Section 3.2. The flux emergence range for newly appearing bipoles is $8 \times 10^{16} - 1 \times 10^{19}$ Mx. Emergence is switched off at $t = 50$ hr, and the simulation is allowed to run for a further 50 hr. Results from this experiment are shown in Figure 3.16.

Figure 3.16(a) shows both the mean field and the number of elements ($N/100$) throughout the simulation. It can be seen that both of these quantities rapidly decrease as soon as emergence is switched off after 50 hr, levelling off and becoming steady at roughly $t = 65$ hr. The total number of magnetic elements becomes very small as all remaining flux within the computational box rapidly cancels and coalesces together at the supergranule boundaries. This is also indicated by the mean size and maximum size of a magnetic element (Figure 3.16(b)). Both increase after emergence has been switched off, but a particularly large increase occurs for the mean size of a magnetic element (red line). It increases from below 2×10^{17} Mx to above 10^{18} Mx, indicating that although the number of remaining elements is small, their flux is large. The maximum size that a magnetic feature reaches is around 7×10^{18} Mx. Since there are so few elements within the

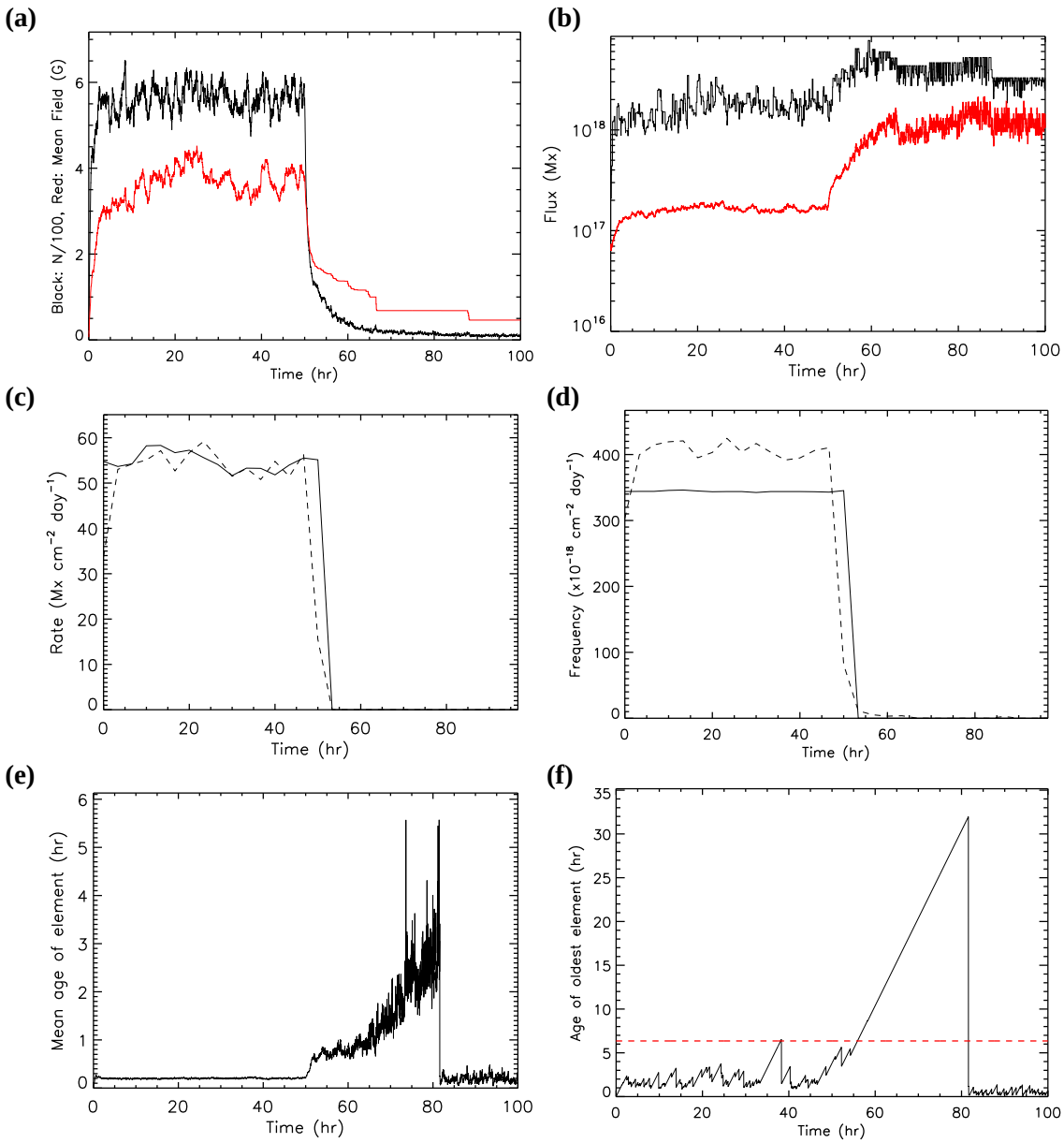

Figure 3.16: A simulation with emergence of bipoles in the range $8 \times 10^{16} - 10^{19}$ Mx. Emergence is switched off after 50 hr ($3,000$ time steps), and the simulation is allowed to run for a further 50 hr. Plots as a function of time: (a) Mean field (red) and number of magnetic elements ($N/100$, black). (b) Maximum flux (black) and mean flux (red) of a magnetic element. (c) Emergence (solid line) and cancellation (dashed line) rates. (d) Emergence (solid line) and cancellation (dashed line) frequencies. (e) Mean lifespan of a magnetic element. (f) Age of oldest existing magnetic element (red line: mean age of oldest magnetic element averaged over the simulation).

simulation towards the end, these elements fragment before they can become even larger. The fact that no more flux is emerging into the simulation also limits the size of magnetic elements.

Figures 3.16(c) and (d) show plots of the emergence (solid line) and cancellation (dashed line) rates and frequencies for the simulation. The emergence and cancellation rates (Figure 3.16(c)) remain roughly equal until $t = 50$, and the cancellation frequency is greater than the emergence frequency (Figure 3.16(d)), as was seen in the previous simulations. Once emergence is switched off, the cancellation rate and frequency also rapidly decrease as the magnetic elements quickly cancel and coalesce together within the first few hours.

Figures 3.16(e) is a plot of the mean age of a magnetic element as a function of time. As expected, the mean age of an element within the simulation increases after emergence stops at $t = 50$ hr. The mean value continues to increase for a time. This is likely due to a contribution from a few small, isolated magnetic elements that do not fragment. Such long-lived elements can be seen in the plot of the maximum age of a magnetic element (Figure 3.16(f)). The maximum age linearly increases from around $t = 50$ hr to beyond $t = 80$ hr. This long-lived element then either fragments or encounters another magnetic element, and the maximum age becomes very small, remaining below 2 hr for the rest of the simulation. The maximum age does not increase significantly again for the remainder of the simulation, most likely because all remaining elements have cancelled or coalesced into larger elements by this stage. Large magnetic elements are much more likely to fragment, setting the elements' lifespans back to zero. Once the maximum age of a magnetic element has significantly decreased (just after $t = 80$ hr), the mean age of a magnetic element also significantly decreases.

A series of synthetic magnetogram images from this simulation are shown in Figure 3.17. The images are taken at $t = 50$, $t = 51$, $t = 52$, $t = 54$, $t = 57$ and $t = 60$ hr; the number of magnetic elements (ns) that make up each magnetogram are given in the figure caption. A movie of this series of magnetograms from $t = 50 - 60$ hr is also given on the CD, named mag_em4_mid.mpg. After emergence has been switched off, the magnetic elements quickly begin to decrease in number. At (a) $t = 50$ hr the magnetogram is composed of 564 magnetic elements; just four hours later (d), only 94 elements make up the magnetogram; and by (e) $t = 60$ hr, only 37 elements remain. In image (f) one can see the few remaining magnetic elements. Towards the end of the movie, it can be seen that these few elements are slow moving and are 'stuck' at the boundaries of the non-evolving supergranules. They are spaced far from one another where the supergranular velocities are small, so they do not encounter one another before the simulation ends. If the supergranular flow profile was also allowed to evolve in time, this would likely aid the process by increasing and randomising further the motion of the remaining magnetic elements, eventually removing them completely from the simulation.

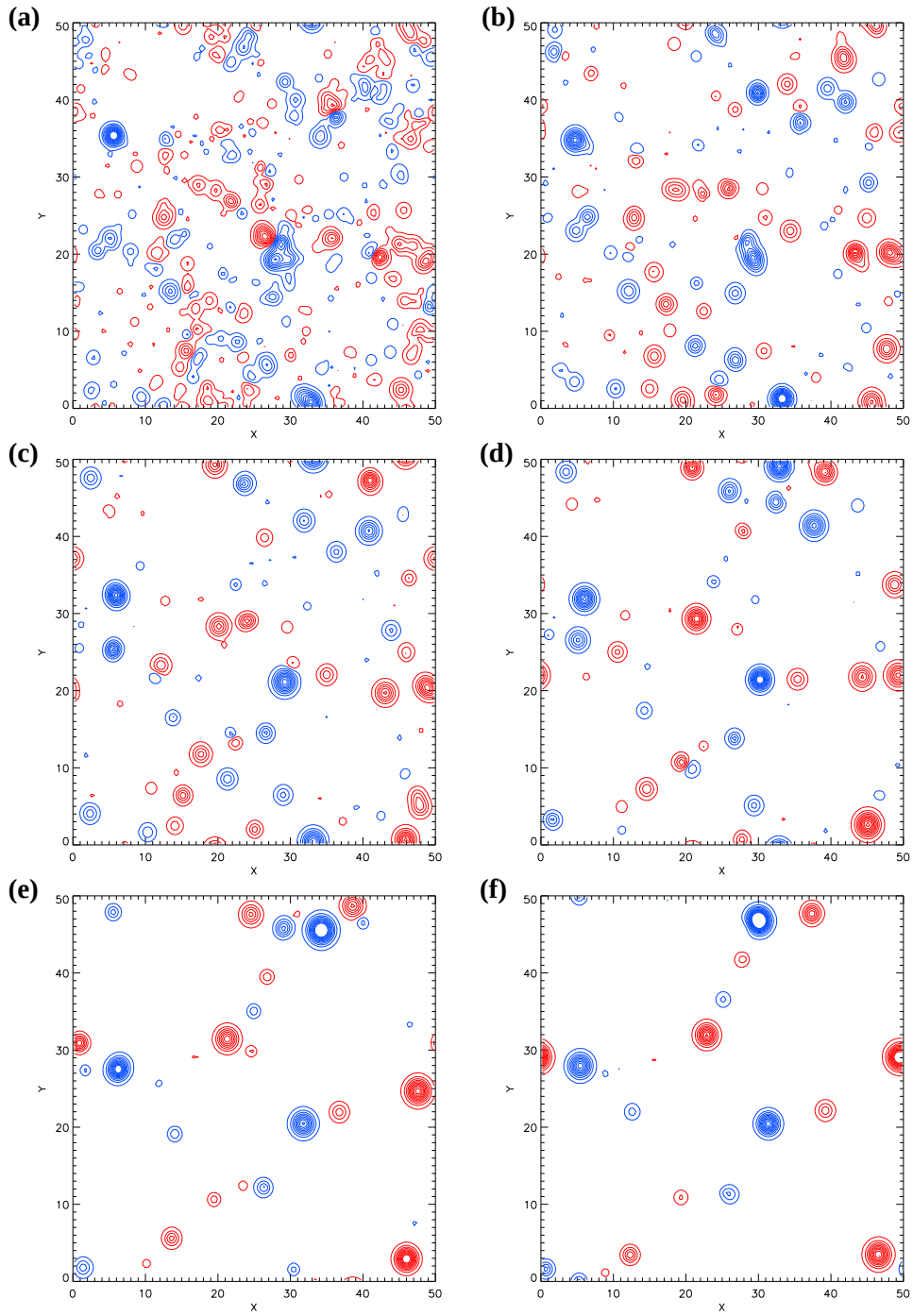

Figure 3.17: Synthetic magnetograms for a simulation with a flux emergence range of $8 \times 10^{16} - 1 \times 10^{19}$ Mx. Red contours represent positive magnetic field, blue contours represent negative, where ten contour levels are shown for each polarity with absolute values spaced evenly between 3.5 G and 66.5 G. Emergence is switched off at $t = 50$ hr. The time in hr at which each image is taken and number of individual elements (ns) composing the magnetogram are as follows: (a) $t = 50$, ns=564, (b) $t = 51$, ns=209, (c) $t = 52$, ns=128, (d) $t = 54$, ns=94, (e) $t = 57$, ns=59 and (f) $t = 60$, ns=37. A movie of the simulation from $t = 50 - 60$ hr, mag_em4_mid.mpg, is given on the CD.

3.3 Discussion and Conclusions

The aim of this chapter was to construct a realistic model for the photospheric evolution of the solar magnetic carpet, which we intend to use as a lower boundary condition in 3D non-potential modelling. We have built into this model the processes of flux emergence, cancellation, coalescence and fragmentation, as well as a steady supergranular flow profile that influences the motion of magnetic elements. Many parameters for the model were taken from studies of observational solar data, such as the probability distribution for newly emerging bipoles (Thornton and Parnell, 2011) and the peak radial velocity of a supergranule (Simon and Leighton, 1964; Paniveni et al., 2004).

A series of nine simulations of length 250 hr were run, keeping all parameters fixed apart from the minimum value of total absolute flux, ϕ_{min}, that a newly emerging bipole may take. The maximum value for newly emerging bipoles was fixed at $\phi_{max} = 10^{19}$ Mx. The lower the value of ϕ_{min} used, the larger the range of emerging magnetic flux elements, and hence the more flux is emerged into the system. The upper bound produces a cap on the size of large elements, and we assume that we are considering a quiet area of the Sun, with no input from active regions. A larger flux emergence range is more realistic so as one would expect, the lower the value of ϕ_{min}, the closer the simulation results agree with solar observations.

For $\phi_{\text{min}} = 4 \times 10^{16}$ Mx and $\phi_{\text{min}} = 8 \times 10^{16}$ Mx in particular, the total absolute flux within the simulation quickly reaches a steady state in which the rates of emergence and cancellation are roughly equal. These simulations also result in a mean magnetic field that is within the range determined from observations. For the less realistic simulations with the highest ϕ_{min} ($\geq 3 \times 10^{17}$ Mx) the total absolute flux takes longer to reach a steady state, illustrated by the fact that the mean emergence rate is slightly higher than the mean cancellation rate. For low ϕ_{min}, the mean field is $4 - 6$ G, which fits observational data. The number of magnetic elements within each simulation, however, very quickly reaches a steady state in all cases. This occurs shortly after the first magnetic elements reach the boundaries of the supergranules and begin to interact with one another.

Although the cancellation and emergence rates, defined in Mx cm^{-2} day^{-1}, become roughly equal for all simulations, it is also the case that the cancellation frequency, defined in cm^{-2} day^{-1}, is always greater than the emergence frequency. This is in rough agreement with the theoretical magnetic carpet model of Parnell (2001), who attribute the difference to large numbers of cancellations between small magnetic elements arising through fragmentation. They suggest that the energy release from so many small cancellation events could significantly contribute to the energy required to heat the solar corona. In future in our 3D simulations, we will consider the energy build up at such locations (Chapter 5).

The power law flux distribution resulting from the simulations that include a larger range of flux emergence are in agreement with the power-law distribution of Parnell et al. (2009). The slope of their fitted line is -1.85, while the slopes produced by our simulations with $\phi_{\text{min}} = 4\times10^{16}$ Mx and $\phi_{\text{min}} = 8 \times 10^{16}$ Mx are -1.85 and -1.82 respectively. Our definition of magnetic elements means that our flux distribution would fit better with a downhill method of feature tracking. A feature tracking study of our synthetic magnetograms using a clumping method would be useful to check the power law, in addition to other values such as lifetimes and physical extent of magnetic elements.

Our model produces a highly dynamic small-scale photosphere as desired, with the mean lifespan of a magnetic element in any of the simulations being just $9 - 20$ min. We also find a photospheric recycle time of just 1.48 hr, this is in good agreement with Hagenaar et al. (2008)'s recycle time time of $1 - 2$ hr.

As suggested in Section 3.2.6, an evolving supergranular flow profile is one improvement that could be made to the model. Simon and Leighton (1964) determine the average lifespan of a supergranule to be 20 hr, whereas Wang and Zirin (1989) find their lifetime to be ≥ 50 hr. Simon et al. (2001) assign lifetimes of between 18 and 42 hr to the supergranules within their model. In any case, these studies show that a magnetic carpet model that runs for longer than around a day should consider a time evolving flow pattern. The flow profile evolution could either be built into the model or taken from observational data using a method such as described by Potts et al. (2004). They track solar photospheric flows by using a ball tracking technique. Even if the flow profile were not time evolving, a more complex supergranular flow profile that included vorticity would have important implications for the coronal evolution. Such surface motions would lead to twisting and braiding of the coronal magnetic field, and as a consequence, heating of the corona.

The fragmentation process is a limitation of our model. Rather than allowing fragmentation to arise naturally as a consequence of photospheric flows, we currently impose it. This is another feature of the model that could be improved in future. It is also of interest to reduce both ϕ_{min} and ϕ_0, to consider a wider range of small-scale magnetic features. The lower detection limit of magnetic features by solar instruments is likely to continue to decrease. For example, the IMaX instrument of the Sunrise mission has detected features of flux on the order of 10^{15} Mx (Barthol et al., 2011). In addition to this, as observational instruments improve and new observational results are obtained, the 2D model can be updated with new parameters.

We conclude that we have successfully produced a realistic model for the photospheric evolution of the solar magnetic carpet that reproduces many observed properties. In Chapter 5, this will be used to produce a 3D model for the small-scale coronal magnetic field under controlled circumstances.

Chapter 4

Analysis of Basic Interactions

This work has been published in Meyer et al. (2012).

Within this chapter we consider the coronal consequences of the interaction of two magnetic elements with one another. In particular, we study magnetic energy build-up, storage and dissipation as a result of emergence, cancellation and flyby of magnetic elements. In the future, these interactions will be the basic building blocks of more complicated simulations involving hundreds of magnetic elements (e.g. Chapter 3). Each interaction is simulated in the presence of an overlying uniform magnetic field, which lies at various orientations with respect to the evolving magnetic elements.

In order to simulate the coronal evolution of these interactions, we have formulated a two-component model. We use a special treatment to describe the evolution of the magnetic elements at the photosphere, as described in Chapter 3. The photospheric model is then coupled to the full 3D model as a lower boundary condition that drives the continuous evolution of the coronal magnetic field through a series of quasi-static, non-linear force-free states. The technique we use to evolve the coronal magnetic field is called the *magnetofrictional method* (van Ballegooijen et al., 2000), and is described in Section 4.1.1.

Previous studies have also considered such interactions, these include full MHD simulations of magnetic flux emergence (e.g. Archontis et al. (2004); MacTaggart and Hood (2009)) and of a magnetic flyby (e.g. Galsgaard et al. (2000); Parnell et al. (2010)). In the paper of Galsgaard and Parnell (2005), the authors study the heating associated with a flyby using full MHD simulations. They show that the amount of energy stored or dissipated within the corona depends on several factors. They conclude that it is not sufficient to know the evolution of the magnetic field at the photospheric boundary to be able to predict the evolution of the coronal field. Knowledge of the strength and direction of the overlying field also plays an important part.

Within the literature, there are no previous studies that compare all three interactions of emergence, cancellation and flyby to one another under the same modelling approximations and using the same parameters. Therefore within the present study, we will consider the flux connectivity of the magnetic elements, the build up and storage of free magnetic energy, and the energy dissipated during these three basic magnetic carpet interactions. In particular, we wish to identify the factors involved in determining the amount of magnetic energy that is stored or dissipated. This study is a preliminary analysis to quantify results expected in more complex simulations involving more magnetic elements, such as will be carried out in Chapter 5.

The chapter is outlined as follows. Section 4.1 discusses our treatment of the photospheric boundary condition and how it couples to the coronal magnetic field model. The set-up and analysis of the three basic interactions are described in Section 4.2. We present the discussion and conclusions in Section 4.3.

4.1 Model

A non-linear force-free magnetic field is a useful approximation to the coronal field, as it allows for the existence of electric currents and free magnetic energy. For a magnetic field to be force-free, it must satisfy:

$$\nabla \times \mathbf{B} = \alpha(\mathbf{r})\mathbf{B}, \tag{4.1}$$

and

$$\nabla \cdot \mathbf{B} = 0. \tag{4.2}$$

The physical conditions required for such an approximation to be valid are described by Régnier (2007) and in Chapter 1. The parameter $\alpha(\mathbf{r})$ describes the twist of the magnetic field. It is a scalar function of position, but must be constant along a given magnetic field line. An important property of a non-linear force-free field is that it allows for regions of both high and low α, along with varying sign of α, so may therefore model a wide variety of coronal structures.

There are several methods for constructing non-linear force-free fields from fixed photospheric boundary conditions; a summary is given by Schrijver et al. (2006). In contrast to these methods, which produce single independent extrapolations, we choose to model a continuous evolution of the coronal field through a series of quasi-static, non-linear force-free equilibria, that are driven by an evolving photospheric boundary condition. The magnetofrictional technique employed to carry this out is described next.

4.1.1 Magnetofrictional Method

Our model for the 3D coronal magnetic field is based upon that of van Ballegooijen et al. (2000); the method is described fully in Mackay et al. (2011). It has been used in the past to study the global coronal magnetic field (Yeates et al., 2008), the evolving magnetic structure of solar filaments (Mackay and van Ballegooijen, 2009), and the decay of an active region (Mackay et al., 2011). The term *magnetofrictional method* was first given to the technique by Yang et al. (1986). Following their method, we introduce an artificial friction-like dissipative term to the MHD equation of motion (Equation 1.6, Chapter 1) to relax the magnetic field towards a force-free state. This gives the equation of motion the form

$$\rho\frac{D\mathbf{v}}{Dt} = \mathbf{j}\times\mathbf{B} - \nabla p + \rho\mathbf{g} - \nu'\mathbf{v}, \tag{4.3}$$

where $\nu' = \nu B^2$ and ν is the coefficient of friction. We may neglect any explicit time dependence as the timescale for relaxation is much shorter than the timescale for photospheric boundary motions. Then under the the same assumptions as given in Section 1.3.3, that the corona is force-free, we may also neglect the pressure and gravity terms. The equation of motion then reduces to the following expression for the plasma velocity

$$\mathbf{v} = \frac{1}{\nu}\frac{\mathbf{j}\times\mathbf{B}}{B^2}, \tag{4.4}$$

where $\mathbf{j} = \nabla\times\mathbf{B}$. Note that this velocity describes the motion of the coronal magnetic field and is distinct from the velocity of the magnetic elements on the photosphere. In the model, we evolve the coronal field by the induction equation,

$$\frac{\partial\mathbf{A}}{\partial t} = \mathbf{v}\times\mathbf{B} + \boldsymbol{\epsilon}, \tag{4.5}$$

where $\mathbf{A}$ is the vector potential and $\mathbf{B} = \nabla\times\mathbf{A}$. Through using this formalisation, the coronal field evolves through a series of approximate, quasi-static, non-linear force-free equilibria. The first term on the right-hand side of Equation 4.5 is an advective term, which incorporates the magnetofrictional velocity. The second term is a non-ideal term that represents hyperdiffusion. The form is chosen to be:

$$\boldsymbol{\epsilon} = \frac{\mathbf{B}}{B^2}\nabla\cdot(\eta_4 B^2\nabla\alpha), \tag{4.6}$$

(Boozer, 1986; Bhattacharjee and Hameiri, 1986; Strauss, 1988), where η_4, the hyperdiffusivity constant, is chosen to be 4.7×10^5 km^4 s^{-1}. The key effect of hyperdiffusion is that it conserves magnetic helicity whilst smoothing gradients in α. For any non-linear force-free field, hyperdiffusion acts to reduce the field towards a linear force-free state containing the same magnetic helicity. It should be noted that the timescales of the present simulations are far too short for a linear force-free field to be reached.

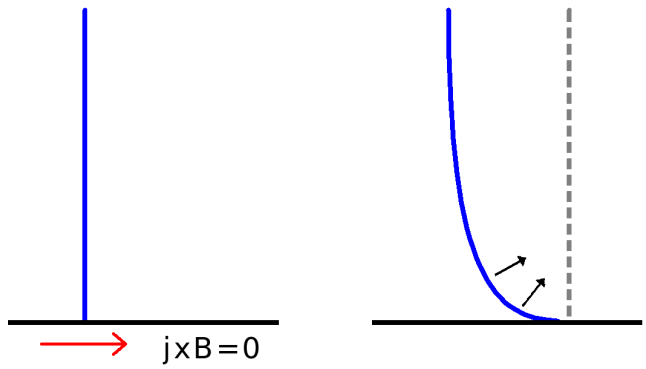

Figure 4.1: Cartoon illustrating the magnetofrictional relaxation technique. The blue lines represent coronal field lines with foot-points anchored in the photosphere (black line). The red arrow represents foot-point motions, while the black arrows represent the Lorentz force.

Figure 4.1 shows a cartoon illustrating the magnetofrictional method. The blue lines represent coronal magnetic field lines that are anchored in the photosphere (horizontal black line). In the left-hand image, the coronal field is in force-free equilibrium. Foot-point motions (red arrow) at the photosphere evolve the coronal field out of equilibrium. The Lorentz force (black arrows) then acts against an artificial friction to relax the field back towards an equilibrium state. This continual stressing and relaxing of the coronal magnetic field in response photospheric boundary motions evolves the field through series of quasi-static, non-linear force-free equilibria.

4.1.2 Magnetic Energy Storage and Dissipation

To consider the effect of the magnetic carpet on the corona, one aspect of the simulations that we are interested in is the build-up and release of energy. At any instant in time in our numerical box of volume V, the total magnetic energy is

$$W = \int_V \frac{B^2}{8\pi} dV. \tag{4.7}$$

Following this, the rate of change of the total magnetic energy is

$$\frac{dW}{dt} = \frac{1}{4\pi} \int_V \frac{d}{dt}\left(\frac{B^2}{2}\right) dV.$$

Substituting in Equation 4.5:

$$\begin{aligned} \frac{d}{dt}\left(\frac{B^2}{2}\right) &= \mathbf{B} \cdot \frac{\partial \mathbf{B}}{\partial t} \\ &= \mathbf{B} \cdot \nabla \times (\mathbf{v} \times \mathbf{B} + \boldsymbol{\epsilon}) \end{aligned}$$

(4.8)

$$\therefore \frac{dW}{dt} = \iint_S \mathbf{I}\, d\mathbf{S} - \iiint_V Q\, dV, \tag{4.9}$$

where

$$\mathbf{I} \equiv \frac{1}{4\pi}\left[(\mathbf{v} \times \mathbf{B} + \boldsymbol{\epsilon}) \times \mathbf{B} + \eta_4 B^2 \alpha \nabla \alpha\right] \tag{4.10}$$

and

$$Q \equiv \frac{B^2}{4\pi}(\nu|\mathbf{v}|^2 + \eta_4|\nabla\alpha|^2). \tag{4.11}$$

The first term on the right hand side of Equation 4.9 represents the energy injected due to surface motions, along with that injected or removed due to flux emergence or cancellation respectively. In addition, there is a contribution from hyperdiffusion. The second term is the rate at which energy is dissipated per unit time, due to the coronal evolution. This dissipated energy, which is released in the coronal volume, may be considered as energy that is available to be converted into heat or plasma motions. While it may be regarded as this, for simplicity, within this thesis we only consider the size of Q, and do not follow the corresponding plasma processes. The full derivation of $\mathbf{I}$ and Q from the magnetic energy equation is given in Appendix B.2.

For the coronal dissipation term (Equation 4.11), the first term represents energy dissipation due to magnetofriction, which is released as the field relaxes to a force-free state. The second term represents energy dissipation due to hyperdiffusion, which is described by van Ballegooijen and Cranmer (2008). In the present simulations, it is found that $\nabla\alpha$ and the relaxation velocity are both largest near the magnetic elements and at locations where the magnetic field lines reconnect. Hence the dissipative term has its largest contribution near the sources, where there is strong magnetic field, $\mathbf{B}$, and at locations of changing magnetic topology.

Another quantity that we study is the free magnetic energy stored within the magnetic field. This is defined to be the difference between the energy of the non-linear force-free field and the corresponding potential field. The free energy at any instant is

$$E_{\mathrm{f}}(t) = W_{\mathrm{nl}}(t) - W_{\mathrm{p}}(t) = \int_V \frac{B_{\mathrm{nl}}^2 - B_{\mathrm{p}}^2}{8\pi} dV, \tag{4.12}$$

where B_{nl} is the non-linear force-free field and B_{p} is the corresponding potential field. Within the simulations we will study first the energy that is continually released and may contribute to the heating of the corona (Equation 4.11). Second, we will consider the energy stored in the magnetic field that may be related to more sporadic dynamic events, such as XBPs or nanoflares (Equation 4.12). The relative importance of these two forms of energy will be discussed for each of the three interactions between magnetic elements.

4.1.3 Photospheric Boundary Condition

To simulate the processes of emergence, cancellation and flyby, each magnetic element at the photosphere is assumed to have a simple Gaussian form. Therefore the normal field component (B_z) of an element is given by:

$$B_z = B_0 e^{-r^2/r_0^2}, \tag{4.13}$$

where B_0 is the peak strength, r_0 the Gaussian half-width and r the distance from the centre of the element. Each magnetic element within our simulations has a peak strength of $B_0 = 88$ G, a Gaussian half-width of $r_0 = 0.6$ Mm and an absolute flux of 10^{18} Mx. The total photospheric magnetic field is made up of the sum of a number of these elements.

A unique feature of the simulations is that B_z during the evolution of the photospheric field is specified analytically at discrete time intervals, T_i ($= 200$ s $= 3.3$ min) apart. Movement of the sources between these time intervals is obtained by changing their central positions, (x, y), rather than advecting them numerically. Through doing so, we avoid undesirable numerical effects such as overshoot due to numerical differentiation, and pile-up at cancellation sites due to forcing.

Using this description for magnetic elements, we may model a wide range of magnetic flux interactions, such as:

(a) Cancellation: Two magnetic elements, one positive and one negative, move together until their centres coincide. If they are of the same strength, they completely cancel. A cancellation occurring over a time period of 100 min ($30\ T_i$) can be seen in Figure 4.2(a).

(b) Emergence: Two magnetic elements, one positive and one negative, have the same strength and initially the same central position. Moving the sources apart then simulates emergence as is seen in observations. An emergence occurring over a time period of 100 min ($30\ T_i$) can be seen in Figure 4.2(b).

(c) Flyby: Two magnetic elements that move relative to one another, but never interact at the photospheric level. A flyby occurring over a time period of 166.7 min ($50\ T_i$) can be seen in Figure 4.2(c).

At any instant in time, the flux through the photosphere is given by

$$\text{Flux} = \int_S B_z dS, \tag{4.14}$$

where S is the photospheric boundary surface. Figure 4.3 shows a plot of the total absolute flux through the photosphere as a function of time for each of the events in Figure 4.2. It can be seen that the curves are all completely smooth. The cancellation curve (black line) is level until

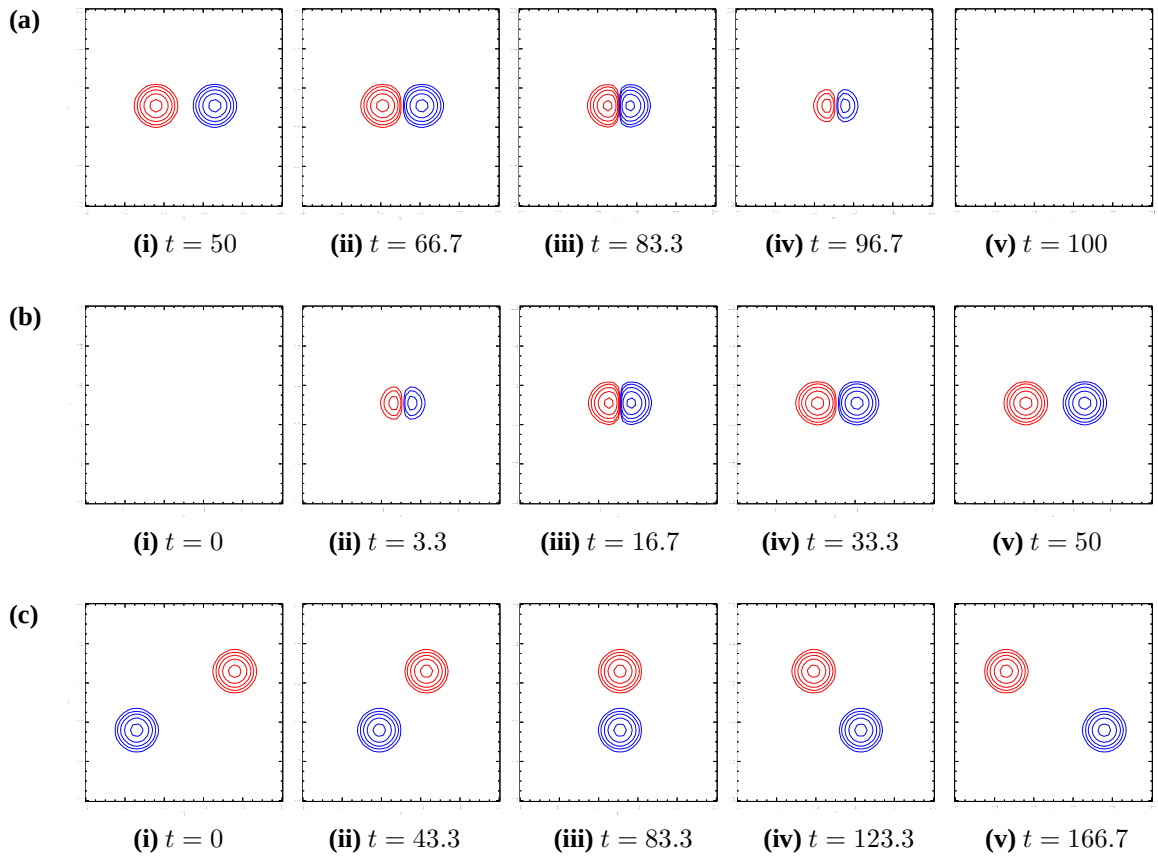

Figure 4.2: Three magnetic flux interactions modelled at the photospheric level. The interactions occur between a positive and a negative magnetic element of equal strength: (a) cancellation, (b) emergence and (c) flyby. In each case, red and blue contours represent the positive and negative polarities respectively, at levels of $\pm[4, 7, 14, 28, 57]$ G. The area shown is of size 10 Mm $\times$ 10 Mm. For each image, the time is given in minutes.

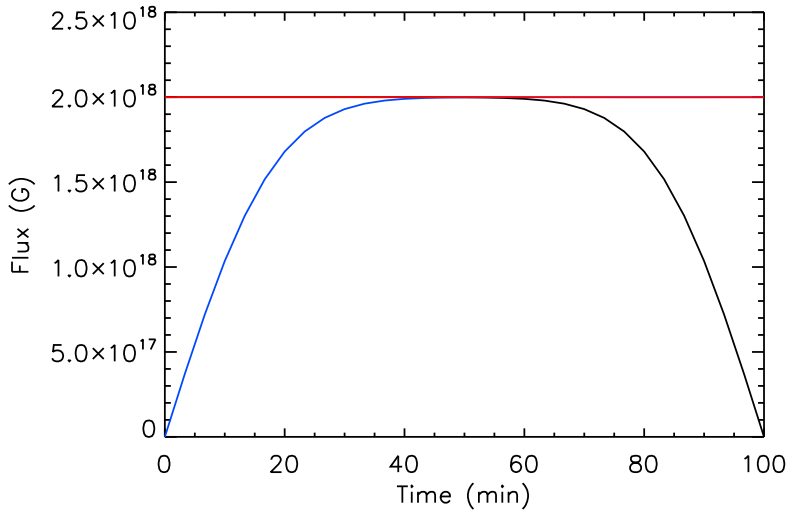

Figure 4.3: Total absolute flux through the photosphere as a function of time for a cancellation (black), emergence (blue) and flyby (red) event.

the magnetic elements encounter one another (around $t = 60$ min); the curve then decreases smoothly to zero at which point the elements completely cancel. The emergence curve (blue line) shows the opposite behaviour, while the flyby curve (red line) remains completely level as no flux emergence or cancellation occurs[1].

To ensure that $\nabla \cdot \mathbf{B} = 0$ within the simulations, the coronal field induction equation is specified in terms of $\mathbf{A}$. Therefore to drive the evolution of the coronal field we require as photospheric boundary data the A_x and A_y corresponding to the analytically specified B_z at each time step T_i. Without loss of generality, we can write A_x and A_y at $z = 0$ in terms of a scalar potential $\Phi(x, y)$, where

$$(A_x, A_y)_{(z=0)} = \nabla \times (\Phi \hat{\mathbf{z}}) = \left(\frac{\partial \Phi}{\partial y}, -\frac{\partial \Phi}{\partial x} \right). \tag{4.15}$$

Then from the z-component of $\mathbf{B} = \nabla \times \mathbf{A}$ we have:

$$B_{z(z=0)} = -\frac{\partial^2 \Phi}{\partial x^2} - \frac{\partial^2 \Phi}{\partial y^2}. \tag{4.16}$$

This may be solved using a fast Fourier transform to find Φ, and hence the A_x and A_y corresponding to B_z at the level of the photosphere.

To produce a continuous time sequence between each interval T_i, where B_z and subsequently A_x and A_y are analytically specified, a linear interpolation of A_x and A_y is carried out between

[1]Note that for the flyby, only $t = 0 - 100$ min is plotted, however the curve remains completely level throughout the entire simulation ($t = 0 - 166.7$ min).

each T_i and T_{i+1}, where 500 interpolation steps are taken between each analytical specification. This means that at each time T_i, the normal field at the photospheric boundary matches the exact analytically specified B_z given by the sum of the Gaussian profiles of the discrete magnetic elements. In response to the photospheric evolution of A_x and A_y at $z = 0$ Mm, the vector potential within the coronal volume, and therefore the coronal field, evolves through a series of quasi-static equilibria as described by Equation 4.5. This treatment of the magnetic field at the photospheric boundary ensures that we still have freedom for A_z, which sits half a grid point up from the photosphere (due to a staggered grid). Any non-potentiality in the coronal field near the photosphere arises from the $z-$component of the vector potential. The initial condition for the coronal field in each simulation is a potential field extrapolated from A_x and A_y at $z = 0$ Mm and $t = T_0$.

Since the evolution of our field is continuous, connectivity within the coronal magnetic field is maintained throughout the simulation. The resultant series of non-potential equilibria retain a memory of flux interactions from one step to the next, and subsequently the build up of non-potential effects. This is a significantly different approach compared to independent potential field extrapolations, and provides a new insight into the energy budget of the quiet Sun corona.

4.2 Basic Interactions of Magnetic Elements

The three basic interactions studied − cancellation, emergence and flyby − are processes that commonly occur between magnetic elements of equal but opposite flux. Each simulation uses the photospheric boundary treatment described in Section 4.1.3, which is then applied to the 3D magnetofrictional model in order to drive the coronal field evolution. Section 4.2.1 describes the features of the set-up that are common to all three cases; Sections 4.2.2 − 4.2.4 then give the results for individual cases. Section 4.2.5 compares the three basic interactions to one another.

4.2.1 Set-up

A numerical box of size $30 \times 30 \times 17.58$ Mm^3 is chosen, composed of $256 \times 256 \times 150$ grid cells. In each case, the interaction between magnetic elements is centred around the midpoint of the box. The box is periodic in the $x-$direction, and closed in the $y-$direction and at the top. We use a staggered grid within our model in order to attain second order accuracy when differentiating variables numerically. Details of the grid are given in Appendix B, as well as various calculations required to convert dimensionless quantities within the code into dimensional values.

For each interaction, the simulation is run under the presence of an overlying uniform magnetic field of strength 1 G, 5 G or 10 G, which points in the $x-$direction. Each interaction is also simulated with three different orientations of the bipole's axis with respect to the overlying field

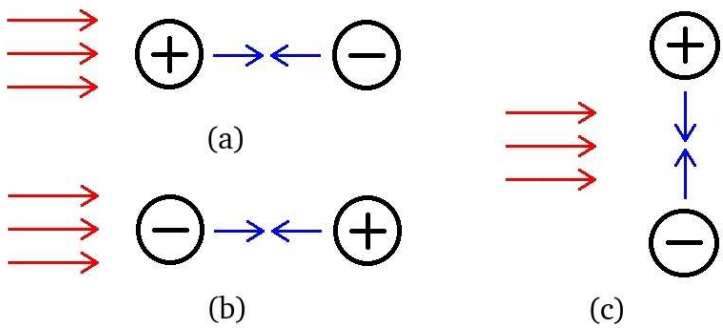

Figure 4.4: Cancellation: The red arrows represent the direction of the overlying field, the blue arrows represent the direction of motion of the magnetic elements. The bipole's axis is oriented (a) parallel to, (b) anti-parallel to, and (c) perpendicular to the overlying field.

(parallel, anti-parallel or perpendicular). The effects of varying the strength of the overlying field and direction of motion of the bipole with respect to the overlying field are investigated. For each simulation, the magnetic elements are advected at a constant velocity of 0.5 km s^{-1}.

4.2.2 Cancellation

The initial set-up for each of the cancellation simulations is illustrated in Figure 4.4. Each magnetic element is initially positioned 3 Mm from box centre. It then takes 100 min to reach the midpoint, where the opposite polarity elements cancel. As seen in Figure 4.3, the total absolute flux through the photosphere (black line) remains constant until the magnetic elements come into contact, at which point the flux rapidly decreases to zero.

Field Lines

Typical examples of the magnetic connectivity during cancellation, for a 5 G overlying field and each orientation of the bipole, can be seen in Figures 4.5 (parallel), 4.6 (anti-parallel) and 4.7 (perpendicular), at $t = 50$ min. Images (a) and (c) show the non-linear force-free field. Although the field configurations for each case are only shown at one time, similar configurations occur up until the point at which the magnetic elements cancel. For parallel cancellation, no matter the strength of the overlying field, all flux from the positive polarity connects to the negative polarity. In contrast, for the anti-parallel and perpendicular cases, as the strength of the overlying field is increased, connectivity between the two magnetic elements decreases.

In Figures 4.5, 4.6 and 4.7, images (b) and (d) show potential field extrapolations at $t = 50$ min, for the same photospheric field distribution as in images (a) and (c). For each case, magnetic

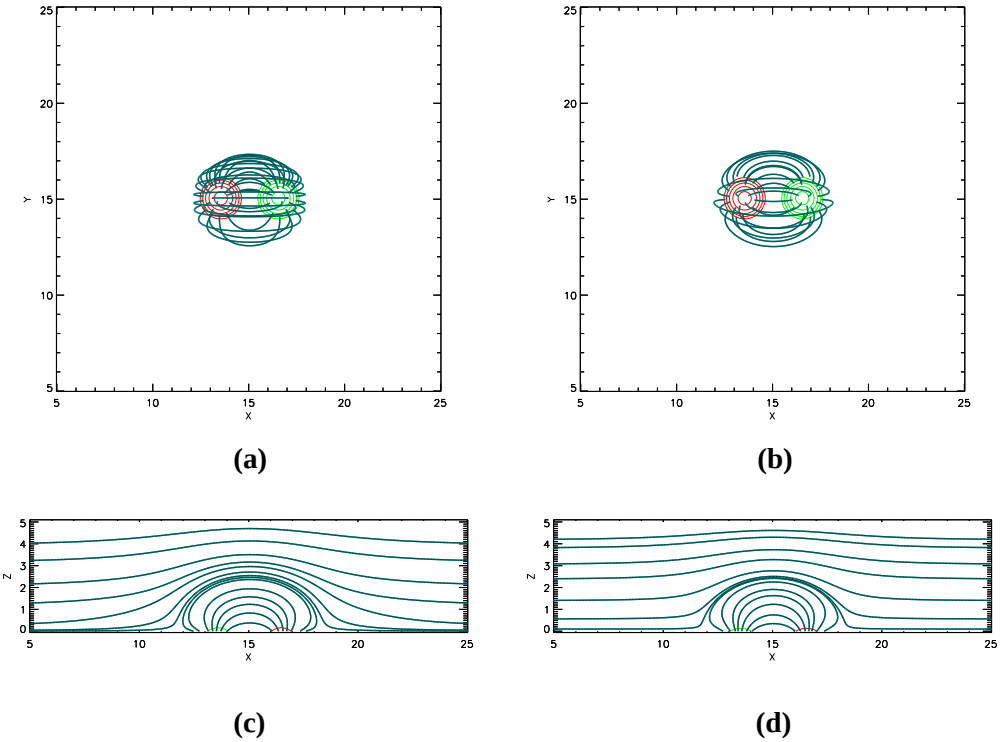

Figure 4.5: Cancellation of a bipole that is aligned parallel to a 5 G overlying field. (a) Non-linear force-free field and (b) potential field as seen in the $x - y$ plane at $z = 0$ Mm. (c) Non-linear force-free field and (d) potential field as seen in the $x - z$ plane at $y = 15$ Mm. A selection of magnetic field lines originating from the bipole at the photospheric level is plotted in each image. In images (c) and (d), some of the overlying field lines have also been plotted. The images are taken at $t = 50$ min. Red and green contours represent positive and negative magnetic field.

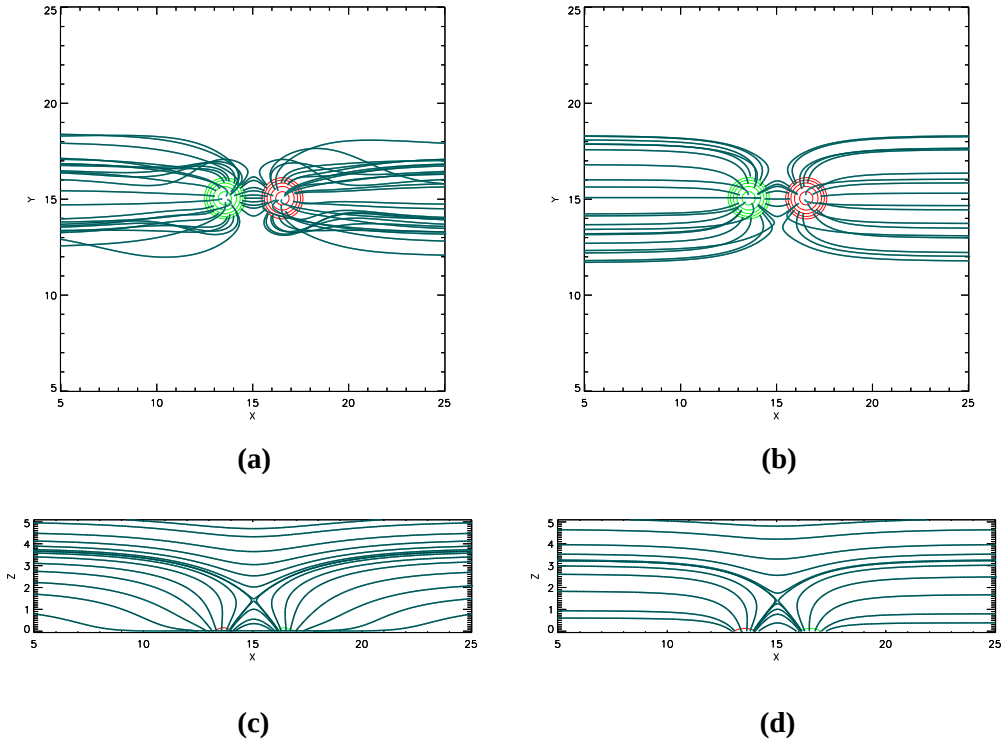

Figure 4.6: Cancellation of a bipole that is aligned anti-parallel to a 5 G overlying field. (a) Non-linear force-free field and (b) potential field as seen in the $x-y$ plane at $z = 0$ Mm. (c) Non-linear force-free field and (d) potential field as seen in the $x - z$ plane at $y = 15$ Mm. A selection of magnetic field lines originating from the bipole at the photospheric level is plotted in each image. In images (c) and (d), some of the overlying field lines have also been plotted. The images are taken at $t = 50$ min. Red and green contours represent positive and negative magnetic field.

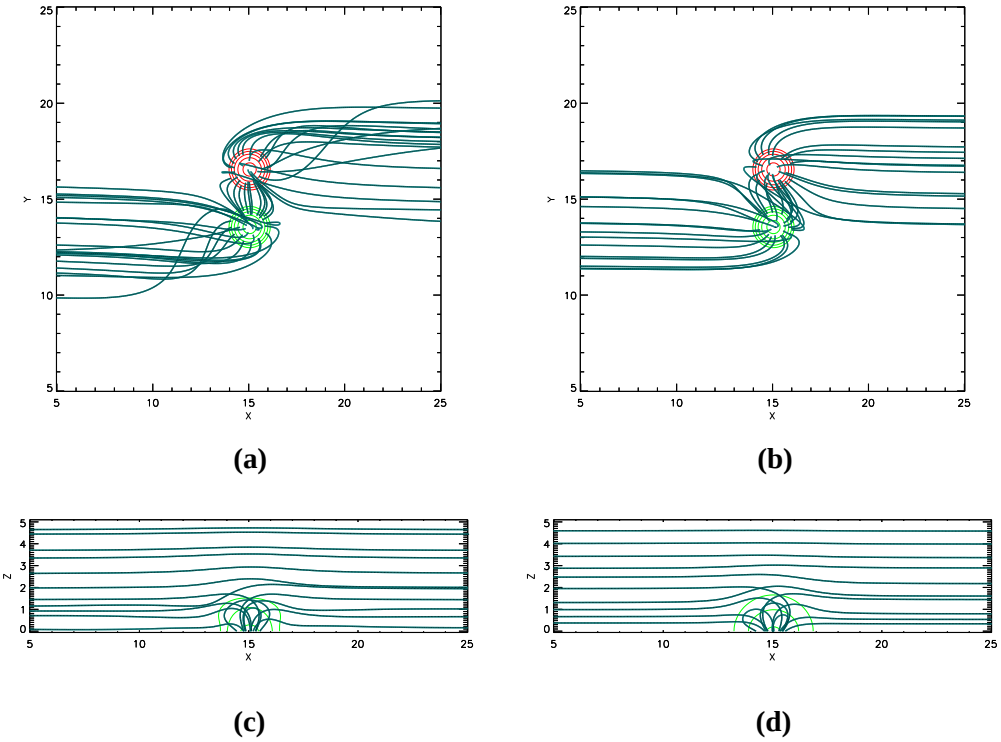

Figure 4.7: Cancellation of a bipole that is aligned perpendicular to a 5 G overlying field. (a) Non-linear force-free field and (b) potential field as seen in the $x - y$ plane at $z = 0$ Mm. (c) Non-linear force-free field and (d) potential field as seen in the $x - z$ plane at $y = 15$ Mm. A selection of magnetic field lines originating from the bipole at the photospheric level is plotted in each image. In images (c) and (d), some of the overlying field lines have also been plotted. The images are taken at $t = 50$ min. Red and green contours represent positive and negative magnetic field.

field lines are plotted from the same starting points as in images (a) and (b). For the parallel cancellation (Figure 4.5), the non-linear force-free field lines are similar to those of the potential field. However, for the anti-parallel and perpendicular cancellation, more twisting and bending of the magnetic field lines can be seen. This indicates that for the anti-parallel and perpendicular cases, the non-linear force-free field produces significantly different results.

Flux Connectivity and Energetics

Figure 4.8(a) shows a plot of the total flux connecting the magnetic elements as a function of time, for parallel (black), anti-parallel (blue) and perpendicular (red) cancellation and a 5 G overlying field. Both the non-linear force-free field (solid lines) and corresponding potential field extrapolation (dashed lines) have been plotted for comparison. The total flux connecting the magnetic elements does not vary significantly between the non-linear force-free field and potential field cases, because the bipole is simply shrinking from an initially potential state, where many of the properties of the initial potential field are preserved. The most flux connects between the magnetic elements for the parallel case, and the least for the anti-parallel case. Similar results are found for the 1 G and 10 G overlying field simulations. However, as the overlying field strength increases, the amount of flux connecting the magnetic elements decreases in the anti-parallel and perpendicular cases.

Figure 4.8(b) shows the total magnetic energy as a function of time, for the perpendicular cancellation and a 5 G overlying field. The red solid line shows the non-linear force-free field energy, while the red dashed line shows the energy of the corresponding potential field. The non-linear force-free field energy initially increases as energy is injected due to surface motions, whereas the potential field energy is continually decreasing. However, both curves decrease as the magnetic elements begin to cancel, and there is an outflow of energy through the photospheric boundary. There is a slight increase in the non-linear force-free field energy towards the end of the simulation, as strongly curved overlying field lines form during the final stages of cancellation of the bipole. In contrast, the overlying field is completely straight in the final potential field.

Figure 4.8(c) shows the variation of the free magnetic energy, $E_{\mathrm{f}}(t)$, as a function of time, as computed using Equation 4.12. Results are shown for the 5 G overlying field, and the line colours show the same orientations as in Figure 4.8(a). The free energy stored ranges from $0.37 - 1.57 \times 10^{26}$ ergs. The parallel cancellation results in the least free energy, while the perpendicular cancellation results in the most. On comparing Figures 4.8(b) and (c), one can see that the free magnetic energy built up within each simulation is small compared to the total energy within the box (around 1% for the 5 G perpendicular case). However, in order to avoid boundary effects, the computational box is large compared to the magnetic elements and their area of evolution. Therefore the evolution of the magnetic elements only perturbs a small volume of the overlying

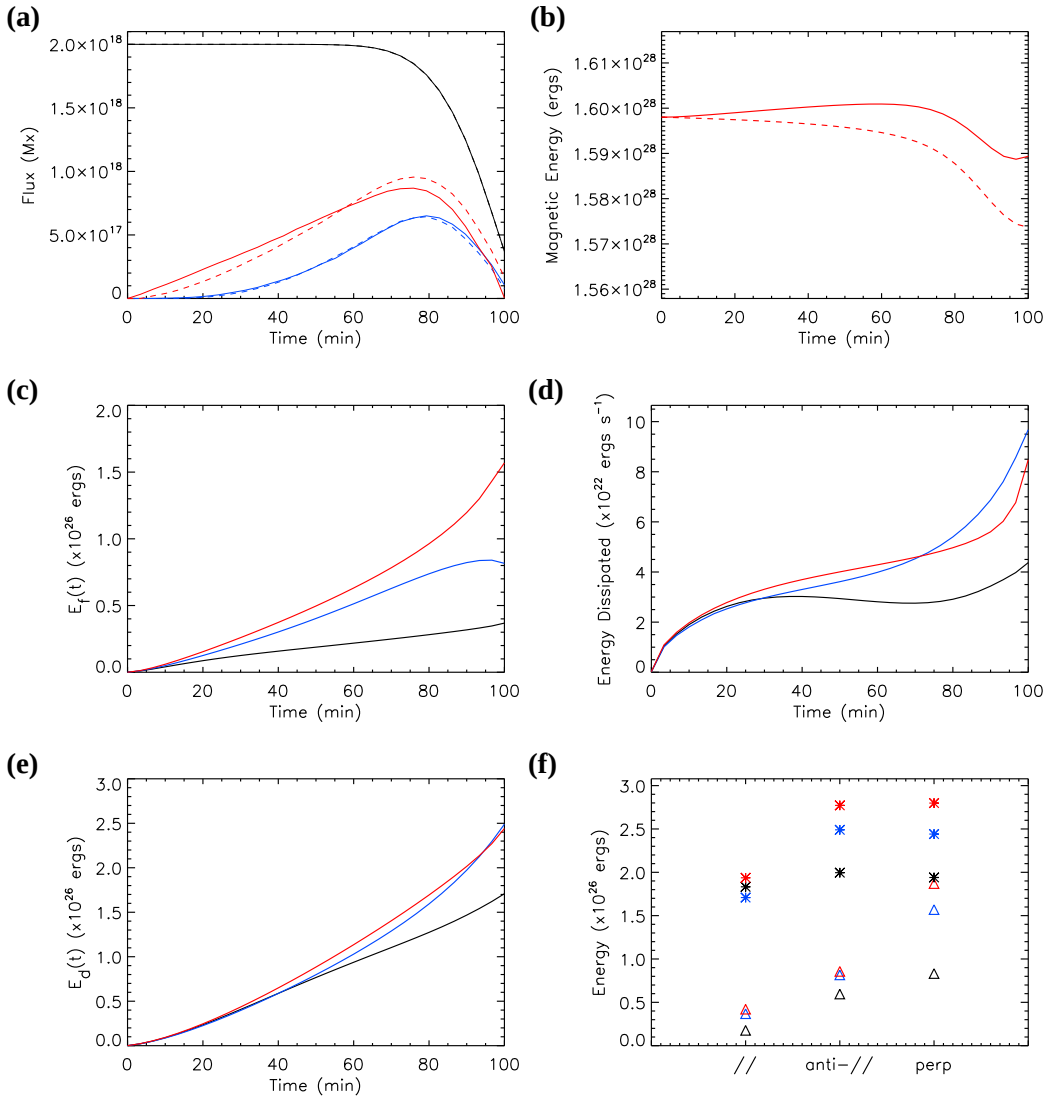

Figure 4.8: Plots as a function of time for a cancelling bipole moving parallel (black), anti-parallel (blue) and perpendicular (red) to a 5 G overlying field, for the non-linear force-free field (solid) and corresponding potential field (dashed). (a) Total flux connecting magnetic elements, (b) total magnetic energy, (c) free magnetic energy, $E_{\rm f}(t)$, (d) energy dissipated, $\int_V QdV$, and (e) cumulative energy dissipated, $E_{\rm d}(t)$. (f) Free magnetic energy (triangles) and cumulative energy dissipated (stars) at the end of each simulation, for a 1 G (black), 5 G (blue) and 10 G (red) overlying field.

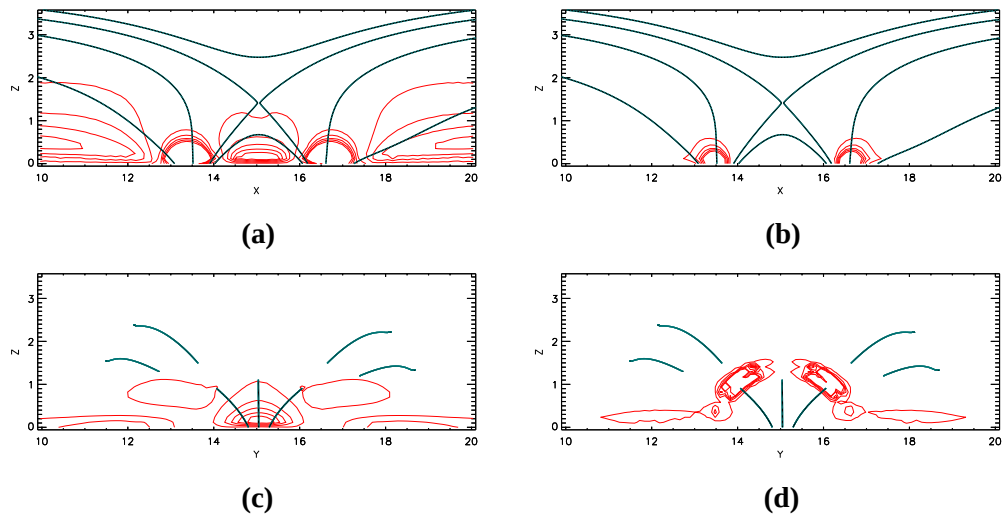

Figure 4.9: Cancellation of a bipole aligned anti-parallel to a 5 G overlying field: normalised contours of (a) Q_{frc} and (b) Q_{hd} as seen in the $x - z$ plane at $y = 15$ Mm, and normalised contours of (c) Q_{frc} and (d) Q_{hd} as seen in the $y - z$ plane at $x = 15$ Mm. In (a), (b) and (c), contour levels are $[0.1, 0.3, 0.5, 0.7, 0.9]$; in (d) contour levels are 200 times less $[0.0005, 0.0015, 0.00250.0035, 0.0045]$. A selection of magnetic field lines originating from the bipole and the overlying field is plotted in each image.

field, and the majority of the overlying field remains in a near potential state. If we compare the free magnetic energy built up to the potential field energy contribution of the bipole, we see that the build up of free energy is significant. From Figure 4.8(b), we compute the potential energy contribution of the bipole to be 2.43×10^{26} ergs (the difference between the initial and final energy of the potential field). This is of similar order to the free energy stored in the 5 G perpendicular case.

In addition to free magnetic energy stored within the system, energy is continually being dissipated, as described by the heating term Q (Equation 4.11). This is illustrated by Figure 4.8(d), which shows Q integrated over the volume at a given instant in time. Again, results are shown for the parallel (black), anti-parallel (blue) and perpendicular (red) cancellation, with a 5 G overlying field. A greater quantity of energy is dissipated towards the end, when full cancellation occurs. More energy is dissipated in the anti-parallel and perpendicular cases than in the parallel case. This is because smaller gradients in α are present in the parallel case as the bipole is simply shrinking and no reconnection occurs with the overlying field.

The dissipated energy may be split into two terms representing energy dissipation due to

magnetofriction, Q_{frc}, and hyperdiffusion, Q_{hd}, where

$$Q_{\text{frc}} = \frac{B^2}{4\pi}\nu|\mathbf{v}|^2 \quad \text{and} \quad Q_{\text{hd}} = \frac{B^2}{4\pi}\eta_4|\nabla\alpha|^2.$$

Figure 4.9 shows normalised contours of Q_{frc} and Q_{hd} in the $x-z$ plane (Figures 4.9(a) and (b)) and the $y-z$ plane (Figures 4.9(c) and (d)) taken at $t = 50$ min for the anti-parallel cancellation with a 5 G overlying field. In each case, the plots are taken through the centre of the bipole. For (a)−(c), the contours are at the same levels, in (d) they are 200 times lower. Considering Figures 4.9(a) and (c), it can be seen that Q_{frc} occurs throughout a large part of the coronal volume, both along field lines connecting the magnetic elements, and along those connecting the magnetic elements to the overlying field. In general, the term is largest low down, where the field lines are perturbed by the motion of the magnetic elements. Also, in Figure 4.9(c), two 'wings' of Q_{frc} can be seen suspended in the coronal volume. These originate due to strongly curved field lines that reconnect between the bipole and the overlying field.

In contrast, from Figures 4.9(b) and (d), it can be seen that Q_{hd} is more localised than Q_{frc}; the reason is that Q_{hd} only arises where gradients in α occur. This happens mainly at two locations: first, near the foot-points of the field lines connecting the magnetic elements, and secondly around the separatrix surface which separates the overlying field lines from the closed connections between the magnetic elements. In all of the simulations discussed in this paper, we see a similar trend as to where energy dissipation occurs. In each case, Q_{frc} is seen to be space filling, whereas Q_{hd} is more localised.

By comparing Figures 4.8(c) and (d), we see that $\int_V Q dV$ (expressed in ergs s^{-1}) is around three orders of magnitude smaller than the free energy (expressed in ergs) stored by the end of the simulation. Although it is three orders of magnitude smaller, the values shown in Figure 4.8(d) are instantaneous values. By integrating Q over both the volume and time, we can see how much energy has been cumulatively dissipated over the whole simulation:

$$E_{\text{d}}(t) = \int_0^t \left[\int_V Q dV\right] dt. \tag{4.17}$$

A plot of the total energy dissipated as a function of time is shown in Figure 4.8(e), for the 5 G case of each orientation (lines are coloured as in 4.8(a)). Cumulatively, a significant amount of energy has been dissipated. By comparing Figures 4.8(c) and (e) it can be seen that by the end of the simulation, more energy is cumulatively released ($1.71 - 2.49 \times 10^{26}$ ergs) than is stored as free magnetic energy.

Although Figures 4.8(a)-(e) only show results for the 5 G overlying field cases, Figure 4.8(f) compares the values of free energy (triangles) and total energy dissipated (stars) at the end of the 1 G (black), 5 G (blue) and 10 G (red) simulations. The highest value of free energy is found for a

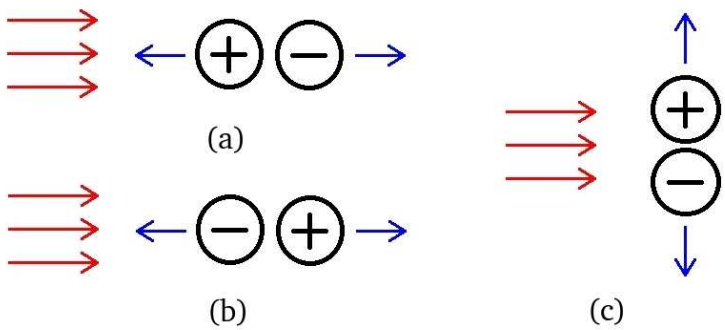

Figure 4.10: Emergence: The red arrows represent the direction of the overlying field, the blue arrows represent the direction of motion of the magnetic elements. The bipole's axis is oriented (a) parallel to, (b) anti-parallel to, and (c) perpendicular to the overlying field.

10 G overlying field, and perpendicular cancellation. In general, higher free energy is found for a stronger overlying field and when a greater volume of the overlying field is disturbed (i.e. perpendicular cancellation). We also see that a stronger overlying field results in more energy dissipation. For all overlying field strengths, parallel cancellation results in the least energy dissipation, however, a similar cumulative amount of energy dissipation occurs for both the anti-parallel and perpendicular cancellation.

4.2.3 Emergence

In the emergence simulations, initially, the net flux through the photosphere is zero. The magnetic elements, which coincide, then move apart until they each reach a separation distance of 3 Mm from the box midpoint after 100 min. As a result, a bipole appears in the photospheric distribution, simulating what can be classed in photospheric magnetograms as an emergence. The blue line in Figure 4.3 shows the total absolute flux through the photosphere as a function of time for the emerging bipole. Figure 4.10 illustrates the initial set-up for each of the simulations.

Field Lines

Figure 4.11 shows images of the 5 G emergence case, for each of the three orientations of the bipole's axis, at $t = 50$ min. At this time, the two magnetic elements have separated and no longer overlap. As in the cancellation simulations, when the emerging bipole's axis is parallel to the overlying field, all flux from the positive polarity connects to the negative polarity. In the anti-parallel and perpendicular cases, connections between the two magnetic elements exist in the early stages of emergence. However in both these cases, for strong overlying fields, connections between the magnetic elements can be completely severed by the end of the simulation.

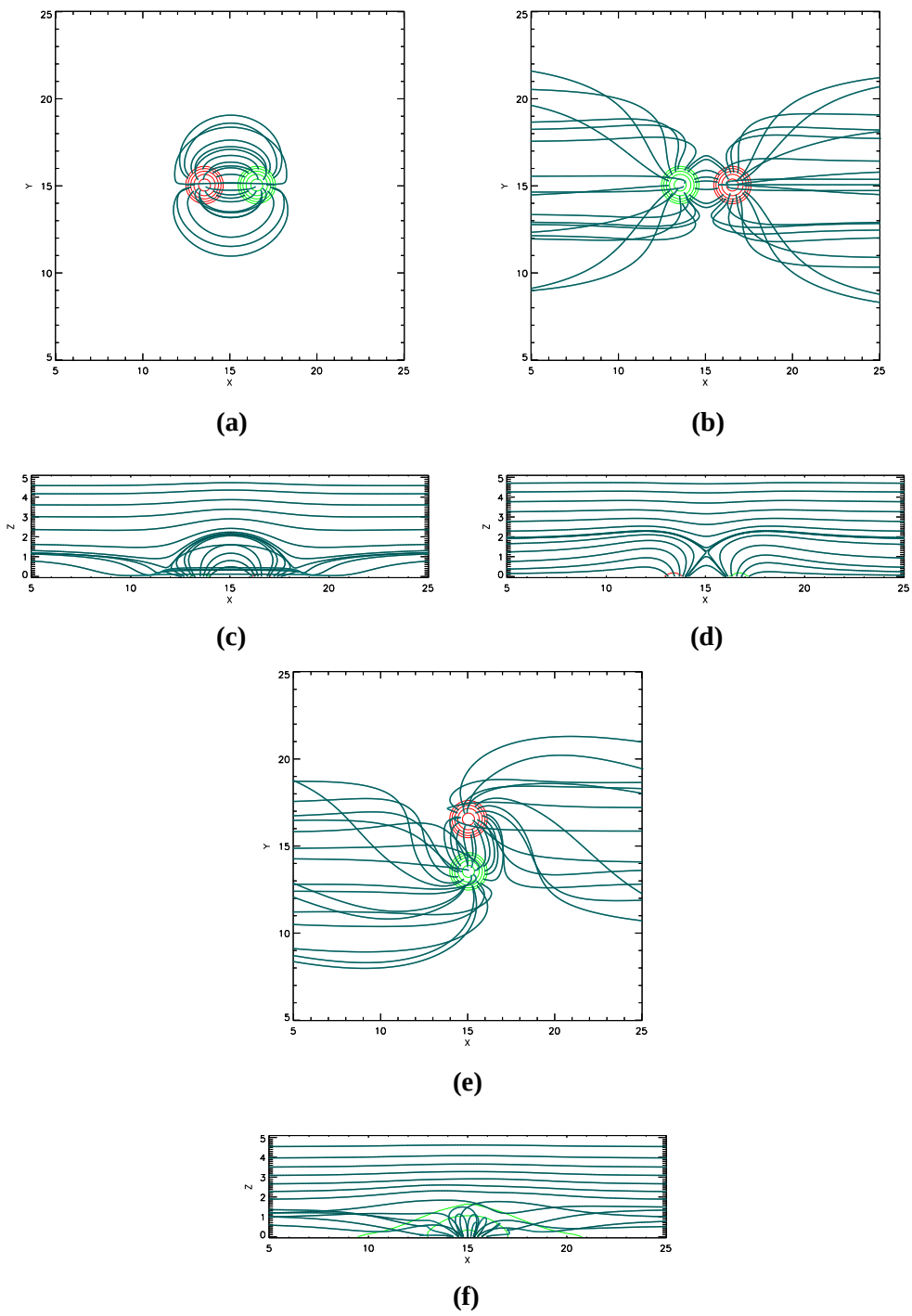

Figure 4.11: Emergence of a bipole in the presence of a 5 G overlying field: (a), (b) and (e) as seen in the $x - y$ plane at $z = 0$ Mm, (c), (d) and (f) as seen in the $x - z$ plane at $y = 15$ Mm. For each case, the images are taken at $t = 50$ min. The bipole's axis is aligned: (a) and (c) parallel to, (b) and (d) anti-parallel to, and (e) and (f) perpendicular to the overlying field. A selection of magnetic field lines originating from the bipole at the photospheric level is plotted on each image. In images (c), (d) and (f), some of the overlying field lines have also been plotted. Red and green contours represent positive and negative magnetic field.

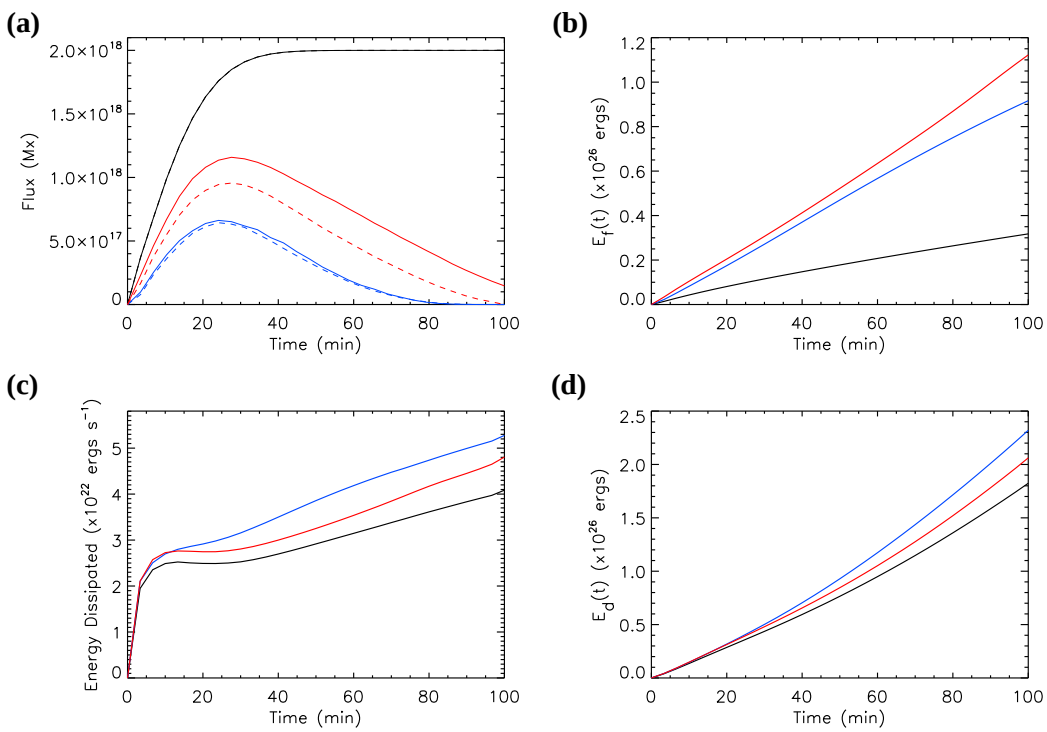

Figure 4.12: Plots for an emerging bipole moving parallel (black), anti-parallel (blue) and perpendicular (red) to a 5 G overlying field, as a function of time: (a) total flux connecting magnetic elements, (b) free magnetic energy, $E_{\rm f}(t)$, (c) energy dissipated, $\int_V QdV$, and (d) cumulative energy dissipated, $E_{\rm d}(t)$.

The photospheric boundary conditions for the cancellation and emergence simulations are exactly the reverse of one another. This means that a potential field extrapolation at $t = n$ min of each emergence case is identical to that at $t = (100 - n)$ min of the corresponding cancellation case. Thus, the same photospheric field distribution exists for both emergence and cancellation at $t = 50$ min. Therefore at this time, the field line plots of the non-linear force-free fields and potential fields in Figures 4.5, 4.6 and 4.7 (cancellation) may be compared to the non-linear force-free fields in Figure 4.11 (emergence). A comparison of these images shows that the emerging bipole's field is significantly different from that of the cancelling bipole or the corresponding potential field. In the parallel emergence case (4.11(c)), the low-lying field lines of the overlying field have been bent and pushed around either side of the bipole as the magnetic elements emerge. This shows that the special boundary treatment that we use allows the elements to emerge as a single flux system into the overlying coronal field.

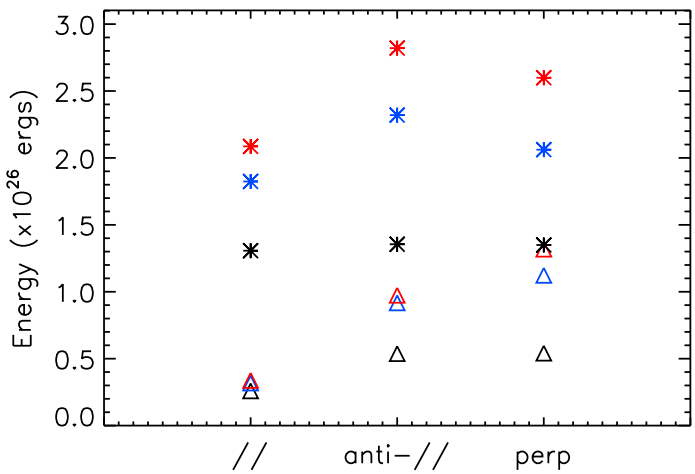

Figure 4.13: Free magnetic energy (triangles) and cumulative energy dissipated (stars) at the end of each emergence simulation, for a 1 G (black), 5 G (blue) and 10 G (red) overlying field.

Flux Connectivity and Energetics

Figure 4.12(a) shows a plot of the total flux connecting the two magnetic elements as a function of time for parallel (black), anti-parallel (blue) and perpendicular (red) emergence with a 5 G overlying field. Both the non-linear force-free field (solid lines) and the corresponding potential field (dashed lines) are shown. For the perpendicular case, much more flux connects between the magnetic elements in the non-linear force-free simulations than in the potential field extrapolations. Due to the continuous nature of the magnetofrictional method, connections that are formed between the two magnetic elements as they first emerge are maintained as they move apart. For the perpendicular case, the flux still connects between the magnetic elements by the end of the non-linear force-free field simulation, but all connections have been completely severed in the potential field extrapolation. A comparison of the perpendicular simulation in Figure 4.12(a) to the corresponding cancellation plot (Figure 4.8(a), red line) indicates that, for this orientation, the emergence shows a much larger departure from the potential field. Less departure is found for the anti-parallel case, since much more reconnection occurs as the bipole emerges into the oppositely aligned overlying field.

Figure 4.12(b) shows the free magnetic energy as a function of time, for each orientation of the bipole with a 5 G overlying field (lines are coloured as in Figure 4.12(a)). The plot shows that perpendicular emergence results in the most free energy, and the parallel emergence in the least, where energy values range from $0.32 - 1.12 \times 10^{26}$ ergs. Figure 4.12(c) shows a plot of the rate of energy dissipation, Q, integrated over the volume as a function of time. In all cases, the energy dissipation rate increases rapidly as the bipole first emerges, and the photospheric flux is

increasing. Subsequently, the rate of energy dissipation continues to increase as the two magnetic elements move apart, but the increase is less rapid. As in the cancellation simulations, if we compare Figures 4.12(b) and (c), it can be seen that the instantaneous energy dissipation is three orders of magnitude less than the free energy by the end of the simulation. Figure 4.12(d) shows the cumulative energy dissipated as a function of time (Equation 4.17), where values range from $1.82-2.32\times10^{26}$ ergs. In contrast to Figure 4.12(b) which shows that a perpendicular emergence results in the greatest build-up of free energy, Figures 4.12(c) and (d) show that more energy is dissipated per unit time and cumulatively in an anti-parallel emergence. This happens because in the anti-parallel case, larger gradients in α are produced and more reconnection takes place as the bipole emerges into the oppositely aligned overlying field.

Figure 4.13 compares the values of free energy (triangles) and total energy dissipated (stars) at the end of each simulation. The amount of free magnetic energy at the end of each emergence simulation follows the same trends as in the cancellation simulations: a stronger overlying field results in the build up of more free energy. The perpendicular emergence tends to result in the most free energy being built up, the parallel emergence in the least. We see that the most energy is dissipated in the anti-parallel case, and the least in the parallel case, as much more reconnection occurs in the anti-parallel case compared to the other two. As with the free energy, a stronger overlying field leads to more energy being dissipated.

To test the results of our simulations, it is possible to estimate the maximum amount of free magnetic energy that can be built up and stored for the anti-parallel emergence simulations. If we assume that no reconnection occurs, a current sheet (see e.g. Parnell and Galsgaard (2004), Archontis et al. (2010)) would separate the bipole's field from the oppositely directed overlying field. The free energy is then given by:

$$E_{\text{max}} = \frac{B_0 \phi D}{2\pi}, \tag{4.18}$$

where B_0 is the strength of the overlying field, ϕ is the absolute flux of each magnetic element and D is the photospheric separation of the magnetic elements. For the 5 G simulation, Equation 4.18 gives 4.8×10^{26} ergs. This is the theoretical maximum value for the free energy built up. We note that within our simulations, the theoretical maximum cannot be obtained due to numerical diffusion and the fact that reconnection occurs as soon as the bipole emerges. We find that the occurrence of reconnection results in a smaller amount of free energy being stored. From Figure 4.13, the amount of free energy stored at the end of the 5 G anti-parallel simulation is approximately 20% of the theoretical maximum. Although the free magnetic energy is one part of the energy calculated in the simulation, we also compute the energy dissipated due to relaxation processes and hyperdiffusion. For the 5 G case, a further 2.3×10^{26} ergs of magnetic energy is cumulatively dissipated (Figure 4.12(d)). Summing the stored energy and the total energy dissipated, we obtain 3.2×10^{26} ergs, which is close to the theoretical maximum of 4.8×10^{26} ergs.

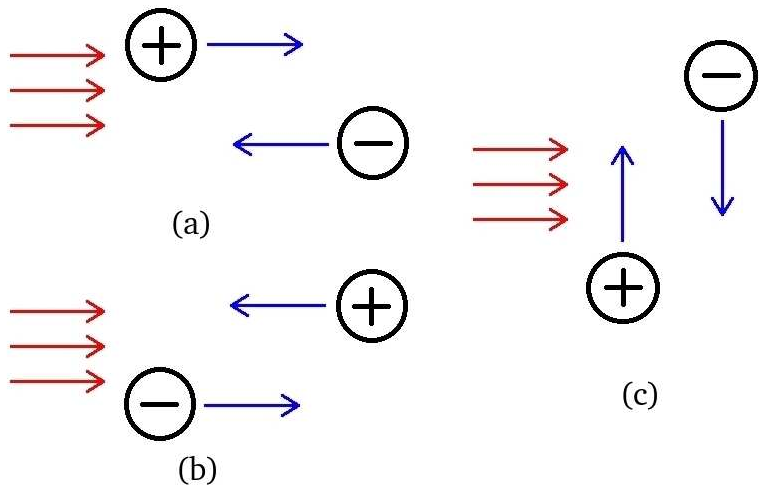

Figure 4.14: Flyby: The red arrows represent the direction of the overlying field, the blue arrows represent the direction of motion of the magnetic elements. The motion of the positive magnetic element is (a) parallel to, (b) anti-parallel to, and (c) perpendicular to the overlying field.

Therefore, by taking into account not only the free energy, but also the energy dissipated when reconnection is allowed, we find a similar total amount energy to the theoretical maximum when reconnection is not allowed.

4.2.4 Flyby

The photospheric boundary distribution for the flyby simulations is slightly different from the previous simulations. The flyby simulations are run for 166.7 min instead of 100 min, and each magnetic element is advected a distance of 5 Mm rather than 3 Mm. The total absolute flux through the photosphere is constant throughout the simulation (Figure 4.3, red line). The two magnetic elements are advected past one another under the presence of an overlying field, so that their final position mirrors their initial position. An illustration of the initial set-up of each flyby simulation is shown in Figure 4.14. In two set-ups the magnetic elements are advected past one another in the $x-$direction. In the first case (Figure 4.14(a)) the motion of the positive magnetic element is parallel to the overlying field, in the second case (Figure 4.14(b)) it is anti-parallel to the overlying field. In the third set of simulations (Figure 4.14(c)) the magnetic elements are advected in the $y-$direction, so that their motion is perpendicular to the overlying field.

Field Lines

Figure 4.15 shows a series of $x-y$ plane images at $t = 0$, 83.3 and 166.7 min for (a) parallel, (b) anti-parallel and (c) perpendicular flyby and a 5 G overlying field. Since the parallel flyby is the

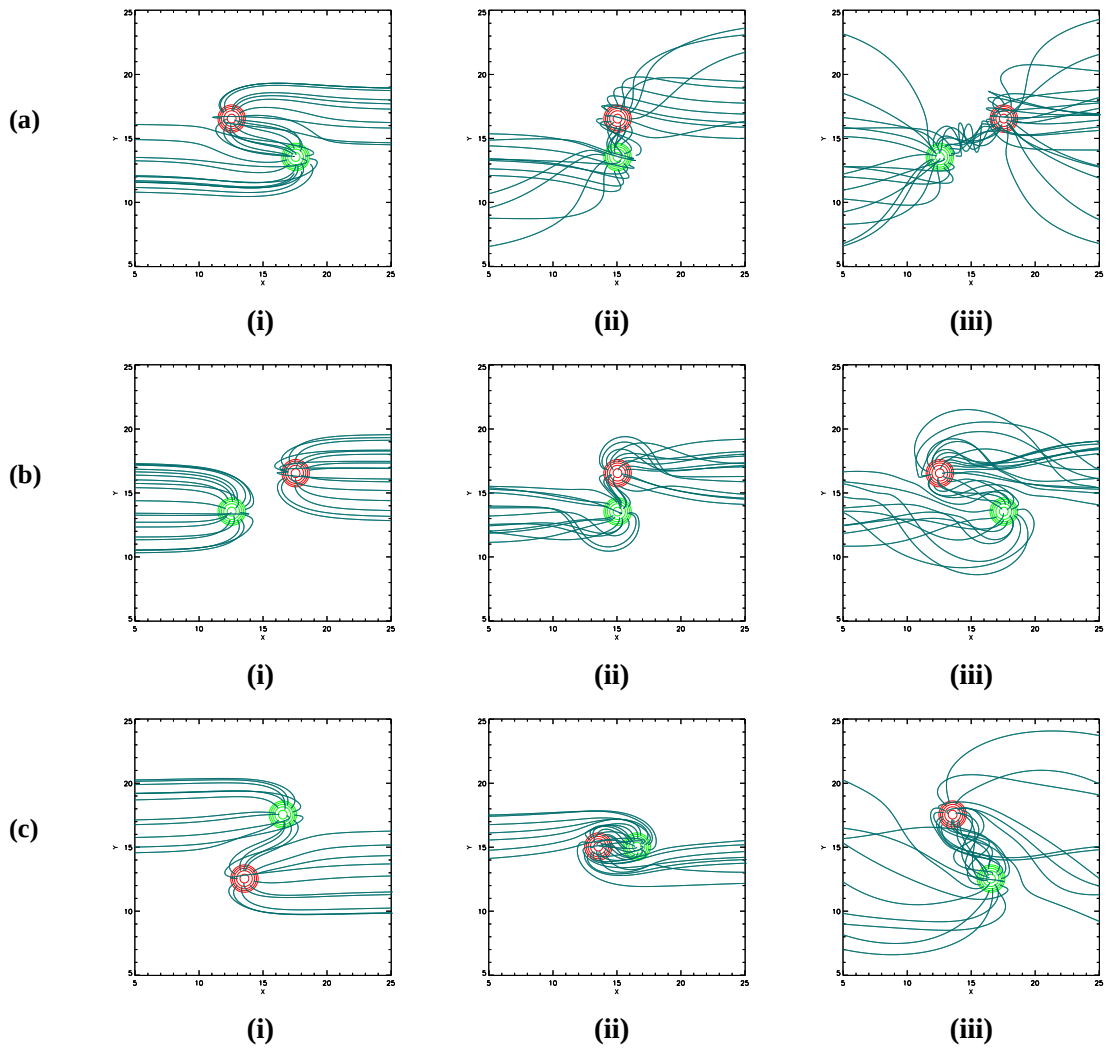

Figure 4.15: A series of $x - y$ plane images for each flyby case with a 5 G overlying field. The red and green contours represent positive and negative magnetic field. The images in each case are taken at (i) $t = 0$ min, (ii) $t = 83.3$ min and (iii) $t = 166.7$ min, and a selection of field lines is plotted originating from the magnetic elements. The positive magnetic element is advected (a) parallel to, (b) anti-parallel to and (c) perpendicular to the overlying field.

reverse of the anti-parallel flyby, the photospheric flux distribution at the start of each case is identical to that at the end of the other. This means that the initial potential fields in Figures 4.15(a)(i) and (b)(i) may be compared with the final non-linear force-free fields in Figures 4.15(b)(iii) and (a)(iii) respectively. It is clear that the non-linear force-free field in each case is quite different from the corresponding potential field. In particular, significant differences can be seen for the parallel flyby. For the non-linear force-free field ((a)(iii)), strong connections exist between the magnetic elements. However, there are no such connections in the potential field ((b)(i)). The field lines connecting the two elements in the non-linear force-free field case are very twisted, and the bipole's magnetic field appears to occupy a much larger volume of the corona than in the corresponding potential field (Figure 4.15(b)(i)).

It is also of interest to compare Figures 4.15(a)(ii) and (b)(ii), as their photospheric distributions are identical to one another. Even though both simulations have been running for the same amount of time (83.3 min), the shape of the bipole's field is very different. For the parallel simulation, the field lines that connect the magnetic elements are much more twisted. This illustrates that when the evolution of the coronal magnetic field is continuous, the properties of the field very much depend on its previous evolution and connectivity, not only on the photospheric boundary distribution.

For the perpendicular flyby (Figure 4.15(c)), the photospheric boundary distributions in (c)(i) and (c)(iii) are symmetric to one another. At the midpoint, the bipole's axis becomes aligned fully parallel to the overlying field, and this results in two major occurrences of reconnection. The first occurs as the magnetic elements move towards one another, and the total flux connecting from one magnetic element to the other rapidly increases. The second occurs after the magnetic elements have passed one another at the midline, causing connections between the magnetic elements to break, and the total connecting flux decreases. More flux remains connected between the two magnetic elements in Figure 4.15(c)(iii) than in the corresponding potential field in Figure 4.15(c)(i). Again, this illustrates the effect of the memory of previous connectivity in our simulations.

Flux Connectivity and Energetics

Figure 4.16(a) shows a plot of the total flux connecting the magnetic elements as a function of time, for a parallel (black), anti-parallel (blue) and perpendicular (red) flyby, with a 5 G overlying field. Both the non-linear force-free field (solid line) and corresponding potential field (dashed line) are shown. For the parallel case, at all times, the total flux connecting the magnetic elements is greater for the non-linear force-free field than the corresponding potential field. In particular, flux still connects between the magnetic elements at the end of the simulation, but does not in the corresponding potential field. For the anti-parallel case, initially, no flux connects between

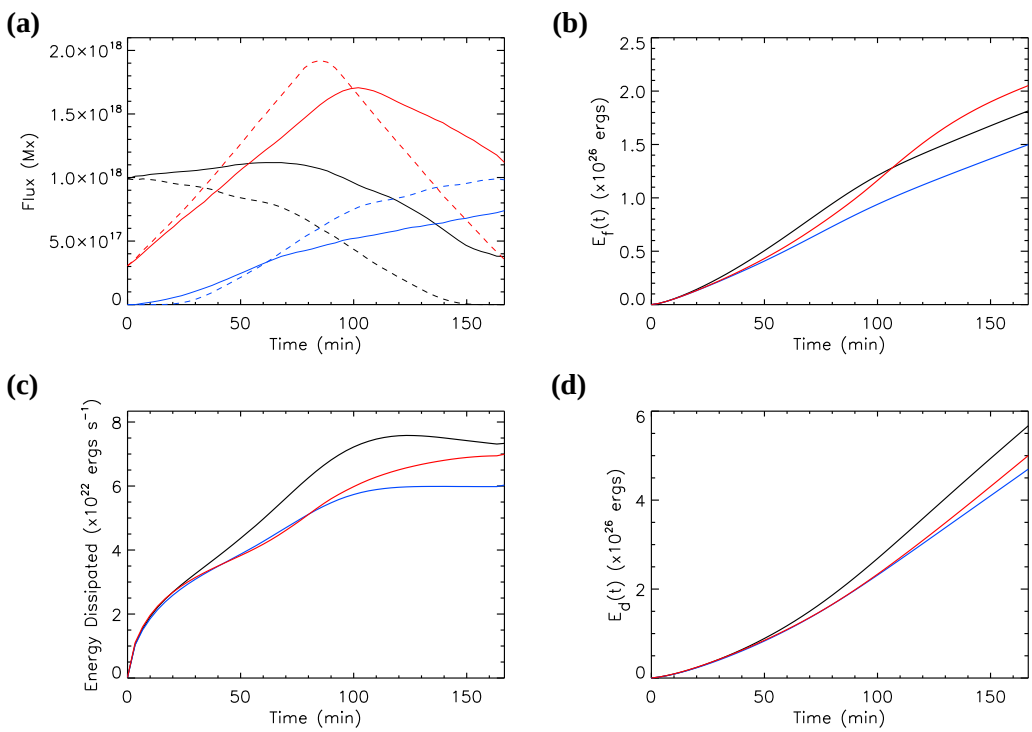

Figure 4.16: Plots for a flyby, where the positive polarity is advected parallel to (black), anti-parallel to (blue) and perpendicular to (red) a 5 G overlying field, as a function of time: (a) total flux connecting the magnetic elements, (b) free magnetic energy, $E_{\rm f}(t)$, (c) energy dissipated, $\int_V Q dV$, and (d) cumulative energy dissipated, $E_{\rm d}(t)$.

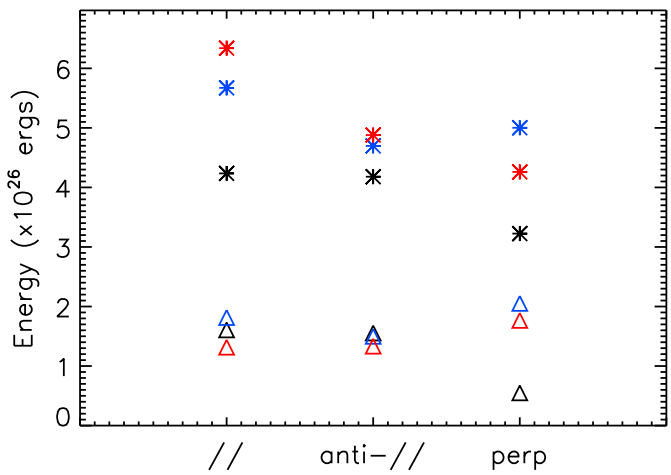

Figure 4.17: Free magnetic energy (triangles) and cumulative energy dissipated (stars) at the end of each flyby simulation, for a 1 G (black), 5 G (blue) and 10 G (red) overlying field.

the magnetic elements. As the magnetic elements are advected past one another, the bipole's axis rotates to become aligned with the overlying field, and the total flux connecting the magnetic elements increases. Even though the connecting flux increases, the total flux connecting the elements is less than that of the potential field.

For the potential field case of the perpendicular flyby (red dashed line), the plot of the total flux connecting the magnetic elements is symmetric about the line $t = 83.3$ min. In contrast, the connecting flux plot for the non-linear force-free field is non-symmetric. Before the polarities have aligned with the overlying field, the flux connecting the magnetic elements is lower than that of the potential field. However, after the elements pass one another at the midpoint, more flux connects between them in the non-linear force-free field than in the potential field case. This once again indicates significant differences between the potential field extrapolations and the non-linear force-free field simulations which retain a memory of flux connectivity.

Figure 4.16(b) shows a plot of the free magnetic energy as a function of time for the 5 G case of each orientation (lines are coloured as in Figure 4.16(a)), where the final values range from $1.50 - 2.05 \times 10^{26}$ ergs. The free energy stored by the end of the parallel flyby is greater than that of the anti-parallel flyby because, in the parallel case, more flux connects between the magnetic elements for a greater amount of time. However, the free energy is greatest for the perpendicular flyby, for two reasons. First, a greater volume of the magnetic field is disturbed by the magnetic elements, building up more free energy. Second, as the elements move past one another, flux from the positive magnetic element is forced to connect to the negative element. Numerous closed connections form and, due to the continuous nature of the magnetofrictional evolution, these flux

connections are maintained as the magnetic elements move apart. Any free magnetic energy may be stored along them.

Figure 4.16(c) shows a plot of the rate of energy dissipation, Q integrated over the volume, as a function of time. In each case, the energy dissipated increases as the magnetic elements move towards one another, then levels off after they have passed one another at the midline. Initially, the curves for the anti-parallel and perpendicular cases are very similar. However, towards the end of the simulations, the rate of energy dissipation becomes greater in the perpendicular case. This happens because in the perpendicular case the amount of flux connecting the magnetic elements is still changing. This can be seen in Figure 4.16(a), where towards the end of the simulation, the slope of the total flux connecting the magnetic elements is much steeper in the perpendicular than in the anti-parallel simulation. Figure 4.16(d) shows the cumulative energy dissipated as a function of time, as calculated by Equation 4.17. One can see from Figures 4.16(c) and (d) that the energy dissipation is greatest in the case of the parallel flyby (5.67×10^{26} ergs in total) and least in the case of the anti-parallel flyby (4.70×10^{26} ergs in total).

Figure 4.17 compares the values of free magnetic energy (triangles) and total energy dissipated (stars) at the end of each flyby simulation. The most free energy tends to be stored in the 5 G case of each orientation, with the greatest amount of free energy resulting from the 5 G perpendicular flyby. Between $2 - 3$ times more energy is cumulatively dissipated by the end of each simulation than is stored as free energy. The greatest amount of energy is dissipated for the parallel flyby with a 10 G overlying field. The exact amount of free energy stored and energy dissipated by the end of each simulation depends on a balance between the strength and orientation of the overlying field, the volume of the coronal field that is disturbed, the amount of reconnection that occurs and, finally, the amount of connections that exist between the magnetic elements throughout their evolution.

In the next section, we compare the cancellation, emergence and flyby simulations to one another.

4.2.5 Comparison of interactions

For each of the three bipole interactions, three different orientations of the interaction with respect to an overlying magnetic field and three different strengths of overlying field have been considered. In this section, we compare the free energy and energy dissipated for all cases. Figure 4.18 shows a plot comparing the free magnetic energy (triangles) and total energy dissipated (stars) at $t = 100$ min for each simulation. Note that each flyby simulation is run for 166.7 min, but here we are plotting the values at $t = 100$ min in order to compare them with values from the cancellation and emergence simulations. The plot is split into three columns representing the cancellation (left),

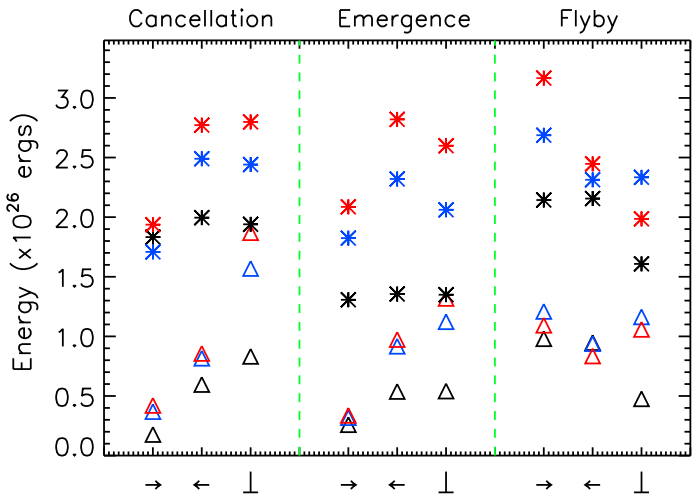

Figure 4.18: Free magnetic energy, $E_f(t)$ (triangles), and cumulative energy dissipated, $E_{\rm d}(t)$ (stars), at $t = 100$ min in each simulation, for a 1 G (black), 5 G (blue) and 10 G (red) overlying field, in the parallel ($\rightarrow$), anti-parallel ($\leftarrow$) and perpendicular ($\perp$) cases. The green dashed lines separate the plot into three columns representing the cancellation (left), emergence (middle) and flyby (right) simulations.

emergence (middle) and flyby (right) simulations. For each interaction, the parallel ($\rightarrow$), anti-parallel ($\leftarrow$) and perpendicular ($\perp$) cases are shown with a 1 G (black), 5 G (blue) and 10 G (red) overlying field. Clearly, for the emergence and cancellation simulations, the smallest amount of free magnetic energy and energy dissipated arises in the parallel cases, while the anti-parallel and perpendicular cases lead to the largest energy stored and dissipated. In contrast, for the flyby, the parallel cases result in the most free energy and energy dissipated. However, for all cases the stronger the overlying field, the larger the energy values tend to be.

The amount of free energy stored in the magnetic field at $t = 100$ min in each simulation varies between $0.2 - 1.9 \times 10^{26}$ ergs, where the greatest value arises for the perpendicular cancellation with a 10 G overlying field. As discussed in Section 4.2.2, these values of free energy are small compared to the total energy within the volume (between $8.7 \times 10^{26} - 6.3 \times 10^{28}$ ergs depending on overlying field strength). However, the box is large compared to the size of the bipole and the bipole's area of interaction. In reality on the Sun, many such magnetic elements would exist within such an area, with many of them continually interacting with one another. If we consider the power law distribution of Parnell et al. (2009), we can determine the number of small magnetic elements with flux in the range $[\phi_1, \phi_2]$ that would exist in the simulation region. Taking

$$N(\phi_1, \phi_2) = \int_{\phi_1}^{\phi_2} \frac{N_{\rm f}}{\psi_0} \left(\frac{\phi}{\psi_0} \right)^{-1.85} d\phi,$$

where $N_{\rm f} = 3.6 \times 10^{-17}$ cm^{-2} and $\psi_0 = 10^{16}$ Mx, the number of magnetic elements expected in a 30×30 Mm region with flux in the range $10^{17} - 10^{18}$ Mx is 46, and the number with flux in the range $10^{16} - 10^{18}$ Mx is 374. Therefore in more complex simulations with a realistic number of magnetic elements, the free energy could be $1 - 2$ orders of magnitude higher. Even though for the simulations here the free energy is small compared to the total energy, the amount of free energy built up in a single event is sufficient to explain sporadic events such as nanoflares, which release energy on the order of 10^{24} ergs (Golub and Pasachoff, 1997).

The average energy dissipation rate for each simulation is $2.1 - 6.2 \times 10^{22}$ ergs s^{-1}. The total amount of energy dissipated by $t = 100$ min varies between $1.3 - 3.2 \times 10^{26}$ ergs, where the simulation that results in the most energy dissipated is the parallel flyby. We may compute the average rate of energy dissipation in ergs cm^{-2} s^{-1} for each simulation. We consider the central region in each case ($x = 10-20$ Mm, $y = 10-20$ Mm) to focus in on the interaction location. We find that the average energy dissipation for each simulation occurs in the range $1.50 - 4.95 \times 10^4$ ergs cm^{-2} s^{-1}. On comparing these values to the radiative losses of either the quiet Sun (3×10^5 ergs cm^{-2} s^{-1}) or of a coronal hole (8×10^5 ergs cm^{-2} s^{-1}, Withbroe and Noyes (1977)), we find that the rate of dissipation for a single event is too low. However, note that there would be many more magnetic elements on the Sun in a region of the size we have considered. Using the figures from above, in a region of size 10 Mm $\times$ 10 Mm, 41 magnetic elements of flux $10^{16} - 10^{18}$ Mx would be expected. This may increase the energy dissipation rate by an order of magnitude to observed levels. In addition, we may compare the radiative losses to those of an XBP. The radiative losses of an XBP have been measured as 5×10^4 ergs cm^{-2} s^{-1} (Habbal and Grace, 1991). This implies that the average energy dissipation in some of our simulations is of the correct size to explain the occurrence of such an event.

4.3 Discussion and Conclusions

The aim of this chapter was to investigate the coronal consequences of three basic photospheric magnetic interactions: cancellation, emergence and flyby. Each interaction was simulated in the presence of an overlying uniform magnetic field, which was taken to be parallel, anti-parallel or perpendicular to the motion of the magnetic elements. The bipoles considered here were representative of small-scale photospheric magnetic features such as ephemeral regions or network features. Each bipole's physical extent was on the order of $3,000 - 4,000$ km and its total absolute flux was 2×10^{18} Mx.

In all cases, the 3D coronal magnetic field was initially in a potential state. A continuous evolution of the coronal field was then produced via a magnetofrictional relaxation technique that evolved the field through a series of quasi-static, non-linear force-free equilibria in response to

applied photospheric boundary motions. Our treatment of the photospheric boundary evolution was discussed in Section 4.1.3. The continuous nature of the coronal evolution means that connectivity within the coronal volume was maintained from one step to the next. In many cases, this continuity allowed connections to exist longer than those found in potential field extrapolations. This allowed free energy to be built up and stored along closed field lines.

For each of the simulations, two forms of energy were studied. First there was the free magnetic energy which was stored in the non-potential magnetic field. This energy may be regarded as that available for sporadic coronal events such as XBPs or nanoflares. Second, energy was continually being dissipated, as described by Equation 4.11 (Q). This may be considered as energy that is available to be converted to heat or plasma motions, although for simplicity, here we did not follow the corresponding plasma processes. With the formalisation used in the present chapter, the dissipated energy arose from the relaxation process employed, along with hyperdiffusion. We found that Q mainly arose low down near the magnetic elements, where the magnetic field departed most from a potential state, and at sites of changing magnetic topology.

The amount of free energy stored at $t = 100$ min in each simulation ranges from $0.2 - 1.9 \times 10^{26}$ ergs. The cumulative energy dissipated in each simulation after the same amount of time is greater than the free energy stored; for each simulation, anywhere from $1.3 - 3.2 \times 10^{26}$ ergs of energy has been dissipated after 100 min. The upper limits to both these values are higher if we consider the values at the end of the flyby simulations, which run for 166.7 min (2.1×10^{26} ergs for free energy, 6.3×10^{26} for dissipated energy). For cancellation and emergence, the amounts of free and dissipated energy are smallest when the motion of the magnetic elements is parallel to the overlying field, and largest when it is perpendicular. In contrast, for flyby, the amounts of free and dissipated energy are greatest in the parallel case. In all cases, a stronger overlying field tends to lead to greater energy storage and dissipation. The simulation that results in the most free energy is the perpendicular cancellation with a 10 G overlying field, while the simulation that results in the most energy cumulatively dissipated is the parallel flyby with a 10 G overlying field. The exact amount of free energy stored and energy dissipated by the end of each simulation depends upon several factors: the strength and orientation of the overlying field, the volume of the overlying field that is disturbed, the amount of reconnection that occurs and, finally, the total flux connecting the magnetic elements.

The free magnetic energy built up in the present simulations is small compared to the total magnetic energy within the volume. However, in each case, the free energy is a significant fraction of the bipole's energy contribution ($8 - 86\%$), and is more than enough to account for small-scale, transient phenomena such as nanoflares or XBPs. The average rate of energy dissipation in each case is between $2.1 - 6.2 \times 10^{22}$ ergs s^{-1}. This could provide a contribution towards the heating rate of an XBP of $3 \times 10^{23} - 10^{24}$ ergs s^{-1}, determined by Habbal and Withbroe (1981). We also find that for the inner 10×10 Mm of each simulation, the energy dissipation rate is between

$1.50 - 4.95 \times 10^4$ ergs cm^{-2} s^{-1}. This is equivalent to $5 - 17\%$ of the energy required to heat the quiet Sun corona (3×10^5 ergs cm^{-2} s^{-1}, Withbroe and Noyes (1977)). Although it is at most 17% of the coronal energy budget, on the Sun, many tens or hundreds of such small-scale magnetic elements would be found in a region of the size modelled here. The continual interaction of these magnetic elements with one another would result in a significantly larger build up of free magnetic energy and greater energy dissipation. With the expected number of magnetic elements in a region of this size, the free energy and energy dissipation rate may easily be $1 - 2$ orders of magnitude larger than those found for the simulations in this paper. This would bring it in line with coronal requirements. It is therefore of key importance to consider more complicated simulations of multiple magnetic elements.

Although a non-linear force-free field is a useful approximation to the coronal magnetic field of the Sun, there are several limitations to our model that it is important to be aware of. Within our coronal model, there is no physical timescale of information transfer, rather there is a relaxation timescale. Since we have neglected the $\frac{\partial \mathbf{v}}{\partial t}$ term within the equation of motion, we do not get waves. Both the fact that we do not resolve wave motions, and that we are assuming the instantaneous transfer of information, lead to a large amount of reconnection occurring within the model. This is why in the cancellation and emergence simulations in particular, the plots of flux connectivity as a function of time (Figures 4.8(a) and 4.12(a)) for the potential fields and non-linear force-free fields are very similar. Another approximation that we have made is that there is no plasma within our model, therefore we get no back-reaction to the motion that we are applying. One effect that the introduction of plasma could have on our model is that a large pressure gradient could halt reconnection, thus resulting in larger differences between our simulated coronal field and the corresponding potential field. The inclusion of plasma within the model will be investigated after completion of the studies within this thesis.

From this study of small-scale interactions between two magnetic elements, the next step is to simulate the coronal evolution of the synthetic magnetograms constructed in Chapter 3. This will allow us to study the energetics of many events at the same time, as occur on the Sun, and will be the aim of Chapter 5. In these more complex simulations, we will study many aspects of the coronal evolution such as global calculations of free magnetic energy and energy dissipation, and where they are located within the corona. These will be related to the dynamic processes occurring in the photospheric evolution.

Chapter 5

Coronal Modelling of Synthetic Magnetograms

In this chapter, we present the preliminary results of 3D simulations of the small-scale coronal field of the magnetic carpet. In contrast to the magnetic carpet models described in Chapter 2, which produce independent potential field extrapolations, we model a continuous evolution of a non-linear force-free coronal field. We use the 2D synthetic magnetograms described in Chapter 3 as a lower boundary condition to drive the evolution of the full 3D coronal field. The coronal field is evolved through a series of quasi-static, non-linear force-free states in response to the evolution of the photospheric magnetic field, using the magnetofrictional technique described in Chapter 4.

The present study is a basic analysis of complex features in the simulations, where the quantities considered are mainly global quantities. A more detailed analysis will be conducted at a later time. Within the 3D simulations, we consider the magnetic energy both stored and dissipated within the coronal volume, as well as velocities and the electric current density. Some of the aspects of these quantities that we study are: how they evolve in time, where they are located spatially, and the effect of varying the strength of the overlying coronal magnetic field. The chapter is outlined as follows. In Section 5.1 we described the setup of the simulations, and revisit some of the properties of the 2D simulation that we are applying as lower boundary data. Sections 5.2-5.6 give the results of the simulations, and Section 5.7 gives discussion and conclusions. To accompany this chapter, there are number of movies that are held on the CD. A list of movies is given in Appendix C.2

5.1 Lower Boundary Condition and Set-up

We choose the most realistic simulation from Chapter 3 to provide the lower boundary condition for our 3D model. This is the simulation which included the largest range of flux values that a newly emerging bipole may take: $\phi_{\text{bp}} = 4 \times 10^{16} - 10^{19}$ Mx. A 250 hour long time series of synthetic magnetograms was produced from this simulation. The magnetograms are each of cadence 1 min and cover an area of 50×50 Mm^2. Full details of the simulation are given in Section 3.2 of Chapter 3.

For the 3D simulations, we take a 48 hour window of the synthetic magnetograms from the full 250 hour set. We choose the range $t = 120 - 168$ hours, a series of 2881 synthetic magnetograms. This time period is chosen as it occurs long after the 2D simulation has reached a steady state, in which the rates of cancellation and emergence are roughly equal. Figure 5.1 shows six contour plots of B_z from the 2D simulation for the range that we are considering, spaced 8 hr apart. Red contours represent positive magnetic field, blue contours represent negative. The magnetic elements are mainly located around the boundaries of the supergranules, forming a magnetic network. As described in Chapter 3, the spatial location of the magnetic network does not vary much during this time period since the supergranular flow profile is steady. However, it can be seen that the exact distribution of magnetic elements is significantly different in each image. Note also that although each magnetic element is given a Gaussian profile, many elements overlap to form large, irregularly shaped magnetic features. A movie showing the photospheric evolution of B_z for this 48 hr period is included on the CD with this thesis (magnet48_bz.mpg), with the contour levels the same as in Figure 5.1. The magnetic network can clearly be seen in the movie, along with a photospheric magnetic field that is continually evolving.

Figure 5.2 shows graphs outlining the properties of the 2D simulation of the photospheric evolution of the magnetic field. Figure 5.2(a) is a plot of the total absolute flux through the photosphere as a function of time for the full 250 hr 2D simulation. Initially, there is no magnetic flux within the numerical box. The total absolute flux rapidly increases as magnetic bipoles emerge through the photosphere. As discussed in Chapter 3, the flux levels off after around 24 hr, and the simulation reaches a steady state. The total flux then oscillates about a mean value of 1.11×10^{20} Mx, with a standard deviation of 1.17×10^{19} Mx, or 10.6%.

In Figure 5.2(a), the total absolute flux for the 48 hr section of the 2D simulation that is used for 3D modelling is indicated in blue, between the vertical red dashed lines at $t = 120$ hr and $t = 168$ hr. A zoomed in plot of this section is shown in Figure 5.2(b). Here, the total absolute flux oscillates about a mean value of 1.19×10^{20} Mx, with a standard deviation of 5.79×10^{18} Mx (4.9%). Therefore, the 2D simulation is in a steady state at this time. This can also be seen in Figure 5.2(c), which shows a plot of the emergence (solid line) and cancellation (dashed line) rates for the 48 hr period. The two are roughly equal throughout, with a mean emergence rate of 107.6

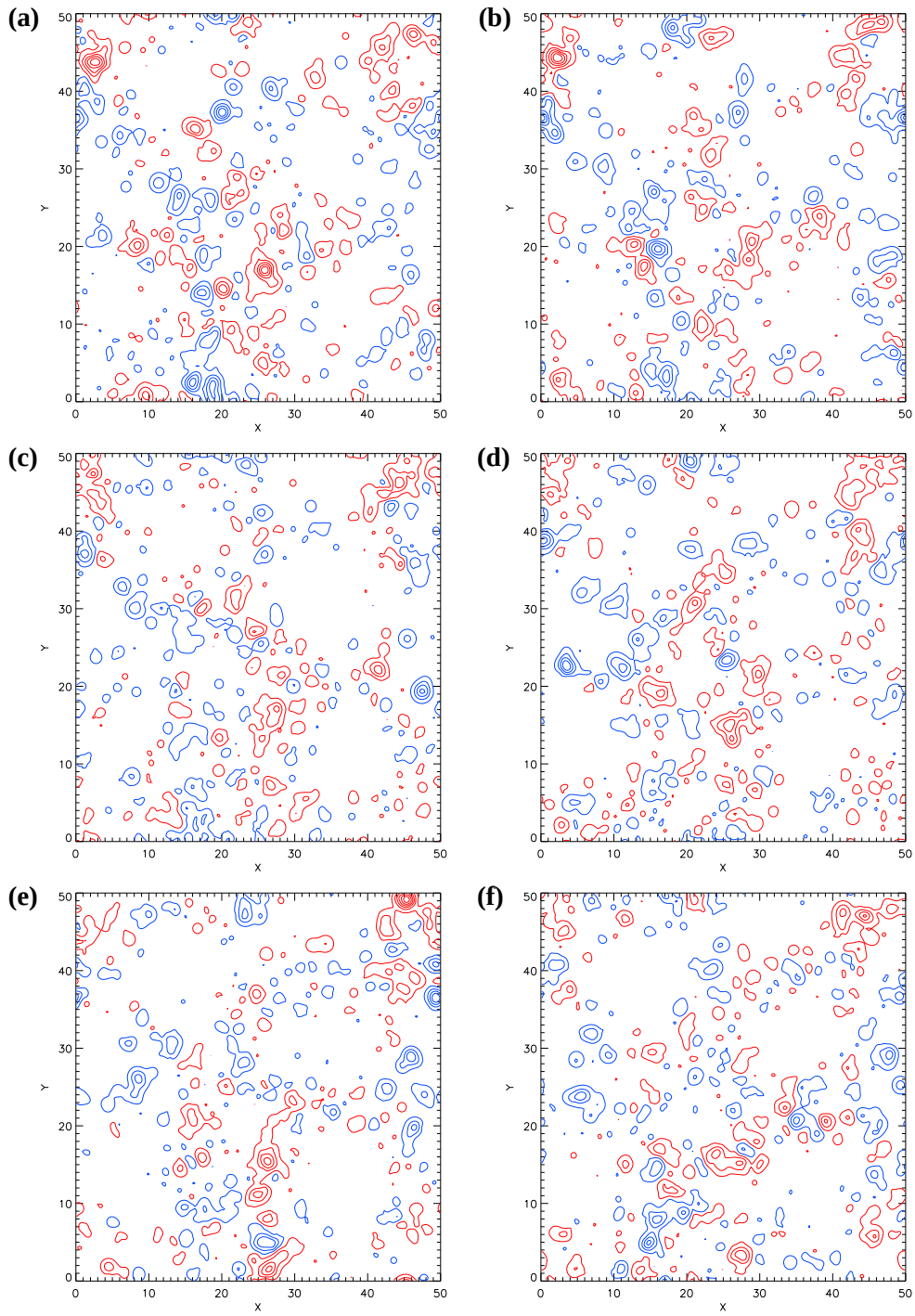

Figure 5.1: Synthetic magnetograms for a simulation with a flux emergence range of 4×10^{16} - 1×10^{19} Mx. Red contours represent positive magnetic field, blue contours represent negative magnetic field, where ten contour levels are shown for each polarity, with absolute values spaced evenly between 7.5 G and 142.5 G. The time, t (hr), at which each image is taken and number of individual elements, ns, composing the magnetogram are as follows: (a) $t = 120$, ns=1499, (b) $t = 128$, ns=1527, (c) $t = 136$, ns=1503, (d) $t = 144$, ns=1535, (e) $t = 152$, ns=1486 and (f) $t = 160$, ns=1590. A movie of the full time series, magnet48_bz.mpg, is given on the CD.

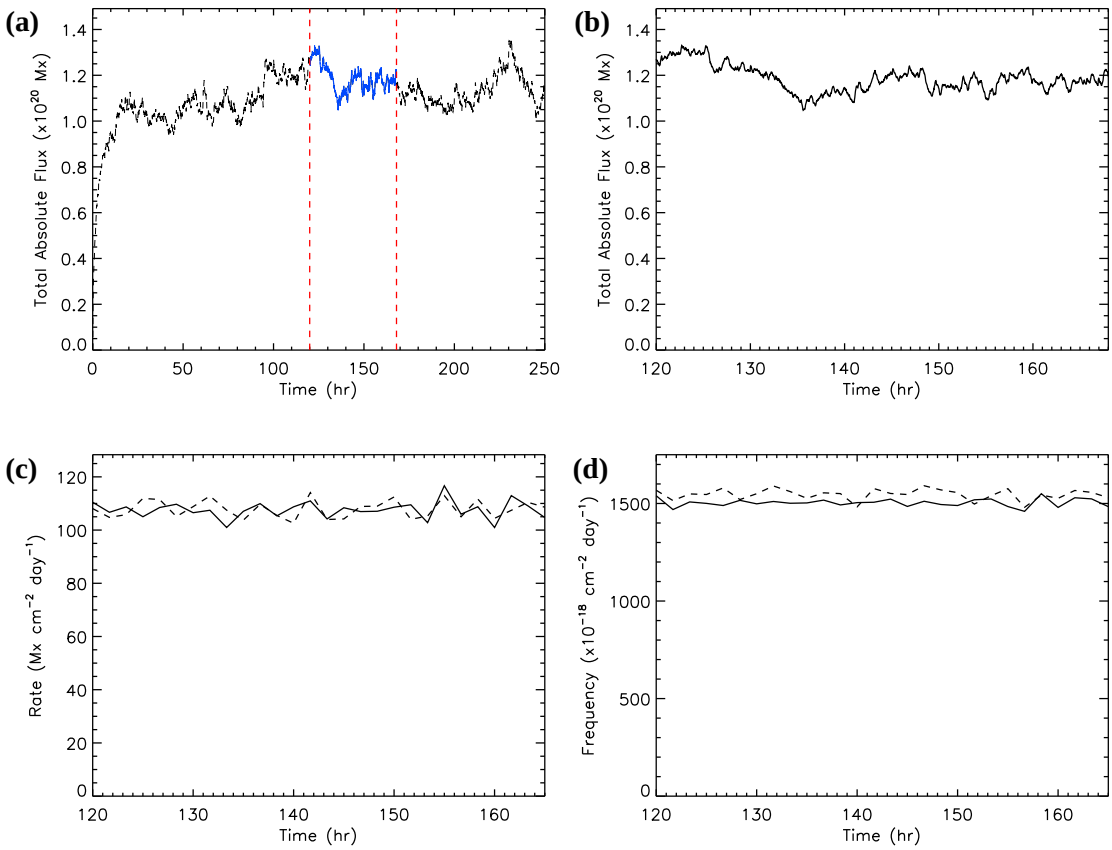

Figure 5.2: Plots for the 2D simulation with flux emergence range $\phi = 4 \times 10^{16} - 10^{19}$ Mx. (a) Total absolute flux through the photosphere as a function of time for the full 250 hr simulation. The section of the simulation that is used as the lower boundary condition for our 3D model lies between the red dashed lines and is highlighted in blue. (b) Total absolute flux through the photosphere as a function of time for the 48 hr series of magnetograms used in our 3D models. (c) Flux emergence (solid) and cancellation (dashed) rates as a function of time, and (d) flux emergence (solid) and cancellation (dashed) frequencies as a function of time, for the 48 hr series.

Mx cm^{-2} day^{-1} and a mean cancellation rate of 107.9 Mx cm^{-2} day^{-1}. The mean cancellation rate is slightly higher than the mean emergence rate, so overall there is a small decrease in the total absolute flux in this 48 hr period. Figure 5.2(d) shows a plot of the emergence (solid line) and cancellation (dashed line) frequencies for the 48 hr period. One can see that the cancellation frequency tends to be slightly higher than the emergence frequency. This is because the minimum quantity of flux that can emerge is 4×10^{16} Mx, whereas the minimum quantity of flux that can be removed due to cancellation is lower, at 10^{16} Mx. A large number of small magnetic elements may be produced as a result of fragmentation, and subsequently cancel with one another. This is discussed in further detail in Chapter 3.

We now discuss the set-up of the 3D model. We choose a numerical box of size $50 \times 50 \times 25$ Mm^3, composed of $512 \times 512 \times 256$ grid cells. The box is periodic in the $x-$ and $y-$directions and closed at the top. The lower boundary treatment is the same as described in Chapter 4. A linear interpolation of the A_x and A_y corresponding to B_z at $z = 0$ Mm is carried out between each synthetic magnetogram. B_z at $z = 0$ Mm is analytically specified at each time step, rather than advected numerically. This avoids certain undesirable numerical effects such as numerical overshoot or pile-up at cancellation sites. These effects would be propagated into the coronal volume during the simulation, so a treatment of the lower boundary condition that prevents them is useful. Again, 500 interpolation steps are taken between each analytical specification, where each step corresponds to 0.12 s. In response to the photospheric evolution, the coronal field is evolved via the magnetofrictional technique described in Chapter 4, with the induction equation (Equation 4.5) specified in terms of the vector potential, $\mathbf{A}$, and the magnetofrictional velocity given by Equation 4.4. The hyperdiffusivity constant, η_4, is chosen to be 7.6×10^5 km^4 s^{-1}. Four simulations are run, each with the same photospheric boundary evolution. Three of the simulations have an overlying, uniform magnetic field of strength 1 G, 3 G or 10 G, which points in the $x-$direction, while the fourth simulation has no overlying field (0 G). Details of the staggered grid that is used within our simulations are given in Appendix B, as well as the calculations required to convert dimensionless quantities within the code into dimensional values.

In the following sections, we give results of the 3D non-potential simulations. We first discuss the field line connectivity between the magnetic elements (Section 5.2), then analyse some of the quantities of interest within the simulations. Section 5.3 focuses on the free magnetic energy, and Section 5.4 on the energy dissipated. For both energies, we first consider the time evolution of the quantity summed over the whole volume, and the effect of varying the strength of the overlying field. We then consider where it is located spatially, and how this may depend upon properties of both the photospheric and coronal evolution. In Sections 5.5 and 5.6 we investigate where enhanced velocities and electric currents are located, along with the effect of the photospheric evolution and the presence of the overlying field on these quantities.

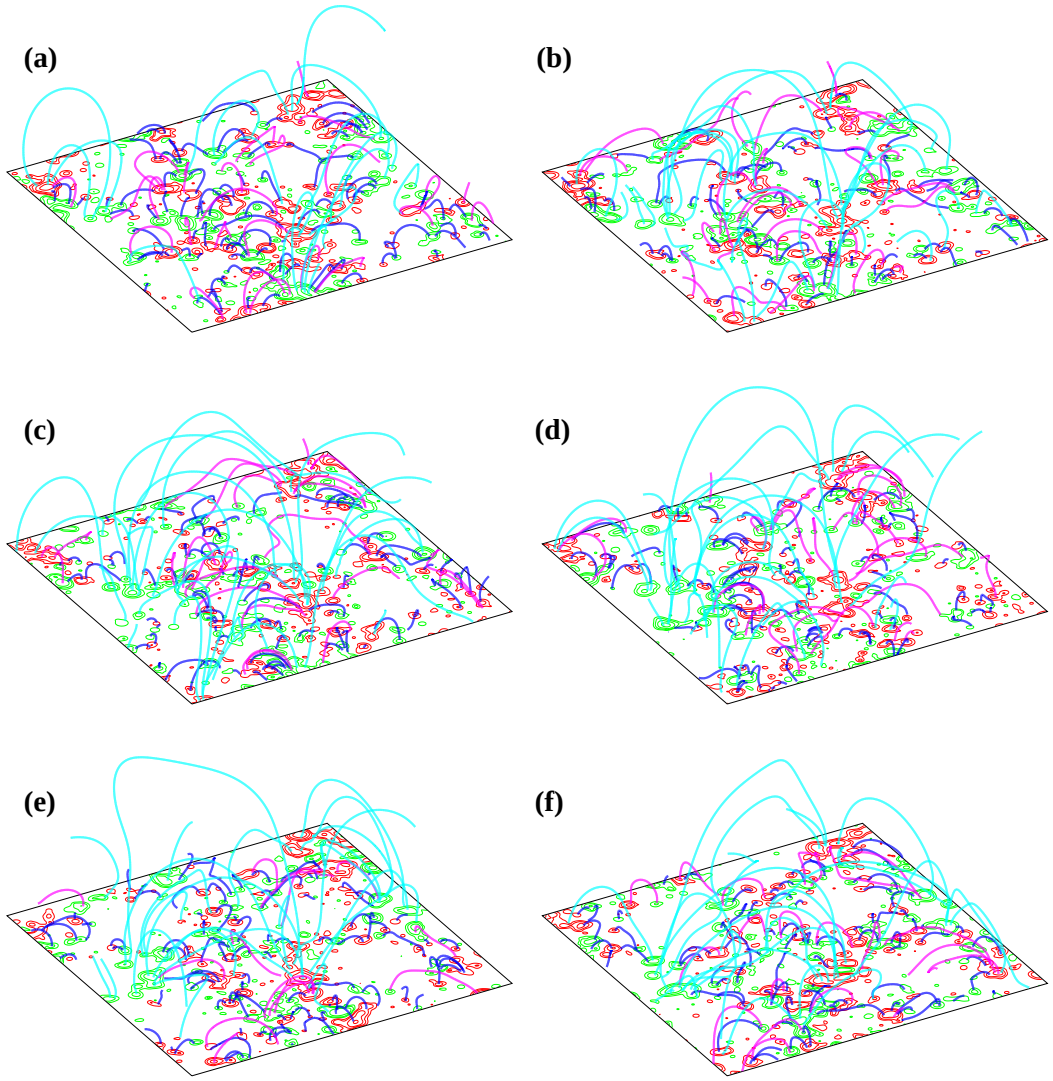

Figure 5.3: Coronal field images for the 3D simulation with no overlying field, for the same magnetograms as shown in Figure 5.1. Red contours represent positive magnetic field, green contours represent negative. A selection of coronal magnetic field lines is shown in each case, coloured as follows: dark blue field lines reach heights of 2.5 Mm or less, magenta field lines between $2.5 - 5$ Mm and pale blue field lines above 5 Mm. (a) $t = 120$ hr, (b) $t = 128$ hr, (c) $t = 136$ hr, (d) $t = 144$ hr, (e) $t = 152$ hr, and (f) $t = 160$ hr.

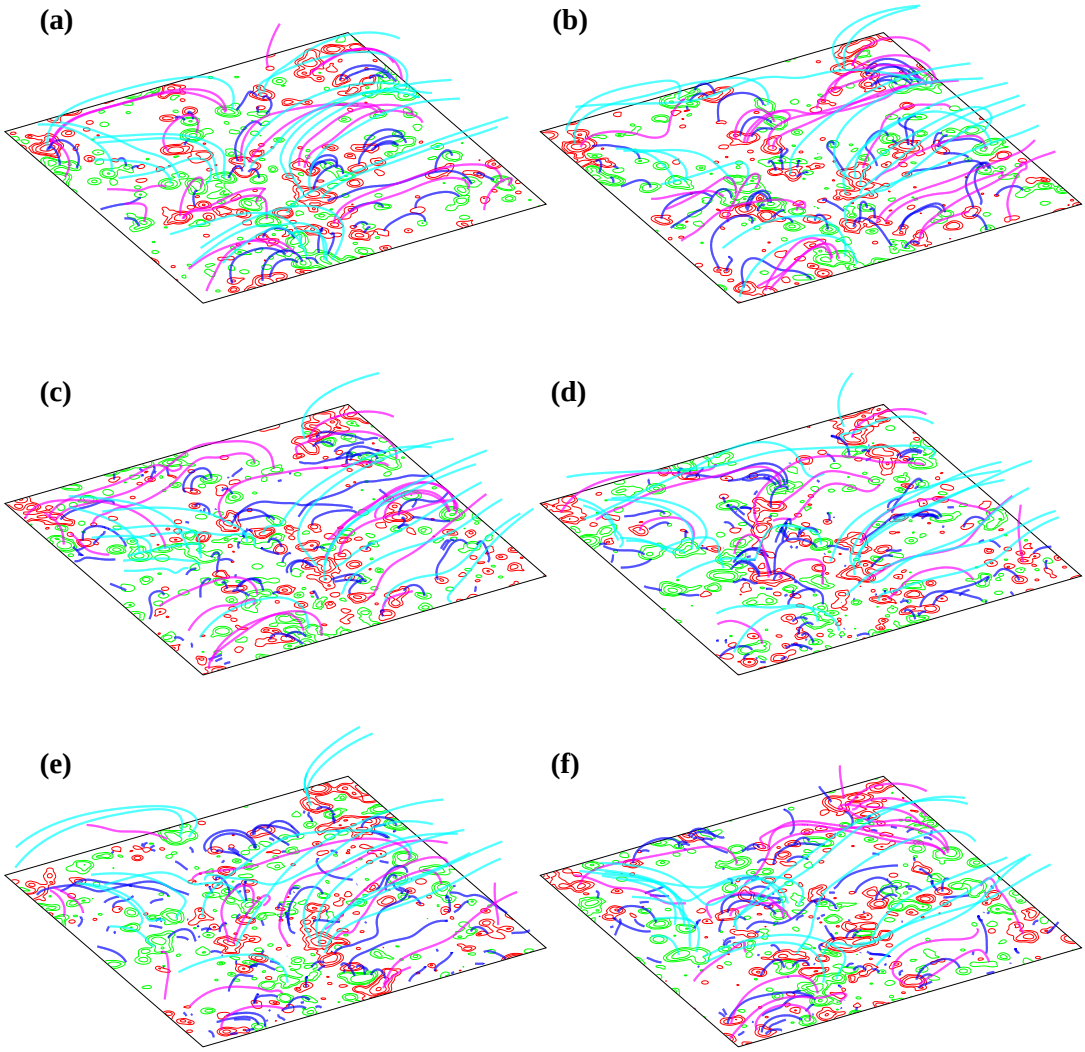

Figure 5.4: Coronal field images for the 3D simulation with a 3 G overlying field, for the same magnetograms as shown in Figure 5.1. Red contours represent positive magnetic field, green contours represent negative. A selection of coronal magnetic field lines is shown in each case, coloured as follows: dark blue field lines reach heights of 2.5 Mm or less, magenta field lines between $2.5 - 5$ Mm and pale blue field lines above 5 Mm. (a) $t = 120$ hr, (b) $t = 128$ hr, (c) $t = 136$ hr, (d) $t = 144$ hr, (e) $t = 152$ hr, and (f) $t = 160$ hr.

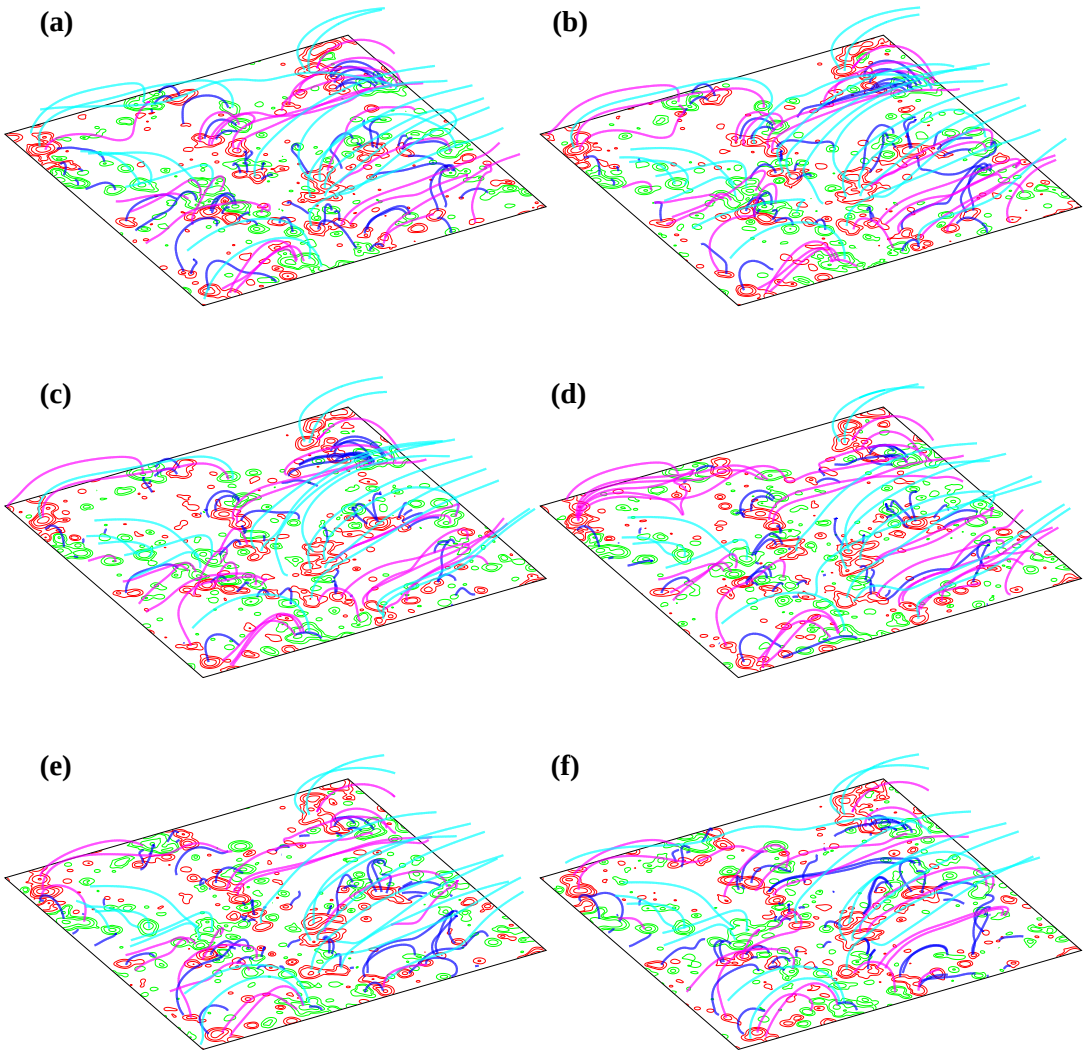

Figure 5.5: Coronal field images for the 3D simulation with a 3 G overlying field. Red contours represent positive magnetic field, green contours represent negative. A selection of coronal magnetic field lines is shown in each case, coloured as follows: dark blue field lines reach heights of 2.5 Mm or less, magenta field lines between $2.5 - 5$ Mm and pale blue field lines above 5 Mm. (a) $t = 128$ hr, (b) $t = 128.17$ hr, (c) $t = 128.33$ hr, (d) $t = 128.5$ hr, (e) $t = 128.67$ hr, and (f) $t = 128.83$ hr.

5.2 Field Lines

Figures 5.3 and 5.4 each show a series of images from the 3D simulations. Figure 5.3 shows the 0 G case, while Figure 5.4 shows the 3 G overlying field case. In both figures, images (a)−(f) are shown at the same times as the synthetic magnetograms in Figure 5.1, spaced 8 hr apart. The red and green contours represent positive and negative photospheric magnetic field. A selection of field lines is plotted on each image, where dark blue field lines have a maximum height of up to 2.5 Mm, magenta field lines reach a maximum height of between $2.5 - 5$ Mm and pale blue field lines reach above 5 Mm. At each time, the coronal field lines shown in Figure 5.3 are plotted from the same starting points as those in Figure 5.4. In both cases, image (a) shows the initial potential field, while subsequent images show the non-potential fields produced by a continuous evolution of the coronal field in response to photospheric boundary motions. One can see that in the 0 G case, field lines originating from the photosphere may reach much higher heights than in the 3 G case, as they are not suppressed by an overlying field. In the 3 G case, the overlying field has caused many of the field lines to be aligned in the $x-$direction. In both the 0 G and 3 G cases, it can be seen that the connectivity between the magnetic elements changes significantly throughout the simulation, with no coherent pattern from one image to the next. This shows that the coronal field is changing significantly within this time period. In Figure 5.5, another series of images from the 3 G simulation are shown, this time spaced only 10 min apart, from $t = 128 - 128.83$ hr. Again, a selection of field lines is plotted on each image, coloured as in Figures 5.3 and 5.4. For this shorter period of only 50 min, some difference is seen in the connectivity between the magnetic elements. It is clear that connectivity is maintained from one step to the next during the magnetofrictional coronal evolution. Figures 5.3−5.5 are intended only to give an indication of what the connectivity is like between the magnetic elements. A more in depth topological analysis will be carried out in future.

5.3 Free Magnetic Energy

The presence of free magnetic energy within our 3D models is a significant difference from the models discussed in Chapter 2, as previous models for the magnetic carpet coronal field are potential field models and hence do not contain free magnetic energy. Figure 5.6(a) shows a plot of the free magnetic energy (ergs) as a function of time, as computed by

$$E_{\mathrm{f}}(t) = W_{\mathrm{nl}}(t) - W_{\mathrm{p}}(t) = \int_V \frac{B_{\mathrm{nl}}^2 - B_{\mathrm{p}}^2}{8\pi} dV, \tag{5.1}$$

where $\mathbf{B}_{\mathrm{nl}}$ is the magnetic field of the non-linear force-free field and $\mathbf{B}_{\mathrm{p}}$ is the magnetic field of the corresponding potential field. Results are shown for the 0 G (green), 1 G (black), 3 G

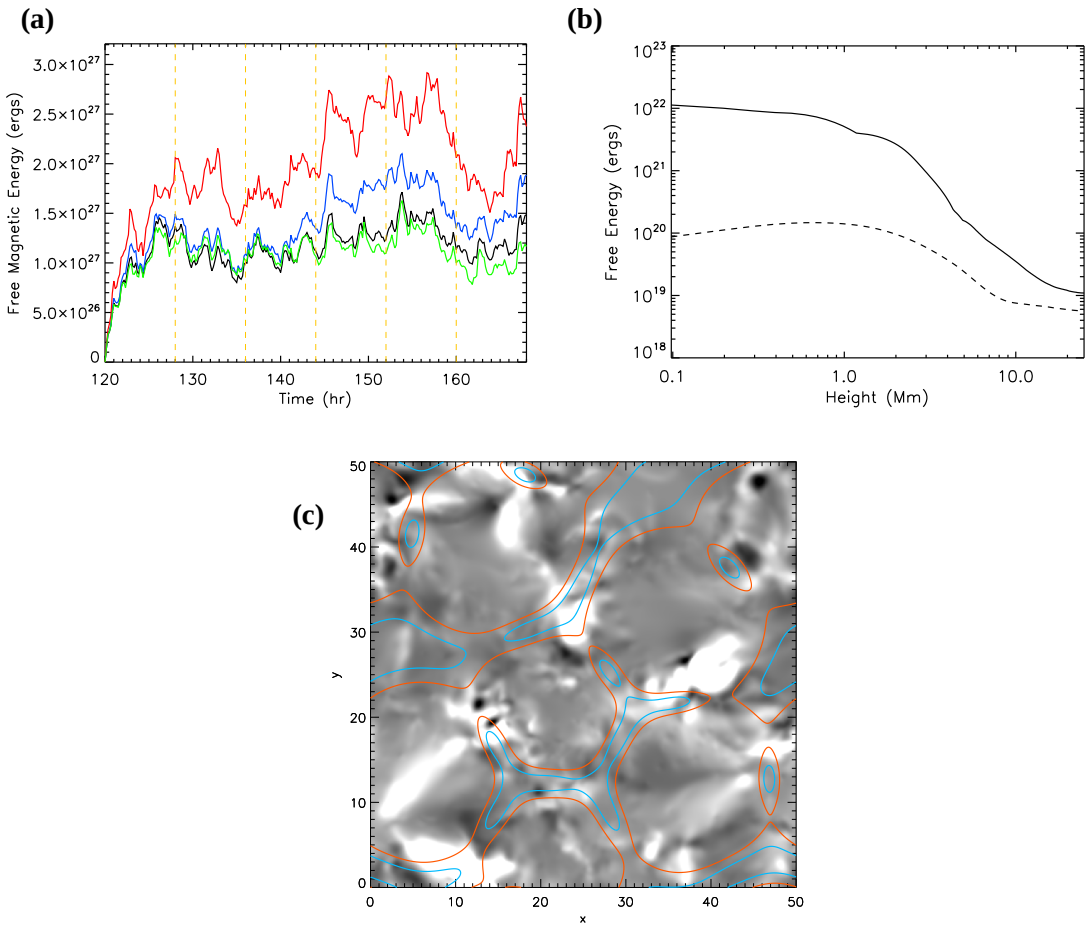

Figure 5.6: (a) Free magnetic energy as a function of time for the 3D simulations with a 0 G (green), 1 G (black), 3 G (blue) and 10 G (red) overlying field. (b) Maximum (solid) and average (dashed) free magnetic energy as a function of height, at $t = 128$ hr in the 3 G simulation. (c) Free magnetic energy density integrated in z, for the 3 G overlying field simulation. The image is shown at $t = 128$ hr, in the $x - y$ plane, saturated at $\pm 1.9 \times 10^{22}$ ergs. White regions are where the free energy density is positive ($B_{\rm nl}^2 > B_{\rm p}^2$), black regions are where the free energy density is negative ($B_{\rm nl}^2 < B_{\rm p}^2$). Contours of $v_{\rm sg}^2 = 0.19$ km^2 s^{-2} and $v_{\rm sg}^2 = 0.1$ km^2 s^{-2} are shown in yellow and blue respectively, to indicate the location of the magnetic network. (Low velocity regions at the supergranule cell centres are omitted).

Simulation (B_0)	Mean Free Magnetic Energy ($\times 10^{27}$ ergs)	Maximum Free Magnetic Energy ($\times 10^{27}$ ergs)
0 G	1.09	1.63
1 G	1.16	1.71
3 G	1.39	2.10
10 G	1.96	2.92

Table 5.1: Mean and maximum values of free magnetic energy for each simulation.

(blue) and 10 G (red) simulations. For each simulation, the free energy first rapidly increases as the coronal field diverges from a potential state due to surface motions. For the 0 G and 1 G cases, the free energy then levels off and oscillates around a mean value of 1.09×10^{27} ergs and 1.16×10^{27} ergs respectively. For the 3 G and 10 G cases, the free energy also levels off to a lower extent, but is less steady. The mean and maximum values of free energy for each simulation are given in Table 5.1. The trend is that a stronger overlying field leads to a greater build-up of free energy. While this is the case, and individual peaks in free energy may differ slightly between the simulations, the general shape of the curve is the same for all four strengths of overlying field. Therefore the overall behaviour of the free magnetic energy is largely dependent on the evolution of the photospheric magnetic field, rather than that of the overlying coronal field.

Figure 5.6(b) shows a plot of the maximum (solid line) and average (dashed line) free magnetic energy (ergs) as a function of height, at $t = 128$ hr in the 3 G simulation. These values are for the maximum and average free magnetic energy in a grid cell ((0.098 Mm)^3) at each height. The average free magnetic energy as a function of height is computed as follows:

$$E_{\mathrm{f}}(z) = \frac{Lz}{N} \int_{y_{\mathrm{min}}}^{y_{\mathrm{max}}} \int_{x_{\mathrm{min}}}^{x_{\mathrm{max}}} \frac{B(x,y,z)_{\mathrm{nl}}^2 - B(x,y,z)_{\mathrm{p}}^2}{8\pi} dxdy,$$

where $x_{\mathrm{min}} = y_{\mathrm{min}} = 0$ Mm, $x_{\mathrm{max}} = y_{\mathrm{max}} = 50$ Mm, $Lz = 0.098$ Mm is the length of a cell in z, $N = (nx)(ny)$ and $nx = ny = 512$ are the number of grid cells in the $x-$ and $y-$directions. It can be seen that the maximum free magnetic energy is found low down. The average free energy peaks higher up, around $z = 0.7$ Mm. Although a plot is shown here at only one time, and for just one strength of the overlying field, similar results are found at all times and for all overlying field strengths. The only difference is that the curve will be shifted up or down. The maximum free energy is found close to the photosphere as this is where the evolution of the coronal field is driven by footpoint motions, resulting in the largest departure of the field from a potential state. However, we will see later (Figure 5.7) that in total, the largest amount of free magnetic energy is found further up, between $z = 0.5$ Mm and $z = 0.8$ Mm.

Figure 5.6(c) shows the free magnetic energy density, $\frac{B_{\mathrm{nl}}^2 - B_{\mathrm{p}}^2}{8\pi}$, integrated in z, in the $x - y$

plane. This is computed as follows:

$$E_{\mathrm{f}}(x,y) = A \int_{z_{\mathrm{min}}}^{z_{\mathrm{max}}} \frac{B(x,y,z)_{\mathrm{nl}}^2 - B(x,y,z)_{\mathrm{p}}^2}{8\pi} dz,$$

where $A = Lx\ Ly$, $Lx = 0.098$ Mm is the length of a cell in x and $Ly = 0.098$ Mm is the length of a cell in y. The image is taken from the 3 G simulation, at $t = 128$ hr. White patches indicate where the free energy density is positive, i.e. where $B_{\mathrm{nl}}^2 > B_{\mathrm{p}}^2$. Black patches are locations where the free energy density is negative, $B_{\mathrm{nl}}^2 < B_{\mathrm{p}}^2$. Contours of the velocity profile of the underlying supergranules, v_{sg}, are overplotted at levels of $v_{\mathrm{sg}}^2 = 0.19$ km^2 s^{-2} (yellow) and $v_{\mathrm{sg}}^2 = 0.1$ km^2 s^{-2} (blue) to indicate where supergranular velocities are lowest.[1] The contours denote where the magnetic network forms. We define free magnetic energy to be 'stored' at locations where the line-of-sight integrated free magnetic energy density is positive. From this image, it can be seen that free magnetic energy may be stored both at the boundaries between supergranular cells and within the cells themselves.

Figure 5.7 shows plots of the total free magnetic energy (ergs) integrated in x and y, as a function of height, for the simulations with a 0 G (top), 1 G (middle) and 3 G (bottom) overlying field. This is computed as follows:

$$E_{\mathrm{f}}(z) = Lz \int_{y_{\mathrm{min}}}^{y_{\mathrm{max}}} \int_{x_{\mathrm{min}}}^{x_{\mathrm{max}}} \frac{B(x,y,z)_{\mathrm{nl}}^2 - B(x,y,z)_{\mathrm{p}}^2}{8\pi} dx dy.$$

The left hand column shows the free energy near the start of the simulation, at $t = 120.17$ hr (black), $t = 121.0$ hr (blue), $t = 121.83$ hr (red), $t = 122.67$ hr (green), $t = 123.5$ hr (yellow) and $t = 124.33$ hr (purple). In each case, the black line is significantly lower than the others. This is because at $t = 120.17$ hr, only 10 min into the simulation, the coronal magnetic field is still close to a potential state. Therefore there is less free magnetic energy within the volume. At later times, however, the lines are not ordered according to time, although a similar trend of the colours relative to one another can be seen for different strengths of the overlying field. The right hand column of Figure 5.7 shows the total free magnetic energy (ergs) as a function of height at times spaced evenly throughout the simulations, at $t = 128$ hr (black), $t = 136$ hr (blue), $t = 144$ hr (red), $t = 152$ hr (green), $t = 160$ hr (yellow) and $t = 168$ hr (purple). Within Figure 5.6(a), which shows the total free magnetic energy as a function of time, vertical yellow dashed lines are overplotted on the graph at intervals of 8 hr, indicating the times at which the plots in the right hand column of Figure 5.7 are taken. Again, it can be seen that the ordering of the lines is not time dependent. Once the coronal field has evolved away from its initial potential state, the total amount of free magnetic energy within the volume depends upon how much is both built up and stored due to surface motions. For each of the curves in Figure 5.7, there is a peak

[1] The supergranular velocities are also low at the centres of the cells, where upflow would be observed on the Sun. These locations are omitted from the image.

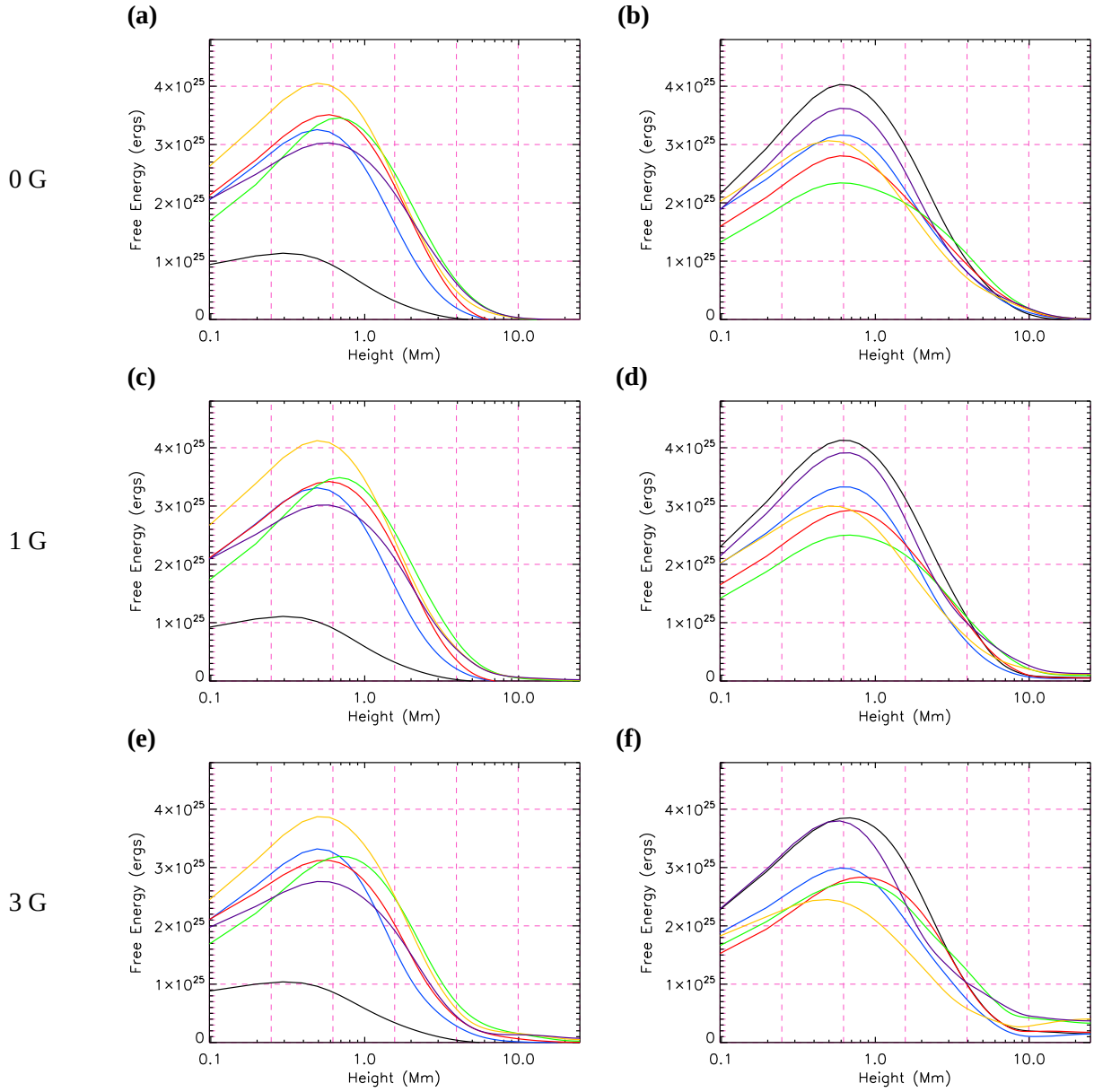

Figure 5.7: Total free magnetic energy as a function of height, for the simulation with a (a) and (b) 0 G, (c) and (d) 1 G, (e) and (f) 3 G overlying field. For plots (a), (c) and (e), the curves show the free energy at $t = 120.17$ hr (black), $t = 121.0$ hr (blue), $t = 121.83$ hr (red), $t = 122.67$ hr (green), $t = 123.5$ hr (yellow) and $t = 124.33$ hr (purple). For plots (b), (d) and (f), the curves show the free energy at $t = 128$ hr (black), $t = 136$ hr (blue), $t = 144$ hr (red), $t = 152$ hr (green), $t = 160$ hr (yellow) and $t = 168$ hr (purple). A movie of the full time series for the 3 G case is given on the CD, named magnet48b_free_ht.mpg.

between roughly $z = 0.5$ Mm and $z = 0.8$ Mm, indicating that this is where the majority of the free magnetic energy is stored. The free energy then drops of rapidly after $z = 1$ Mm. As in Chapter 4, we find that the field departs most from a potential state low down in the corona, as this is close to where we are driving the evolution of the field by photospheric motions. In addition, most closed connections between magnetic elements are found to be low lying (e.g. Close et al. (2003)), and it is along these connections that free energy is stored. A movie showing the time evolution of the free magnetic energy as a function of height for the 3 G simulation is included on the CD, named magnet48b_free_ht.mpg. The movie shows that the free energy is highly dynamic and rapidly evolving. The height of the curve is continually changing, however it can be seen that the peak in the curve tends to remain between $z = 0.5$ Mm and $z = 0.8$ Mm.

Figure 5.8 shows a series of six images from the 3 G simulation, spaced 8 hr apart between $t = 128$ hr and $t = 168$ hr. As in Figure 5.6(c), the images show the free magnetic energy density in the $x - y$ plane, integrated in z, with contours of $v_{\rm sg}^2$ overplotted to indicate the location of the supergranule cell boundaries. Also overplotted are contours of B_z at the photosphere, where red and green contours represent positive and negative magnetic field. Although images are shown here only for the 3 G simulation, similar results are found for the other simulations. In Chapter 4, it was found that when the magnetic elements disturbed a larger volume of the overlying field, a greater amount of free energy was built up. It was also found that closed connections between the magnetic elements are required, along which the free energy may be stored. In agreement with Chapter 4, we find that free energy is stored mainly in two locations. Firstly, we see that white patches are located around supergranule cell boundaries where the magnetic network is formed. Large numbers of magnetic elements are swept to these locations by supergranular flows, and continually interact with one another, cancelling, coalescing and fragmenting. This continual evolution of the magnetic elements results in a large build up of free energy, which may then be stored along the multiple connections that form between nearby magnetic elements that lie in the network. The second location where we see free energy stored is along long-lived, far-reaching, twisted connections between magnetic elements. Such connections may stretch across supergranule cells, between magnetic elements located at opposite boundaries (examples of this will be given later, in Figure 5.10). Longer connections will clearly disturb a larger volume of the surrounding coronal magnetic field, hence building up free energy. The regions of positive free magnetic energy density are highly dynamic, with no clear pattern from one 8 hr period to the next.

Figure 5.9 shows another series of six images from the 3 G simulation, this time spaced just 1 hr apart between $t = 128$ hr and $t = 133$ hr. This series of images gives an impression of the lifespan of some typical regions of positive free magnetic energy density. Regions can be seen forming and disappearing. Some regions are long-lived, lasting for several hours. For example, at $t = 128$ hr (Figure 5.9(a)), a large band of positive free energy density can be seen across the

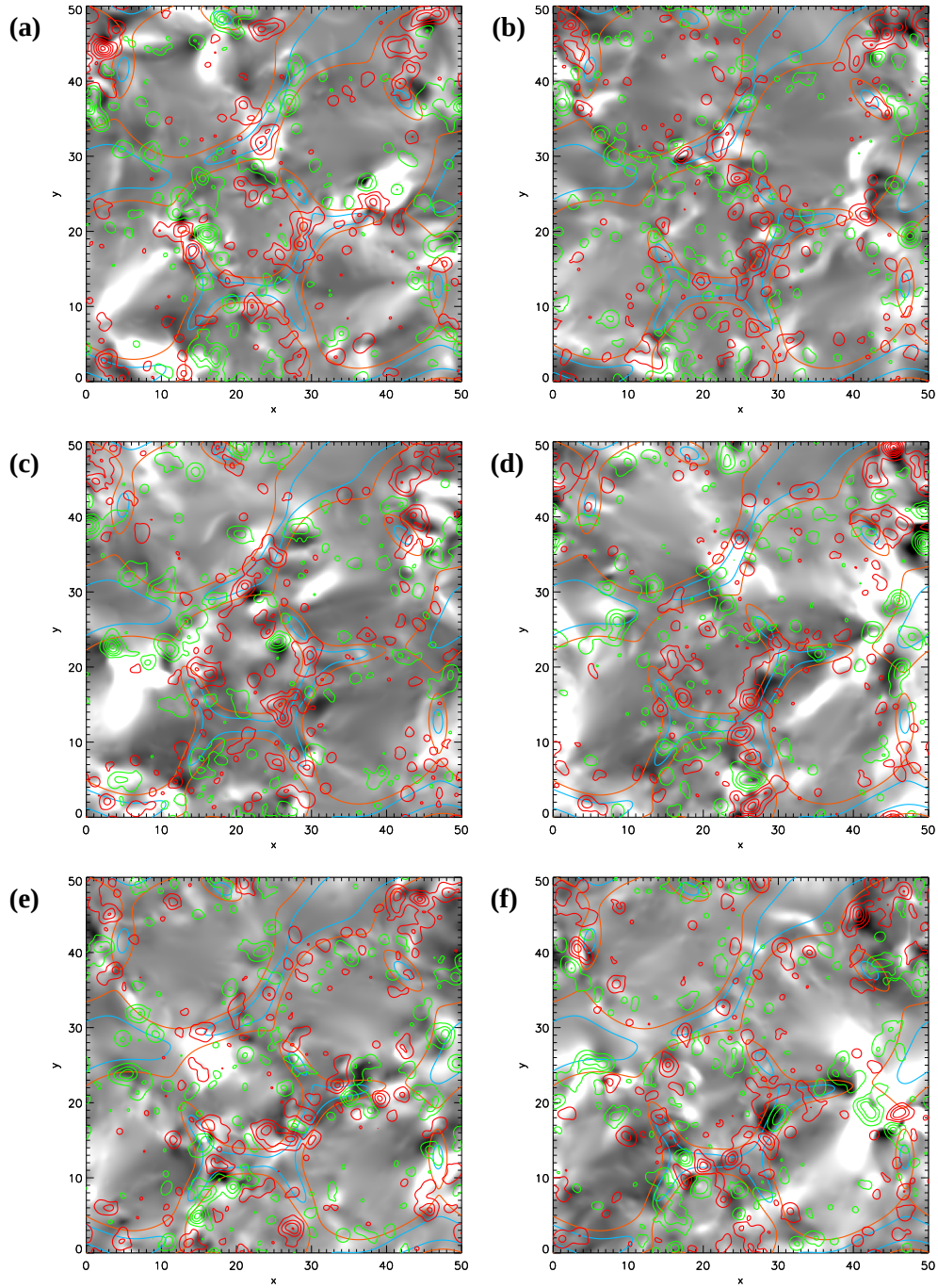

Figure 5.8: Free magnetic energy density integrated in z, for the 3 G overlying field simulation. The images are shown in the $x - y$ plane, saturated at $\pm 1.9 \times 10^{22}$ ergs. The images are white in regions where the free energy density is positive, black where the free energy density is negative. Contours of $v_{\rm sg}^2 = 0.1$ km^2 s^{-2} and $v_{\rm sg}^2 = 0.19$ km^2 s^{-2} are shown, coloured as in Figure 5.6. Contours of B_z at $z = 0$ Mm are also overplotted, where red contours represent positive magnetic field and green contours represent negative, at levels of $\pm[7, 13, 27, 53, 106]$ G. The images are shown at (a) $t = 128$ hr, (b) $t = 136$ hr, (c) $t = 144$ hr, (d) $t = 152$ hr, (e) $t = 160$ hr and (f) $t = 168$ hr. A movie of the full time series, magnet48b_free_xy_bz.mpg, is given on the CD.

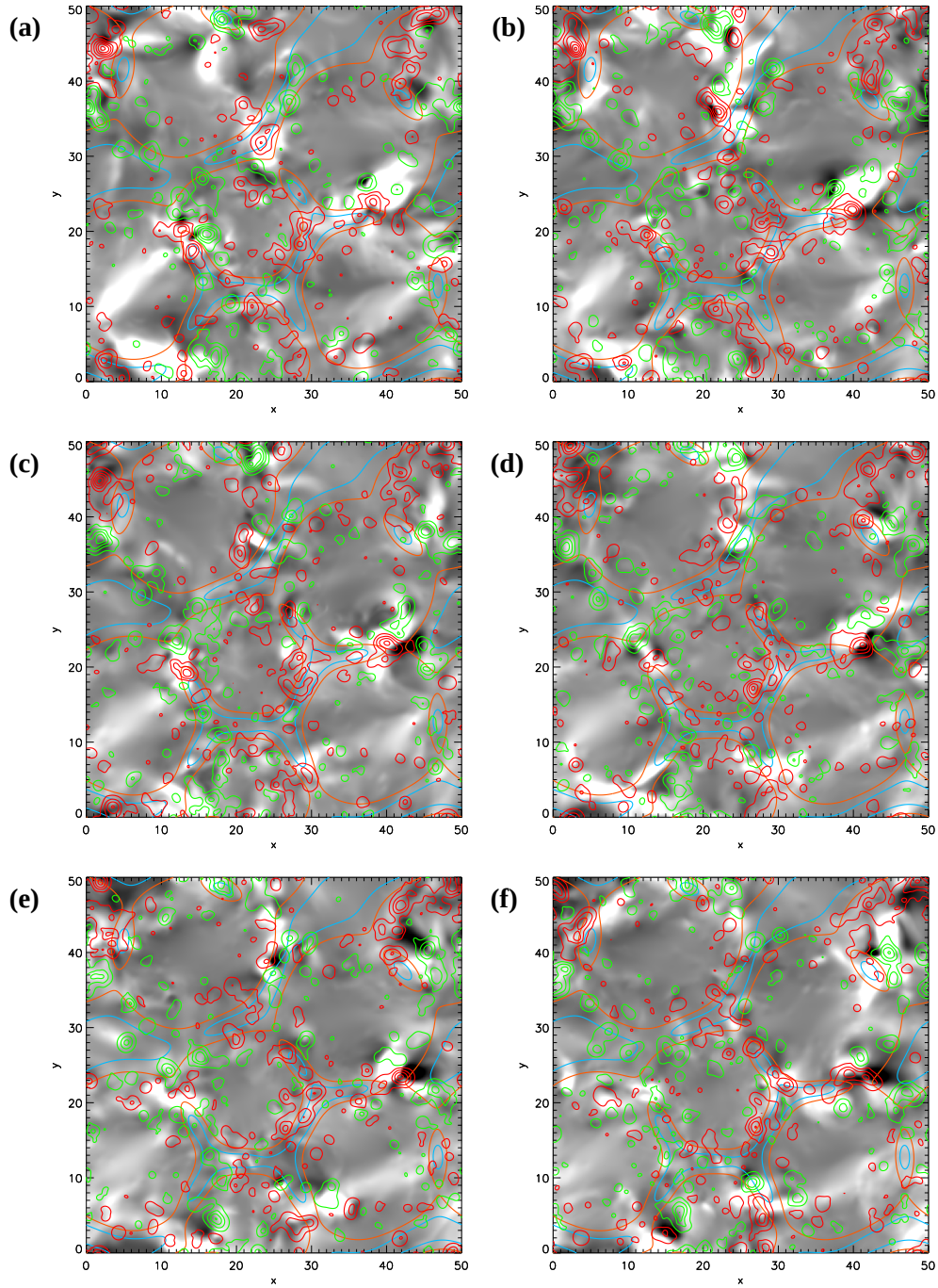

Figure 5.9: Free magnetic energy density integrated in z, for the 3 G overlying field simulation. The images are shown in the $x - y$ plane, saturated at $\pm 1.9 \times 10^{22}$ ergs. The images are white in regions where the free energy density is positive, black where the free energy density is negative. Contours of $v_{\rm sg}^2 = 0.1$ km^2 s^{-2} and $v_{\rm sg}^2 = 0.19$ km^2 s^{-2} are shown, coloured as in Figure 5.6. Contours of B_z at $z = 0$ Mm are also overplotted, where red contours represent positive magnetic field and green contours represent negative, at levels of $\pm[7, 13, 27, 53, 106]$ G. The images are shown at (a) $t = 128$ hr, (b) $t = 129$ hr, (c) $t = 130$ hr, (d) $t = 131$ hr, (e) $t = 132$ hr and (f) $t = 133$ hr. A movie of the full time series, magnet48b_free_xy_bz.mpg, is given on the CD.

lower-left supergranule. This band becomes fainter with increasing time, but can still be seen five hours later (Figure 5.9(f)). There is also a long-lived region of positive free energy density that lies in the magnetic network at roughly $x = 35 - 45$ Mm, $y = 22 - 30$ Mm. This region can be seen in all six of the images, although it shrinks from $t = 128 - 133$ hr. In addition to long-lived regions of positive free energy density, there are some that do not even last one hour. In contrast to these long-lived examples, at $t = 129$ hr (Figure 5.9(b)), a region of positive free energy density can be seen around $x = 21 - 29$ Mm, $y = 37 - 46$ Mm; this region is not present in the images shown one hour before or after (Figures 5.9(a) and (c) respectively).

Three movies showing the free magnetic energy density in the $x - y$ plane for the 3 G simulation are included on the CD. All three show the free magnetic energy density integrated in z, and saturated at $\pm 1.9 \times 10^{22}$ ergs. The first movie (magnet48b_free_xy.mpg) shows just the line-of-sight integrated free magnetic energy density. The second (magnet48b_free_xy_bz.mpg) includes contours of B_z at the photosphere on top of the line-of-sight integrated free energy density, where red and green contours represent positive and negative magnetic field. The third movie (magnet48b_free_xy_nulls.mpg) includes the $x - y$ positions of coronal null points, overplotted in yellow. The locations of coronal null points within the simulations are computed using the nullfinder code of Haynes and Parnell (2007). Only null points of height $z = 0.5$ Mm or higher are shown, as a large number of photospheric nulls are found where $B_z = 0$ G at $z = 0$ Mm. Within the movies, one can see that the regions of positive free energy density are continually evolving in response to the photospheric motions, where occasional large patches of positive free energy density develop around the magnetic network. These occur where many large magnetic features are interacting with one another. One can also see long-lived bands of positive free energy density stretching across supergranules, between magnetic elements.

Figures 5.10(a) and (b) show two zoomed in sections of the $x - y$ plane images of the line-of-sight integrated free energy density taken at $t = 128$ hr and $t = 168$ hr respectively. A selection of closed field lines connecting between magnetic elements has been overplotted in blue in each case. Figure 5.10(a) shows the band of positive free energy density that can be seen lying across the lower left supergranule in Figure 5.8(a), while Figure 5.10(b) shows the band of positive free energy density across the lower right supergranule in Figure 5.8(f). In both zoomed in images, twisted magnetic field lines produced by surface braiding connect between various magnetic elements on either side of the supergranule. The free energy is stored along these connections. Figure 5.10(c) shows an $x - z$ plane image of free energy density integrated in y at $t = 128$ hr, and is a side view of the band of positive free energy density in Figure 5.10(a). Similarly, Figure 5.10(d) is a side view of the band of positive free energy density in Figure 5.10(b) and shows a $y - z$ plane image of free energy density integrated in x at $t = 168$ hr. For each of the cases, a complex structure of the field can be seen.

Figure 5.11 shows $x - z$ plane images of free magnetic energy density for the 3 G simulation.

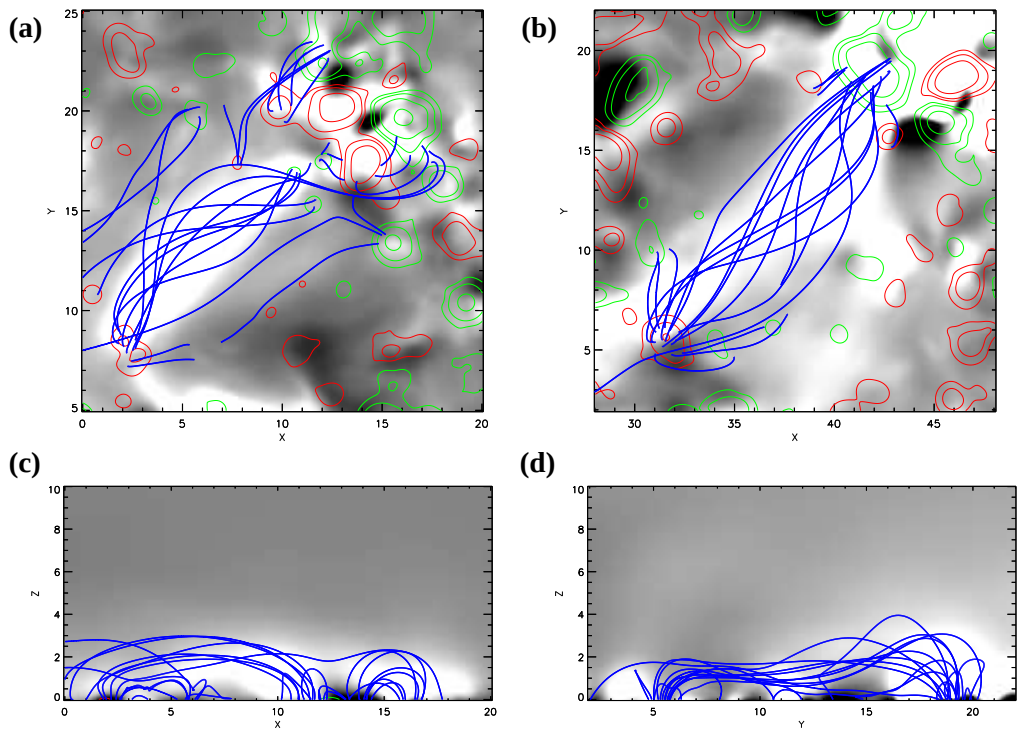

Figure 5.10: (a) and (b) Free magnetic energy density integrated in z, shown in the $x - y$ plane, for the 3 G overlying field simulation. The images are white in regions where the free energy density is positive, black where the free energy density is negative. Contours of B_z at $z = 0$ Mm are overplotted, where red contours represent positive magnetic field and green contours represent negative, at levels of $\pm[7, 13, 27, 53, 106]$ G. The images are shown at (a) $t = 128$ hr and (b) $t = 168$ hr. (c) Free magnetic energy integrated in y, shown in the $x - z$ plane at $t = 128$ hr. (d) Free magnetic energy density integrated in x, shown in the $y - z$ plane at $t = 168$ hr. A selection of field lines is overplotted in blue on each image.

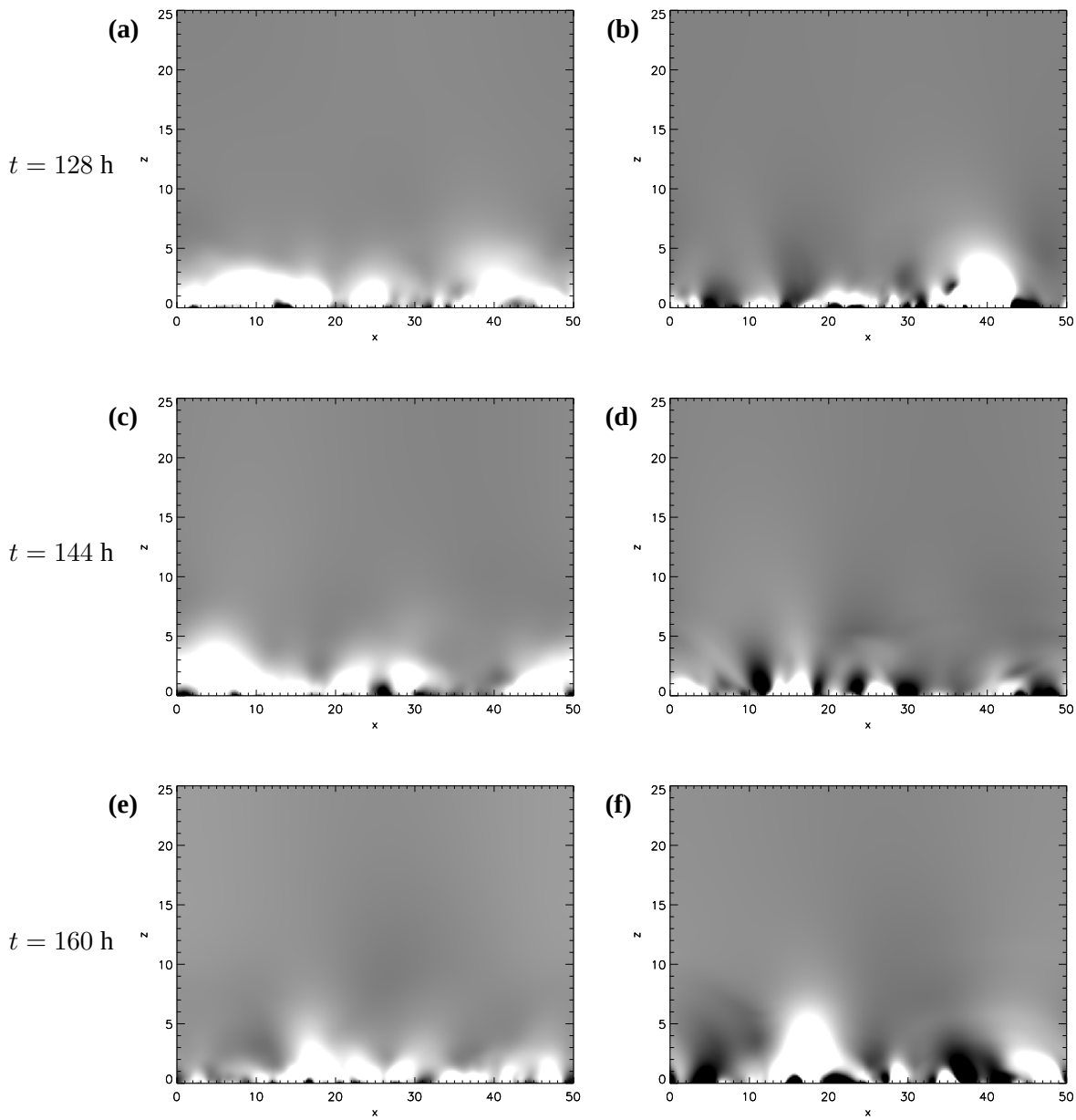

Figure 5.11: (a), (c) and (e) free magnetic energy density integrated in y, for the 3 G overlying field simulation. The images are shown in the $x - z$ plane, saturated at $\pm 4.8 \times 10^{22}$ ergs. (b), (d) and (f) free magnetic energy density shown in the $x - z$ plane at $y = 25$ Mm, saturated at $\pm 1.9 \times 10^{20}$ ergs. The images are white in regions where the free energy density is positive, black where the free energy density is negative. The images are shown at (a) and (b) $t = 128$ hr, (c) and (d) $t = 144$ hr, (e) and (f) $t = 160$ hr. A movie of the full time series for images (a), (c) and (e) is given on the CD, named magnet48b_free_xz.mpg.

The left-hand column shows images of the line-of-sight integrated free energy density, saturated at $\pm 4.8 \times 10^{22}$ ergs. The right-hand column shows the free energy density in the $x - z$ plane, within the plane at $y = 25$ Mm, saturated at $\pm 1.9 \times 10^{20}$ ergs. The images are taken at (a) and (b) $t = 128$ hr, (c) and (d) $t = 144$ hr, (e) and (f) $t = 160$ hr. It can be seen that the free energy is mainly located low down, where many closed connections exist between the magnetic elements and a larger departure of the magnetic field from a potential state is found. For the time period shown, the extension of the free energy into the corona is dynamic and is seen to vary significantly. Considering the images in the right-hand column, large, localised patches of black can be seen where $B_{\text{nl}}^2 < B_{\text{p}}^2$. In comparison, in the line-of-sight integrated images in the left-hand column, the free energy density is predominantly positive and any patches of black are very small. Therefore overall, as we would expect, the energy of the non-potential field is higher than that of the potential field (see Figure 5.6(a), the total free magnetic energy as a function of time). Movies of free magnetic energy density in the $x - z$ (magnet48b_free_xz_nulls.mpg) and $y - z$ (magnet48b_free_yz_nulls.mpg) planes in the 3 G simulation are included on the CD, where the free magnetic energy density is integrated in either the y or x direction respectively. The movies are saturated at $\pm 4.8 \times 10^{22}$ ergs, and coronal null points of height $z = 0.5$ Mm or greater are overplotted as yellow stars[2]. Note that in the movies, only the region $z = 0 - 15$ Mm is shown. As discussed previously, the free energy is mainly located low down, with the bulk of it being below $z = 3$ Mm. One can see the locations of positive free energy density are highly dynamic and there exist long-lived 'bulbs' of positive free energy density, where it is stored within the corona along closed connections between magnetic elements.

5.4 Energy Dissipated

In addition to the free magnetic energy stored within the system, we consider energy that is being continually dissipated due to the relaxation processes within the corona. This is described by the heating term,

$$Q \equiv \frac{B^2}{4\pi}(\nu|\mathbf{v}|^2 + \eta_4|\nabla\alpha|^2). \tag{5.2}$$

This equation may be split into two components:

$$Q_{\text{frc}} = \frac{B^2}{4\pi}\nu|\mathbf{v}|^2 \quad \text{and} \quad Q_{\text{hd}} = \frac{B^2}{4\pi}\eta_4|\nabla\alpha|^2.$$

The first term, Q_{frc}, represents energy dissipation due to magnetofriction, which is released as the coronal magnetic field relaxes towards a force-free state. The second term, Q_{hd}, represents energy dissipation due to hyperdiffusion. Figure 5.12(a) shows a plot of the rate of energy dissipation due to magnetofriction, $\int_V Q_{\text{frc}}\, dV$, as a function of time, for the 0 G (green), 1 G (black), 3 G

[2]Movies without null points are also included, named magnet48b_free_xz.mpg and magnet48b_free_yz.mpg.

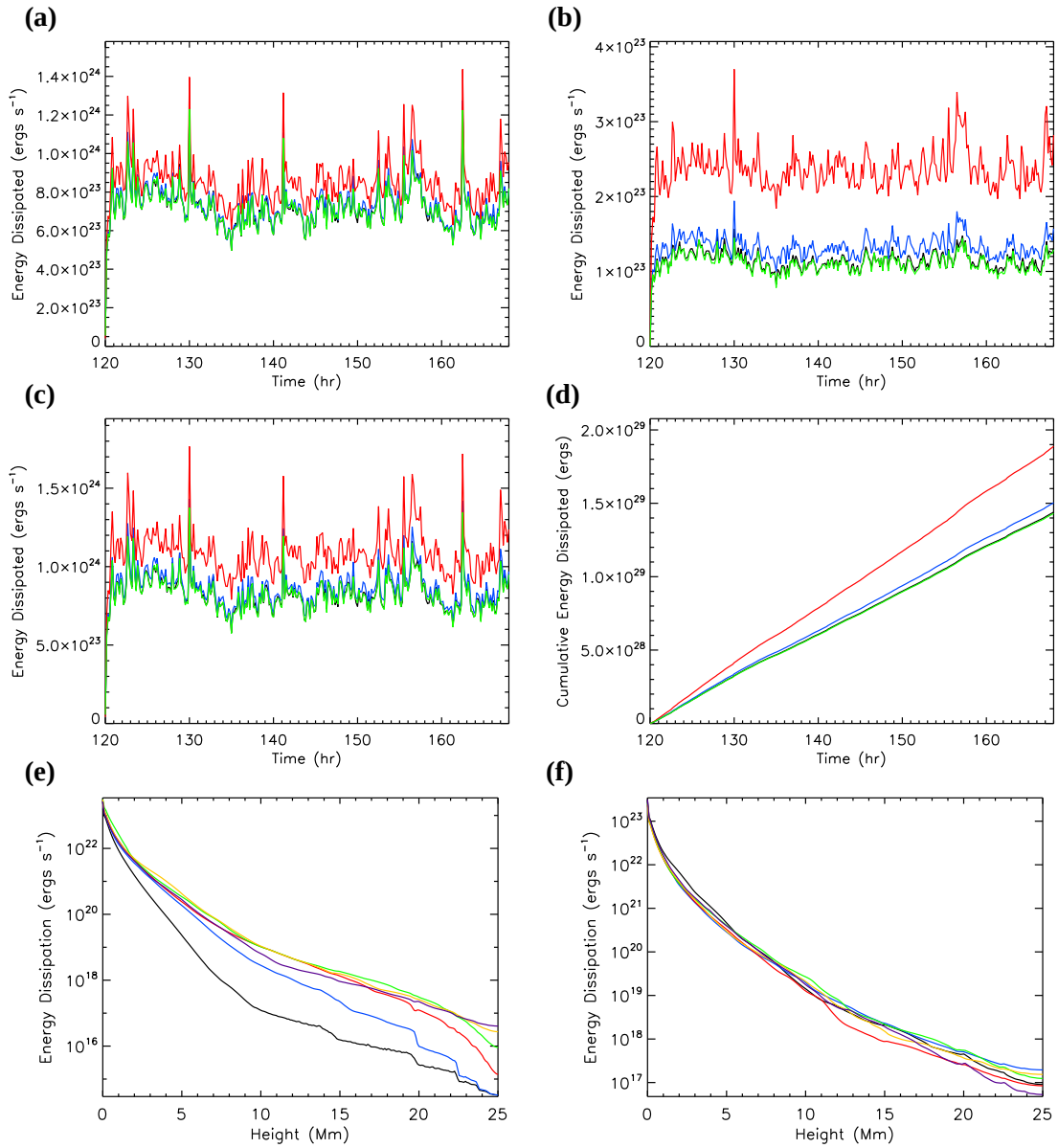

Figure 5.12: Energy dissipated as a function of time for the 3D simulations with a 0 G (green), 1 G (black), 3 G (blue) and 10 G (red) overlying field. (a) Rate of energy dissipation due to magnetofriction, $\int_V Q_{\rm frc}\, dV$, (b) rate of energy dissipation due to hyperdiffusion, $\int_V Q_{\rm hd}\, dV$, and (c) total rate of energy dissipation, $\int_V Q\, dV$. (d) Cumulative energy dissipated as a function of time, $E_{\rm d}(t)$. (e) Rate of energy dissipation (integrated in x and y) as a function of height for the 3 G simulation. The curves show the energy dissipation rate at $t = 120.17$ hr (black), $t = 121.0$ hr (blue), $t = 121.83$ hr (red), $t = 122.67$ hr (green), $t = 123.5$ hr (yellow) and $t = 124.33$ hr (purple). (e) Rate of energy dissipation (integrated in x and y) as a function of height for the 3 G simulation. The curves show the energy dissipation rate at $t = 128$ hr (black), $t = 136$ hr (blue), $t = 144$ hr (red), $t = 152$ hr (green), $t = 160$ hr (yellow) and $t = 168$ hr (purple). A movie of the full time series for plots (e) and (f) is given on the CD, named magnet48b_q_ht.mpg.

B_0	Q_{frc} ($\times 10^{23}$ ergs s^{-1})		Q_{hd} ($\times 10^{23}$ ergs s^{-1})		Q ($\times 10^{23}$ ergs s^{-1})		$\int\int_V Q dV dt$
	Mean	Maximum	Mean	Maximum	Mean	Maximum	($\times 10^{29}$ ergs)
0 G	7.15	12.31	1.11	1.45	8.25	13.75	1.43
1 G	7.16	12.42	1.13	1.57	8.30	13.82	1.44
3 G	7.35	12.75	1.32	1.94	8.67	14.31	1.50
10 G	8.52	14.37	2.36	3.70	10.89	17.67	1.89

Table 5.2: Mean and maximum values of Q_{frc}, Q_{hd} and Q integrated over the volume, and cumulative energy dissipated for each simulation.

(blue) and 10 G (red) simulations. It can be seen that Q_{frc} is not strongly dependent on overlying field strength. A stronger overlying field leads to slightly higher Q_{frc}, but the variation of values of Q_{frc} within each curve is much larger than the variation of values between the curves for different overlying field strengths. Table 5.2 shows the mean and maximum values of Q_{frc} for each overlying field strength. The difference in mean values between the 0 G and 10 G cases is just 1.4×10^{23} ergs s^{-1}. However, from the plot in Figure 5.12(a), each curve has a variation of around $7 - 8 \times 10^{23}$ ergs s^{-1} between its maximum and minimum. Therefore, the energy dissipation due to magnetofriction is predominantly dependent upon the evolution of the photospheric magnetic field driving change within the coronal field.

Figure 5.12(b) shows the rate of energy dissipation due to hyperdiffusion, $\int_V Q_{\text{hd}}\, dV$, as a function of time, where lines are coloured as in Figure 5.12(a). Very little difference can be seen between the curves for the 0 G and 1 G cases. The 3 G case results in slightly higher Q_{hd}, while the 10 G case results in significantly higher Q_{hd} and larger variation in the values of Q_{hd} than in the 0 G or 1 G cases. While this is the case, the general shape of all of the curves are the same, implying that like Q_{frc}, Q_{hd} is strongly dependent on the evolution of the photospheric magnetic field driving changes within the coronal volume. However, it can also be seen that Q_{hd} is more dependent on the strength of the overlying field than Q_{frc}. The mean and maximum values for Q_{hd} for each strength of overlying field are given in Table 5.2. For each case, the mean values for Q_{hd} are $3.6 - 6.4$ times smaller than the mean values for Q_{frc}, and the maximum values for Q_{hd} are $3.8 - 8.5$ times smaller than the maximum values for Q_{frc}.

Figure 5.12(c) shows a plot of the total rate of energy dissipation, $\int_V Q\, dV$, as a function of time, with lines coloured as in Figure 5.12(a). Since throughout each simulation, Q_{frc} is larger than Q_{hd}, the curves for Q follow the same trend as those for Q_{frc}. A stronger overlying field leads to slightly higher Q, but the variation of Q within each curve ($8.0 - 9.8 \times 10^{23}$ ergs s^{-1}) is larger than the variation between the simulations with different overlying field strengths (2.6×10^{23} ergs s^{-1} difference between the mean values for the 0 G and 10 G cases). Therefore, the overall energy dissipation is determined mainly by the photospheric evolution of the magnetic field. The mean and maximum values of Q for each simulation are given in Table 5.2. Figure 5.12(d) shows the cumulative energy dissipated as a function of time, $E_{\text{d}}(t)$, for each strength of overlying field,

obtained by integrating Q over both the volume and time:

$$E_{\rm d}(t) = \int_0^t \left[\int_V Q dV \right] dt. \tag{5.3}$$

We see that a stronger overlying field leads to a greater cumulative amount of energy dissipated. The values for the total energy dissipated by the end of each simulation are given in Table 5.2.

Figures 5.12(a)−(d) consider the volume integrated rate of energy dissipation over the entire 3D simulation for each strength of overlying field. We now consider where Q is spatially located within individual frames of the 3 G simulation. Although results are presented here only for the 3 G simulation, similar results are found for other strengths of the overlying field. Figures 5.12(e) and (f) show the rate of energy dissipation (integrated in x and y) as a function of height, for the 3 G simulation. This is computed with units of ergs s^{-1} as follows:

$$E_{\rm q}(z) = Lz \int_{y_{\rm min}}^{y_{\rm max}} \int_{x_{\rm min}}^{x_{\rm max}} Q(x, y, z) dx dy.$$

Figure 5.12(e) shows the rate of energy dissipation near the start of the simulation, at $t = 120.17$ hr (black), $t = 121.0$ hr (blue), $t = 121.83$ hr (red), $t = 122.67$ hr (green), $t = 123.5$ hr (yellow) and $t = 124.33$ hr (purple). The line for $t = 120.17$ hr (black) is lowest, followed by the line for $t = 121.0$ hr (blue), as at these times the coronal field is still close to potential. At later times, there is less difference between the lines as a near steady rate of dissipation is reached. Figure 5.12(f) shows the rate of energy dissipation at 8 hr intervals throughout the 3 G simulation, at $t = 128$ hr (black), $t = 136$ hr (blue), $t = 144$ hr (red), $t = 152$ hr (green), $t = 160$ hr (yellow) and $t = 168$ hr (purple). One can see that there is very little difference between the lines, even with 8 hr between them. This suggests that the total energy dissipation is roughly steady throughout the simulation as a result of the steady evolution of the total flux. At each time in Figures 5.12(e) and (f), the greatest rate of energy dissipation is found low down, near the photosphere. This is not surprising when we consider the equation describing Q (Equation 5.2). From this equation, Q is larger for stronger magnetic field, $\mathbf{B}$, larger velocities, $\mathbf{v}$, and higher gradients in α. The magnetic field is largest low down, near the magnetic sources. Considering Figures 5.12(e) and (f), we see that the rate of energy dissipation rapidly drops with increasing height, having decreased by more than an order of magnitude by $z = 2$ Mm. Therefore, the energy dissipation term Q has its largest effect close to the photosphere. The movie magnet48b_q_ht.mpg, included on the CD, shows the rate of energy dissipation as a function of height throughout the 3 G simulation. At the start of the movie, at greater heights, the rate of energy dissipation gradually increases until the curve becomes more or less steady. One can see occasional kinks in the curve at low z, which then propagate upward.

Figure 5.13 shows a series of six images of Q integrated in z, in the $x - y$ plane, from the 3

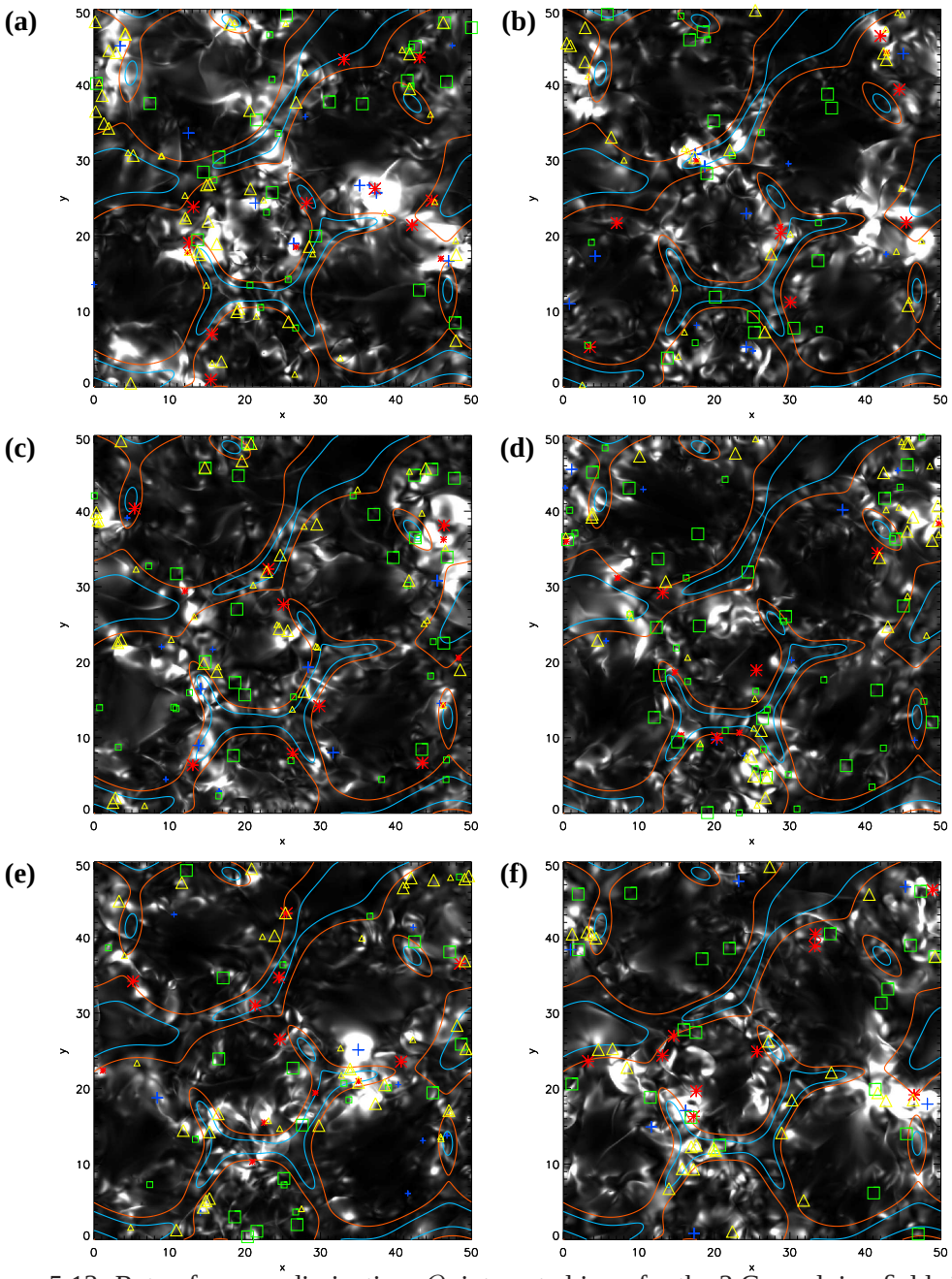

Figure 5.13: Rate of energy dissipation, Q, integrated in z, for the 3 G overlying field simulation. The images are shown in the $x-y$ plane, saturated at 1.5×10^5 ergs cm^{-2} s^{-1}. Contours of $v_{\rm sg}^2 = 0.1$ km^2 s^{-2} and $v_{\rm sg}^2 = 0.19$ km^2 s^{-2} are shown, coloured as in Figure 5.6. The occurrence of flux evolution processes are indicated by symbols representing emergence (blue $+$), cancellation (red $*$), coalescence (green $\square$) and fragmentation (yellow $\triangle$), where the process has occurred within the last 20 min (large symbols) or will occur within the next 20 min (small symbols). The images are shown at (a) $t = 128$ hr, (b) $t = 136$ hr, (c) $t = 144$ hr, (d) $t = 152$ hr, (e) $t = 160$ hr and (f) $t = 168$ hr. A movie of the full time series, magnet48b_q_xy.mpg, is given on the CD (without flux evolution processes).

Process	Colour	Symbol	Flux Threshold (Mx)	Explanation
Emergence	Blue	$+$	$\geq 4 \times 10^{17}$	Total absolute flux of bipole
Cancellation	Red	$*$	$\geq 4 \times 10^{17}$	Flux lost in cancellation
Coalescence	Green	$\square$	$\geq 6 \times 10^{17}$	Flux of newly formed element
Fragmentation	Yellow	$\triangle$	$\geq 6 \times 10^{17}$	Flux of original element

Table 5.3: Symbols and colours representing the flux evolution processes in Figure 5.13. Only events involving fluxes above the threshold flux values are overplotted.

G simulation. This is computed with units of ergs cm^{-2} s^{-1} as follows:

$$E_{\mathrm{q}}(x, y) = \int_{z_{\mathrm{min}}}^{z_{\mathrm{max}}} Q(x, y, z) dz.$$

The images are spaced 8 hr apart between $t = 128$ hr and $t = 168$ hr, and are saturated at a level of 1.5×10^5 ergs cm^{-2} s^{-1}. As in Figure 5.8, contours of v_{sg}^2 are overplotted to indicate the location of the boundaries between supergranules. One can see that Q is more localised than the free magnetic energy. Patches of Q tend to lie around the magnetic network, but not necessarily at the same locations as free magnetic energy as is seen in Figure 5.8. In addition, we do not see far-reaching bands of Q across the supergranules as we did with the free energy. In Chapter 4, it was determined that Q is mainly located at sites of changing magnetic topology and low down, near the magnetic elements. Therefore, it is unsurprising that in these simulations, Q is seen mainly at the magnetic network, as this is where large numbers of magnetic elements lie, and the magnetic topology is constantly changing due to the continual interaction of these elements with one another. We now consider where such interactions between magnetic elements occur, and attempt to relate them to nearby regions of energy dissipation.

Symbols representing each of the four flux evolution processes; emergence, cancellation, coalescence and fragmentation are overplotted on the images in Figure 5.13. Table 5.3 describes which process each symbol represents. Two sizes of symbol are plotted on the images for each flux evolution process. A large symbol indicates that the process is currently occurring or has occurred within the last 20 min of the simulation. A small symbol indicates that the process will occur within the next 20 min of the simulation. The reasoning behind this is that some events, such as cancellation, will influence the evolution of the coronal magnetic field before they have ‘occurred’, while others will continue to have an effect in the corona after they have ‘occurred’. To clarify, we define each of the processes to ‘occur’ at exact times as follows. An emergence occurs at the time when the bipole is first inserted into the simulation, with the two opposite polarity magnetic elements overlapping completely. A cancellation or coalescence occurs at the time when one or both of the magnetic elements is removed from the simulation due to partial or full cancellation or coalescence. A fragmentation occurs at the time when the original magnetic element first begins to split into two. Only processes that involve fluxes greater than a certain threshold are plotted, as

several hundred of each process occur within a 40 min time period. Since there are much fewer large magnetic elements than smaller ones (see flux power law of Parnell et al. (2009)), there are also much fewer occurrences of flux evolution processes between large magnetic elements than small ones. In addition, it is likely that processes involving larger fluxes will contribute more to energy dissipation (the heating term, Q, is dependent upon the size of $\mathbf{B}$), and are therefore of greater interest for us to consider.

A more detailed study would be required in order to say for certain exactly which processes lead to each localised burst of Q within the images in Figure 5.13. However, within the present chapter, we simply indicate a number of occurrences of flux evolution processes that seem likely to have contributed to a large patch of Q. Table 5.4 gives some examples of large emergences, cancellations, coalescences and fragmentations that occur within the 48 hr simulation[3]. The location of each of these may be seen in the images in Figure 5.13 at the corresponding time. Some regions of interest within the six images are as follows. At $t = 128$ hr (Figure 5.13(a)), a large emergence is occurring, of total absolute flux 35.8×10^{17} Mx, at $x = 37.4$ Mm, $y = 25.7$ Mm. A large region of Q can be seen around the location of this emergence, where at some points the rate of energy dissipation is greater than 3×10^5 ergs cm^{-2} s^{-1}, the required heating rate to maintain the quiet Sun corona (Withbroe and Noyes, 1977). A nearby emergence of 6×10^{17} Mx of flux and a cancellation removing 9.4×10^{17} Mx of flux are also likely to be contributing to the energy dissipation rate in this region. All three of these flux evolution events are listed in Table 5.4. At $t = 168$ hr (Figure 5.13(f)), an emergence of 12×10^{17} Mx of flux at $x = 16.2$ Mm, $y = 17.1$ Mm can be seen, with nearby cancellations removing fluxes of 5.6×10^{17} Mx and 4.2×10^{17} Mx. These events lie within a region of Q, which again reaches an energy dissipation rate of more than 3×10^5 ergs cm^{-2} s^{-1} in some places. Many more such examples can be seen within the six images.

While this is the case, there do not always appear to be large emergences or cancellations associated with a region of high Q. There are many events that could lead to a large amount of energy dissipation; some of these are discussed below. In some locations, we see a number of fragmentations occurring around a region of high energy dissipation, such as at $t = 152$ hr (Figure 5.13(d)) around $x = 24 - 28$ Mm, $y = 0 - 8$ Mm and at $t = 160$ hr (Figure 5.13(e)) around $x = 33 - 39$ Mm, $y = 18 - 23$ Mm. It is therefore possible that fragmentation could provide a significant contribution to Q. The coordinates of these fragmentations and other examples are given in Table 5.4. Another possibility is that a large number of small events, such as the emergence and cancellation of flux on the order of 10^{16} Mx, may contribute to Q, but by only considering larger flux here, we do not pick it up. We also know from Chapter 4, that a flyby between magnetic elements can both build up and dissipate a significant amount of energy. Flyby events will be occurring continually between magnetic elements within the simulation as they are

[3]For each of the processes given in Table 5.4, the process may be occurring any time from 20 min before to 20 min after the time given in the table.

Time (hr)	Process	x (Mm)	y (Mm)	Flux ($\times 10^{17}$Mx)
128	Emergence	37.4	25.7	35.8
		21.4	24.4	11.0
		26.4	19.0	8.0
		35.2	26.7	6.0
		3.5	45.2	5.8
	Cancellation	37.2	26.3	9.4
		42.1	21.4	7.4
		44.7	24.7	5.8
136	Emergence	17.5	30.8	25.8
		18.7	29.2	7.8
		24.2	5.3	4.4
	Cancellation	42.0	46.5	8.8
		45.4	21.8	7.8
144	Emergence	13.8	9.0	7.6
		14.1	16.5	4.2
	Cancellation	46.4	38.1	4.2
	Coalescence	46.8	33.9	9.1
		42.6	36.5	7.0
152	Emergence	1.1	45.5	5.4
	Fragmentation	25.2	4.9	15.1
		26.9	4.7	14.5
		24.9	7.5	12.4
		26.8	2.0	12.1
160	Emergence	35.0	25.1	14.0
	Coalescence	27.6	15.2	7.9
	Fragmentation	35.0	20.8	20.1
		38.5	20.5	8.7
		33.9	22.6	8.7
		37.3	18.0	6.9
168	Emergence	16.2	17.1	12.0
		45.3	46.7	10.0
		48.2	18.0	6.0
	Cancellation	48.9	46.3	7.2
		46.5	19.2	6.8
		17.6	19.7	5.6
		17.3	16.3	4.2
	Coalescence	41.3	19.9	6.4
	Fragmentation	42.7	18.4	12.9
		41.6	19.4	12.1

Table 5.4: A selection of emergences, cancellations, coalescences and fragmentations from the 48 hr series of synthetic magnetograms. For each process, the co-ordinates of its occurrence (x, y) are given, along with the total absolute flux emerged; lost through cancellation; coalescing or the flux of the original element fragmenting. The position of each of the processes listed can be seen in the image for the corresponding time in Figure 5.13.

swept past one another by supergranular flows, although it would be difficult to detect and track such events efficiently. From the six images in Figure 5.13, in general, coalescences do not appear to be related to regions of increased energy dissipation. However, several examples of coalescence are included in Table 5.4.

Three movies showing Q in the $x - y$ plane for the 3 G simulation are included on the CD. They show Q integrated in z, and saturated at 1.5×10^5 ergs cm^{-2} s^{-1}. The first (magnet48b_q_xy.mpg) shows just Q integrated in z. The second movie (magnet48b_q_xy_bz.mpg) shows Q integrated in z and includes contours of B_z at $z = 0$ Mm, with red and green contours representing positive and negative magnetic field. The third movie (magnet48b_q_xy_nulls.mpg) includes null points of height 0.5 Mm or greater as yellow stars. The movies show that the locations and evolution of Q are very different to those of the positive free magnetic energy density (magnet48b_free_xy.mpg). While many of the patches of positive free magnetic energy density were seen to be long-lived, regions of Q are seen to be very short-lived, occurring in rapidly evolving 'bursts'. Within the free energy density movie, patches of positive free energy density are often seen stretched across the supergranular cells, whereas Q tends to be much more localised, occurring predominantly within the magnetic network where large magnetic elements lie. This is consistent with the physical processes that lead to the dissipation of magnetic energy. Several large bursts of Q can be seen throughout the 48 hr period, in regions where many magnetic elements are emerging and interacting with one another. While some patches of Q are located around nulls, there are many locations of Q at which there are no null points. Such locations could, for example, be QSLs (Priest and Démoulin, 1995). Note that the evolution of Q that we see in these movies is dominated by Q low down, since the rate of energy dissipation rapidly decreases with increasing z (Figures 5.12(e) and (f)). We now consider the spatial location of Q further up in the corona.

Figures 5.14(a) and (b) show $x - y$ plane images of Q at $z = 3$ Mm in the 3 G simulation, at $t = 128$ hr and $t = 168$ hr respectively. Q at height z is given by $Q(x, y, z)\Delta z$. As in Figure 5.13, many patches of Q can be seen located above the boundaries between supergranules. However, in contrast to Figure 5.13, within Figures 5.14(a) and (b) one can also see much more fine-scale structure to Q when it is not integrated in the line of sight. Also in contrast to Figure 5.13, where Q integrated over z is predominantly located at the magnetic network, here we see long strands of Q which lie across the supergranules at $z = 3$ Mm. These are localised regions of energy dissipation that are found mainly at sites of changing magnetic topology. Figures 5.14(c) and (d) show the same $x - y$ plane images of Q at $z = 3$ Mm, with a selection of magnetic field lines overplotted in red. In several locations where the field lines encounter a patch of Q, one can see nested field lines or x shapes formed by sets of field lines with different connectivity. These indicate the presence of boundaries between distinct topological regions. At these locations, different sets of field lines may have very different values of α, and hence large gradients in α present. Figures 5.14(e) and (f) show $x - z$ plane images of Q at $y = 25$, also at $t = 128$ hr and $t = 168$ hr. The images show

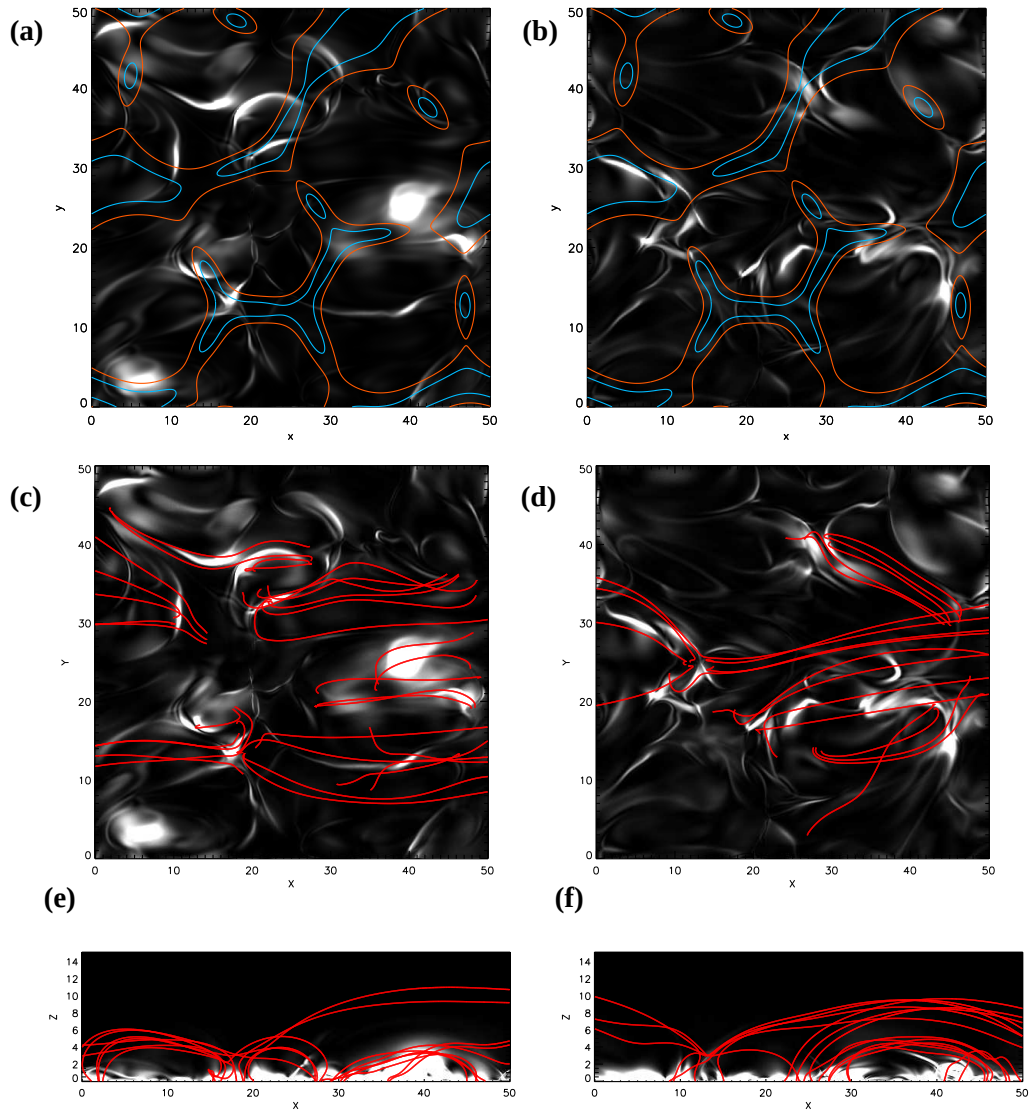

Figure 5.14: Rate of energy dissipation, Q, saturated at 810 ergs cm^{-2} s^{-1}, for the 3 G overlying field simulation. (a) and (b) are shown in the $x-y$ plane at $z = 3$ Mm. Contours of $v_{\rm sg}^2 = 0.1$ km s^{-2} and $v_{\rm sg}^2 = 0.19$ km s^{-2} are shown, coloured as in Figure 5.6. (c) and (d) are shown in the $x-y$ plane at $z = 3$ Mm, with a selection of magnetic field lines overplotted in red. (e) and (f) are shown in the $x-z$ plane at $y = 25$ Mm, with a selection of magnetic field lines overplotted in red. The images are shown at (a), (c) and (e) $t = 128$ hr, (b), (d) and (f) $t = 168$ hr.

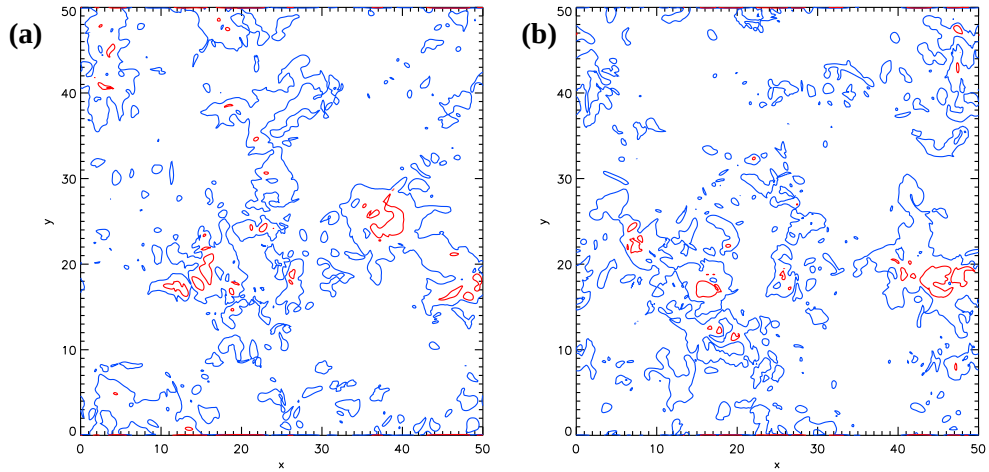

Figure 5.15: Images showing contours of Q integrated in z, for the 3 G simulation. Contours are at levels of 5×10^4 ergs cm^{-2} s^{-1} (blue) and 3×10^5 ergs cm^{-2} s^{-1} (red). The images are shown at (a) $t = 128$ hr and (b) $t = 168$ hr.

the magnetic field lines of Figures 5.14(c) and (d) from the side. Several movies of Q above the photosphere are included with this thesis. The movie magnet48b_q_xy_3_10.mpg shows Q in the $x - y$ plane, integrated between $z = 3$ Mm and $z = 10$ Mm:

$$E_{\text{q,3-10}}(x, y) = \int_{z=3\text{ Mm}}^{z=10\text{ Mm}} Q(x, y, z)dz,$$

in units of ergs cm^{-2} s^{-1}. The movie is saturated at 3×10^3 ergs cm^{-2} s^{-1}. At this height, the rate of energy dissipation is much lower than at the photosphere, as the coronal field is less rapidly evolving and less non-potential. The result of this is that Q is also less rapidly evolving than it is lower down. In addition, between these heights, Q is seen to occur anywhere within the $x-y$ plane and not just above the magnetic network. The movie magnet48b_q_xy_3_10_nulls.mpg shows the same as the latter, with nulls that occur between $z = 3$ Mm and $z = 10$ Mm overplotted as yellow stars. Few nulls are found at this height, but those that are can be seen around large bursts of Q. However, the majority of Q locations do not have any nulls. Also of interest are the movies magnet48b_q_xy_6_10.mpg and magnet48b_q_xy_6.mpg. The first movie shows Q in the $x - y$ plane, integrated between $z = 6$ Mm and $z = 10$ Mm and saturated at 1×10^3 ergs cm^{-2} s^{-1}. The second movie shows Q in the $x - y$ plane at $z = 6$ Mm, saturated at 146 ergs cm^{-2} s^{-1}. Again, Q at these heights is seen to be less rapidly evolving than Q lower down, with more fine-scale, further reaching structures.

Figure 5.15 shows contours of Q integrated in z at levels of 5×10^4 ergs cm^{-2} s^{-1} (blue) and 3×10^5 ergs cm^{-2} s^{-1} (red). According to the literature, these are the values for the radiative losses of an XBP (Habbal and Grace, 1991) and the amount of heating required to maintain the quiet Sun corona (Withbroe and Noyes, 1977) respectively. The images are taken at $t = 128$

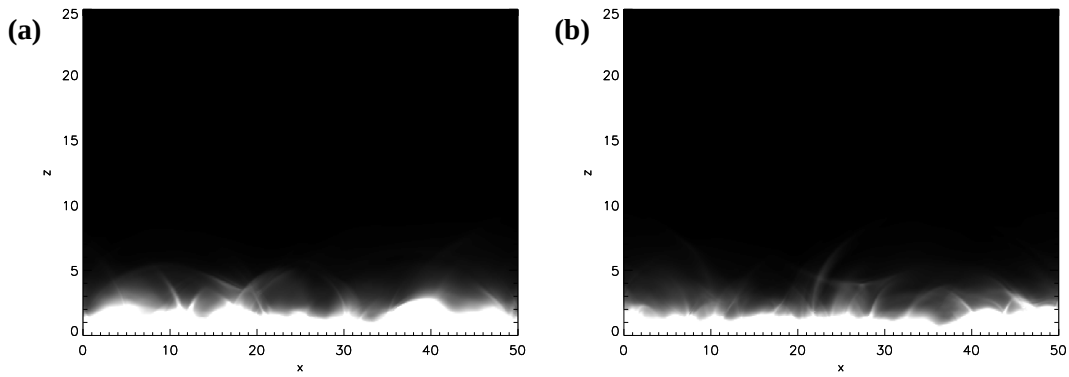

Figure 5.16: Images of Q in the $x - z$ plane integrated in y, for the 3 G simulation. The images are saturated at 1.5×10^5 ergs cm^{-2} s^{-1} and are shown at (a) $t = 128$ hr and (b) $t = 168$ hr. A movie of the full time series, magnet48b_q_xz.mpg, is given on the CD.

hr and $t = 168$ hr in the 3 G simulation. Similar results are found at other times and for other strengths of overlying field. One can see from the images that we obtain energy dissipation at the rate required to maintain the quiet corona only in very small, localised areas. In fact, at $t = 128$ hr (Figure 5.15(a)) the rate of energy dissipation is high enough in only 1.2% of the area of the photosphere. Similarly, at $t = 168$ hr, only 1.1% of the area of the photosphere attains a high enough energy dissipation rate. Considering the mean values for the total rate of energy dissipation within each simulation (Table 5.2), we find a mean dissipation rate per unit area of $3.3 - 4.4 \times 10^4$ ergs cm^{-2} s^{-1}, which is $11 - 15\%$ of the energy requirement for the quiet Sun. Therefore our model cannot fully explain the heating of the quiet corona, but can provide a contribution to it. This is to be expected, however, as many simplifications have been made for the model. For example, our model contains no mass (plasma), and we do not resolve wave motions. The simplifications made for the magnetofrictional technique and the implications of these are discussed in more detail in Section 4.1. Although the energy dissipation is small compared to coronal heating requirements, at $t = 128$ hr (Figure 5.15(a)) the dissipation rate is high enough in 21.9% of the photospheric area to meet the radiative losses of an XBP ($> 5 \times 10^4$ ergs cm^{-2} s^{-1}), and at $t = 168$ hr (Figure 5.15(b)) it is high enough in 19.3% of the photospheric area. Therefore our model may be able to explain such small-scale, transient phenomena.

For interest, several additional movies from the 3 G simulation accompany this section on energy dissipation, they are included on the CD. A side view of the evolution of Q integrated in y or x may be seen in the movies magnet48b_q_xz_nulls.mpg and magnet48b_q_yz_nulls.mpg, saturated at 1.5×10^5 ergs cm^{-2} s^{-1}, and the logarithm of these, magnet48b_q_xz_log_nulls.mpg and magnet48b_q_yz_log_nulls.mpg. Note that within the movies, only the region $z = 0 - 15$ Mm is shown. In all four of these movies, magnetic null points are indicated by yellow stars. As

before, only nulls of height $z = 0.5$ Mm or greater are shown[4]. From these movies, it can be seen that the energy dissipation is greatest low down, in agreement with Figures 5.12(e) and (f). For Q integrated in y (magnet48b_q_xz_nulls.mpg) and x (magnet48b_q_yz_nulls.mpg), fine-scale structure can be seen between $z = 2.5$ Mm and $z = 5$ Mm. Still images of Q in the $x - z$ plane, integrated in y, can be seen in Figure 5.16. The images are shown at (a) $t = 128$ hr and (b) $t = 168$ hr in the 3 G simulation. Within the log movies (magnet48b_q_yz_log_nulls.mpg and magnet48b_q_xz_log_nulls.mpg), one can see that fine structures also exist higher up in the corona, where the energy dissipation is much weaker. In each of the movies, occasional 'bursts' can be seen, where a feature will drift upwards and disappear (or rather, become too small to be shown at the current level of saturation). For example, in the movie magnet48b_q_yz_nulls.mpg, around $t = 149$ hr a feature rises up from low down between $y = 26$ Mm and $y = 30$ Mm, which disappears from view as it travels upwards. It can be seen travelling slightly higher in the corresponding log movie (magnet48b_q_yz_log_nulls.mpg). If we now consider the movie showing energy dissipation as a function of height (magnet48b_q_ht.mpg), the event can also be seen here, as a kink that appears near the photosphere around $t = 149$ hr then propagates upwards. From these movies, we find that the energy dissipated and summed along the line of sight provides a fine-scale dynamic structure that is in qualitative agreement with what is observed on the Sun low down.

5.5 Velocities

We now consider locations of increased $\mathbf{v}^2$ within the simulations, where $\mathbf{v}$ is the magnetofrictional velocity,

$$\mathbf{v} = \frac{1}{\nu}\frac{\mathbf{j} \times \mathbf{B}}{B^2}. \tag{5.4}$$

There is always a background contribution to $\mathbf{v}^2$ due to the relaxation of the coronal magnetic field, but locations of enhanced $\mathbf{v}^2$ are of interest as they can be related to sites of changing magnetic topology. We consider $\mathbf{v}^2$ rather than $\mathbf{v}$, as $|\mathbf{v}|^2$ appears in the equation for Q (5.2). Figure 5.17 shows a series of images of $\mathbf{v}^2$ summed in z. This is computed as follows:

$$\mathbf{v}(i,l)^2 = \sum_{k=0}^{nz-1} \mathbf{v}(i,l,k)^2,$$

where nz is the number of grid cells in the $z-$direction. The images are shown in the $x - y$ plane for the 3 G simulation, with contours of $v_{\rm sg}^2$ overplotted at the same levels as in Figure 5.6. Large regions of $\mathbf{v}^2$ are seen both in the magnetic network, and within the supergranular cells. The $x - y$ positions of coronal null points are indicated by gold stars, where only nulls of height $z = 0.5$ Mm

[4]Versions of each of the four movies without null points are also included, named magnet48b_q_xz.mpg, magnet48b_q_yz.mpg, magnet48b_q_xz_log.mpg and magnet48b_q_yz_log.mpg.

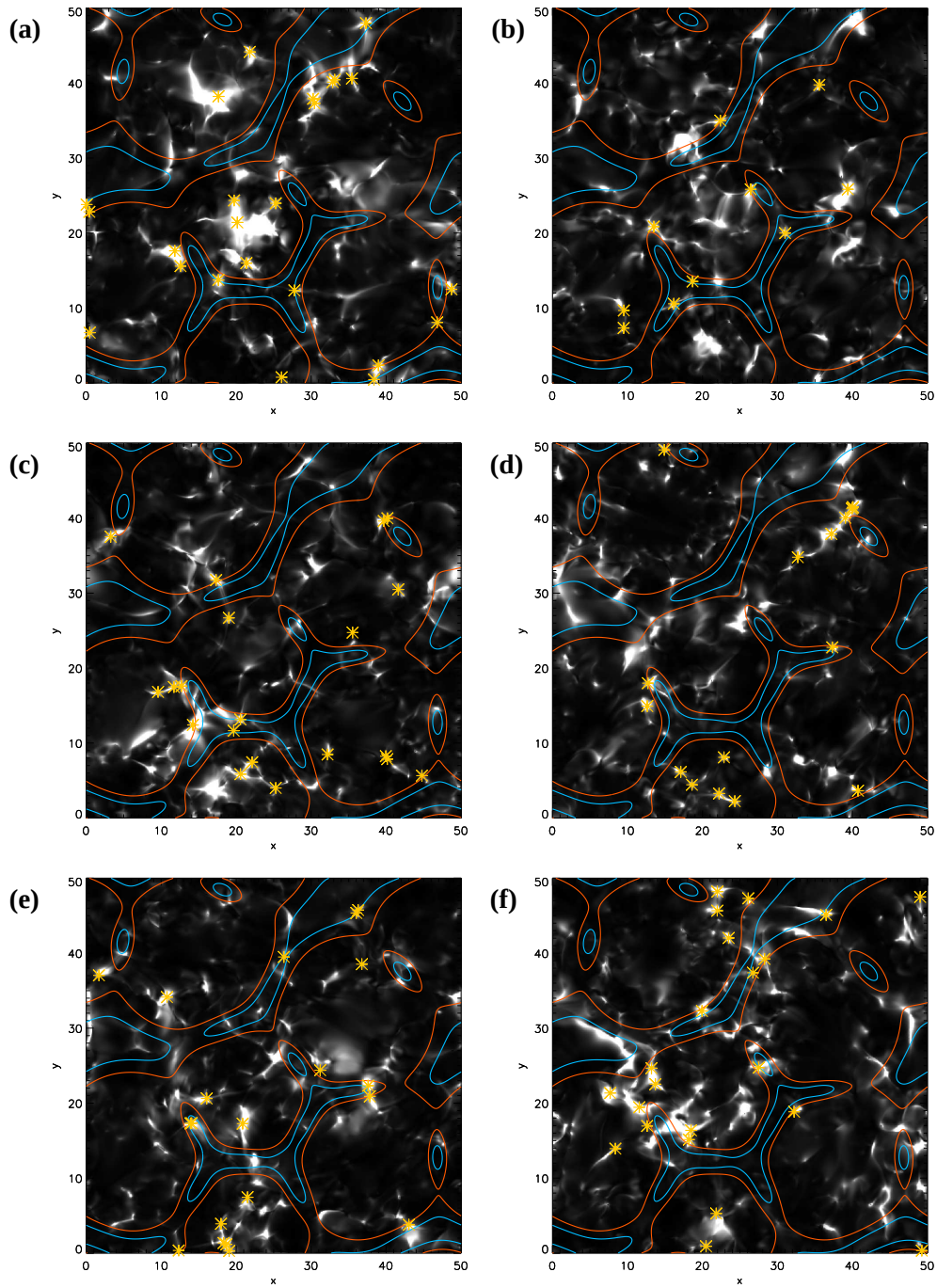

Figure 5.17: $\mathbf{v}^2$ (where $\mathbf{v}$ is the magnetofrictional velocity) integrated in z, for the 3 G simulation. The images are shown in the $x-y$ plane, saturated at 85.3 km^2 s^{-2} ((9.2 km s^{-1})^2). Contours of $v_{\rm sg}^2 = 0.1$ km^2 s^{-2} and $v_{\rm sg}^2 = 0.19$ km^2 s^{-2} are shown, coloured as in Figure 5.6. The $x-y$ positions of null points of height greater than 0.5 Mm are indicated by gold stars. The images are shown at (a) $t = 128$ hr, (b) $t = 136$ hr, (c) $t = 144$ hr, (d) $t = 152$ hr, (e) $t = 160$ hr and (f) $t = 168$ hr. A movie of the full time series, magnet48b_v_xy_nulls.mpg, is given on the CD.

or higher are shown. Coronal null points are of interest because they indicate possible locations of changing magnetic topology, although in 3D reconnection may occur in the absence of null points. We would expect an increase in $\mathbf{v}^2$ at sites of changing magnetic topology, as sharply curved field lines straighten out in response to the Lorentz force. Considering the images in Figure 5.17, one can see that the null points tend to coincide with locations where $\mathbf{v}^2$ is high. We now consider where $\mathbf{v}^2$ is largest in the $z-$direction.

The left-hand column of Figure 5.18 shows plots of the average $\mathbf{v}^2$ as a function of height for the (a) 0 G, (c) 1 G and (e) 3 G simulations. This is computed as follows:

$$\mathbf{v}(k)^2 = \frac{1}{N} \sum_{i=0}^{nx-1} \sum_{l=0}^{ny-1} \mathbf{v}(i,l,k)^2,$$

where $N = (nx)(ny)$. The different coloured curves show $\mathbf{v}^2$ at $t = 128$ hr (black), $t = 136$ hr (blue), $t = 144$ hr (red), $t = 152$ hr (green), $t = 160$ hr (yellow) and $t = 168$ hr (purple). To put these values in context, the maximum velocity that a magnetic element within the 2D photospheric model can take is 3.7 km s^{-1} ($\mathbf{v}^2 = 13.69$ km^2 s^{-2}). For the 1 G and 3 G cases, one can see that the average $\mathbf{v}^2$ decreases rapidly with increasing height. The highest average $\mathbf{v}^2$ is found low down in each case, as this is where photospheric footpoint motions create bends in the magnetic field lines originating at $z = 0$ Mm. The magnetofrictional velocity then acts to restore these field lines back towards an equilibrium state. Although the majority of this relaxation process takes place during the 500 magnetofrictional steps between synthetic magnetograms, many field lines will not yet have fully relaxed. High up in the corona (> 10 Mm), the average $\mathbf{v}^2$ is very small, as most connections from the photosphere do not reach this high. The overlying field lines in the upper half of the box remain more or less straight and unperturbed. On comparing Figure 5.18(c) and (e), one can see that the average $\mathbf{v}^2$ falls of less rapidly in the 1 G than the 3 G case. This is because the weaker 1 G overlying field is more easily deformed by the evolution of the coronal magnetic field driven by photospheric motions. Any deformation of the overlying field results in a magnetofrictional velocity to restore it back towards its equilibrium state. In the 0 G case (Figure 5.18(a)), connections from the photosphere are not inhibited by any overlying field. Therefore, the average $\mathbf{v}^2$ does not decrease as rapidly with increasing height as in the 1 G and 3 G cases. The average $\mathbf{v}^2$ always tends to be greater than 1 km^2 s^{-2}, and in fact there is an increase in $\mathbf{v}^2$ towards $z = 25$ Mm due to boundary effects.

The right-hand column of Figure 5.18 shows plots of the maximum $\mathbf{v}^2$ as a function of height for the (b) 0 G, (d) 1 G and (f) 3 G simulations. The different curves represent different times within each simulation, and are coloured as in Figure 5.18(a), (c) and (e). Considering first the cases with an overlying field, spikes can be seen in the maximum $\mathbf{v}^2$ between roughly $0 - 9$ Mm in the 1 G case and $0 - 4$ Mm in the 3 G case. This increase in the maximum $\mathbf{v}^2$ is most likely due to sites of rapidly changing magnetic topology at these heights, where there is a change

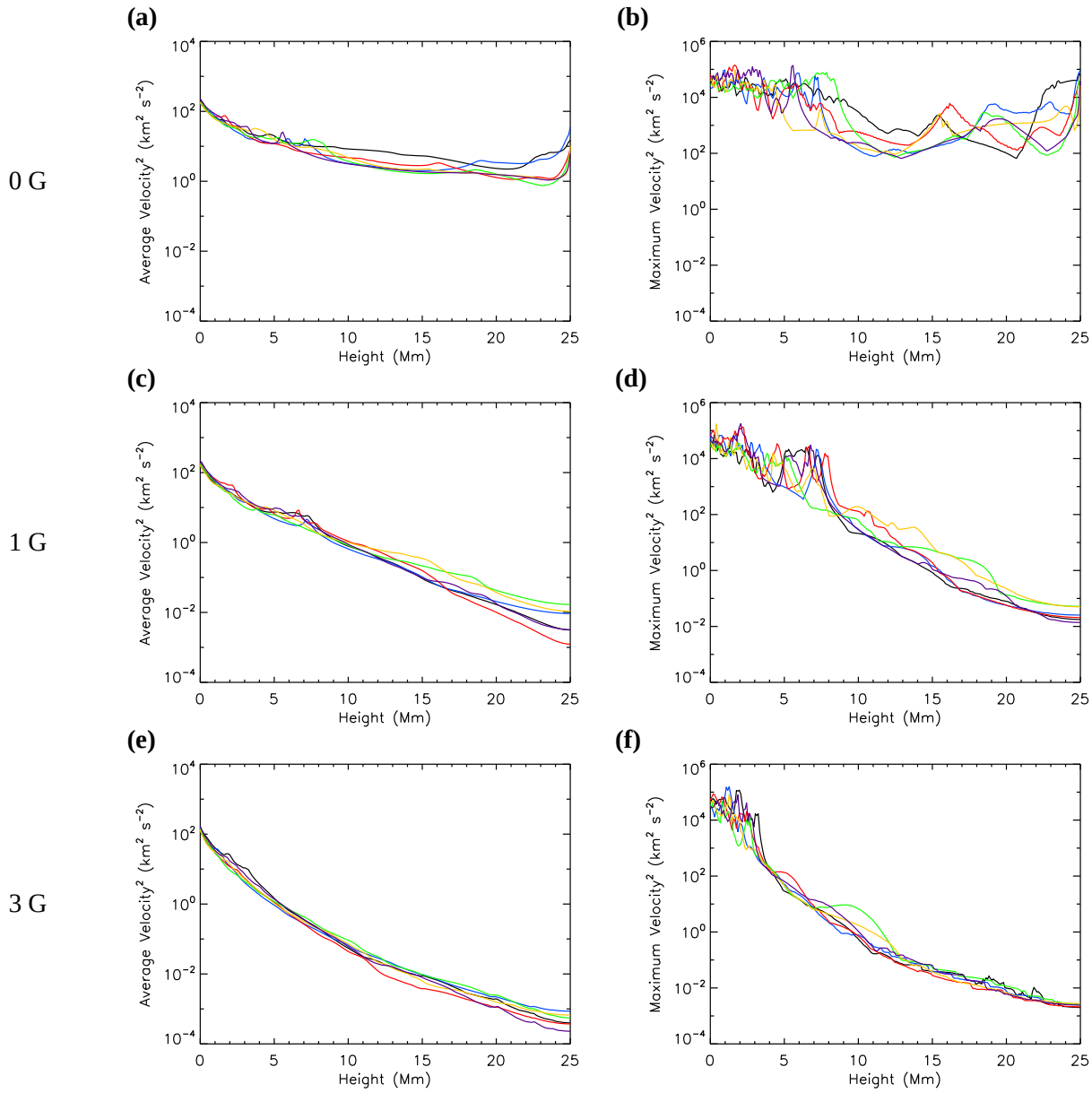

Figure 5.18: Left-hand column: average $\mathbf{v}^2$ as a function of height for the (a) 0 G, (c) 1 G and (e) 3 G simulations. Right-hand column: maximum $\mathbf{v}^2$ as a function of height for the (b) 0 G, (d) 1 G and (f) 3 G simulations. In each plot, the curves show $\mathbf{v}^2$ at $t = 128$ hr (black), $t = 136$ hr (blue), $t = 144$ hr (red), $t = 152$ hr (green), $t = 160$ hr (yellow) and $t = 168$ hr (purple).

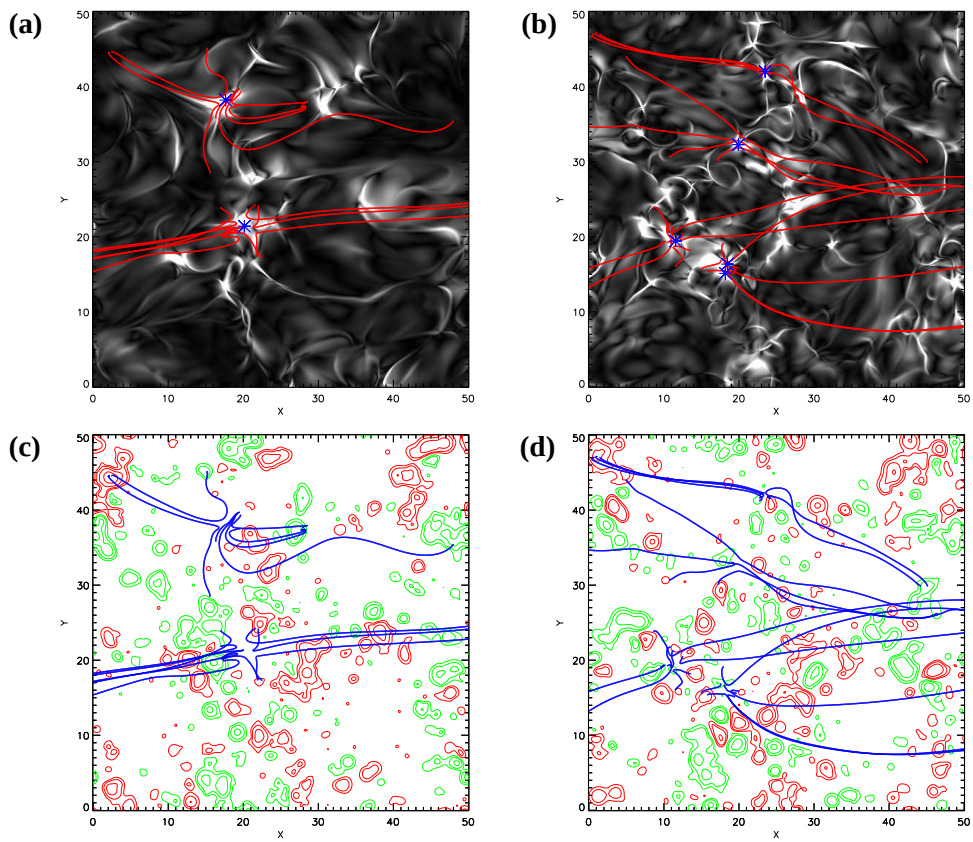

Figure 5.19: $\mathbf{v}^2$ in the $x-y$ plane, saturated at 2.78 km^2 s^{-2} ($(1.67$ km s$^{-1})^2$), at (a) $t = 128$ hr, $z = 2$ Mm and (b) $t = 168$ hr, $z = 1$ Mm. In each image, a selection of coronal null points have been overplotted in blue, along with nearby field lines in red. (c) and (d) B_z at $z = 0$ Mm, where red and green contours represent positive and negative magnetic field, at the same contour levels as in Figure 5.8. The images are shown at (c) $t = 128$ hr and (d) $t = 168$ hr, with the same field lines as in images (a) and (b) respectively, shown in blue.

from the magnetic elements' field dominating to the overlying field dominating. One can see spikes in the maximum $\mathbf{v}^2$ higher in the corona in the 1 G case than in the 3 G case, as for the weaker overlying field connections from the photosphere are less suppressed and the interface is higher. In the case with no overlying field (Figure 5.18(b)), one can see spikes in the maximum $\mathbf{v}^2$ throughout z, since connections from the photosphere can reach any height within the box. However, most of the spikes appear to occur within $z = 0 - 10$ Mm, implying that this is where the most changing magnetic topology occurs. We now consider some examples of enhanced $\mathbf{v}^2$ above the photosphere, and their locations in the $x-y$ plane.

Figures 5.19(a) and (b) show $\mathbf{v}^2$ in the $x-y$ plane at (a) $t = 128$ hr, $z = 2$ Mm and (b) $t = 168$ hr, $z = 1$ Mm. Some null points (blue stars) that lie close to the height of the plane are overplotted, along with a selection of field lines. Around the null points, one can see enhanced $\mathbf{v}^2$, as well as $x-$shapes and nested field lines, indicating boundaries between different topological

regions. Figures 5.19(c) and (d) show the same field lines as in (a) and (b) respectively, along with the magnetic field at $z = 0$ Mm.

Figure 5.20 shows images of $\mathbf{v}^2$ integrated in y in the $x - z$ plane. Whilst the $x - z$ plane images of free magnetic energy and energy dissipated are very similar for each strength of overlying field, more of a difference can be seen between images of $\mathbf{v}^2$ for different overlying field strengths. The top two images in Figure 5.20 are from the 0 G simulation, the middle two are from the 1 G simulation, and the bottom two are from the 3 G simulation. Each of the images is taken at $t = 144$ hr, but $x - z$ plane images at other times are similar. The left-hand column shows $\mathbf{v}^2$ integrated in y, whilst the right-hand column shows the logarithm of the images on the left. From the left-hand column, one can see that regions of enhanced $\mathbf{v}^2$ are mainly located low down; mostly between $0 - 10$ Mm in the 0 G case (Figure 5.20(a)), $0 - 9$ Mm in the 1 G case (Figure 5.20(c)) and $0 - 4$ Mm in the 3 G case (Figure 5.20(e)). In the 0 G case, enhanced $\mathbf{v}^2$ can also be seen higher in the volume, including near $z = 25$ Mm due to boundary effects. From images (c) and (e), it is clear that regions of enhanced $\mathbf{v}^2$ are found higher in the corona in the 1 G case than in the 3 G case. In the right-hand column, the log images show $\mathbf{v}^2$ for a wider range of values. One can see structure higher in the corona in each of the images due to weaker $\mathbf{v}^2$. The $x - z$ positions of coronal null points are indicated in Figure 5.20 by gold stars, where only the nulls of height $z = 0.5$ Mm or higher are shown. In all of the images, the nulls appear to be situated at locations of enhanced $\mathbf{v}^2$, however $\mathbf{v}^2$ is not only located at nulls. As mentioned previously, there is a background contribution to $\mathbf{v}^2$ throughout the coronal volume due to the relaxation of the field, as well as enhanced regions of $\mathbf{v}^2$ due to sites of reconnection. It is these enhanced regions of $\mathbf{v}^2$ that tend to be associated with coronal null points.

Six movies of $\mathbf{v}^2$ accompany this thesis and are held on the CD. The movies for the 0 G and 3 G simulations are included, since a significant difference in plane images of $\mathbf{v}^2$ can be seen for different strengths of overlying field. For the 3 G simulation, magnet48b_v_xy_nulls.mpg, magnet48b_v_xz_log_nulls.mpg and magnet48b_v_yz_log_nulls.mpg show $\mathbf{v}^2$ integrated in the line of sight in the $x - y$, $x - z$ and $y - z$ planes respectively. Similarly, for the 0 G simulation, magnet48_v_xy_nulls.mpg, magnet48_v_xz_log_nulls.mpg and magnet48_v_yz_log_nulls.mpg show $\mathbf{v}^2$ integrated in the line of sight in the $x - y$, $x - z$ and $y - z$ planes. For the $x - z$ and $y - z$ movies from each simulation, the logarithm of $\mathbf{v}^2$ is shown, so that a wider range of values can be seen. In all six movies, coronal nulls of height ≥ 0.5 Mm are indicated by yellow stars. Within the $x - z$ and $y - z$ plane movies, the fainter regions of $\mathbf{v}^2$ are mostly due to the background magnetofrictional velocity that relaxes the coronal field throughout the volume. The brighter regions of $\mathbf{v}^2$ are more likely due to sites of changing magnetic topology, particularly those regions that are associated with coronal null points. Comparing the $x - z$ and $y - z$ movies for the 0 G and 3 G overlying field cases, regions of enhanced $\mathbf{v}^2$ can be seen throughout the volume in the 0 G case (magnet48_v_xz_log_nulls.mpg and magnet48_v_yz_log_nulls.mpg), but are suppressed in the 3 G

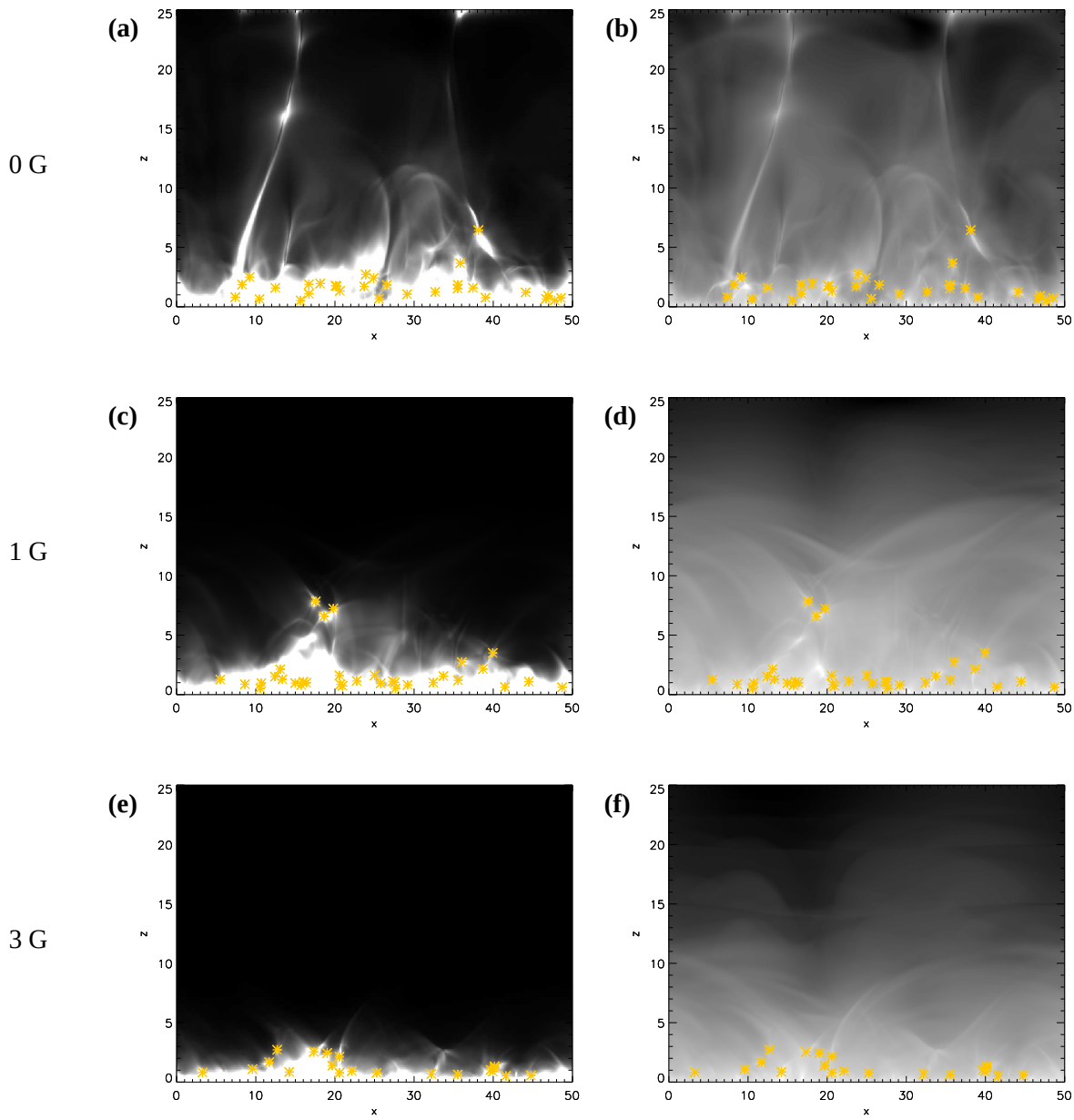

Figure 5.20: Plots for the 0 G (top), 1 G (middle) and 3 G (bottom) cases. (a), (c) and (e) show $\mathbf{v}^2$ integrated in y, in the $x - z$ plane. The images are saturated at 142.2 km^2 s^{-2} ($(11.9$ km s$^{-1})^2$). (b), (d) and (f) show the logarithm of (a), (c) and (e) respectively. The $x - z$ positions of any null points with height greater than 0.5 Mm are indicated by gold stars. The images are shown at $t = 144$ hr. A movie of the full time series for image (b) (0 G case) is given on the CD, named magnet48_v_xz_log_nulls.mpg. A movie of the full time series for image (f) (3 G case) is also included, named magnet48b_v_xz_log_nulls.mpg.

case (magnet48b_v_xz_log_nulls.mpg and magnet48b_v_yz_log_nulls.mpg). Note that in the $x-z$ and $y-z$ movies, the whole $z-$range ($0-25$ Mm) is shown for the 0 G case, but only the range $0-15$ Mm is shown for the 3 G case.

5.6 Current Density

Figures 5.21(a) and (b) show plots of the average $\mathbf{j}^2$ as a function of height, where $\mathbf{j} = \nabla \times \mathbf{B}$, for the (a) 1 G and (b) 3 G simulations. This is computed as follows:

$$\mathbf{j}(k)^2 = \frac{1}{N} \sum_{i=0}^{nx-1} \sum_{l=0}^{ny-1} \mathbf{j}(i,l,k)^2,$$

where $N = (nx)(ny)$. The values are given in non-dimensional units. $\mathbf{j}^2$ is of interest because it indicates locations of Ohmic heating, $\frac{\mathbf{j}^2}{\sigma}$. For each simulation, curves are plotted for $t = 128$ hr (black), $t = 136$ hr (blue), $t = 144$ hr (red), $t = 152$ hr (green), $t = 160$ hr (yellow) and $t = 168$ hr (purple). From these plots, $\mathbf{j}^2$ is largest low down. Its value then decreases rapidly with height, in each case having decreased by more than an order of magnitude by $z = 2$ Mm. By definition, $\mathbf{j} \times \mathbf{B} = 0$ within a force-free field, hence $\mathbf{j}$ is parallel to $\mathbf{B}$ and we can express it as $\mathbf{j} = \alpha\mathbf{B}$, where α is a scalar representing the twist of the field with respect to the corresponding potential field (see Chapter 1, Section 1.3.3). Therefore it makes sense that $\mathbf{j}^2$ is at its largest near the magnetic sources. We would also expect to find increased values of $\mathbf{j}^2$ at locations where the magnetic field is non-potential, i.e. $|\alpha| > 0$. As discussed previously, the magnetic field is furthest from potential low down in the corona, as this is where the evolution of the field is being driven by photospheric motions. Note that the average $\mathbf{j}^2$ is not at its largest at exactly $z = 0$ Mm, but slightly above. This is because any non-potentiality arises from A_z, which sits a half grid point up (see Chapter 4). Considering the plots of the average $\mathbf{j}^2$ as a function of height at larger z (e. g. $z > 10$ Mm), the average $\mathbf{j}^2$ increases with increasing time throughout the simulation ($t = 128 - 168$ h). Higher up in the 1 G and 3 G simulations, connections do not reach high enough to perturb the overlying field significantly, so it stays roughly at its uniform value. The overlying field does change weakly with time however; these small-scale perturbations in $\mathbf{B}$ lead to an increase in $\mathbf{j}^2 (= |\nabla \times \mathbf{B}|^2 \propto \frac{\mathbf{B}}{L})$ at greater heights. Therefore non-potentiality is propagated upwards within the coronal volume as the simulation progresses. As a consequence, we would also expect the value of $|\alpha|$ at greater heights to be increasing. Indeed, if we consider plots of the average value of α as a function of height (Figure 5.21(c) for the 1 G and (d) for the 3 G simulation), where

$$\alpha = \frac{\mathbf{j} \cdot \mathbf{B}}{B^2},$$

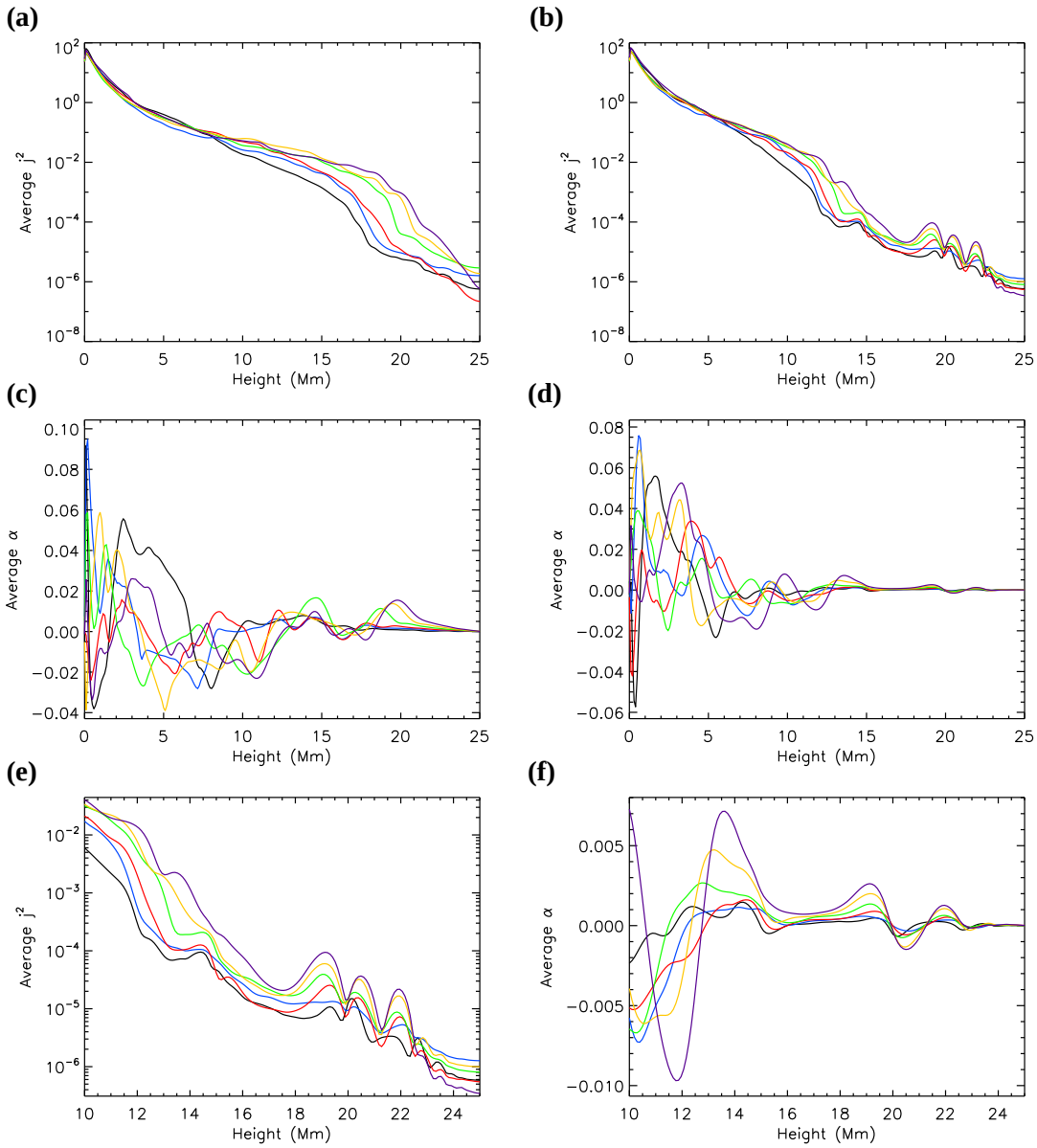

Figure 5.21: (a) and (b) average normalised $\mathbf{j}^2$ as a function of height for the (a) 1 G and (b) 3 G simulations. (c) and (d) average normalised α as a function of height for the (c) 1 G and (d) 3 G simulations. (e) and (f) zoomed in plots of the region $z \geq 10$ Mm, for (e) average normalised $\mathbf{j}^2$ as a function of height and (f) average normalised α as a function of height, in the 3 G simulation. In each plot, the curves show the quantity ($\mathbf{j}^2$ or α) at $t = 128$ hr (black), $t = 136$ hr (blue), $t = 144$ hr (red), $t = 152$ hr (green), $t = 160$ hr (yellow) and $t = 168$ hr (purple).

we see that this is the case. Increasing values of $|\alpha|$ can be seen particularly clearly in Figure 5.21(c) at around $z = 20$ Mm. Figure 5.21(e) shows a zoomed in section of Figure 5.21(b), the average $\mathbf{j}^2$ as a function of height, while Figure 5.21(f) shows a zoomed in section of Figure 5.21(d), the average value of α as a function of height, both for $z \geq 10$ Mm. In Figure 5.21(f), the peaks and trough of average α around $z = 19$, 20.5 and 22 Mm match very well to the peaks in average $\mathbf{j}^2$ at the same locations in Figure 5.21(e).

Figure 5.22 shows six images of $\mathbf{j}^2$ summed in z in the $x - y$ plane. This is computed as follows:

$$\mathbf{j}(i,l)^2 = \sum_{k=0}^{nz-1} \mathbf{j}(i,l,k)^2.$$

Contours of B_z at $z = 0$ Mm and of $v_{\rm sg}^2$ are overplotted at the same levels as in Figure 5.8. The images are spaced 8 hr apart from $t = 128 - 168$ hr. On comparison with the $x - y$ plane images of free magnetic energy density in Figure 5.8, the locations of high $\mathbf{j}^2$ and of positive free energy density seem to match very well. The regions of high $\mathbf{j}^2$ appear to be strongest in the magnetic network, as this is where $\mathbf{B}$ is strongest and the field is most non-potential, but we also see fainter bands of $\mathbf{j}^2$ stretching across supergranules, often in the same places as strong bands of positive free magnetic energy density are seen. It makes sense for regions of strong $\mathbf{j}^2$ to be co-located with regions of positive free magnetic energy density, as free magnetic energy is built up at locations of high non-potentiality (large α) which arise due to non-zero $\mathbf{j}$ ($\mathbf{j} = \alpha\mathbf{B}$). The evolution of $\mathbf{j}^2$ integrated in z in the $x - y$ plane can be seen in the movie included on the CD, magnet48b_j_xy_bz.mpg, for the 3 G simulation, with contours of B_z at $z = 0$ Mm overplotted as in Figure 5.22.

Figure 5.23 shows images of $\mathbf{j}^2$ in the $x - z$ plane. Very little difference is seen between images of $\mathbf{j}^2$ for different strengths of the overlying field, therefore only images from the 3 G simulation are shown here. The left-hand column shows images at $t = 128$ hr, the right-hand column shows images at $t = 160$ hr. Figure 5.23(a) and (b) show $\mathbf{j}^2$ at $y = 25$ Mm. The regions of increased $\mathbf{j}^2$ appear to be quite structured, and to follow the shape of the magnetic field (as $\mathbf{j}$ is parallel to $\mathbf{B}$). Figure 5.23(c) and (d) show $\mathbf{j}^2$ integrated in y, whilst (e) and (f) show the logarithm of the images in (c) and (d). As we would expect, the strongest contribution from $\mathbf{j}^2$ is seen low down. In the logarithmic images, a wider range of $\mathbf{j}^2$ can be seen, and hence structures further up in the corona where $\mathbf{j}^2$ is weaker. Again, $\mathbf{j}^2$ is seen to follow the shape of the magnetic field, including higher in the corona along overlying field lines. The evolution of the logarithm of $\mathbf{j}^2$ integrated in y and in x can be seen in the movies included on the CD, magnet48b_j_xz_log_nulls.mpg and magnet48b_j_yz_log_nulls.mpg respectively, for the 3 G simulation. Again, null points of height $z \geq 0.5$ Mm are overplotted as yellow stars. Later on in the simulation, $\mathbf{j}^2$ can be seen following curved overlying field lines in the $x - z$ plane between $z = 10 - 14$ Mm.

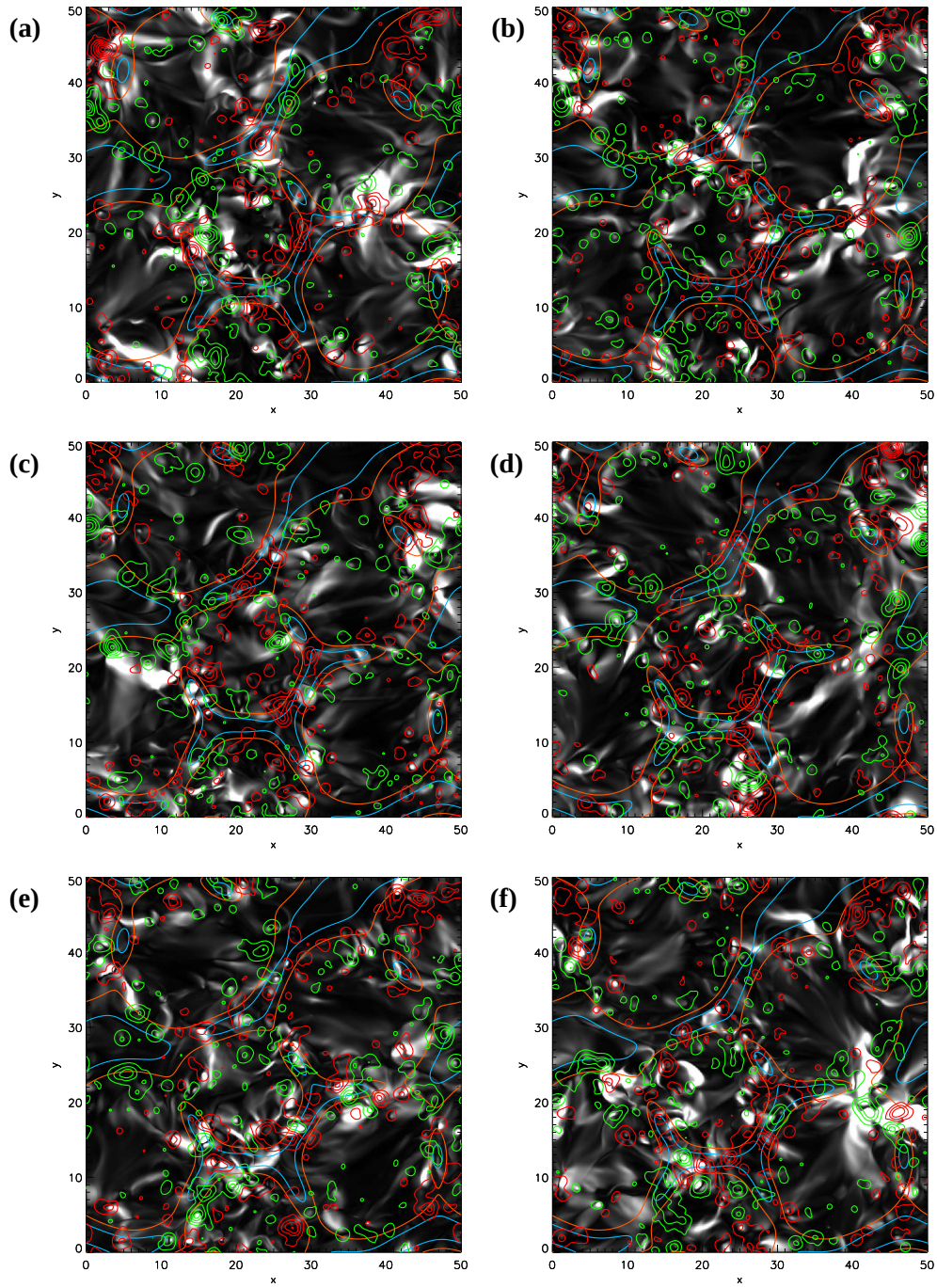

Figure 5.22: Normalised $\mathbf{j}^2$ integrated in z, for the 3 G overlying field simulation. The images are shown in the $x - y$ plane. Contours of $v_{\rm sg}^2 = 0.1$ km^2 s^{-2} and $v_{\rm sg}^2 = 0.19$ km^2 s^{-2} are shown, coloured as in Figure 5.6. Contours of B_z at $z = 0$ Mm are also overplotted, where red contours represent positive magnetic field and green contours represent negative, at the same levels as in Figure 5.8. The images are shown at (a) $t = 128$ hr, (b) $t = 136$ hr, (c) $t = 144$ hr, (d) $t = 152$ hr, (e) $t = 160$ hr and (f) $t = 168$ hr. A movie of the full time series, magnet48b_j_xy_bz.mpg, is given on the CD.

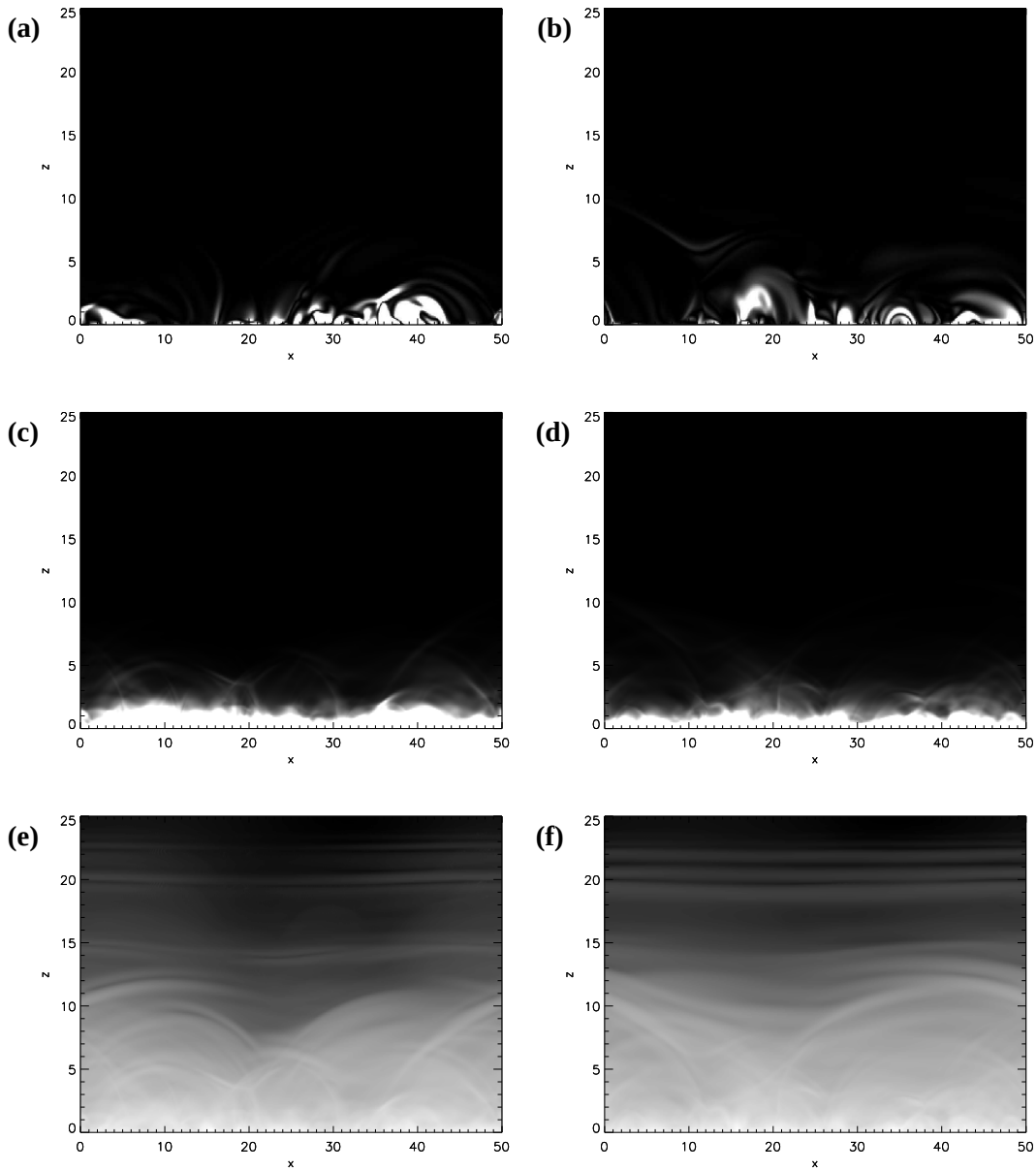

Figure 5.23: (a) and (b) normalised $\mathbf{j}^2$ in the $x-z$ plane at $y = 25$ Mm. (c) and (d) normalised $\mathbf{j}^2$ integrated in y in the $x-z$ plane. (e) and (f) logarithm of the images in (c) and (d). Images (a), (c) and (e) are shown at $t = 128$ hr, (b), (d) and (f) are shown at $t = 160$ hr. A movie of the full time series for images (e) and (f) is given on the CD, named magnet48b_j_xz_log_nulls.mpg.

5.7 Discussion and Conclusions

The aim of this chapter was to carry out a preliminary analysis of a set of non-linear force-free field simulations driven by synthetic magnetograms produced by the model described in Chapter 3. Four simulations were run, each driven by the same lower boundary data, with four different strengths of overlying field: 0 G, 1 G, 3 G and 10 G. The lower boundary data consisted of a 48 hr series of synthetic magnetograms of area 50×50 Mm^2 and of cadence 1 min. The initial condition for each simulation was a potential field. The coronal field was then evolved through a series of quasi-static, non-linear force-free equilibria, via a magnetofrictional relaxation technique, in response to photospheric boundary motions. As described in Chapter 4, the continuous nature of this coronal evolution technique means that current systems and connectivity are maintained within the corona from one step to the next. This allows for the build-up and storage of free magnetic energy – one of the quantities studied within this chapter. The presence of free magnetic energy within our model shows a significant departure from previous models for the magnetic carpet coronal field, which use potential fields (Chapter 2). The other quantities considered were the energy dissipated, the magnetofrictional velocity and the electric current density.

For each simulation, both the free magnetic energy and energy dissipation rate initially rapidly increase, before levelling off and oscillating about a mean value. The mean free magnetic energy for each simulation is $1.09 - 1.96 \times 10^{27}$ ergs, whilst the mean energy dissipation rate is $0.8 - 1.1 \times 10^{24}$ ergs s^{-1}, resulting in $1.43 - 1.89 \times 10^{29}$ ergs being cumulatively dissipated over each 48 hr simulation. For both the free and dissipated energies, a stronger overlying field results in higher values, although the effect is more significant for the free energy. It is also clear that the evolution of both the free and dissipated energies is highly dependent upon the evolution of the photospheric magnetic field.

In Chapter 4, the energy dissipation rate for each of the basic interactions was found to be $1.95 - 4.95 \times 10^4$ ergs cm^{-2} s^{-1}. It was hypothesised that for the correct number of magnetic elements in a given area, the energy dissipation rate could be an order of magnitude higher. We find that this is not the case for the simulations in this chapter, however, as each simulation results in an energy dissipation rate of $3.30 - 4.36 \times 10^4$ ergs cm^{-2} s^{-1}. There are several reasons for why this could be the case. One possible reason is that our values for η_4 are not the same in both studies ($\eta_4 = 4.715 \times 10^5$ km^4 s^{-1} in Chapter 4, while $\eta_4 = 7.579 \times 10^5$ km^4 s^{-1} in Chapter 5). From earlier simulations, it is known that decreasing the value of η_4 leads to an increase in the rate of energy dissipation (and in fact an increase in the free magnetic energy). An additional simulation will be run using the same setup as in Chapter 5, but taking $\eta_4 = 4.715 \times 10^5$ km^4 s^{-1} as in Chapter 4, to determine whether this has a significant effect on results. Another possible reason that the energy dissipation rate is not found to be an order of magnitude higher than that of the simulations in Chapter 4 is that most of the magnetic elements in the simulations in the present

chapter are much smaller than those in Chapter 4. The two magnetic elements in Chapter 4 were of absolute flux 10^{18} Mx, whereas the average size of a magnetic element in the synthetic magnetograms used in Chapter 5 is just 1.1×10^{17} Mx (as calculated by Equation 3.15 from Chapter 3).

While there are similarities between the evolution of the two types of energy integrated over the volume, they are seen to be less alike when we consider their location within each simulation. The bulk of the free magnetic energy is located above the photosphere, between $z = 0.5 - 0.8$ Mm. This is stored along closed connections between magnetic elements. Regions of positive free energy density can be seen both in the magnetic network and across supergranular cells; such regions may also be long-lived. In contrast, the largest amount of energy dissipation is found low down, near the magnetic sources, and values decrease rapidly with increasing height. Regions of increased energy dissipation are seen predominantly in the magnetic network, although weaker, fine-scale strands are also seen above the photosphere at sites of changing magnetic topology. Also unlike the free magnetic energy density, the large regions of energy dissipation seen in the $x - y$ plane are much more rapidly evolving (compare movies magnet48b_free_xy_bz.mpg and magnet48b_q_xy_bz.mpg). From the analysis in this chapter, regions of increased energy dissipation do appear to be related to the various flux evolution processes that occur at the photosphere. However, a more in-depth analysis would be required to quantify this. The amount of free magnetic energy built up and stored in each simulation is sufficient to account for such small-scale transient phenomena as nanoflares and XBPs. The energy dissipation rate is not high enough to be able to explain the heating of the quiet corona, but provides a contribution of around $11 - 15\%$ to the required 3×10^5 ergs cm^{-2} s^{-1} of Withbroe and Noyes (1977).

The location and evolution of increased magnetofrictional velocities and electric current density are also examined in this chapter. There is a background contribution to $\mathbf{v}^2$ throughout the corona due to the relaxation of the magnetic field, however we find that regions of increased velocities can be related to sites of changing magnetic topology, reinforced by the fact that coronal null points tend to lie within such regions. Regions of increased $\mathbf{v}^2$ are seen both at the magnetic network and within supergranular cells. The average $\mathbf{v}^2$ rapidly decreases with height in the presence of an overlying field, and the stronger the overlying field, the faster this fall-off is. This is unsurprising due to the $\frac{1}{B^2}$ factor in the equation for the magnetofrictional velocity (Equation 5.4). If no overlying field is present, locations of increased $\mathbf{v}^2$ can be seen throughout the coronal volume.

Locations of increased $\mathbf{j}^2$ are found to be co-located with regions of positive free magnetic energy density, as both are dependent on the magnetic field being non-potential. The average $\mathbf{j}^2$ is largest near the magnetic sources, and decreases rapidly with increasing z. Visually, $\mathbf{j}^2$ is seen to follow the shape of the magnetic field where α is non-zero. Small-scale perturbations in the overlying magnetic field cause $\mathbf{j}^2$ at greater heights to gradually increase with time. Increasing the strength of the overlying field causes $\mathbf{j}^2$ to be larger in total, as $\mathbf{B}$ is larger in total. Table 5.5

Quantity	Location	Increasing Height	Increasing O/L Field Strength
Free Energy	Magnetic network and across s/g cells.	Mostly stored $z = 0.5 - 0.8$ Mm then rapid decrease with increasing z.	Significant increase in total.
Q	Magnetic network and sites of changing magnetic topology.	Rapid decrease.	Slight increase in total.
$\mathbf{v}^2$	Sites of changing magnetic topology.	Rapid decrease in presence of overlying field.	Decrease. Suppressed to lower heights.
$\mathbf{j}^2$	Magnetic network and non-potential regions. Follows field lines.	Rapid decrease. Slowly propagates higher with increasing time.	Slight increase in total.

Table 5.5: Summary of results for free magnetic energy; energy dissipated, Q; magnetofrictional velocity, $\mathbf{v}^2$ and current density, $\mathbf{j}^2$.

gives a summary of results for each of the four quantities studied in this chapter, indicating their locations and the effect of increasing the strength of the overlying field.

There are several avenues for future work using the non-linear force-free coronal modelling technique described here. The simulations presented in this chapter will be studied in more detail. For example, a more in depth study of the connectivity of the magnetic field could be conducted, similar to the study of Close et al. (2003), who analysed potential coronal fields. It would also be of interest to investigate in more detail the effect of each of the photospheric flux evolution processes on the evolution of the coronal field and each of the quantities discussed in this chapter. We already know the flux, location and time of occurrence of each of the processes within the synthetic magnetogram series. Were we to run additional simulations using different sets of synthetic magnetograms, there are several aspects of the simulations that we could investigate. Within the synthetic magnetogram series used in this chapter, the total absolute flux was slightly decreasing during the simulation. If we were to model a set of magnetograms where the absolute flux was gradually increasing, would the free magnetic energy be greater? As suggested in Chapter 3, a more complex supergranular flow profile within the 2D model would have implications for the 3D model. In particular, vortical motions at the photosphere would introduce twist and non-potentiality within the corona. The magnetofrictional technique can also be applied to real magnetogram data, such as from Hinode/SOT or SDO/HMI. A study could be carried out to compare regions of interest within a simulated non-linear force-free coronal field driven by observed magnetograms to events occurring in corresponding coronal images (e.g. using various

wavelengths of SDO/AIA). What is clear is that within this single, relatively 'simple' simulation, a wide range of processes and dynamics is occurring. A careful and detailed analysis of these and other non-linear force-free field simulations of the magnetic carpet coronal field will be carried out in future.

Chapter 6

Conclusions and Future Work

The aim of this thesis was to produce a realistic non-potential magnetic field model for the photospheric and coronal evolution of the solar magnetic carpet. It is a two-component model: a 2D model for the photospheric evolution of the magnetic carpet (Chapter 3) produced synthetic magnetograms. These were used as the lower boundary condition to drive the continuous evolution of the full 3D non-linear force-free coronal magnetic field (Chapters 4 and 5). We now summarise the main results of each of the chapters.

Chapter 2 provided a literature review of previous magnetic field models for magnetic carpet, both in the photosphere and in the corona. The purpose of this chapter was to determine from these models which properties of the magnetic carpet would be important to include in our own model, and how we could improve on the models that already exist. From this review, we decided to incorporate the following features in our 2D model for the magnetic carpet, described in Chapter 3. We included a mathematically specified, steady supergranular flow profile. We also included random motions representing granulation, a consequence of which was that magnetic elements were prevented from becoming stationary at the boundaries between supergranules. In addition to this, we built into the model the flux evolution processes of emergence, cancellation, coalescence and fragmentation; where flux emergence was determined by the observationally determined probability distribution of Thornton and Parnell (2011).

In Chapter 3 we concluded that we had successfully produced a realistic model for the photospheric evolution of the magnetic carpet. Having experimented with varying the range of fluxes that a newly emerging bipole may take, we determined that the most realistic results were produced for the largest range of fluxes, $4 \times 10^{16} - 10^{19}$ Mx. For each case, the model quickly reached a steady state, in which the rates of emergence and cancellation of magnetic flux (Mx cm^{-2} day^{-1}) were roughly equal. For the most realistic simulation, the average value of the mean field was 6.6 G, in agreement with what is observed. Visually, we saw the formation of a magnetic

network around the boundaries of our modelled supergranule cells. Since the supergranular flow profile was not time evolving, the general shape of the network did not vary, however the exact distribution of magnetic elements changed significantly. Although a steady flow profile was used, this did not lead to the formation of unphysically large magnetic elements. The model was found to be highly dynamic, with the two most realistic simulations resulting in a photospheric recycle time of 1.48 hr and 1.75 hr, in agreement with the observed recycle time of $1-2$ hr determined by Hagenaar et al. (2008). We also found that the mean age of a magnetic element within our models was $9-20$ min, which is typical of an internetwork feature (de Wijn et al., 2008; Zhou et al., 2010), while the maximum age of a magnetic element in our models was $3-4$ hr, as may be observed for an ephemeral region (Harvey and Martin, 1973).

In Chapter 4, we introduced the magnetofrictional method, which was used to produce a continuous evolution of a non-linear force-free coronal field in response to photospheric boundary motions. This is in contrast to the coronal models described in Chapter 2, which used potential fields and independent extrapolations of the coronal field for each frame. We applied the magnetofrictional method to study the coronal interactions of three basic photospheric processes between two magnetic elements of equal flux but opposite polarity: cancellation, emergence and flyby. Each interaction was simulated in the presence of an overlying field of varying strength – 1 G, 5 G or 10 G, and at three different angles of interaction of the magnetic elements with respect to the overlying field – parallel, anti-parallel or perpendicular. We studied the energy built up and stored in the field in the form of free magnetic energy and energy dissipated within the coronal volume in response to the relaxation processes occurring. It was found that, in general, a stronger overlying field led to a greater amount of stored free energy and energy dissipated. The simulation resulting in the most free energy was a perpendicular cancellation with a 10 G overlying field, the simulation that resulted in the greatest energy dissipation was a parallel flyby with a 10 G overlying field. For each case, the free energy stored by the end of the simulation was $0.2-1.9\times10^{26}$ ergs. The average energy dissipation rate for each simulation ranged from $2.1-6.2\times10^{22}$ ergs s^{-1}, leading to a cumulative energy dissipation of $1.3-3.2\times10^{26}$ ergs over the whole 48 hr simulation. The exact amount of energy stored and dissipated at the end of each simulation depended upon several factors: the strength and orientation of the overlying field, the volume of the overlying field that was disturbed, the amount of reconnection that occurred and the total flux connecting from one magnetic element to the other. It was found that the energy dissipation was greatest low down in the corona, near the magnetic sources and where the field is most non-potential. An increased rate of energy dissipation was also found at sites of changing magnetic topology. A similar study was conducted in Chapter 5, where we considered the coronal evolution of a larger region, involving many hundreds of magnetic elements.

In Chapter 5, we chose a 48 hr time series of synthetic magnetograms produced from the model in Chapter 3. This series was used as the lower boundary condition to drive the continuous

evolution of a non-linear force-free coronal field, using the magnetofrictional method described in Chapter 4. The results presented in Chapter 5 are very much a preliminary analysis of the complex 3D simulations of the magnetic carpet coronal field. Within this chapter, we studied four simulations that used the same lower boundary data, with four different strengths of uniform overlying coronal field $-$ 0 G, 1 G, 3 G and 10 G. In particular, the four quantities studied were the free magnetic energy, the energy dissipated, the square of the magnetofrictional velocity, $\mathbf{v}^2$, and the square of the current density, $\mathbf{j}^2$. In agreement with Chapter 4, we found that a stronger overlying field led to a greater amount of free energy stored and energy dissipated. The mean free magnetic energy stored in each simulation varied between $1.09 - 1.96 \times 10^{27}$ ergs, whilst the mean dissipation rate was $0.8 - 1.1 \times 10^{24}$ ergs s^{-1}, leading to a cumulative energy dissipation of $1.43 - 1.89 \times 10^{29}$ ergs by the end of each simulation. When viewed in the $x - y$ plane, regions of positive free magnetic density energy were seen both in the magnetic network and across supergranules. Many of these regions were long-lived, lasting for several hours. The free magnetic energy within the volume was found to be stored along closed connections between magnetic elements, with most of the free energy being stored between $z = 0.5 - 0.8$ Mm. In contrast to the free energy density, regions of dissipated energy were much more rapidly evolving, and were predominantly seen in the magnetic network when viewed in the $x - y$ plane. As in Chapter 4, the energy dissipation term was at its largest low down near the magnetic elements and at sites of changing magnetic topology. It was also found to rapidly decrease with increasing height. From the analysis in Chapter 5, there was a clear relationship between the flux evolution processes occurring in the photospheric model and the rate of energy dissipation occurring in the corona above. However, further analysis is required to fully quantify this. In both Chapters 4 and 5, the free magnetic energy built up and stored was more than enough to account for small-scale transient phenomena such as XBP and nanoflares. The energy dissipation obtained was not high enough to entirely explain the heating of the quiet corona, however, from Chapter 5, each of the simulations could provide a contribution of $11 - 15\%$ to the required 3×10^5 ergs cm^{-2} s^{-1} of Withbroe and Noyes (1977).

Locations of $\mathbf{v}^2$ and $\mathbf{j}^2$ were also considered within Chapter 5. For $\mathbf{v}^2$, a background contribution was always present throughout the coronal volume due to the relaxation processes, in addition to regions of enhanced $\mathbf{v}^2$. Regions of enhanced $\mathbf{v}^2$ are of interest as they can be related to sites of changing magnetic topology, as well as the relaxation of the coronal magnetic field towards an equilibrium state. When viewed in the $x - y$ plane, such regions were seen both in the magnetic network and within the supergranule cells. The average value of $\mathbf{v}^2$ was found to rapidly decrease with height in the presence of an overlying field, however spikes in the maximum value of $\mathbf{v}^2$ were seen up to heights of a few Mm due to changing magnetic topology occurring in this region. If no overlying field was present, locations of increased $\mathbf{v}^2$ were seen throughout the coronal volume. Considering the current density, when viewed in the $x - y$ plane, regions of increased $\mathbf{j}^2$ were found to be co-located with regions of positive free magnetic energy density. This is due

to the dependence of both quantities on the field being non-potential. The average $\mathbf{j}^2$ was found to be largest low down, near the magnetic elements, and decreased rapidly with increasing height. At greater heights, $\mathbf{j}^2$ was seen to gradually increase with time, indicating that non-potentiality was slowly being propagated upwards as the simulations progressed.

6.1 Future Work

There are many possible future projects that could extend from both the 2D and 3D models presented in this thesis, as well as many improvements that could be made to both models. For the 2D model presented in Chapter 3, it would be of interest to conduct a feature tracking study (e.g. DeForest et al. (2007); Lamb et al. (2008, 2010)) on the synthetic magnetograms produced. This would allow us to more accurately compare our results with the results of studies of observed magnetograms (e.g. Hagenaar et al. (2008); de Wijn et al. (2008); Parnell et al. (2009); Zhou et al. (2010)). Another project that could be conducted with the 2D model is to allow a flux emergence range that extends down to flux values much lower than can currently be observed, for example $\phi_{\text{min}} = 10^{14}$ Mx or $\phi_{\text{min}} = 10^{15}$ Mx. This would allow us to test whether extending the flux emergence probability distribution down to such values still correctly reproduces the observed distribution of magnetic fluxes, as well as other properties we have considered in Chapter 3, such as the photospheric recycle time. There are many improvements that could be made to our 2D model in the future. One such improvement would be to include an evolving supergranular flow; this could easily be taken from observed data using the balltrack method of Potts et al. (2004). Even if the flow profile were not time evolving, a more complex flow profile in the photospheric model could have interesting implications for the evolution of the coronal model. For example, as discussed in Section 3.3, a flow profile that included vorticity would introduce twisting and braiding into the coronal magnetic field. Also discussed in Section 3.3, the fragmentation process is a limitation of our model. It is currently artificially imposed, however, it could instead be modelled to be dependent upon underlying granulation, as could be the case on the Sun (Parnell, 2001). In addition to this, the 2D model can be continually updated as observational instruments are improved and new observational results are obtained. In future, the 2D model will be extended to cover the whole surface of the Sun. This would allow us to produce global simulations of an extremely quiet Sun, such as may arise during a grand minimum in solar activity (e.g. Eddy (1976)). With the global simulation a key feature would be the inclusion of a non-steady supergranular flow.

For the 3D model presented in Chapters 4 and 5 there are many possibilities for future projects using the magnetofrictional method as it is now, and for improving it. For the simulations discussed in Chapter 5, a more in-depth analysis will be carried out. We will study the connectivity of the magnetic elements; topological features such as coronal nulls and the magnetic skeleton

(e.g. Parnell et al. (2008)); and consider the coronal remap time of our model (Close et al., 2004). We will also investigate in more detail how the flux evolution processes occurring in the photospheric model influence the evolution of the coronal magnetic field. In the future, the magnetofrictional technique will be applied to real magnetogram data, observed using a magnetograph such as SDO/HMI. Initially we will consider the 'global' evolution of quantities with the simulations, for example the free energy and energy dissipated integrated over the volume. Subsequently, a more in-depth analysis of these simulations will also be carried out. It would be of particular interest to compare locations of free energy storage and energy dissipation within the simulated coronal field to corresponding coronal images taken for example by SDO/AIA. In addition to this, we intend to extend the present magnetofrictional model to contain plasma by including the pressure and density terms in the equations of MHD.

Appendix A

Parameters, Arrays and Subroutines for 2D Model

This appendix details the parameters, arrays and some of the subroutines within our 2D model for the photospheric evolution of the magnetic carpet.

A.1 Parameters

The following are parameters that are read in by the code through the 'modelname_param' file.

nx, ny, nz: These are the number of grid cells in the x, y and z directions respectively. Normally they are a power of 2.

x_{max}: Currently $y_{\text{max}} = x_{\text{max}}$, and $y_{\text{min}} = x_{\text{min}} = 0$. These parameters are specified in Mm.

nminor: The number of minor time steps per major time step, normally set to 10. This is the basic time step for the model. The length of one minor time step in minutes is given by the parameter step_length.

nmajor: The number of major time steps that the simulation will run for. In general, 1 major time step equals 10 minor time steps. If 1 minor step represents 1 minute, 1 major time step then represents 10 minutes.

ϕ_0: The smallest unit of flux. All magnetic elements within the code have an absolute flux that is an integer multiple of ϕ_0. In general, $\phi_0 = 10^{16}$ Mx.

$f_{\text{min}}/f_{\text{max}}$: The minimum and maximum values of flux for emerging bipoles in Mx. Since each emerging magnetic element will have an absolute flux of exactly half that of the bipole, the

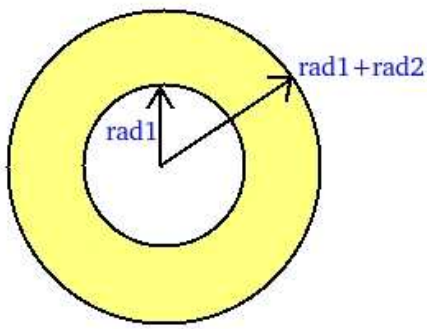

Figure A.1: Bipoles emerge within the region $[(\frac{\text{rad1}}{2})R_{\text{sg}}, (\frac{\text{rad1+rad2}}{2})R_{\text{sg}}]$ of a supergranule, where $R_{\text{sg}} = A_0 R_0 (x_{\text{max}} - x_{\text{min}})$.

minimum value f_{min} can not be less than $2\phi_0$. In addition, both f_{min} and f_{max} should be integer multiples of ϕ_0.

step_length: The number of minutes that one minor time step represents. The default value is 1 minute, which means that a major time step represents 10 minutes.

rad1, rad2: These represent the region within a supergranule cell in which emergence can occur. So if rad1=1.0 and rad2=0.5, emergence of new bipoles occurs in the range $[(\frac{\text{rad1}}{2})R_{\text{sg}}, (\frac{\text{rad1+rad2}}{2})R_{\text{sg}}] = [0.5R_{\text{sg}}, 0.75R_{\text{sg}}]$, where $R_{\text{sg}} = 2A_0 R_0 (x_{\text{max}} - x_{\text{min}})$ (see Figure A.1). The initial position of a newly emerging bipole is restricted to this range. However, the individual elements of each bipole may travel outwith this range as they separate during the emergence process.

ψ: Parameter involved in determining whether fragmentation will occur for a magnetic element of absolute flux ϕ. $\psi = 8 \times 10^{18}$ Mx is chosen to be the same as that of Parnell (2001), with the result that, within the simulations discussed in Chapter 3, all magnetic elements with absolute flux $\phi \geq 0.25\psi = 2 \times 10^{18}$ Mx are guaranteed to fragment within a given time, unless some other process takes over their evolution before then.

frag_rate: This parameter determines the frequency at which fragmentation occurs. If frag_rate $= R_{\text{f}} = 1.5 \times 10^{-4}$ s^{-1} then a magnetic element will fragment roughly once every $1/R_{\text{f}} =$ 6667 seconds $\approx$ 1 hour 50 mins. Parnell (2001) suggests that a fragmentation rate of greater than 1.2×10^{-4} s^{-1} is required to reproduce the correct absolute flux density and flux distribution.

e_{rad}: The two magnetic elements within a bipole will continue to move apart along their tilt axis until they reach a certain separation from each other, determined by this value. Once this separation distance has been reached, the supergranular flow profile takes over the motion of each feature. We set $e_{\text{rad}} = 1.5$, so that a magnetic element j must reach a distance

of $1.5d(\phi_j)$ from its original emergence point before supergranular flows take over, where $d(\phi_j)$ is the width of an element j of flux ϕ_j, defined by Equation (3.3). This is equivalent to a separation of $0.75(d(\phi_j) + d(\phi_k))$ since j and k are of equal width.

c_{rad}: This value determines the separation distance that two magnetic elements must be within before they will cancel or coalesce. We set $c_{\text{rad}} = 0.5$, so that if the separation of two elements, j and k, is less than or equal to $0.5(d(\phi_j) + d(\phi_k))$, they will move towards one another and cancel or coalesce. It is important that this separation distance is less than the separation achieved by emergence or fragmentation so that pairs of elements that have just undergone these processes do not immediately cancel or coalesce with one another once more.

f_{rad}: Determines the distance that a magnetic element will travel from its original fragmentation point before the fragmentation process no longer determines its motion. $f_{\text{rad}} = 1.5$, which means that a magnetic element j will travel a distance of $1.5d(\phi_j)$ from the point at which it fragmented before supergranular flows take over. However, since fragmentation is not a dominant process, it may be determined that j will cancel or coalesce with another element before it reaches this distance. (An element is forbidden to coalesce with the element it has just split from until after they have reached a separation of $1.5d(\phi)$ from their fragmentation point, however.)

fpush: When an element fragments, depending on the process it was undergoing beforehand it may take on the same velocity as the underlying supergranular flow at the fragmentation location, as described in Section 3.1.4. However, in the network supergranular flows tend to be small. If this is the case, the two elements resulting from the split may be given a 'push' to help them separate. A typical value for fpush is 0.2 km s^{-1}.

maxsg: This parameter specifies the peak value that arises in the supergranular flow pattern. After the initial flow pattern is computed as in Section 3.1.2, it is scaled so that the maximum is maxsg. From observations, a typical value is maxsg$= 0.5$ km s^{-1}.

A.2 Arrays

The following is a summary of the arrays used within the code.

emerge_step: This array has length equal to nmajor $\times$ nminor. Each entry emerge_step(i) is an integer that corresponds to the number of bipoles that will emerge in minor time step i. Clearly, the number of individual magnetic elements emerging during step i will be $2\times$emerge_step(i). A new set of parameter arrays is generated every n_time_step steps (normally n_time_step$= 200$) to keep arrays from becoming too large in long simulations. Every

n_time_step steps the emerge_step array is updated with the next n_time_step entries as a new set of emerging bipole parameters is computed.

The following six arrays are randomly generated before the main evolution program is run: $xc1$, $yc1$, flux1, wid1, sign1, and tilt1. The coordinates for all newly emerging magnetic elements are stored in the arrays $xc1$ and $yc1$. Their absolute flux, sign, width and tilt angle for emergence are similarly stored in the appropriate arrays of label 1.

So that this information is not lost, identical copies of these arrays are created and named $xc3$, $yc3$, etc. The arrays of label 3 will be edited as the magnetic elements evolve. New entries are added to the arrays in the appropriate positions when fragmentation occurs, and entries are removed from the arrays in the case of coalescence or cancellation. This prevents indices from being confused when newly emerging magnetic elements are introduced. Every time a new set of arrays of label 1 is created, they are added to the end of the arrays of label 3 as a new set of emerging bipoles. A third set of arrays of label 2 contain the information for only those magnetic elements that exist within the current minor time step. The label 2 arrays are updated every minor time step with new coordinates, fluxes, widths and signs where appropriate.

At the end of each minor time step t, entries for newly emerging magnetic elements are added to the arrays $xc2$, $yc2$, flux2, etc. The way that we do this is to set

$$n_1 = n\_elements(xc2) \quad \text{and} \quad n_2 = n_1 + 2 \times \text{emerge\_step}(t).$$

Then

$$xc2 = [xc2, xc3(n_1 : n_2 - 1)],$$

$$yc2 = [yc2, yc3(n_1 : n_2 - 1)],$$

$$\text{flux2} = [\text{flux2}, \text{flux3}(n_1 : n_2 - 1)],$$

and so on.

When an element must be removed from the arrays due to cancellation or coalescence, we simply remove the same index from all the arrays of label 2 and label 3 (see Section A.5). The fragmentation case is slightly more complicated. We add a new element onto the end of all the arrays of label 2, but this element must most likely be added somewhere in the middle of the arrays of label 3, at the n_1th index (see Section A.4).

Below is a description of the parameter arrays of label 2 and 3.

$xc2/xc3$: $xc2$ contains the $x-$coordinate for every magnetic element within the simulation during the current minor time step. The entries are updated every minor time step as the mag-

netic elements move due to various processes. At the end of each minor time step, the x-coordinates of all newly emerging magnetic elements must be added on to the end of the $xc2$ array. These values are taken from the array $xc3$. The value in each entry j in $xc3$ does not change throughout the simulation unless fragmentation occurs. In the case of fragmentation, entry j is replaced with the x coordinate of the point where fragmentation took place. This means that $xc3$ can be used along with $xc2$ to keep track of the distance that a magnetic element has travelled from its emergence or fragmentation point. This is important, since the processes of emergence and fragmentation are determined to end once a magnetic element has travelled a certain distance.

$yc2$/$yc3$: These arrays work in exactly the same way as is described above for $xc2$ and $xc3$, except for the $y-$coordinate of each magnetic element.

flux2/flux3: These arrays contain the absolute flux values for each magnetic element. The values in flux3 do not change throughout the simulation, but the array is lengthened and shortened due to cancellation, coalescence and fragmentation. Values within flux2 do change, however, due to the same three processes. Flux values for newly emerging magnetic elements are added on to the end of flux2 from flux3.

wid2/wid3: As above, widths for newly emerging magnetic elements are added to wid2 from wid3, and the values within wid3 do not change throughout the simulation. Elements within wid2 are assigned a new width when their flux changes due to cancellation, coalescence or fragmentation.

sign2/sign3: Values within sign3 do not change throughout the simulation. The only time that a value within sign2 will change is in the case of a partial cancellation. During a partial cancellation, the element with the highest index is removed from all of the arrays, while the element with the lower index is updated with the new combined values from both magnetic elements. If the lower index element has a smaller absolute flux than the higher index element, the resulting flux will be of the same sign as that of the original higher element but will take the place of the lower element in the sign2 array.

tilt2/tilt3: The only time the values within these arrays change during the simulation is when an emerging element fragments. The two resultant elements continue to evolve according to the emergence process, but in different directions determined by the tilt angle. The array lengths change due to cancellation, coalescence, fragmentation and the emergence of new elements. The tilt angle is only required in the first stage of a newly emerging magnetic element's lifetime, to determine the angle with respect to the x-direction of its axis of emergence.

sgcell: This array is created before the main program is run, along with the six parameter arrays described above. Its length is the same as that of $xc1$, and it is used to keep note of the index

of the supergranule cell in which each magnetic element emerges. When the main program begins, an identical array sgcell3 is created, whose length will be edited along with the other arrays of label 3 due to cancellation, coalescence and fragmentation. When cancellation or coalescence occur, the new element is assigned the same supergranule cell as the original element of lower index. When fragmentation occurs, both new elements have the same supergranule index as the original element.

vx, vy: These arrays store the $x-$ and $y-$components of the velocity for every magnetic element that currently exists within the simulation. Every minor time step i, new arrays vx and vy are created of length $n\_elements(xc2)$. A loop over all magnetic elements j determines each element's velocity in turn depending on the various processes described in Section 3.1, to give $vx(j)$ and $vy(j)$ in km s^{-1}.

type: This array contains an integer entry for every magnetic element, to keep track of which process is currently determining that element's evolution. The integers $0, 1, 2$ and 3 represent supergranular flows, emergence, cancellation/coalescence and fragmentation respectively.

lifetime: This array keeps track of how long each magnetic element's evolution has been determined by the current mechanism. Every time an element j begins a new process, we set lifetime$(j) = 0$. Every minor time step we update the lifetime array by adding 1 onto every entry just before the positions of the magnetic elements are updated. This is used to keep track of how long magnetic elements live for. It is also used in the fragmentation process, where older elements are more likely to fragment (see Section 3.1.4).

c_array: This array keeps track of pairs of magnetic elements that are cancelling or coalescing. The default value for all entries within this array is -1. When it is determined that two elements j and k will cancel/coalesce, we set c_array$(j) = k$ and c_array$(k) = j$.

canc_ind: This array is the same length as $xc2$, and indicates when two magnetic elements cancel or coalesce together. The default value for entries within this array is 0. When j and k are determined to meet and cancel/coalesce we set canc_ind$(j) = 1$ and canc_ind$(k) = 1$. At the end of each time step, pairs of elements with this label are combined into one element or completely removed if full cancellation has occurred.

f_array: When two elements j and k initially split from one another during fragmentation, we set f_array$(j) = k$ and f_array$(k) = j$ to indicate that they should not immediately be allowed to coalesce with one another.

frag_vx/frag_vy: The $x-$ and $y-$components of a fragmenting magnetic element's velocity are determined at the point where it initially fragments. These values are stored in the arrays frag_vx and frag_vy so that the element's velocity remains constant throughout the fragmentation process.

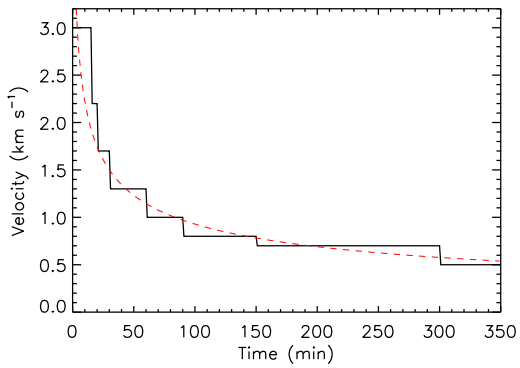

Figure A.2: Separation velocity, v_{sep}, as a function of time, for newly emerging magnetic elements. A curve is fitted to the separation velocities within the code, and is overplotted as a red dashed line.

A.3 Emergence Velocities

A magnetic element will undergo emergence until it has travelled a certain distance from its initial position, defined to be $e_{\text{rad}} \times d(\phi) = 1.5d(\phi)$, where $d(\phi)$ is the width of an element of flux ϕ, defined by Equation (3.3). During emergence, the feature's velocity depends upon its age, tilt angle θ and sign. If an element's age in minutes is t, then its velocity in km s^{-1} is:

- $0 \leq$ t $\leq$ 15 mins: $v_{\text{sep}} = 3.0$ km s^{-1},
- 15 $<$ t $\leq$ 20 mins: $v_{\text{sep}} = 2.2$ km s^{-1},
- 20 $<$ t $\leq$ 30 mins: $v_{\text{sep}} = 1.7$ km s^{-1},
- 30 $<$ t $\leq$ 60 mins: $v_{\text{sep}} = 1.3$ km s^{-1},
- 60 $<$ t $\leq$ 90 mins: $v_{\text{sep}} = 1.0$ km s^{-1},
- 90 $<$ t $\leq$ 150 mins: $v_{\text{sep}} = 0.8$ km s^{-1},
- 150 $<$ t $\leq$ 300 mins: $v_{\text{sep}} = 0.7$ km s^{-1},
- t $>$ 300 mins: $v_{\text{sep}} = 0.5$ km s^{-1}.

A plot of v_{sep} as a function of time is shown in Figure A.2. The curve

$$\ln(v_{\text{sep}}) = -0.013\ln(t)^2 - 0.305\ln(t) + 1.603$$

is fitted to the velocities for t in min, and is overplotted as a red dashed line. Having defined the separation velocities, for a positive magnetic element we then have

$$v_x = v_{\text{sep}}\cos(\theta + \pi),$$

$$v_y = v_{\text{sep}}\sin(\theta + \pi),$$

and for a negative magnetic element

$$v_x = v_{\text{sep}}\cos(\theta),$$

$$v_y = v_{\text{sep}}\sin(\theta).$$

This ensures that a pair of emerging magnetic elements will always move in the opposite direction to one another, along the axis given by their tilt angle.

A.4 Adding an Element to an Array

If a magnetic feature is determined to fragment, we add a new index to all of the arrays in preparation. This new index is added to the end of the $xc2$ array, and all other arrays of the same length. The index will be added to the middle of the arrays of length $n\_elements(xc3)$ if they are longer than $xc2$; in this case, the index is added to the position $n\_elements(xc2)$.

An element of index k is added to an array in the following manner:

$k = n\_elements(xc2)$

first $= 0$

last $= n\_elements(array) - 1$

case k of

first: $array = [element, array]$

last: $array = [array, element]$

else: $array = [array[first : k], element, array[k + 1, last]]$

endcase

Parameters are assigned to the new magnetic element, such as position and flux, as each array is updated.

A.5 Removing an Element from an Array

When cancellation or coalescence occurs between two magnetic elements j and k, we must remove either one or both of them from all of the parameter arrays, depending on whether full cancellation has occurred. We remove an index k from an array as follows:

first= 0

last= $n\_elements(array) - 1$

case k of

first: $array = array[1 : *]$

last: $array = array[first : last - 1]$

else: $array = [array[first : k - 1], array[k + 1, last]]$

endcase

If partial cancellation or coalescence has occurred, the parameters for the remaining magnetic element are updated for its new combined flux value. If full cancellation has occurred then index j is also removed from all of the arrays.

Appendix B

Calculations for the Magnetofrictional Code

B.1 Staggered Grid

For the 3D coronal field model in Chapters 4 and 5, we use a staggered grid in order to achieve second order accuracy when differentiating variables numerically. Figure B.1 shows a cartoon indicating where each of the variables is located in a grid cell. The components of $\mathbf{B}$ are located on the cell faces, while the components of the vector potential, $\mathbf{A}$, are located on the ribs, so that $\mathbf{B} = \nabla \times \mathbf{A}$ may be computed to second order accuracy. Similarly, the components of $\mathbf{j}$ are located on the ribs, as $\mathbf{j} = \nabla \times \mathbf{B}$. So that we may compute $\mathbf{j} = \nabla \times \mathbf{B}$ to second order, $\mathbf{B}$ must be extended beyond the boundaries of the numerical box in the form of ghost points. This is illustrated in the $x - y$ plane in Figure B.2, where

- B_z is located on the cell faces (blue dots),
- A_x and j_x lie on the $x-$ribs (red dots),
- A_y and j_y lie on the $y-$ribs (red dots),
- v_x, v_y and v_z are located at cell corners (black dots).

We extend $\mathbf{B}$ beyond the boundaries of the box as follows. If the boundary is closed, then the ghost values of B_z beyond the boundary are set equal to the adjacent values of B_z inside the box (Figure B.3(a)). If the boundary is periodic, then the ghost values of B_z beyond the boundary are set equal to the values of B_z inside the box at the opposite boundary (Figure B.3(b)). For example, consider B_z in the model in Chapter 4, where the numerical box is closed in the $y-$direction and

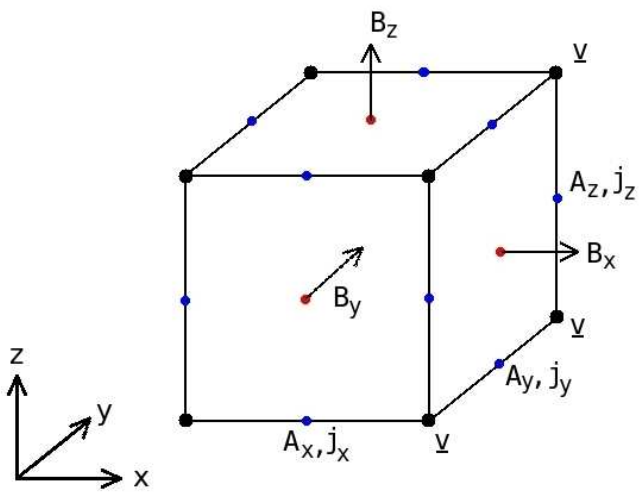

Figure B.1: A cell in the computational box for the 3D coronal model, indicating the locations of variables.

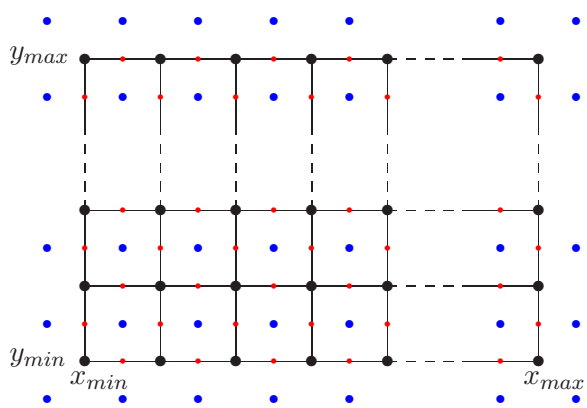

Figure B.2: The computational grid in the $x - y$ plane, with B_z extended beyond the boundaries. Blue dots in the cell faces represent B_z; red dots on the ribs represent A_x or j_x on the horizontal $x-$ribs and A_y or j_y on the vertical $y-$ribs; black dots at the cell corners represent v_x, v_y or v_z.

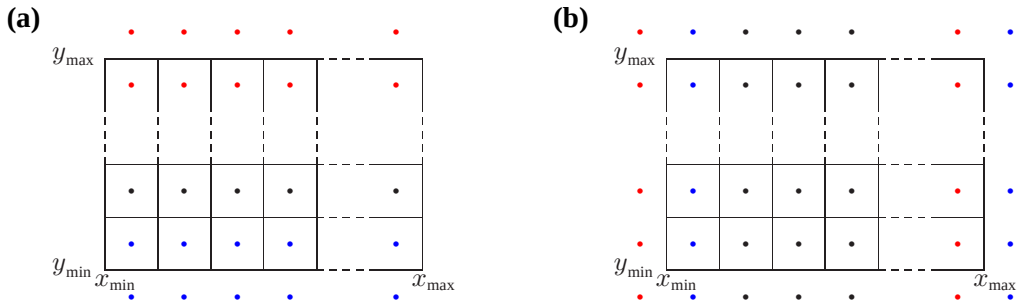

Figure B.3: (a) For a numerical box that is closed in the $y-$direction, B_z is extended beyond the $y-$boundaries into ghost cells. The top row of red ghost values is equal to the row of red values immediately beneath, within the numerical box. Similarly, the bottom row of blue values is equal to the row of blue values immediately above, within the numerical box. (b) For a numerical box that is periodic in the $x-$direction, B_z is extended beyond the $x-$boundaries into ghost cells. The left-hand column of red ghost values is equal to the column of red values on the right, within the numerical box. The right-hand column of blue ghost values on the right is equal to the column of blue values on the left, within the numerical box.

periodic in the $x-$direction. Viewed in the $x-y$ plane, B_z is located on the cell faces, as illustrated by the blue dots in Figure B.2. The numerical box has dimensions $(nx) \times (ny) \times (nz)$; therefore the variable B_z has dimensions $(nx+2) \times (ny+2) \times (nz+1)$ - this comes from having two rows of ghost values in both the $x-$ and $y-$directions, and the nz cells in the $z-$direction resulting in $nz+1$ faces in the $z-$direction. $B_z(1:nx, 1:ny, 0:nz)$, which is contained within the numerical box, excluding the ghost cells, is known. Since the box is closed in the $y-$ direction, we extend B_z outside the $y-$boundaries as follows:

$$B_z(1:nx, 0, 0:nz) = B_z(1:nx, 1, 0:nz)$$

and

$$B_z(1:nx, ny+1, 0:nz) = B_z(1:nx+1, ny, 0:nz),$$

i.e. the 0th row equals the first row and the $(ny+1)$th row equals the (ny)th row (Figure B.3(a)). To extend B_z in the $x-$direction, which is periodic, we compute:

$$B_z(0, 0:ny+1, 0:nz) = B_z(nx, 0:ny+1, 0:nz)$$

and

$$B_z(nx+1, 0:ny+1, 0:nz) = B_z(1, 0:ny+1, 0:nz),$$

i.e. the 0th column equals the (nx)th column and the $(nx+1)$th column equals the 1st column (Figure B.3(b)). Once the components of $\mathbf{B}$ have been extended beyond the boundaries of the

numerical box, we can compute the components of **j**, e.g.

$$\begin{aligned} j_x &= \frac{B_z(0:nx+1, 1:ny+1, 0:nz) - B_z(0:nx+1, 0:ny, 0:nz)}{\Delta y} \\ &\quad - \frac{B_y(0:nx+1, 0:ny, 1:nz+1) - B_y(0:nx+1, 0:ny, 0:nz)}{\Delta z}, \end{aligned}$$

and similarly for j_y and j_z. The components of $\mathbf{v}$ are located on the cell corners. In order to compute $\mathbf{v}$, the components of $\mathbf{B}$ and **j** must first be moved to the cell corners by averaging, then

$$\mathbf{v} = \frac{1}{\nu}\frac{\mathbf{j} \times \mathbf{B}}{B^2}.$$

If we wish to compute the integral of a variable over the numerical volume, that variable must first be moved to the centres of the grid cells, and will hence occupy an array of size $(nx) \times (ny) \times (nz)$.

B.2 Calculating Energy Dissipation

The energy dissipation term, Q, is discussed in Chapters 4 and 5. This section describes how Q is derived from the equation for magnetic energy. We compute the rate of change of the magnetic energy as follows:

$$W = \int_V \frac{B^2}{8\pi} dV,$$

$$\therefore \frac{dW}{dt} = \frac{1}{4\pi}\int_V \frac{d}{dt}\left(\frac{B^2}{2}\right) dV.$$

$$\frac{d}{dt}\left(\frac{B^2}{2}\right) = \mathbf{B} \cdot \frac{\partial \mathbf{B}}{\partial t}$$

We expand this out by substituting in the coronal field induction equation,

$$\frac{\partial \mathbf{A}}{\partial t} = \mathbf{v} \times \mathbf{B} + \boldsymbol{\epsilon},$$

and using the equations for hyperdiffusion

$$\boldsymbol{\epsilon} = \frac{\mathbf{B}}{B^2}\nabla \cdot (\eta_4 B^2 \nabla \alpha),$$

the magnetofrictional velocity

$$\mathbf{v} = \frac{1}{\nu}\frac{\mathbf{j} \times \mathbf{B}}{B^2},$$

where $\mathbf{j} = \nabla \times \mathbf{B}$, and α

$$\alpha = \frac{(\nabla \times \mathbf{B}) \cdot \mathbf{B}}{B^2}.$$

We also make use of the following vector identities:

$$\begin{aligned}
\mathbf{B} \cdot \nabla \times \mathbf{A} &= \nabla \cdot (\mathbf{A} \times \mathbf{B}) + \mathbf{A} \cdot \nabla \times \mathbf{B}, \\
(\mathbf{A} \times \mathbf{B}) \cdot \mathbf{C} &= -(\mathbf{C} \times \mathbf{B}) \cdot \mathbf{A}, \\
f \nabla \cdot \mathbf{A} &= \nabla \cdot f\mathbf{A} - \mathbf{A} \cdot \nabla f,
\end{aligned}$$

where $\mathbf{A}$, $\mathbf{B}$ and $\mathbf{C}$ are vectors and f is a scalar. This gives

$$\begin{aligned}
\frac{d}{dt}\left(\frac{B^2}{2}\right) &= \mathbf{B} \cdot \nabla \times (\mathbf{v} \times \mathbf{B} + \boldsymbol{\epsilon}) \\
&= \nabla \cdot [(\mathbf{v} \times \mathbf{B} + \boldsymbol{\epsilon}) \times \mathbf{B}] \; + \; (\mathbf{v} \times \mathbf{B} + \boldsymbol{\epsilon}) \cdot (\nabla \times \mathbf{B}) \\
&= \nabla \cdot [(\mathbf{v} \times \mathbf{B} + \boldsymbol{\epsilon}) \times \mathbf{B}] \; - \; [(\nabla \times \mathbf{B}) \times \mathbf{B}] \cdot \mathbf{v} \\
&\quad + (\nabla \times \mathbf{B}) \cdot \frac{\mathbf{B}}{B^2} \nabla \cdot (\eta_4 B^2 \nabla \alpha) \\
&= \nabla \cdot [(\mathbf{v} \times \mathbf{B} + \boldsymbol{\epsilon}) \times \mathbf{B}] \; - \; \nu B^2 |\mathbf{v}|^2 \; + \; \alpha \nabla \cdot (\eta_4 B^2 \nabla \alpha) \\
&= \nabla \cdot [(\mathbf{v} \times \mathbf{B} + \boldsymbol{\epsilon}) \times \mathbf{B}] \; - \; \nu B^2 |\mathbf{v}|^2 \; + \; \nabla \cdot (\eta_4 B^2 \alpha \nabla \alpha) \\
&\quad - \eta_4 B^2 \nabla \alpha \cdot \nabla \alpha
\end{aligned}$$

$$\begin{aligned}
\therefore \frac{dW}{dt} &= \frac{1}{4\pi} \iiint_V \Big[\nabla \cdot [(\mathbf{v} \times \mathbf{B} + \boldsymbol{\epsilon}) \times \mathbf{B} \; + \; \eta_4 B^2 \alpha \nabla \alpha] \\
&\quad - \nu B^2 |\mathbf{v}|^2 \; - \; \eta_4 B^2 |\nabla \alpha|^2 \Big] \, dV.
\end{aligned}$$

We now apply the Divergence Theorem:

$$\iiint_V (\nabla \cdot \mathbf{B})\, dV = \iint_S \mathbf{B} \cdot dS,$$

where S is the surface bounding the volume V. Within the simulations discussed in this thesis, all boundaries other than the lower boundary are either closed or periodic. Hence magnetic flux may only enter or exit the box through the lower boundary surface, and we may take S to represent only the lower boundary surface. Therefore

$$\begin{aligned} \frac{dW}{dt} &= \frac{1}{4\pi} \iint_S [(\mathbf{v} \times \mathbf{B} + \boldsymbol{\epsilon}) \times \mathbf{B} \; + \; \eta_4 B^2 \alpha \nabla \alpha]\, dS \\ &\quad - \iiint_V B^2 (\nu |\mathbf{v}|^2 \; + \; \eta_4 |\nabla \alpha|^2)\, dV \\ &= \iint_S \mathbf{I}\, dS \; - \; \iiint_V Q\, dV, \end{aligned}$$

where

$$\mathbf{I} \equiv \frac{1}{4\pi} \Big[(\mathbf{v} \times \mathbf{B} + \boldsymbol{\epsilon}) \times \mathbf{B} + \eta_4 B^2 \alpha \nabla \alpha \Big]$$

and

$$Q \equiv \frac{B^2}{4\pi} (\nu |\mathbf{v}|^2 + \eta_4 |\nabla \alpha|^2).$$

The first term in **I** describes energy that is injected or removed through the lower boundary surface, due to surface motions, emergence and cancellation. The second term describes energy injected or removed through the lower boundary due to hyperdiffusion. Within this thesis, we do not compute **I** in our simulations.

The rate of energy dissipation, Q, may be separated into terms due to magnetofriction and hyperdiffusion

$$Q_{\text{frc}} = \frac{B^2}{4\pi} \nu |\mathbf{v}|^2 \quad \text{and} \quad Q_{\text{hd}} = \frac{B^2}{4\pi} \eta_4 |\nabla \alpha|^2.$$

Q is discussed in more detail in Chapters 4 and 5.

B.3 Dimensional Values

This appendix describes some of the calculations required to convert dimensionless quantities from the magnetofrictional FORTRAN code into dimensional values.

B.3.1 Time Steps

Within the magnetofrictional code, there are three types of time step. These are

major: Major time steps are the largest time steps within the code. Parameters within the code are normalised so that one major time step is one unit of time.

- Chapter 4: one major time step represents 33.3 min = 2000 s.
- Chapter 5: one major time step represents 10 min = 600 s.

minor: There are 10 minor time steps to one major time step. The arrays A_x, A_y and A_z are written out to a file every minor time step.

- Chapter 4: one minor time step represents 3.3 min = 200 s.
- Chapter 5: one minor time step represents 1 min = 60 s.

nrep: The smallest time steps are nreps, these are the time steps for magnetofrictional relaxation between each analytically specified photospheric boundary distribution. There 500 nreps per minor time step.

- Chapter 4: one nrep represents 0.4 s.
- Chapter 5: one nrep represents 0.12 s.

B.3.2 η_4

The hyperdiffusivity constant, η_4, is dependent on numerical resolution. Within the FORTRAN code it is given by

$$\eta_4 = \eta_{4\_0} \frac{(\Delta x)^4}{\Delta t_{\text{nrep}}},$$

where η_{4_0} is a value we choose, Δx is the size of the grid spacing, and Δt_{nrep} is the size of one magnetofrictional step in terms of major time steps.

$$\Delta t_{\text{nrep}} = \frac{\text{nmajor}}{5000}$$

In both Chapters 4 and 5, we have assumed that one unit of distance within the code represents 1 Mm. The scalings for major and minor time steps are given above. Therefore we have:

Chapter 4:

$$\eta_{4\_0} = 0.001 \tag{B.1}$$

$$\Delta x = \frac{30}{256} = 0.117 \text{ Mm}$$

$$\text{nmajor} = 2000 \text{ s}$$

$$\eta_4 = 0.001 \times \frac{(117 \text{ km})^4 \times 5000}{2000 \text{ s}} = 4.715 \times 10^5 \text{ km}^4 \text{ s}^{-1}$$

Chapter 5:

$$\eta_{4\_0} = 0.001 \tag{B.2}$$

$$\Delta x = \frac{50}{512} = 0.098 \text{ Mm}$$

$$\text{nmajor} = 600 \text{ s}$$

$$\eta_4 = 0.001 \times \frac{(98 \text{ km})^4 \times 5000}{600 \text{ s}} = 7.579 \times 10^5 \text{ km}^4 \text{ s}^{-1}$$

B.3.3 Magnetofrictional Velocity $\mathbf{v}$

The magnetofrictional velocity, $\mathbf{v}$, is computed in terms of Mm per major time step within the code. Therefore, in order to convert to km s^{-1}, velocities must be multiplied by

$$\frac{10^3}{2000}$$

in Chapter 4, and by

$$\frac{10^3}{600}$$

in Chapter 5.

B.4 Q

Within the FORTRAN code, ν and η_4 are both calculated per major time step. So Q is calculated in ergs per major time step. The quantity must therefore be divided by 2000 s in Chapter 4 or 600 s in Chapter 5 to convert it to ergs s^{-1}.

Appendix C

List of Movies

Several movies are included with this thesis and are held on the two accompanying CDs. The following is a short description of each of them. For a fuller description, see the corresponding chapters.

C.1 CD1: Chapter 3

For each of the movies, red contours represent positive magnetic field and blue contours represent negative magnetic field. Ten contour levels are shown for each polarity, with absolute values spaced evenly between 5 G and 95 G, unless stated otherwise.

- *sgflow.mpg*
  The steady supergranular flow profile used in each of the simulations in this chapter, with random granular contributions added on.
- *mag2_em.mpg*
  Examples of newly emerging bipoles. Twenty contour levels are shown for each polarity, with absolute values spaced evenly between 1.8 G and 68.3 G.
- *mag3_frag.mpg*
  Examples of fragmentation of magnetic elements. Fifteen contour levels are shown for each polarity, with absolute values spaced evenly between 2.3 G and 67.7 G.
- *mag1_canc.mpg*
  Examples of cancellation and coalescence of magnetic elements. Fifteen contour levels are shown for each polarity, with absolute values spaced evenly between 2.3 G and 67.7 G.

- *mag1_start.mpg*
  Synthetic magnetogram series with a flux emergence range of $10^{17} - 10^{19}$ Mx, shown from $t = 0 - 20$ hr.

- *mag1_mid.mpg*
  Synthetic magnetogram series with a flux emergence range of $10^{17} - 10^{19}$ Mx, shown from $t = 50 - 60$ hr.

- *mag4_start.mpg*
  Synthetic magnetogram series with a flux emergence range of $4 \times 10^{16} - 10^{19}$ Mx, shown from $t = 0 - 20$ hr.

- *mag4_mid.mpg*
  Synthetic magnetogram series with a flux emergence range of $4 \times 10^{16} - 10^{19}$ Mx, shown from $t = 50 - 60$ hr.

- *mag_em4_mid.mpg*
  Synthetic magnetogram series where emergence is switched off at $t = 50$ hr, shown from $t = 50 - 60$ hr.

C.2 CD2: Chapter 5

All movies listed below are for the 3 G simulation, unless stated otherwise. Where null points are included, only nulls of height $z = 0.5$ Mm or above are shown. Where contours of B_z are included, red contours represent positive magnetic field and green contours represent negative magnetic field. Contours are shown at levels of $\pm[7, 13, 27, 53, 106]$ G, unless stated otherwise.

- *magnet48_bz.mpg*
  48 hr series of synthetic magnetograms used as the lower boundary condition for the 3D simulations, from $t = 120 - 168$ hr. Red and blue contours respresent positive and negative magnetic field, with ten contour levels for each polarity, spaced evenly between 7.5 G and 142.5 G.

- *magnet48b_free_ht.mpg*
  Free magnetic energy (integrated in x and y) as a function of height.

- *magnet48b_free_xy.mpg*
  Free magnetic energy density (integrated in z) viewed in the $x - y$ plane. The movie is saturated at $\pm 1.9 \times 10^{22}$ ergs.

- *magnet48b_free_xy_bz.mpg*
  Free magnetic energy density (integrated in z) viewed in the $x - y$ plane, with contours of B_z at $z = 0$ Mm. The movie is saturated at $\pm 1.9 \times 10^{22}$ ergs.

- *magnet48b_free_xy_nulls.mpg*
  Free magnetic energy density (integrated in z) viewed in the $x - y$ plane, with null points (yellow stars). The movie is saturated at $\pm 1.9 \times 10^{22}$ ergs.

- *magnet48b_free_xz.mpg*
  Free magnetic energy density (integrated in y) viewed in the $x - z$ plane. The movie is saturated at $\pm 4.8 \times 10^{22}$ ergs.

- *magnet48b_free_yz.mpg*
  Free magnetic energy density (integrated in x) viewed in the $y - z$ plane. The movie is saturated at $\pm 4.8 \times 10^{22}$ ergs.

- *magnet48b_free_xz_nulls.mpg*
  Free magnetic energy density (integrated in y) viewed in the $x - z$ plane, with null points (yellow stars). The movie is saturated at $\pm 4.8 \times 10^{22}$ ergs.

- *magnet48b_free_yz_nulls.mpg*
  Free magnetic energy density (integrated in x) viewed in the $y - z$ plane, with null points (yellow stars). The movie is saturated at $\pm 4.8 \times 10^{22}$ ergs.

- *magnet48b_q_ht.mpg*
  Energy dissipation, Q, (integrated in x and y) as a function of height.

- *magnet48b_q_xy.mpg*
  Energy dissipation, Q, (integrated in z) viewed in the $x - y$ plane. The movie is saturated at 1.5×10^5 ergs cm^{-2} s^{-1}.

- *magnet48b_q_xy_bz.mpg*
  Energy dissipation, Q, (integrated in z) viewed in the $x - y$ plane, with contours of B_z at $z = 0$ Mm. The movie is saturated at 1.5×10^5 ergs cm^{-2} s^{-1}.

- *magnet48b_q_xy_nulls.mpg*
  Energy dissipation, Q, (integrated in z) viewed in the $x - y$ plane, with null points (yellow stars). The movie is saturated at 1.5×10^5 ergs cm^{-2} s^{-1}.

- *magnet48b_q_xy_3_10.mpg*
  Energy dissipation, Q, integrated between $z = 3 - 10$ Mm, viewed in the $x - y$ plane. The movie is saturated at 3×10^3 ergs cm^{-2} s^{-1}.

- *magnet48b_q_xy_3_10_nulls.mpg*
  Energy dissipation, Q, integrated between $z = 3 - 10$ Mm, viewed in the $x - y$ plane, with null points (yellow stars). The movie is saturated at 3×10^3 ergs cm^{-2} s^{-1}.

- *magnet48b_q_xy_6_10.mpg*
  Energy dissipation, Q, integrated between $z = 6 - 10$ Mm, viewed in the $x - y$ plane. The movie is saturated at 1×10^3 ergs cm^{-2} s^{-1}.

- *magnet48b_q_xy_6.mpg*
  Energy dissipation, Q, viewed in the $x - y$ plane at $z = 6$ Mm. The movie is saturated at 146 ergs cm^{-2} s^{-1}.

- *magnet48b_q_xz.mpg*
  Energy dissipation, Q, (integrated in y) viewed in the $x - z$ plane. The movie is saturated at 1.5×10^5 ergs cm^{-2} s^{-1}.

- *magnet48b_q_yz.mpg*
  Energy dissipation, Q, (integrated in x) viewed in the $y - z$ plane. The movie is saturated at 1.5×10^5 ergs cm^{-2} s^{-1}.

- *magnet48b_q_xz_nulls.mpg*
  Energy dissipation, Q, (integrated in y) viewed in the $x - z$ plane, with null points (yellow stars). The movie is saturated at 1.5×10^5 ergs cm^{-2} s^{-1}.

- *magnet48b_q_yz_nulls.mpg*
  Energy dissipation, Q, (integrated in x) viewed in the $y - z$ plane, with null points (yellow stars). The movie is saturated at 1.5×10^5 ergs cm^{-2} s^{-1}.

- *magnet48b_q_xz_log.mpg*
  Logarithm of energy dissipation, Q, (integrated in y) viewed in the $x - z$ plane.

- *magnet48b_q_yz_log.mpg*
  Logarithm of energy dissipation, Q, (integrated in x) viewed in the $y - z$ plane.

- *magnet48b_q_xz_log_nulls.mpg*
  Logarithm of energy dissipation, Q, (integrated in y) viewed in the $x - z$ plane, with null points (yellow stars).

- *magnet48b_q_yz_log_nulls.mpg*
  Logarithm of energy dissipation, Q, (integrated in x) viewed in the $y - z$ plane, with null points (yellow stars).

- *magnet48b_v_xy_nulls.mpg*
  Magnetofrictional velocity squared, $\mathbf{v}^2$, (summed in z) viewed in the $x-y$ plane, with null points (yellow stars). The movie is saturated at 85.3 km^2 s^{-2} ((9.2 km s^{-1})^2).

- *magnet48b_v_xz_log_nulls.mpg*
  Logarithm of $\mathbf{v}^2$ (integrated in y) viewed in the $x-z$ plane, with null points (yellow stars).

- *magnet48b_v_yz_log_nulls.mpg*
  Logarithm of $\mathbf{v}^2$ (integrated in x) viewed in the $y-z$ plane, with null points (yellow stars).

- *magnet48_v_xy_nulls.mpg*
  For the 0 G simulation: Magnetofrictional velocity squared ($\mathbf{v}^2$) (summed in z) viewed in the $x-y$ plane, with null points (yellow stars). The movie is saturated at 85.3 km^2 s^{-2} ((9.2 km s^{-1})^2).

- *magnet48_v_xz_log_nulls.mpg*
  For the 0 G simulation: Logarithm of $\mathbf{v}^2$ (integrated in y) viewed in the $x-z$ plane, with null points (yellow stars).

- *magnet48_v_yz_log_nulls.mpg*
  For the 0 G simulation: Logarithm of $\mathbf{v}^2$ (integrated in x) viewed in the $y-z$ plane, with null points (yellow stars).

- *magnet48b_j_xy_bz.mpg*
  Current density squared, $\mathbf{j}^2$, (integrated in z) viewed in the $x-y$ plane, with contours of B_z at $z=0$ Mm.

- *magnet48b_j_xz_log_nulls.mpg*
  Logarithm of $\mathbf{j}^2$ (integrated in y) viewed in the $x-z$ plane, with null points (yellow stars).

- *magnet48b_j_yz_log_nulls.mpg*
  Logarithm of $\mathbf{j}^2$ (integrated in x) viewed in the $y-z$ plane, with null points (yellow stars).

Appendix D

Carrot Cake

For the cake:

- 10 oz/315 g caster sugar
- 8 fl oz/250 ml sunflower oil
- 3 eggs
- 6 oz/185 g
- $1\frac{1}{2}$ tsp baking powder
- $1\frac{1}{2}$ tsp ground cinnamon
- $\frac{1}{2}$ tsp ground cloves
- $\frac{1}{2}$ tsp sea salt
- 8 oz/250 g carrots, grated finely
- 4 oz/ 125 g walnuts, finely chopped

1. Preheat oven to $180°$C/$350°$F/Gas 4. Line a round cake tin with buttered greaseproof paper.
2. Mix the sugar and oil together in a large bowl, beating with a wooden spoon.
3. Break in the eggs, one at a time, beating each until it is amalgamated.
4. Sift the flour into another bowl with baking powder, cinnamon, cloves and salt. Add spoonful by spoonful to the first mixture, continuing to beat.

5. Finally, stir in the carrots and nuts.
6. Spoon the mixture into the cake tin and bake for $70 - 80$ min until cooked.

For the cream cheese frosting:

- 3 oz/90 g cream cheese
- $1\frac{1}{2}$ oz/45 g unsalted butter
- 3 tbsp caster sugar

1. Beat the cream cheese until smooth.
2. Add the butter, cut into small bits at room temperature, mashing into the cheese until blended.
3. Stir in the sugar, beating until smooth.
4. When the cake has cooled, spread the frosting over the top.

Bibliography

V. Archontis, F. Moreno-Insertis, K. Galsgaard, A. Hood, and E. O'Shea. Emergence of magnetic flux from the convection zone into the corona. *Astron. Astrophys.*, 426:1047–1063, November 2004.

V. Archontis, K. Tsinganos, and C. Gontikakis. Recurrent solar jets in active regions. *Astron. Astrophys.*, 512:L2, March 2010.

P. Barthol, A. Gandorfer, S. K. Solanki, M. Schüssler, B. Chares, W. Curdt, W. Deutsch, A. Feller, D. Germerott, B. Grauf, K. Heerlein, J. Hirzberger, M. Kolleck, R. Meller, R. Müller, T. L. Riethmüller, G. Tomasch, M. Knölker, B. W. Lites, G. Card, D. Elmore, J. Fox, A. Lecinski, P. Nelson, R. Summers, A. Watt, V. Martínez Pillet, J. A. Bonet, W. Schmidt, T. Berkefeld, A. M. Title, V. Domingo, J. L. Gasent Blesa, J. C. Del Toro Iniesta, A. López Jiménez, A. Álvarez-Herrero, L. Sabau-Graziati, C. Widani, P. Haberler, K. Härtel, D. Kampf, T. Levin, I. Pérez Grande, A. Sanz-Andrés, and E. Schmidt. The Sunrise Mission. *Solar Phys.*, 268:1–34, January 2011.

M. A. Berger. Structure and stability of constant-alpha force-free fields. *Astrophys. J. Suppl.*, 59: 433–444, November 1985.

A. Bhattacharjee and E. Hameiri. Self-consistent dynamolike activity in turbulent plasmas. *Physical Review Letters*, 57:206–209, July 1986.

A. H. Boozer. Ohm's law for mean magnetic fields. *Journal of Plasma Physics*, 35:133–139, February 1986.

P. K. Browning, R. van der Linden, C. Gerrard, R. Kevis, and A. Hood. Coronal Heating by Nanoflares: a Reconnection Model. In R. W. Walsh, J. Ireland, D. Danesy, & B. Fleck, editor, *SOHO 15 Coronal Heating*, volume 575 of *ESA Special Publication*, pages 210–215, December 2004.

P. K. Browning, C. Gerrard, A. W. Hood, R. Kevis, and R. A. M. van der Linden. Heating the corona by nanoflares: simulations of energy release triggered by a kink instability. *Astron. Astrophys.*, 485:837–848, July 2008.

P. J. Cargill. The Fine Structure of a Nanoflare-Heated Corona. *Solar Phys.*, 147:263–268, October 1993.

J. Chae, S. F. Martin, H. S. Yun, J. Kim, S. Lee, P. R. Goode, T. Spirock, and H. Wang. Small

Magnetic Bipoles Emerging in a Filament Channel. *Astrophys. J.*, 548:497–507, February 2001.

R. M. Close, C. E. Parnell, D. H. Mackay, and E. R. Priest. Statistical Flux Tube Properties of 3D Magnetic Carpet Fields. *Solar Phys.*, 212:251–275, February 2003.

R. M. Close, C. E. Parnell, D. W. Longcope, and E. R. Priest. Recycling of the Solar Corona's Magnetic Field. *Astrophys. J. Lett.*, 612:L81–L84, September 2004.

S. R. Cranmer and A. A. van Ballegooijen. Can the Solar Wind be Driven by Magnetic Reconnection in the Sun's Magnetic Carpet? *Astrophys. J.*, 720:824–847, September 2010.

I. De Moortel and K. Galsgaard. Numerical modelling of 3D reconnection due to rotational footpoint motions. *Astron. Astrophys.*, 451:1101–1115, June 2006.

B. de Pontieu. Chromospheric Dynamics: Spicules and Waves. In K. Shibata, S. Nagata, & T. Sakurai, editor, *New Solar Physics with Solar-B Mission*, volume 369 of *Astronomical Society of the Pacific Conference Series*, pages 231–242, October 2007.

A. G. de Wijn, B. W. Lites, T. E. Berger, Z. A. Frank, T. D. Tarbell, and R. Ishikawa. Hinode Observations of Magnetic Elements in Internetwork Areas. *Astrophys. J.*, 684:1469–1476, September 2008.

C. E. DeForest, H. J. Hagenaar, D. A. Lamb, C. E. Parnell, and B. T. Welsch. Solar Magnetic Tracking. I. Software Comparison and Recommended Practices. *Astrophys. J.*, 666:576–587, September 2007.

J. A. Eddy. The Maunder Minimum. *Science*, 192:1189–1202, June 1976.

R. Erdélyi. Coronal heating: Heating in the solar atmosphere. *Astronomy and Geophysics*, 45(4): 4.34–4.37, August 2004.

K. Galsgaard and Å. Nordlund. Heating and activity of the solar corona 1. Boundary shearing of an initially homogeneous magnetic field. *J. Geophys. Res.*, 101:13445–13460, June 1996.

K. Galsgaard and C. E. Parnell. Elementary heating events - magnetic interactions between two flux sources. III. Energy considerations. *Astron. Astrophys.*, 439:335–349, August 2005.

K. Galsgaard, C. E. Parnell, and J. Blaizot. Elementary heating events - Magnetic interactions between two flux sources. *Astron. Astrophys.*, 362:395–405, October 2000.

L. Golub and J. M. Pasachoff. *The Solar Corona*. September 1997.

L. Golub, A. S. Krieger, J. K. Silk, A. F. Timothy, and G. S. Vaiana. Solar X-Ray Bright Points. *Astrophys. J. Lett.*, 189:L93–L97, April 1974.

S. R. Habbal and E. Grace. The connection between coronal bright points and the variability of the quiet-sun extreme-ultraviolet emission. *Astrophys. J.*, 382:667–676, December 1991.

S. R. Habbal and G. L. Withbroe. Spatial and temporal variations of EUV coronal bright points. *Solar Phys.*, 69:77–97, January 1981.

H. J. Hagenaar. Ephemeral Regions on a Sequence of Full-Disk Michelson Doppler Imager Magnetograms. *Astrophys. J.*, 555:448–461, July 2001.

H. J. Hagenaar, C. J. Schrijver, and A. M. Title. The Distribution of Cell Sizes of the Solar Chromospheric Network. *Astrophys. J.*, 481:988–995, May 1997.

H. J. Hagenaar, C. J. Schrijver, and A. M. Title. The Properties of Small Magnetic Regions on the Solar Surface and the Implications for the Solar Dynamo(s). *Astrophys. J.*, 584:1107–1119, February 2003.

H. J. Hagenaar, M. L. DeRosa, and C. J. Schrijver. The Dependence of Ephemeral Region Emergence on Local Flux Imbalance. *Astrophys. J.*, 678:541–548, May 2008.

G. E. Hale. On the Probable Existence of a Magnetic Field in Sun-Spots. *Astrophys. J.*, 28: 315–347, November 1908.

W. Hanle. Über magnetische Beeinflussung der Polarisation der Resonanzfluoreszenz. *Zeitschrift fur Physik*, 30:93–105, December 1924.

K. L. Harvey. *Magnetic Bipoles on the Sun*. PhD thesis, , Univ. Utrecht, (1993), 1993.

K. L. Harvey and S. F. Martin. Ephemeral Active Regions. *Solar Phys.*, 32:389–402, October 1973.

A. L. Haynes and C. E. Parnell. A trilinear method for finding null points in a three-dimensional vector space. *Physics of Plasmas*, 14(8):082107, August 2007.

J. Heyvaerts and E. R. Priest. Coronal heating by phase-mixed shear Alfven waves. *Astron. Astrophys.*, 117:220–234, January 1983.

J. Heyvaerts and E. R. Priest. Coronal heating by reconnection in DC current systems - A theory based on Taylor's hypothesis. *Astron. Astrophys.*, 137:63–78, August 1984.

A. W. Hood, P. K. Browning, and R. A. M. van der Linden. Coronal heating by magnetic reconnection in loops with zero net current. *Astron. Astrophys.*, 506:913–925, November 2009.

M. Kramar and B. Inhester. Inversion of coronal Zeeman and Hanle observations to reconstruct the coronal magnetic field. *Memorie della Societa Astronomica Italiana*, 78:120–125, 2007.

M. Kramar, B. Inhester, and S. K. Solanki. Vector tomography for the coronal magnetic field. I. Longitudinal Zeeman effect measurements. *Astron. Astrophys.*, 456:665–673, September 2006.

M. Kuperus, J. A. Ionson, and D. S. Spicer. On the theory of coronal heating mechanisms. *Annual. Rev. Astron. Astrophys.*, 19:7–40, 1981.

D. A. Lamb, C. E. DeForest, H. J. Hagenaar, C. E. Parnell, and B. T. Welsch. Solar Magnetic Tracking. II. The Apparent Unipolar Origin of Quiet-Sun Flux. *Astrophys. J.*, 674:520–529, February 2008.

D. A. Lamb, C. E. DeForest, H. J. Hagenaar, C. E. Parnell, and B. T. Welsch. Solar Magnetic Tracking. III. Apparent Unipolar Flux Emergence in High-resolution Observations. *Astrophys. J.*, 720:1405–1416, September 2010.

F. Leblanc. *An Introduction to Stellar Astrophysics*. 2010.

R. B. Leighton. Transport of Magnetic Fields on the Sun. *Astrophys. J.*, 140:1547–1562, November 1964.

J. L. Leroy, V. Bommier, and S. Sahal-Brechot. The magnetic field in the prominences of the polar crown. *Solar Phys.*, 83:135–142, February 1983.

B. W. Lites. A new perspective on quiet Sun magnetism. *Science in China G: Physics and*

Astronomy, 52:1660–1664, November 2009.

S. H. B. Livi, J. Wang, and S. F. Martin. The cancellation of magnetic flux. I - On the quiet sun. *Australian Journal of Physics*, 38:855–873, 1985.

D. Longcope. Quantifying Magnetic Reconnection and the Heat it Generates. In R. W. Walsh, J. Ireland, D. Danesy, & B. Fleck, editor, *SOHO 15 Coronal Heating*, volume 575 of *ESA Special Publication*, pages 198–209, December 2004.

D. W. Longcope. A Model for Current Sheets and Reconnection in X-Ray Bright Points. *Astrophys. J.*, 507:433–442, November 1998.

D. W. Longcope and C. C. Kankelborg. Coronal Heating by Collision and Cancellation of Magnetic Elements. *Astrophys. J.*, 524:483–495, October 1999.

D. H. Mackay and A. A. van Ballegooijen. A Non-Linear Force-Free Field Model for the Evolving Magnetic Structure of Solar Filaments. *Solar Phys.*, 260:321–346, December 2009.

D. H. Mackay, L. M. Green, and A. van Ballegooijen. Modeling the Dispersal of an Active Region: Quantifying Energy Input into the Corona. *Astrophys. J.*, 729:97–107, March 2011.

D. MacTaggart and A. W. Hood. On the emergence of toroidal flux tubes: general dynamics and comparisons with the cylinder model. *Astron. Astrophys.*, 507:995–1004, November 2009.

S. F. Martin. The identification and interaction of network, intranetwork, and ephemeral-region magnetic fields. *Solar Phys.*, 117:243–259, September 1988.

S. F. Martin. Small-Scale Magnetic Features Observed in the Photosphere. 138:129–146, 1990.

S. F. Martin, S. H. B. Livi, and J. Wang. The cancellation of magnetic flux. II - In a decaying active region. *Australian Journal of Physics*, 38:929–959, 1985.

S. W. McIntosh, A. R. Davey, D. M. Hassler, J. D. Armstrong, W. Curdt, K. Wilhelm, and G. Lin. Observations Supporting the Role of Magnetoconvection in Energy Supply to the Quiescent Solar Atmosphere. *Astrophys. J.*, 654:650–664, January 2007.

C. Mellor, C. L. Gerrard, K. Galsgaard, A. W. Hood, and E. R. Priest. Numerical Simulations of the Flux Tube Tectonics Model for Coronal Heating. *Solar Phys.*, 227:39–60, March 2005.

K. A. Meyer, D. H. Mackay, A. A. van Ballegooijen, and C. E. Parnell. Solar Magnetic Carpet I: Simulation of Synthetic Magnetograms. *Solar Phys.*, 272:29–58, August 2011.

K. A. Meyer, D. H. Mackay, and A. A. van Ballegooijen. Solar Magnetic Carpet II: Coronal Interactions of Small-Scale Magnetic Fields. *Solar Phys.*, 278:149–175, May 2012.

R. Mitalas and K. R. Sills. On the photon diffusion time scale for the sun. *Astrophys. J.*, 401: 759–760, December 1992.

R. W. Noyes. *The sun, our star*. 1982.

U. Paniveni, V. Krishan, J. Singh, and R. Srikanth. Relationship between horizontal flow velocity and cell lifetime for supergranulation from SOHO Dopplergrams. *Mon. Not. Roy. Astron. Soc.*, 347:1279–1281, February 2004.

E. N. Parker. Nanoflares and the solar X-ray corona. *Astrophys. J.*, 330:474–479, July 1988.

C. E. Parnell. A model of the Solar Magnetic Carpet. *Solar Phys.*, 200:23–45, May 2001.

C. E. Parnell. Nature of the magnetic carpet - I. Distribution of magnetic fluxes. *Mon. Not. Roy.*

Astron. Soc., 335:389–398, September 2002.

C. E. Parnell and K. Galsgaard. Elementary heating events - magnetic interactions between two flux sources. II. Rates of flux reconnection. *Astron. Astrophys.*, 428:595–612, December 2004.

C. E. Parnell, A. L. Haynes, and K. Galsgaard. Recursive Reconnection and Magnetic Skeletons. *Astrophys. J.*, 675:1656–1665, March 2008.

C. E. Parnell, C. E. DeForest, H. J. Hagenaar, B. A. Johnston, D. A. Lamb, and B. T. Welsch. A Power-Law Distribution of Solar Magnetic Fields Over More Than Five Decades in Flux. *Astrophys. J.*, 698:75–82, June 2009.

C. E. Parnell, A. L. Haynes, and K. Galsgaard. Structure of magnetic separators and separator reconnection. *Journal of Geophysical Research (Space Physics)*, 115:A02102, February 2010.

K. J. H. Phillips. *Guide to the sun*. 1992.

H. E. Potts, R. K. Barrett, and D. A. Diver. Balltracking: An highly efficient method for tracking flow fields. *Astron. Astrophys.*, 424:253–262, September 2004.

E. R. Priest. *Solar Magnetohydrodynamics*. D. Reidel Publishing Company, Dordrecht, 1982.

E. R. Priest and P. Démoulin. Three-dimensional magnetic reconnection without null points. 1. Basic theory of magnetic flipping. *J. Geophys. Res.*, 100:23443–23464, December 1995.

E. R. Priest, C. E. Parnell, and S. F. Martin. A converging flux model of an X-ray bright point and an associated canceling magnetic feature. *Astrophys. J.*, 427:459–474, May 1994.

E. R. Priest, J. F. Heyvaerts, and A. M. Title. A Flux-Tube Tectonics Model for Solar Coronal Heating Driven by the Magnetic Carpet. *Astrophys. J.*, 576:533–551, September 2002.

E. R. Priest, D. W. Longcope, and J. Heyvaerts. Coronal Heating at Separators and Separatrices. *Astrophys. J.*, 624:1057–1071, May 2005.

N.-E. Raouafi, S. K. Solanki, and T. Wiegelmann. Hanle Effect Diagnostics of the Coronal Magnetic Field: A Test Using Realistic Magnetic Field Configurations. 405:429–434, June 2009.

S. Régnier. Nonlinear force-free field extrapolation: numerical methods and applications. *Memorie della Societa Astronomica Italiana*, 78:126–135, 2007.

S. Régnier, C. E. Parnell, and A. L. Haynes. A new view of quiet-Sun topology from Hinode/SOT. *Astron. Astrophys.*, 484:L47–L50, June 2008.

A. L. Restante. *The investigation of quasi-separatrix layers in solar magnetic fields*. PhD thesis, University of St Andrews ¡EMAIL¿annalisa@mcs.st-and.ac.uk¡/EMAIL¿, 2011.

M. Rieutord and F. Rincon. The Sun's Supergranulation. *Living Reviews in Solar Physics*, 7:2, June 2010.

B. Roberts. Waves and Oscillations in the Corona - (Invited Review). *Solar Phys.*, 193:139–152, April 2000.

Y. Sakamoto, S. Tsuneta, and G. Vekstein. A Nanoflare Heating Model and Comparison with Observations. *Astrophys. J.*, 703:2118–2130, October 2009.

P. H. Scherrer, R. S. Bogart, R. I. Bush, J. T. Hoeksema, A. G. Kosovichev, J. Schou, W. Rosenberg, L. Springer, T. D. Tarbell, A. Title, C. J. Wolfson, I. Zayer, and MDI Engineering Team. The Solar Oscillations Investigation - Michelson Doppler Imager. *Solar Phys.*, 162:129–188,

December 1995.

P. H. Scherrer, J. Schou, R. I. Bush, A. G. Kosovichev, R. S. Bogart, J. T. Hoeksema, Y. Liu, T. L. Duvall, J. Zhao, A. M. Title, C. J. Schrijver, T. D. Tarbell, and S. Tomczyk. The Helioseismic and Magnetic Imager (HMI) Investigation for the Solar Dynamics Observatory (SDO). *Solar Phys.*, 275:207–227, January 2012.

C. J. Schrijver and A. M. Title. The topology of a mixed-polarity potential field, and inferences for the heating of the quiet solar corona. *Solar Phys.*, 207:223–240, June 2002.

C. J. Schrijver and A. M. Title. The Magnetic Connection between the Solar Photosphere and the Corona. *Astrophys. J. Lett.*, 597:L165–L168, November 2003.

C. J. Schrijver, A. M. Title, A. A. van Ballegooijen, H. J. Hagenaar, and R. A. Shine. Sustaining the Quiet Photospheric Network: The Balance of Flux Emergence, Fragmentation, Merging, and Cancellation. *Astrophys. J.*, 487:424–436, September 1997.

C. J. Schrijver, M. L. Derosa, T. R. Metcalf, Y. Liu, J. McTiernan, S. Régnier, G. Valori, M. S. Wheatland, and T. Wiegelmann. Nonlinear Force-Free Modeling of Coronal Magnetic Fields Part I: A Quantitative Comparison of Methods. *Solar Phys.*, 235:161–190, May 2006.

G. W. Simon and R. B. Leighton. Velocity Fields in the Solar Atmosphere. III. Large-Scale Motions, the Chromospheric Network, and Magnetic Fields. *Astrophys. J.*, 140:1120–1149, October 1964.

G. W. Simon, A. M. Title, and N. O. Weiss. Sustaining the Sun's Magnetic Network with Emerging Bipoles. *Astrophys. J.*, 561:427–434, November 2001.

A. Skumanich and B. W. Lites. Stokes profile analysis and vector magnetic fields. I - Inversion of photospheric lines. *Astrophys. J.*, 322:473–482, November 1987.

S. K. Solanki. Smallscale Solar Magnetic Fields - an Overview. *Space Science Reviews*, 63, March 1993.

H. C. Spruit, A. Nordlund, and A. M. Title. Solar convection. *Annual. Rev. Astron. Astrophys.*, 28:263–301, 1990.

J. O. Stenflo. Solar physics: Hidden magnetism. *Nature*, 430:304–305, July 2004.

J. O. Stenflo. Solar magnetic fields. *Journal of Astrophysics and Astronomy*, 29:19–28, March 2008.

H. R. Strauss. Turbulent reconnection. *Astrophys. J.*, 326:412–417, March 1988.

L. M. Thornton. *Small-Scale Magnetic Feature Evolution as Observed by Hinode/NFI and SOHO/MDI*. PhD thesis, Univ. St Andrews, 2011.

L. M. Thornton and C. E. Parnell. Small-Scale Flux Emergence Observed Using Hinode/SOT. *Solar Phys.*, 269:13–40, March 2011.

A. Title. Magnetic fields below, on and above the solar surface. 358:657–668, February 2000.

A. A. van Ballegooijen and S. R. Cranmer. Hyperdiffusion as a Mechanism for Solar Coronal Heating. *Astrophys. J.*, 682:644–653, July 2008.

A. A. van Ballegooijen, P. Nisenson, R. W. Noyes, M. G. Löfdahl, R. F. Stein, Å. Nordlund, and V. Krishnakumar. Dynamics of Magnetic Flux Elements in the Solar Photosphere. *Astrophys.*

J., 509:435–447, December 1998.

A. A. van Ballegooijen, E. R. Priest, and D. H. Mackay. Mean Field Model for the Formation of Filament Channels on the Sun. *Astrophys. J.*, 539:983–994, August 2000.

B. von Rekowski, C. E. Parnell, and E. R. Priest. Solar coronal heating by magnetic cancellation - I. Connected equal bipoles. *Mon. Not. Roy. Astron. Soc.*, 366:125–136, February 2006.

H. Wang. On the relationship between magnetic fields and supergranule velocity fields. *Solar Phys.*, 117:343–358, September 1988.

H. Wang and H. Zirin. Study of supergranules. *Solar Phys.*, 120:1–17, March 1989.

J. Wang, H. Wang, F. Tang, J. W. Lee, and H. Zirin. Flux distribution of solar intranetwork magnetic fields. *Solar Phys.*, 160:277–288, September 1995.

D. F. Webb, S. F. Martin, D. Moses, and J. W. Harvey. The correspondence between X-ray bright points and evolving magnetic features in the quiet sun. *Solar Phys.*, 144:15–35, March 1993.

A. L. Wilmot-Smith, D. I. Pontin, A. R. Yeates, and G. Hornig. Heating of braided coronal loops. *ArXiv e-prints*, November 2011.

G. L. Withbroe and R. W. Noyes. Mass and energy flow in the solar chromosphere and corona. *Annual. Rev. Astron. Astrophys.*, 15:363–387, 1977.

W. H. Yang, P. A. Sturrock, and S. K. Antiochos. Force-free magnetic fields - The magneto-frictional method. *Astrophys. J.*, 309:383–391, October 1986.

A. R. Yeates, D. H. Mackay, and A. A. van Ballegooijen. Modelling the Global Solar Corona II: Coronal Evolution and Filament Chirality Comparison. *Solar Phys.*, 247:103–121, January 2008.

G. P. Zhou, J. X. Wang, and C. L. Jin. Solar Intranetwork Magnetic Elements: Evolution and Lifetime. *Solar Phys.*, 267:63–73, November 2010.

H. Zirin. Evolution of weak solar magnetic fields. *Australian Journal of Physics*, 38:961–969, 1985.